Novel Approaches to the Investigation and Remediation of the Environmental Impacts of Mercury in the Environment

A thesis submitted to the University of Manchester for the degree of Doctor of Philosophy in the Faculty of Science and Engineering

2021

Alexander James Tait

Department of Earth and Environmental Sciences

Contents

Figures

Tables

Abbreviations

16S rRNA	16S Ribosomal Ribonucleic Acid
ACC	Activated Carbon Colloid
AFS	Atomic Fluorescence Spectroscopy
ATSDR	Agency of Toxic Substances and Disease Registry
CEC	Cation Exchange Capacity
CMC	Carboxymethyl Cellulose
COSHH	Control of Substances Hazardous to Health
CV-AFS	Cold Vapour - Atomic Fluorescence Spectroscopy
DEFRA	Department for Environment, Food and Rural Affairs
DIRB`	Dissimilatory Sulfate-Reducing Bacteria
DIW	Deionised Water
DOC	Dissolved Organic Carbon
DOM	Dissolved Organic Matter
DSRB	Dissimilatory Sulfate-Reducing Bacteria
EC	European Commission
EDS	Energy Dispersive X-Ray Spectroscopy
EDTA	Ethylenediaminetetraacetic Acid
EEA	European Environment Agency
EFSA	European Food Safety Authority
EST	Estuarine Sediment
EU	European Union
EXAFS	Extended X-Ray Absorption Fine Structure

GEM	Gaseous Elemental Mercury
HCV	Health Criteria Values
IC	Ion Chromatography
ICP-AES	Inductively Coupled Plasma – Atomic Emission Spectrometry
ICP-MS	Inductively Coupled Plasma – Mass Spectrometry
IRB	Iron-Reducing Bacteria
LOI	Loss on Ignition
MLR	Marsh Lock, Runcorn (UK)
$NADPH_2$	Reduced Nicotinamide Adenine Dinucleotide Phosphate Dehydrogenase
NBAF	Nutrient Broth Acetate Formate
NICOLE	Network for Industrially Contaminated Land in Europe
nZVI	Nanoscale Zero Valent Iron
OM	Organic Matter
ORP / Eh	Oxidation Reduction Potential
ppb	Parts Per Billion
ppm	Parts Per Million
ppt	Parts Per Trillion
RT	Room Temperature
SEM	Scanning Electron Microscopy
SEP	Sequential Extraction Protocol
SI	Supplementary Information
SGVs	Soil Guideline Values
SRB	Sulfate-Reducing Bacteria

TDI	Total Daily Intake
TEM	Transmission Electron Microscopy
THg	Total Hg
UNEP	United Nations Environmental Programme
UV-Vis	Ultraviolet–visible Spectrophotometry
WHO	World Health Organisation
WRC	Williamson Research Centre for Molecular Environmental Science
XANES	X-ray Absorption Near Edge Structure
XAS	X-ray Absorption Spectroscopy
XPS	X-ray Photoelectron Spectroscopy
XRD	X-ray Diffraction
XRF	X-Ray Fluorescence
ZVI	Zero Valent Iron [Fe^0]

Thesis Abstract

The focus of this project was to develop and apply novel approaches to investigate Hg chemical speciation in the environment and explore methods that could be used for its remediation. Findings are presented as three research papers. Better understanding the mobility and chemical speciation of solid phase Hg at a site is critical for thorough risk assessment. In Paper 1, advanced analytical techniques [e.g. X-ray Absorption Spectroscopy (XAS)] were applied to identify the chemical speciation of Hg in a canal bed (MLR) sediment impacted by legacy discharge from industry. A sequential extraction protocol (SEP), in combination with ICP-MS, was applied to establish the potential mobility and potential bioavailability of highly toxic Hg. X-ray Diffraction (XRD) indicated that the sediment mineralogy was dominated by calcite and brucite, which are key components of solid waste from Hg-cell chlor-alkali plants. SEPs revealed that the bulk of Hg (>97%) was recalcitrant, likely strongly complexed, or mineral bound, and therefore relatively immobile with limited bioavailability. XAS revealed that >85% Hg was beta-HgS, and the bulk of the remaining portion was likely Hg(II) sorbed to sediment. Organometallic methylmercury (MeHg) [55 ± 1 μg/kg] potentially poses the largest risk, despite contributing <0.1% of total Hg [86 ± 1 mg/kg], due to its high toxicity and its tendency to bioaccumulate. 16S rRNA gene sequencing identified bacterial species potentially capable of catalysing both sulfidation and methylation reactions in the sediment.

Iron-based nanoparticles and biostimulation via slow-release electron donor based organic substrates have previously shown capacity for the immobilisation of mobile contaminant metals [e.g. Cr(VI) and Tc(VII)] in anoxic subsurface water and sediment. The impact of four treatments [NanoFER 25S (nZVI)], Carbo-Iron® (nZVI and activated carbon composite), biogenic magnetite (biomagnetite) and organic electron donors) on Hg chemical speciation in two sediments [MLR and estuarine (EST)], were investigated in Paper 2 in the context of changes to key biogeochemical parameters. Analysis of microcosms, containing anoxic Hg-contaminated artificial groundwater (AGW) and sediment, suggested that solid phase Hg transformations were influenced by the type of treatment, the unique geochemical characteristics of sediment matrices and their respective microbial populations. Treatments containing nZVI (NanoFER 25S and Carbo-Iron®) were considered to pose the greatest risk in respect to potential reductive mobilisation (via Hg(0) volatilisation) and Hg methylation. Hg chemical speciation in samples was identified by k^3-weighted L_{III}-edge EXAFS linear combination fitting to known Hg standard reference materials. Results suggest that NanoFER 25S may present a risk, in respect to potential volatilisation of Hg as Hg(0). nZVI treatments induced and maintained reducing conditions for the duration of the experiment (911 days) independent of sediment type, consistent with the reduction of sorbed Hg(II), and also formation of immobile beta-HgS, identified in the MLR sediment. Notably, Hg methylation increased in both sediments following addition of Carbo-Iron®.

Biomagnetite and biostimulation with organic electron donors both accelerated Hg immobilisation, via sulfidation, in EST sediment, but appeared to inhibit sulfidation in MLR sediment when compared to no treatment controls. Natural attenuation of Hg by sulfidation was effective at immobilising Hg(II) as beta-HgS irrespective of sediment type. This work emphasises the importance of considering not only the type of treatment, but also the individual site conditions (e.g. sediment matrix chemical composition, microbial community diversity, additional contaminants, etc.) when considering applying treatments *in situ*. Findings add to the portfolio of scientific information required to assess the suitability of iron-based nanoparticles (e.g. magnetite, nZVI and Carbo-Iron®) for remediation of Hg-contaminated waters and sediment. Application of treatment materials should be undertaken with caution, as despite potentially beneficial immobilising effects in respect to one contaminant [e.g. Cr(VI)) under specific site conditions, intervention may have potentially adverse effects in respect to mobilisation of other contaminants [e.g. Hg(II)].

Mitigating risks posed by formation of volatile Hg(0) in treatment systems, must be a consideration prior to application of iron-based nanoparticles, especially nZVI. Existing technologies that attempt to reduce Hg(II) often require costly capture mechanisms for gaseous Hg(0). A multi-contaminant approach to remediating Hg-contaminated AGW was investigated in Paper 3. Hg amalgams have historically been used widely in dentistry. Amalgam formation with other metals (e.g. Ag and Cu) provide benefits in respect to mechanical strength and stability, potentially reducing the tendency of Hg(0) to volatilise. Hg and Cu were both rapidly removed from AGW following addition of all particle treatments. Hg L_{III}-edge EXAFS linear combination fitting revealed that a solid Hg-Cu amalgam ($HgCu_{AM}$) likely formed in three treatment systems in which: (1) NanoFER 25S had been pre-coated with Cu prior to treatment of aqueous Hg(II) in AGW [Cu-NanoFER 25S Hg(II)]; (2) biomagnetite had been pre-coated with Cu prior to treatment of aqueous Hg(II) in AGW [Cu-biomagnetite Hg(II)]; and (3) NanoFER 25S had been applied for treatment of AGW containing aqueous Hg(II) and Cu(II). Cu-coating biomagnetite was an important step to enable $HgCu_{AM}$ formation but was of less importance with respect to application of NanoFER 25S. SEP recovery data suggested $HgCu_{AM}$ formed in Cu-biomagnetite Hg(II) microcosms may be less stable than that formed in the NanoFER 25S systems containing Cu. Hg and Cu recovery was lowest in extracts from $HgCu_{AM}$ formed in Cu-containing NanoFER 25S systems. However, recovery was lowest for both Hg [50%] and Cu [43%] from endpoint solids in Cu-NanoFER 25S Hg(II) systems, likely due to the formation of a more recalcitrant $HgCu_{AM}$. However, due to the volatility of Hg(0) there is uncertainty regarding whether the bulk of residual Hg is associated with Cu as an immobile alloy or whether some gaseous Hg(0) may have been emitted to headspace. There are concerns over the long-term fate, transformation, and eco-toxicity of nanoscale treatment technologies in environmental systems. Therefore, Cu-coated particles maybe more easily applied for treatment of Hg-contaminated industrial wastewaters at the point of pollution source in the shorter term. Future work including advance-TEM, particle size analysis, column experiments and gaseous Hg(0) monitoring are discussed.

Declaration

No portion of the work referred to in the thesis has been submitted in support of an application for another degree or qualification of this or any other university or other institute of learning.

Copyright statement

i. The author of this thesis (including any appendices and/or schedules to this thesis) owns certain copyright or related rights in it (the "Copyright") and s/he has given The University of Manchester certain rights to use such Copyright, including for administrative purposes.

ii. Copies of this thesis, either in full or in extracts and whether in hard or electronic copy, may be made only in accordance with the Copyright, Designs and Patents Act 1988 (as amended) and regulations issued under it or, where appropriate, in accordance

iii. The ownership of certain Copyright, patents, designs, trademarks and other intellectual property (the "Intellectual Property") and any reproductions of copyright works in the thesis, for example graphs and tables ("Reproductions"), which may be described in this thesis, may not be owned by the author and may be owned by third parties. Such Intellectual Property and Reproductions cannot and must not be made available for use without the prior written permission of the owner(s) of the relevant Intellectual Property and/or Reproductions.

iv. Further information on the conditions under which disclosure, publication and commercialisation of this thesis, the Copyright and any Intellectual Property and/or Reproductions described in it may take place is available in the University IP Policy (see http://documents.manchester.ac.uk/DocuInfo.aspx?DocID=24420) , in any relevant Thesis restriction declarations deposited in the University Library, The University Library's regulations (see http://www.library.manchester.ac.uk/about/regulations/) and in The University's policy on Presentation of Theses

COVID-19 Impact Statement

The multiple lockdown situation that has be implemented to minimise the impacts of COVID-19 have severely impacted my ability access core data, laboratory facilities and liaise with colleagues, due to various remote IT issues and access restriction to the workplace.

A 6 month extension was granted to allow me extra time to summit my PhD thesis to the required standard following the initial lockdown in the spring of 2020. The extension allowed me to submit the PhD thesis write up of my project by my updated deadline of 31st July. I note I had ongoing health issues during the write up and examination period that were exacerbated by the pandemic restrictions but that my perseverance has allowed me to present this corrected thesis.

Acknowledgements

This thesis is dedicated to the family, friends, teachers, and colleagues that have supported me on my journey through life and have helped me build up the courage to take on the challenge of this PhD project. My fiancée Hania; My mother Gill; My father Ian; My sister Fiona; My brother Chris; My grandparents Edna, Joan, Stan, and James all deserve a special mention as without them I would not be submitting this work today.

I would like to thank my main project supervisor Prof Jon Lloyd for giving me the opportunity to take on this project and providing valuable support throughout. This was big risk for him as I had little experience working in a laboratory and I had not worked in an academic setting for over 4 years before taking on this challenge.

The project co-supervisors all deserve a special thanks. Prof Sam Shaw, Prof David Polya and Prof Russell Thomas (WSP) have all helped me navigate some challenging terrain encountered over the course of completing this project.

Many thanks to the funders of this CASE award PhD project, without the financial support of the Engineering and Physical Science Research Council (EPSRC), WSP and AkzoNobel this important research work could not have been carried out.

I would like to thank past and current members of the Geomicro Research Group and Technical Support Staff for their help and support through this project. Sul Mulroy, Rick Kimber, Luke Townsend, Chris Boothman and Gianni Vettese all deserve a special mention for mentoring me in key laboratory and analytical techniques.

About The Author

The author grew up in rural Herefordshire and moved to Manchester in 2005, where he studied Biology at the University of Manchester, graduating in 2008 with an Upper 2nd Class (Hons) BSc degree. He spent time working as a Customer Services Advisor in Worcester before spending 4 months travelling in South-East Asia. He returned to Manchester in summer 2009 and worked as a Data Administrator for a clinical research company. Making a realisation that he wanted to better understand the Environmental Sciences, he studied Pollution and Environmental Control at the University of Manchester graduating in 2012 with a Distinction MSc degree. He subsequently worked as an Environmental Consultant for a multi-disciplinary consultancy company until he returned to the University of Manchester to undertake this PhD project at the age of 29 years and 8 months. It is never too late to take on a personal challenge, but having completed too many experiments to count, carried out hours of analysis, and now written and submitted this thesis in July 2021, I can say for sure that this was by far the most challenging work that I have done so far. Hopefully, scientific findings from this research project will have a positive impact on society as we attempt to make change to address the adverse environmental impacts society has caused through an era of uncontrolled global industrialisation.

1.0 Project Introduction

This research project set out to provide scientific information that could be used to better characterise Hg chemical speciation and mobility at contaminated sites and assist in the development of new approaches to remediation. Despite improvements to industrial processes (e.g. chlor-alkali chemical production) to minimise Hg discharge, in many parts of the world there is ongoing Hg pollution and a legacy of Hg-contamination in all environmental compartments (atmosphere, oceans, freshwater, sediments, etc.) related to human activities (UNEP, 2019). Mercury (Hg) and its compounds, especially organometallic methylmercury species, are pollutants of significant global concern due to their extensive global biogeochemical cycle and their high toxicity to ecosystems (Gfeller et al., 2021).

1.1 Aims & Objectives

The overall focus of this project was to develop and apply novel approaches for the investigation and mitigation of the environmental impacts of Hg in the environment. State-of-the-art analytical techniques were applied to identify the chemical speciation of Hg and explore the impact of remediation approaches including the addition of organic electron donors, and nanoscale iron-based particles. The aims of this project were to extend the literature base in relation to (1) investigating and remediating the environmental impacts of Hg, (2) quantifying the efficacy of existing *in situ* remediation techniques on Hg in anoxic subsurface sediment and groundwater and (3) innovating novel approaches to Hg remediation to ultimately assist in the development of future field and industrial remediation technologies. This project planned to address these aims with the following specific objectives:

(i) Determine the potential mobility of Hg in Hg-contaminated sediments using a selective sequential extraction protocol (SEP) in combination with ICPMS (Section 4.3.3).

(ii) Identify and quantify the compound specific inorganic Hg chemical speciation in sediments with XAS analysis (Section 4.3.4, Section 5.3.2, and Section 6.3.2).

(iii) Quantify organometallic MeHg species in sediments via specific targeted extraction and CV-AFS in collaboration with a commercial laboratory (Section 4.3.4, and Section 5.3.2).

(iv) Identify bacteria capable of influencing Hg chemical speciation (e.g. Hg reduction, sulfidation and methylation) via phylogenetic characterisation of communities in sediments using 16S rRNA gene sequencing techniques (Section 4.3.5 and Section 5.3.4).

(v) Set up long-term microcosm experiments to investigate the effectiveness of a portfolio of existing treatment strategies for remediating Hg-contaminated sediments utilising iron-based nanoparticle and organic electron donor technologies: (1) NanoFER25S, (2) Carbon-Iron, (3) Biogenic magnetite, and (4) Organic electron donors (Section 5).

(vi) Monitor changes to key biogeochemical parameters [pH, oxidation reduction potential (ORP), nitrate (NO_3^-), sulfate (SO_4^{2-}), Fe(II), microbial phylogenetics and Hg chemical speciation] in microcosms to establish temporal variation in the efficacy of treatment strategies in relation to potential Hg mobility and toxicity (Section 5.3).

(vii) Synthesise these complex datasets to establish how sediment geochemistry, native microbial populations, and specific environmental context can influence transformations in Hg chemical speciation (Section 4.4, Section 5.4 and Section 7).

(viii) Innovate and investigate a novel cost-effective approach that may have the potential to remediate Hg-contaminated water and sediment, in an environmental or industrial context (Section 6).

Findings of experimental work done as part of this project are presented here as three core research papers (Sections 4 – 6) and conclusions and future work (Section 7).

1.2 Thesis Structure

Section 2 – Literature Review

An overview of relevant previously published work on Hg, including sources to the environment, human health impacts, regulatory context, chemical speciation, environmental cycle, biogeochemistry, and remediation.

Section 3 – Experimental Methods & Analytical Techniques

An overview of methods applied during the experimental programme carried out to meet the research objectives. Basic principles of key analytical techniques employed for samples analysis.

Section 4 – Paper 1: Chemical speciation and potential environmental mobility of mercury in a contaminated canal bed sediment.

Baseline characterisation of a Hg-contaminated canal bed sediment, Hg chemical speciation was investigated in the context of biogeochemical parameters.

Section 5 – Paper 2: Investigating the impacts of iron nanoparticle and biostimulation treatments on biogeochemistry and mercury chemical speciation in anoxic sediment and artificial groundwater systems.

Batch microcosm systems, containing anoxic Hg-contaminated artificial groundwater (AGW) and sediment, were setup to investigate the impact of four treatments [NanoFER 25S (nZVI), Carbo-Iron® (nZVI and activated carbon], biogenic magnetite (biomagnetite) and organic electron donor biostimulation) on solid phase Hg chemical speciation in the context of changes to key biogeochemical parameters.

Section 6 – Paper 3: Investigating the impacts of Cu-coated iron nanoparticles on chemical speciation and potential mobility of Hg in artificial groundwater.

Iron-based nanoparticles [biomagnetite and nZVI (NanoFER 25S)] and Cu-coated particles were added to microcosms containing anoxic AGW containing aqueous Hg(II) [and Cu(II)]. Hg chemical speciation and potential mobility of Hg and Cu in endpoint solids were investigated.

Section 7 – Conclusions and Future Work

A summary of the finding from the three core research papers and future work that add to the scientific data presented.

Section 8 – Professional Development

An outline of events and activities not directly related to my experimental work that have helped build, maintain, and enhance my knowledge and skills.

Section 9 – References

1.3 Paper Author Contributions

Paper 1: Alex Tait, Sam Shaw, David Polya and Jon Lloyd designed the experimental programme; Alex Tait carried out collected samples (with assistance from contractors), performed total and sequential Hg extractions, prepared samples for analysis, collected XAS data and processed and interpreted XAS data; Sam Shaw assisted with XAS data collection and interpretation; and Chris Boothman performed DNA extraction, amplification, and sequencing and bioinformatic analysis. Alex Tait wrote the manuscript; Sam Shaw, David Polya, Jon Lloyd, Chris Boothman and Russell Thomas gave their valuable inputs, critically evaluated, and edited the manuscript.

Paper 2: Alex Tait, Sam Shaw, David Polya and Jon Lloyd designed the experimental programme; Alex Tait set up and monitored microcosm experiments, prepared samples for analysis, collected XAS data, and processed and interpreted XAS data; Dominic Mulroy assisted with XAS sample/standard preparation and XAS data collection, Sam Sham assisted with XAS data collection and interpretation; and Chris Boothman performed DNA extraction, amplification, and sequencing and bioinformatic analysis. Alex Tait wrote the manuscript; Sam Shaw, David Polya, Jon Lloyd, Chris Boothman and Russell Thomas gave their valuable inputs; David Polya and Jon Lloyd critically evaluated and edited the manuscript.

Paper 3: Alex Tait, Rick Kimber, Sam Shaw, and Jon Lloyd designed the experimental programme; Alex Tait synthesised biomagnetite, assisted with setting up and monitored microcosm experiments, assisted with sequential Hg extraction, prepared samples for analysis, collected XAS data, and processed and interpreted XAS data, Yue Wang set up and monitored microcosm experiments, carried out sequential Hg extraction, prepared samples for analysis and Sam Sham assisted with XAS data collection and interpretation. Alex Tait wrote the manuscript; Rick Kimber, Sam Shaw, David Polya, Jon Lloyd, and Russell Thomas gave their valuable inputs.

2.0 Literature Review

2.1 Introduction

Mercury (Hg) is a ubiquitous trace metal that poses a serious threat to human health and biota worldwide due to its toxicity, mobility and persistence in the atmosphere (Mahbub et al., 2017). The solubility, transport, and potential bioavailability of Hg are controlled by its chemical speciation. Hg exists in three forms that have different properties and levels of toxicity, these are: elemental Hg(0), inorganic ionic (e.g. Hg(II) and organic (e.g. CH_3Hg^+). Elemental Hg(0) is the only metallic element that is a liquid at room temperature, its unique properties make it volatile under environmental conditions. Inorganic Hg species are present in two oxidation states Hg(I) and Hg(II), Hg(II) is more common under environmental conditions (Morgan et al., 2009). Hg has a complex environmental cycle and biogeochemistry, which is discussed further in Section 2.6. Methylation is considered the most toxic transformation, often occurring in anoxic sediments, inorganic Hg(II) can be converted into organic methylmercury (MeHg) species by anaerobic bacteria (Wiatrowski et al., 2009). Monomethyl- and dimethyl-mercury [MMeHg (CH_3Hg^+), DMeHg ($(CH_3)_2Hg$)] are potent neurotoxins that can bioaccumulate in the food chain (Mahbub et al., 2017). The toxic effect is caused by MeHg binding to thiol groups of enzymes and membrane proteins, in living tissue (Wagner-Döbler et al., 2003).

2.2 Human Health Impacts & Regulatory Context

The World Health Organisation (WHO) consider Hg as one of the top ten chemicals or groups of chemicals of major public health concern (WHO, 2017). Hg is regarded as a ‘priority hazardous substance’ by the Agency of Toxic Substances and Disease Registry (ATSDR) in the United States (US). It has been ranked third on the ATSDR ‘priority list of hazardous substances’ due to its toxicity, mobility and persistence in the atmosphere (ATSDR, 2019). Elemental, inorganic ionic and organic forms of Hg differ in their degree of toxicity and in their effects on the nervous, digestive, and immune systems, as well as on lungs, kidneys, skin, and eyes (WHO, 2017). Although all chemical forms of Hg are toxic, public health concerns are focused on MeHg. The main risk of exposure for human beings is through food, in particular the consumption of large predatory fish, as MeHg bioaccumulates in the food web (EEA, 2018). Elevated MeHg levels have been identified in fish inhabiting surface waters receiving hydrologic inputs from Hg-contaminated sites (Wiatrowski et al., 2009). Also, rice from Hg mining areas in China is now recognised as a key route of human exposure to MeHg (Feng et al., 2008). However, Hg toxicity affects all groups of organisms and influences ecosystem processes, including microbial, floral and faunal mediated processes (J. Wang et al., 2012).

The socio-economic consequences of Hg contamination have prompted the implementation of policies and regulations to limit Hg releases from human activities and to control its transport within and between environmental compartment (e.g. atmospheric, lithospheric, oceanic and freshwater partitions) at local, regional and global scales (Driscoll et al., 2013). The United Nations Environmental Programme (UNEP) 2013 'Minamata Convention on Mercury' is a key driver for more scientific research investigating novel approaches to investigating and remediating Hg in the environment. The main objective of the multilateral environmental agreement is to 'protect human health and the environment from anthropogenic emissions and releases of mercury and mercury compounds' (www.mercuryconvention.org). As the convention moves into force, more scientific information and assessments are needed to support decision making and management towards meeting its objectives. The European Union (EU) signed the 'Minamata Convention on Mercury' in October 2013 and is thereby committed to ensure its ratification and implementation in member states, building on the existing 'Community Strategy concerning Mercury' adopted in 2005, which included a comprehensive plan aimed at addressing Hg use and pollution, in particular, to reduce Hg emissions, to cut Hg supply and demand and to protect people against exposure (EC, 2010) . It focuses on reducing Hg emissions to air, on banning export of Hg and of certain Hg compounds, and on restrictions to Hg-containing products and industrial processes using Hg. However, recent changes to the political landscape in the United Kingdom of Great Britain and Northern Ireland (UK), means there are ongoing changes to the regulatory context.

Historic UK soil guideline values (SGVs) for Hg are presented in Table 1. These values were retracted in 2018 as the European Food Safety Authority (EFSA) recommended oral Total Daily Intake (TDI) values for both inorganic ionic Hg and MeHg that are lower than the oral Health Criteria Values (HCV) that was used in deriving the SGV (CL:AIRE, 2018). As the Environment Agency (EA) no longer undertakes work to derive new SGV or Toxicology reports there is currently not a plan to update them, but they continue to recommend that relevant public health bodies are consulted should industry develop alternative guideline criteria (CL:AIRE, 2018). Retracted SGV values for inorganic Hg(II) ranged from 80 mg/kg in allotments, where plant uptake can lead to bioaccumulation, 170 mg/kg in residential areas, to 3600 mg/kg in commercial and industrial areas, where the exposure to sensitive receptors is much lower (Morgan et al., 2009). Generally, background concentrations of Hg in soil range from 0.03 to 0.1 mg/kg, with an average value of 0.06 mg/kg (J. Wang et al., 2012). The UK Drinking Water Inspectorate has a standard for Hg of 1 µg/L (AnglianWater, 2018).

Table 1: Historic soil guideline values (SGV) for mercury (Morgan et al., 2009)

Land use	**Soil Guideline Value (mg kg^{-1} DW)^{1,2}**		
	Elemental Hg(0) ^{4}	**Inorganic Hg^{2+}**	**MeHg ^{4}**
Residential	1.0	170	11
Allotment^3	26	80	8
Commercial^3	26	3,600	410

^{1} Based on a sandy loam soil (Environment Agency, 2009b) and 6% SOM.

^{2} Figures are rounded to one or two significant figures.

^{3} SGV is based on the vapour saturation limit.

^{4} For the purposes of modelling the vapour inhalation pathway, elemental mercury and methylmercury are treated as organic.

2.3 Anthropogenic & Natural Sources

Hg in the environment comes from two distinct sources – natural and anthropogenic (Issaro et al., 2009). However, it is important to differentiate between primary and secondary sources. Primary sources, both natural and anthropogenic, mobilise Hg from long-lived geological reservoirs increasing the amount of Hg in surface reservoirs, thus increasing the global pool, whereas secondary sources redistribute Hg between surface reservoirs (Driscoll et al., 2013). Primary Hg emissions from natural processes, such as volcanic activity, and secondary re-emission from aquatic and terrestrial surfaces, such as ocean evasion and biomass burning, are significantly higher than the primary and secondary emissions from anthropogenic sources (Amos et al., 2013; Pirrone et al., 2010). However, anthropogenic emissions are significant, leading to increased Hg-contamination of land and water, which poses a serious threat to biota worldwide (Mahbub et al., 2017). Human activities contributing to the release of large amounts of Hg to the environment include fossil fuel combustion, Hg-mining, artisanal and small-scale gold (Au) mining, additional non-ferrous metal production, chlor-alkali chemical production, cement production, dental amalgam in teeth, and waste management (e.g. incineration and landfill) (J. Wang et al., 2012).

Hg contamination in soil, sediment, water and air is associated with potential toxicity to humans and ecosystems (Lei Wang et al., 2020). The most recent United Nations Environment Programme (UNEP) Global Mercury Assessment report published in 2018 (UNEP, GMA 2018) estimated that global Hg emissions to air from anthropogenic sources in 2015 were 2220 tons. Waste management (43%), ore mining and processing (40%), and energy (17%) were the major sector contributing to the estimated 580 tonnes of Hg released to aquatic environment in 2015 (UNEP, 2019). Artisanal and small-scale Au-mining is the largest single activity causing mercury releases worldwide, 1220 tonnes of Hg were estimated to be released worldwide in 2015 for this sector, combining releases to both water and land, as respective contributions to each environmental compartment cannot reliably be separated due to the informal nature of this activity (UNEP, 2019)

The impact of Hg pollution to the atmosphere from industrial processes that do not directly use Hg (e.g. fossil fuel combustion) can be higher than from those using Hg (e.g. chlor-alkali plants using Hg electrolysis) (Richter and Flachberger, 2010). However, anthropogenic releases from industrial activities using Hg have the potential to cause localised point source contamination to soils, sediments and water on or around the industrial site (Biester et al., 2002). Hg released from spills and waste disposal typically enters the subsurface as inorganic Hg, which can be transformed into species with varying mobility and toxicity depending on local geochemistry (Wiatrowski et al., 2009). These transformations are controlled by pH, temperature, organic matter (OM), reduction-oxidation (redox) potential, cation exchange capacity, grain size and porosity (Phipps et al., 2013). Bernaus *et al.* (2006) observed Hg concentrations between 4.3 and 1150 mg/kg in soils during investigation of Hg-contamination near a chlor-alkyl plant in the Netherlands. Speciation analysis of total Hg content in soil samples from the site, as determined by X-ray Absorption Spectroscopy (XAS), identified alpha-HgS (26-37%), HgO (6-86%), $HgSO_4$ (17-80%), and $Hg_3S_2Cl_2$ (33-37%) (Bernaus et al., 2006). However, natural processes may transport and deposit Hg released from anthropogenic sources to the wider environment causing indirect (non-point source) contamination on regional to global scales (Pirrone et al., 2010). Primary gaseous emissions to the atmosphere from coal combustion are considered the largest input associated with human activities, contributing between 750 and 1500 metric tons per year, deposition to terrestrial and oceanic systems causes indirect contamination (Randall and Chattopadhyay, 2013; Richter and Flachberger, 2010).

Global biogeochemical models with fully coupled atmospheric, terrestrial, and oceanic Hg partitions have been applied to better understand the human influence on Hg cycling and estimate timescales for responses (Amos et al., 2013). Amos *et al.* (2013) suggested that the accumulated burden of legacy anthropogenic Hg means that future deposition will increase even if primary anthropogenic emissions are held constant. Therefore, even if source control of Hg discharge is achievable, it may take a significant time period, perhaps decades, for contaminated freshwater and terrestrial systems to reach relatively safe levels naturally, as historically emitted Hg can be retained in anoxic sediments where they may be later mobilised and transformed to MeHg (Randall and Chattopadhyay, 2013). Development and application of new cost-effective remediation technologies for contaminated sites, and identification of new long-term sinks for Hg, could play a crucial role in offsetting anthropogenic inputs to the biosphere far beyond the local area. Considering that the concentration of mercury in the hair of normal people is 2 ppm, 5 mg/70 kg is defined as mercury poisoning, and 150 to 300 mg/70 kg is a lethal dose (Hong et al., 2012).

2.4 Microbe-Metal Interactions

The capacity of microorganisms to bring about transformations in organic and inorganic compounds has long been recognised (Francis, 1990). Microorganisms play important roles in the environmental fate of toxic metals, with numerous mechanisms influencing transformations between soluble and insoluble forms; the most important of these are identified in Figure 1. The mechanisms by which microorganisms influence changes in metal (e.g. Hg) chemical speciation and mobility are fundamental components of natural biogeochemical cycles (Section 2.6), but also have potential applications in respect to bioremediation of contaminated sediments (Gadd, 2000).

Most metal–microbe interactions have been examined in the context of environmental bioremediation for removal, recovery or detoxification of toxic metal or radionuclide pollutants (Gadd, 2000). Redox transformation to more soluble chemical species and production of organic chelates that can form soluble metal complexes are two important microbial mechanisms that can enhance metal dissolution and limit immobilisation (Ren et al., 2009).

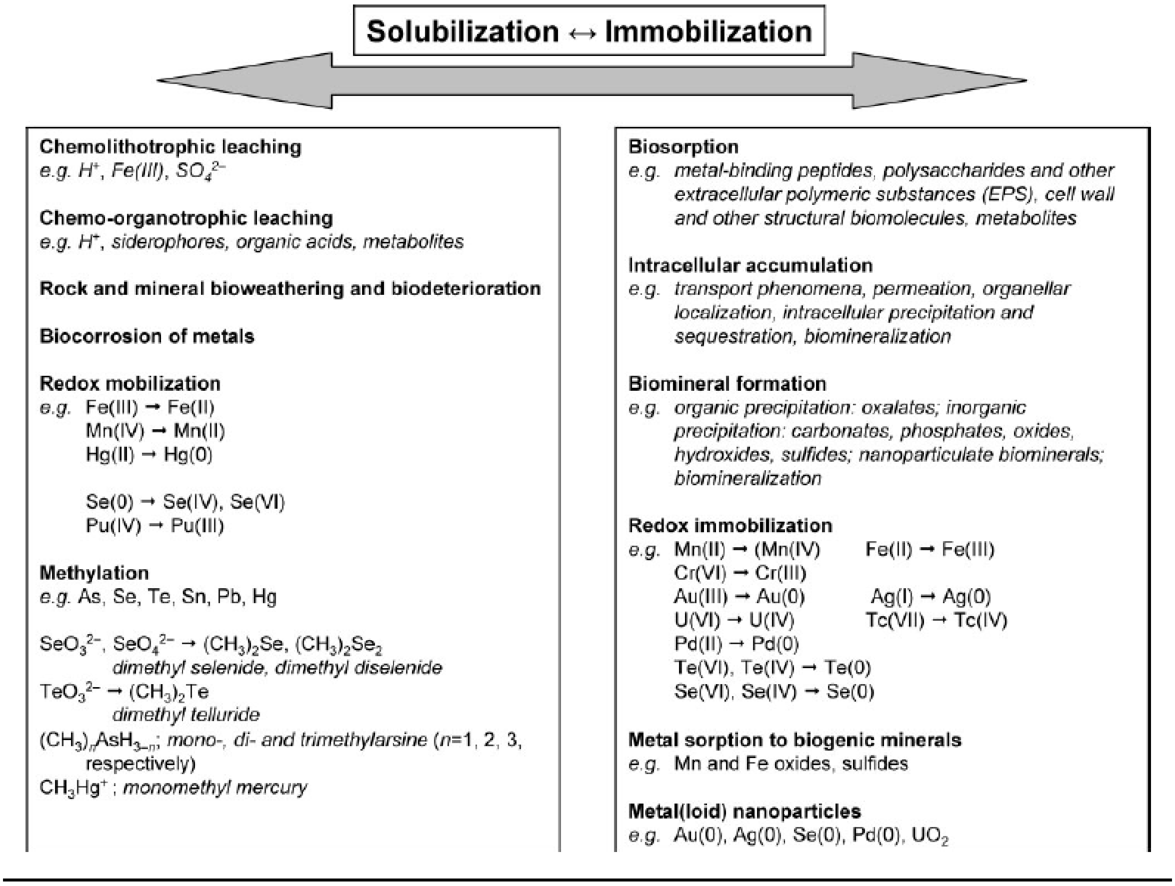

Figure 1: Diagram depicting the major mechanisms of microbial metal transformations between soluble and insoluble metal species (Gadd, 2010).

2.5 Mercury Chemical Speciation

Hg has a complex environmental cycle and biogeochemistry. The unique physicochemical properties of Hg present significant technical challenges for Hg-contaminated site assessment, as well as additional health and safety risks (Phipps et al., 2013). Bioavailability, toxicity, leachability, and volatility of Hg in sediments are dependent on the solid phase Hg species present (Barnett et al., 1997). The main processes that can influence Hg mobility and toxicity are redox changes and methylation. Understanding Hg chemical speciation in the context of local biogeochemistry provides insight into long-term behaviour, migration pathways and potential receptors, thus allowing appropriate risk management. Solid phase chemical speciation is critical to understanding and modelling metal contaminated systems (Bloom et al., 2003). Although the retention and accumulation of Hg in soils is highly dependent on its chemical form, mobility of a particular Hg species may also be controlled by physical-chemical transport in a more mobile phase (e.g. soil water) and soil properties (pH, Oxidation Reduction Potential (ORP), cation exchange capacity (CEC), mineral composition, soil texture, OM content etc.) (Sánchez et al., 2005). Hg-contaminated sediments constitute complex systems where many interdependent factors, including the amount and composition of Organic Matter (OM) and clays, oxidised minerals (e.g. Fe/Mn oxides), reduced elements (e.g. HS^-), as well as sediment pH and redox conditions affect Hg chemical speciation (O'Connor et al., 2019). Particle size plays an important role as nano-sized Hg particles (e.g. nHgS) are more mobile and available (O'Connor et al., 2019; Xu et al., 2021).

Hg can form salts of varying solubility in combination with various anions. Figure 2 is a Pourbaix diagram for Hg with chlorine (Cl) and sulfur (S), which illustrates potential thermodynamically stable phases of an aqueous electrochemical system at chemical equilibrium. In the presence of excess chloride (e.g. seawater) Hg forms more soluble chloride species (e.g. $HgCl_2$) (Phipps et al., 2013). High chloride levels could also have significant implications on microbial diversity within a sediment (von Canstein et al., 1999).

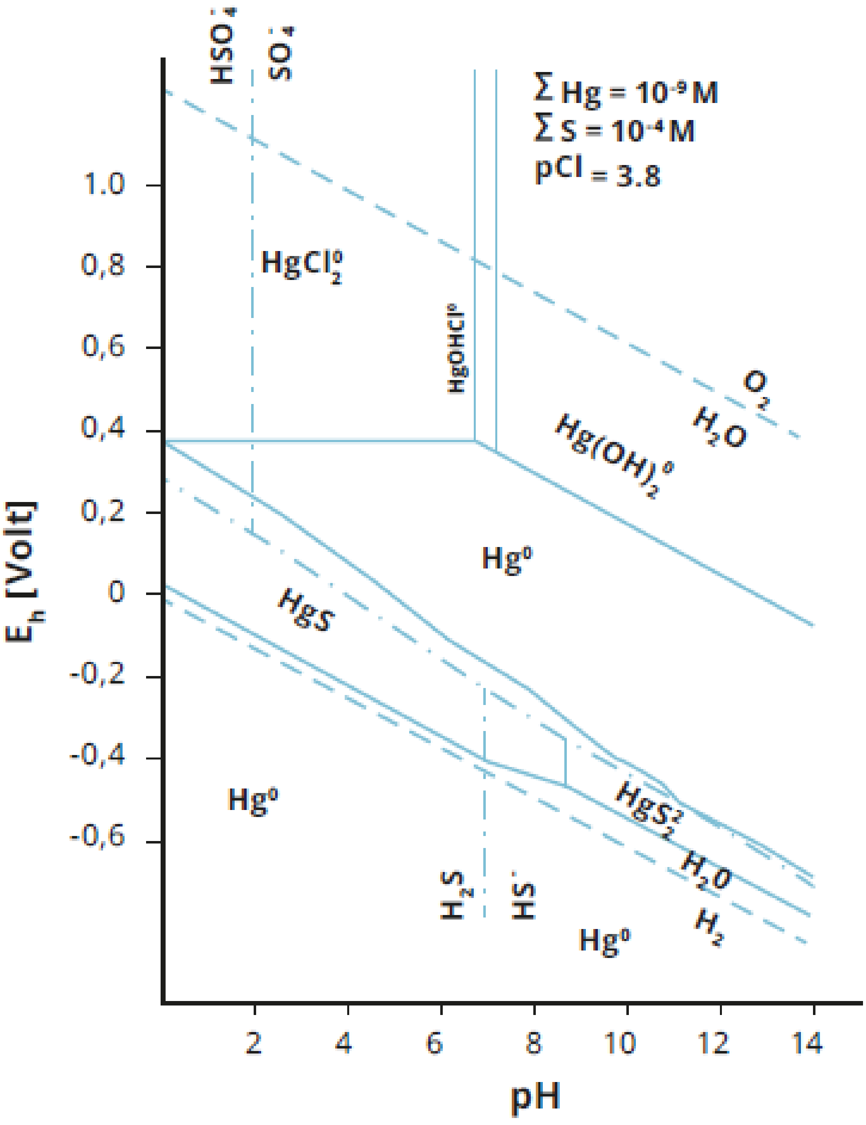

Figure 2: Hg Pourbaix Diagram (Phipps et al., 2013).

The Pourbaix diagram show that under redox conditions less than 0.4 volts, Hg(0) forms at pH less than 7, but HgS can also exist depending on pH. Under redox conditions greater than 0 volts and pH greater than 7, Hg(II) chemical species dominate, but Hg (0) can also exist (Phipps et al., 2013). This highlights the complexity of resolving Hg chemical speciation in the context of Eh and pH.

Hg can also form soluble complexes with dissolved organic matter (DOM). Strong binding between Hg and DOM is attributed to coordination of Hg at reduced sulfur sites within the OM (Ravichandran, 2004). DOM can compete with sulfide for Hg binding and inhibit the precipitation of insoluble mercuric sulfide (HgS). Microbial reduction of sulfate in anoxic Hg-contaminated sediments, can lead to the formation HgS (O'Connor et al., 2019). HgS is a dimorphous mercuric compound found in two mineral forms (1) cinnabar (α-HgS) and (2) metacinnabar (β-HgS).

The chemical speciation and potential mobility of Hg, must be understood before any decisions relating to potential remediation options are made (Sánchez et al., 2005). Organic Hg species (e.g. MeHg) are at least an order of magnitude more mobile than inorganic Hg species, therefore more toxic and more readily bioaccumulated. Sulfate-Reducing Bacteria (SRB) predominantly methylate Hg in freshwater and estuarine sediments under reducing conditions, but this is usually limited by the availability of sulfate in freshwater sediments (Compeau and Bartha, 1985; Hellal et al., 2015).

Organic and water-soluble inorganic Hg(II) species contribute the major portion of potential Hg toxicity in soil due to their mobility (Han et al., 2003). In general, soils from Au-mining areas and industrial sites have a relatively high proportion of bioavailable Hg as the chemical species released are more soluble, but soils from Hg-mining areas generally have less bioavailable Hg, as most is insoluble HgS (J. Wang et al., 2012). Chemotrophic and phototrophic microorganisms inhabiting soils and aquatic environments are capable of affecting Hg chemical speciation, thus influencing mobility and toxicity of Hg (Gregoire and Poulain, 2014). Accurately monitoring key geochemical conditions, Hg chemical speciation and the microbial community in a system, during treatment is crucial for better understanding the impacts of potential remedial agent, and ultimately establishing its effectiveness at immobilising and/or detoxifying Hg. Applying methods and analytical techniques that can accurately identify and quantify the contribution of individual Hg species in Hg-contaminated sediment and water is essential. This information can be utilised for site risk assessment, as well as to guide the development, and assess the effectiveness of, remediation strategies tailored to specific industrial and environmental contexts. Solid phase chemical speciation is critical to establishing risk, because the particular distribution of metal compounds and their interaction with the sediment interface under aqueous conditions determine their environmental mobility and bioavailability (Bloom et al., 2003).

2.6 Mercury Cycling in the Environment

Hg in inorganic compounds can be oxidation state Hg(I) or Hg(II), although due to the scarcity of Hg(I) under environmental condition it is not discussed in this section. Hg cycles naturally through geochemical reservoirs, but human activities have been increasing the Hg flux from the mineral reservoir to the atmosphere (Amos et al., 2013; Pirrone et al., 2010). Atmospheric release of Hg^0 is the largest source of Hg to the environment, it can travel long distances from its origin before it is deposited into terrestrial or aquatic systems (Mahbub et al., 2017). Natural processes play an important role in the redistribution of Hg across terrestrial, freshwater, and marine ecosystems. Atmospheric oxidants (ozone, bromine, HClO, HSO^{3-} and OH^-) can cause oxidation to Hg(II) during atmospheric travel, most of which becomes deposited in aquatic and terrestrial environmental partitions, although a small portion can be transformed by photoreduction (Mahbub et al., 2017). The complex atmospheric processes governing potential reactions and chemical speciation are not discussed further as they fall outside the scope of this work. After deposition, some Hg(II) returns to the atmosphere as Hg(0) following reduction processes, but the major portion cycles through soils, sediments and waters (Amos et al., 2013). Both abiotic and microbial transformations reduce Hg(II) to Hg(0), as Hg(0) is volatile and has low water solubility it tends to evaporate from surface waters and sediments (Wiatrowski et al., 2006). Figure 3 illustrates key processes in the emission and cycling of Hg through the environment.

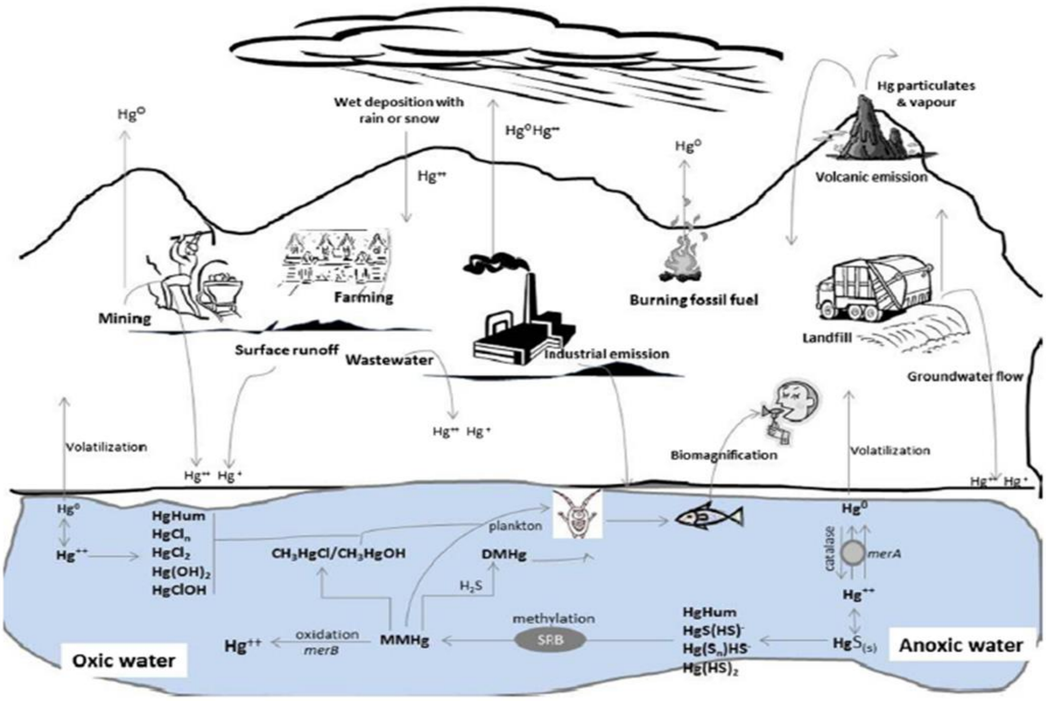

Figure 3: Emissions and cycling of mercury in the environment (Mahbub et al., 2017)

Most Hg(II) deposited in oceanic waters eventually returns to the atmosphere as volatile Hg(0) following transformation during biological and chemical processes, although some accumulates in oceanic sediments (Mahbub et al., 2017). However, most Hg(II) deposited in terrestrial bodies is accumulated in soils and aquatic sediments, becoming enriched in the surface layers. Due to its strong tendency to form complexes with chloride (Cl^-), hydroxide (OH^-), and sulfide (S^{2-}) anions, as well as OM, it is rarely found in soil solution under natural conditions and the major fraction is bound in soil minerals, or adsorbed to either inorganic mineral surfaces or to OM (Morgan et al., 2009). Hg(II) can sorb to OM, clays, humic and fulvic acids, amorphous iron sulfides (e.g. FeS), as well as oxides of aluminium (Al), iron (Fe), and manganese (Mn) (Wiatrowski et al., 2006). OM content is thought to play an important role in controlling the distribution of Hg in soil and its transport through soil profiles (J. Wang et al., 2012). Yin *et al*. (1996) observed that soil adsorption decreased significantly above pH 5 as increasing amounts of OM become dissolved and there was a tendency for Hg to complex strongly with the dissolved organic carbon (DOC). However, the trend was reversed in soils with low OM content, soil adsorption increased under alkaline conditions (Yin et al., 1996). Hg(II) tends to form insoluble mercuric sulfide (HgS), a solid precipitate, in the presence of sulfide, but also soluble neutral compounds (e.g. $HgCl_2$) that are likely substrates for methylation (Wiatrowski et al., 2006).

The mobility and availability of Hg(II) species in aquatic environments is strongly influenced by their solubility. Hg(II) chemical speciation is influenced by the presence of inorganic and organic ligands;

chloride (Cl^-), hydroxide (OH^-) and sulfide (S^{2-}) anions are considered to have an important role (Randall and Chattopadhyay, 2013). Hg(II) hydroxide complexes are thought to be the dominant species in the absence of chelating agents, whereas in low pH and/or high chloride waters Hg chloride complexes are thought to be important (Randall and Chattopadhyay, 2013). Hg(II) can become associated with suspended mineral particles, OM and other substrates that can become deposited in bed sediment, leaving the mobile phase (Randall and Chattopadhyay, 2013). Mercury sulfide particles are known to nucleate in anoxic zones, by reaction of thiol-bound Hg with biogenic sulfide (Manceau et al., 2015). Calcium has been shown to enhance metacinnabar aggregation even in the presence of DOM, but the magnitude of the effect was dependent on the concentrations of DOM, Hg, and Ca. Inhibition of metacinnabar precipitation appears to be a result of strong DOM-Hg binding, with adsorption of DOM and electrostatic repulsion appearing to prevent aggregation of colloidal particles (Ravichandran et al., 1999). Coordination of Hg(II) to natural organic matter (NOM) and sulfides governs its chemical speciation and has implication for the bioavailability and mobility of mercury in water and sediment (Deonarine and Hsu-Kim, 2009).

Redox changes and methylation are key processes that influence Hg mobility in soils and sediments. Figure 4 is a simplified schematic illustrating redox, methylation and demethylation pathways. As previously mentioned, bioavailability, toxicity, leachability, and volatility of Hg is dependent on its solid phase chemical speciation. MeHg species are the most toxic to ecosystems and human health due to their tendency for biomagnification in the food chain. In contrast, HgS particles are much less toxic, less mobile, and less bioavailable, and generally considered to be more stable under environmental conditions.

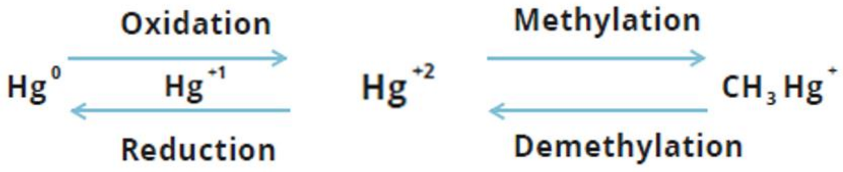

Figure 4: Redox, methylation and demethylation pathways, adapted from (Phipps et al., 2013)

Abiotic and biotic Hg(II) reduction is responsible for evasion of Hg from terrestrial and aquatic systems as volatile Hg(0). Photoreduction, mixed phase iron minerals [containing Fe(II) and Fe(III)] and reactive groups on humic substances are key abiotic reduction pathways (Allard and Arsenie, 1991; Gustin et al., 2002; O'Loughlin et al., 2003). However, Hg reduction also occurs via biological pathways involving naturally occurring microorganisms in the environment (Gregoire and Poulain, 2014). Hg-resistant microbial communities are ubiquitous and can play a role in mobilising Hg(II) from soils and sediments, resistance is derived from the *mer* operon. Figure 5 illustrates the key pathways and transformations in the Hg-resistance mechanism. The merA gene encodes mercuric reductase, a cytoplasmic enzyme that can reduce Hg(II) to volatile Hg(0) that subsequently returns to the atmosphere (Mahbub et al., 2017). The transformation inside the cell is a stoichiometric reaction that requires $NADPH_2$ dehydrogenase to act as an electron donor, transport proteins merP and merT transport Hg(II) through the inner and outer cell membrane into the cytoplasm (Wagner-Döbler et al., 2003). Genes encoding functional proteins involved in the resistance mechanism cluster to form the *mer* operon, often located on a plasmid, enabling it to spread through microbial population via horizontal gene transfer (Nascimento and Chatone-Sonza, 2003). However, due to the tendency of Hg(II) to form insoluble complexes with OM and sulfide, and adsorb to insoluble mineral phases, it can have a limited bioavailability for transport into Hg-resistant microbial cells, leading to accumulation in soils and sediments, thus increasing the terrestrial load (Mahbub et al., 2017).

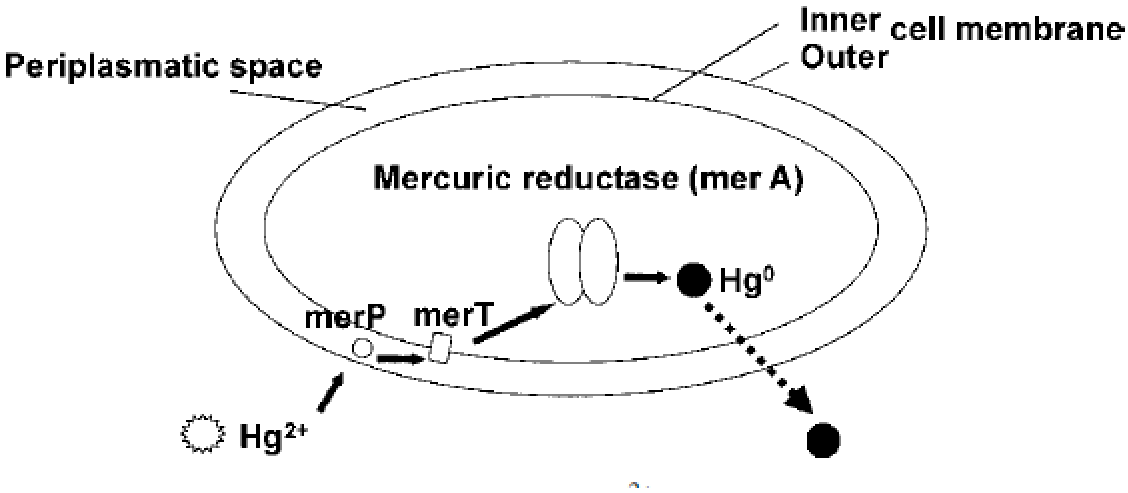

Figure 5: Principle of mercury resistance (Wagner-Döbler et al., 2003)

Hg methylation can occur under aerobic and anaerobic conditions by abiotic or biotic mechanisms (Figueiredo et al., 2018). Methylmercury (MeHg) can be formed in the environment when oxidised Hg species react with a methyl group (Barkay and Wagner-Döbler, 2005). Microbial activity is a critical factor controlling MeHg formation in aquatic environments, microbes can mediate the transformation of Hg to highly neurotoxic organometallic MeHg species, that bioaccumulate in food webs (Figueiredo et al., 2018; Lin et al., 2021). Hg methylation requires the gene pair hgcAB, which encodes proteins that drive the process, and has been well described for anoxic environments (Lin et al., 2021). Methylation occurring on the surface layers of sediments, at the sediment-water interface, may play a major role in determining the extent of MeHg flux to the water column (Mason et al., 2006). Recent research suggests that additional bacterial groups may also play a role in environmental methylation in the oxic zone of global oceans (e.g. *Nitrospina* species) (Gionfriddo et al., 2016). MeHg species are more mobile in the environment than as they interact less strongly than inorganic Hg(II) with soil and sediment constituents (Wiatrowski et al., 2006).

Olson & Cooper (1976) identified that the net amount of methylmercury (MeHg) produced under anoxic conditions was greater than that found under oxic conditions, and that the amount of OM in sediments greatly affected methylation capability, with sediments containing more OM producing more MeHg (Olson and Cooper, 1976). Methylation rates are reduced when Hg is sequestered in crystalline mercury sulfides or bound to thiol groups in macromolecular natural organic matter (NOM) (Manceau et al., 2015). Fagerstrom and Jernelov (1971) have suggested that the presence of H_2S in lake sediments reduces the rate of Hg methylation, due to the formation of mercuric sulfide, which is methylated much more slowly than mercuric chloride (Fagerström and Jernelöv, 1971). However, Gerbig et al (2011) propose that disordered nanocolloidal metacinnabar-like species may form in DOM containing sulfidic systems, and that these species need to be considered when addressing Hg biogeochemistry (Gerbig et al., 2011). Previous research work reported that the octanol–water partitioning of inorganic Hg decreased with increasing sulfide, these results help explain the decreased availability of Hg to methylating bacteria under sulfidic conditions, and the inverse relationship between sulfide and methylmercury observed in sediments (Benoit et al., 1999).

MeHg is produced mainly in anoxic sediments and soils, primarily intracellularly by dissimilatory sulfate- and iron-reducing bacteria (DSRB and DIRB) belonging to the Deltaproteobacteria (Gilmour et al., 1992; Graham et al., 2012a; Kerin et al., 2006). DSRB are thought to drive this environmental process, with more recent research identifying the role of DIRB in environmental Hg methylation (Kerin et al., 2006). Gilmour (2013) identified methylation in two methanogens, and in a wide variety of Firmicutes, extending scientific knowledge of Hg-methylating microorganisms outside of the Deltaproteobacteria for the first time (Gilmour et al., 2013). Recent work has found possible MeHg formation in suboxic seawater, findings revealed potential novel marine Hg-methylating microorganisms with a greater oxygen tolerance and broader habitat range than previous identified (Lin et al., 2021). Critical to understanding the formation of MeHg is an accurate knowledge of the chemical reactions that proceed as Hg(II) moves from contaminant sources to methylation zones (Wiatrowski et al., 2006). Methylation is thought to be an intracellular process limited by the availability and uptake of Hg(II) (Gregoire and Poulain, 2014). Iron sulfides could have a role in limiting bioavailability of Hg(II) to methylating microbes (Liu et al., 2009). Hu *et al.* (2013) identified that some SRB and IRB can methylate oxidised forms of Hg. For example, *Geobacter sulfurreducens* PCA was able to oxidise and methylate elemental Hg(0) in the presence of cysteine (Hu et al., 2013). Cellular uptake of inorganic Hg(II) is a key step in microbial formation of neurotoxic MeHg. Recent research has shown that the iron reducing bacterium *Geobacter sulfurreducens* produces and exports low molecular mass thiols that largely control the chemical speciation and bioavailability of Hg(II) by the formation of Hg(II)-complexes. The thermodynamic stability of Hg(II)-complexes is a principal controlling factor for Hg(II) methylation by this bacterium such that less stable complexes with mixed ligation methylated at higher rates (Adediran et al., 2019).

DOM is generally thought to lower metal bioavailability in aquatic systems due to the formation of metal−DOM complexes that reduce free metal ion concentrations (Graham et al., 2012a). Periphyton communities that support an active microbial sulfur cycle may support Hg methylation, which has implications for trophic transfer of methylmercury since periphyton can be the base of the food web in aquatic ecosystems (Cleckner et al., 1999). However, recent research has suggested that small HgS nanoparticles, stabilised against aggregation by DOM, are bioavailable to Hg-methylating bacteria, not only dissolved Hg chemical species (Graham et al., 2012a). However, there is uncertainty regarding the uptake mechanism for HgS nanoparticles, HgS particle size exerts strong control over nanoparticle solubility, reactivity and bioavailability (Graham et al., 2012a). DOM has been proposed to limit adhesion of nanoscale particles to bacterial cell surfaces (Li et al., 2010). Graham et al (2012) suggest that inhibitory effects of DOM on nanoparticle−cell surface interactions may be counterbalanced by reduced particle growth in the presence of DOM (Graham et al., 2012a). Recent research has identified a thermodynamically favourable chemical reaction mechanism, in which thiol-bound Hg polymerizes to mercury–sulfur clusters, in absence of sulfide, under oxic conditions (Manceau et al., 2015).

The formation of MeHg is the net result of methylation and demethylation reactions (Skyllberg, 2010). Microbial reductive demethylation converts toxic MeHg to volatile Hg(0), thus has an important role in reducing net methylation (Mahbub et al., 2017). Microbial resistance to MeHg is attributed to the presence of the merB gene, encoding an organomercury lyase enzyme, as part of the mer-operon (Gregoire and Poulain, 2014). This pathway is dependent on the oxidation reduction potential (ORP) and MeHg availability, it generally favours high MeHg concentrations under oxic condition, these conditions typically occur at the oxic/anoxic transition zone where concentrations of MeHg are higher (Gregoire and Poulain, 2014; Lu et al., 2016). Oxidative demethylation is an alternative microbial pathway that converts MeHg to Hg^{2+} that is not limited by MeHg availability and is thought to be more common under anoxic conditions, although it can also occur under oxic conditions (Gregoire and Poulain, 2014; Lu et al., 2016).

2.7 Biogeochemical Cascade

In terrestrial and aquatic environments, oxygen becomes depleted with depth. Sediments and waters can be defined as oxic, suboxic or anoxic, with reducing oxygen levels. There are implications in respect to primary electron acceptors used in respiration processes with depth, which can influence porewater geochemistry in a sediment. Heterotrophic degradation of the various monomers can proceed either aerobically or anaerobically (Olli, 2021). Below the oxic horizon, other oxidants (NO_3^-, MnO_x. FeO_x, SO_4^{2-}, CO_2) become important for heterotrophic degradation of OM (Olli, 2021). Figure 6 shows the depth distribution of sedimentary diagenetic zones, as defined by the chemical energy liberated by the redox process (Roberts, 2015). Aerobic respiration is followed by denitrification, manganese reduction, iron reduction, sulfate reduction, and then methanogenesis in the biogeochemical cascade.

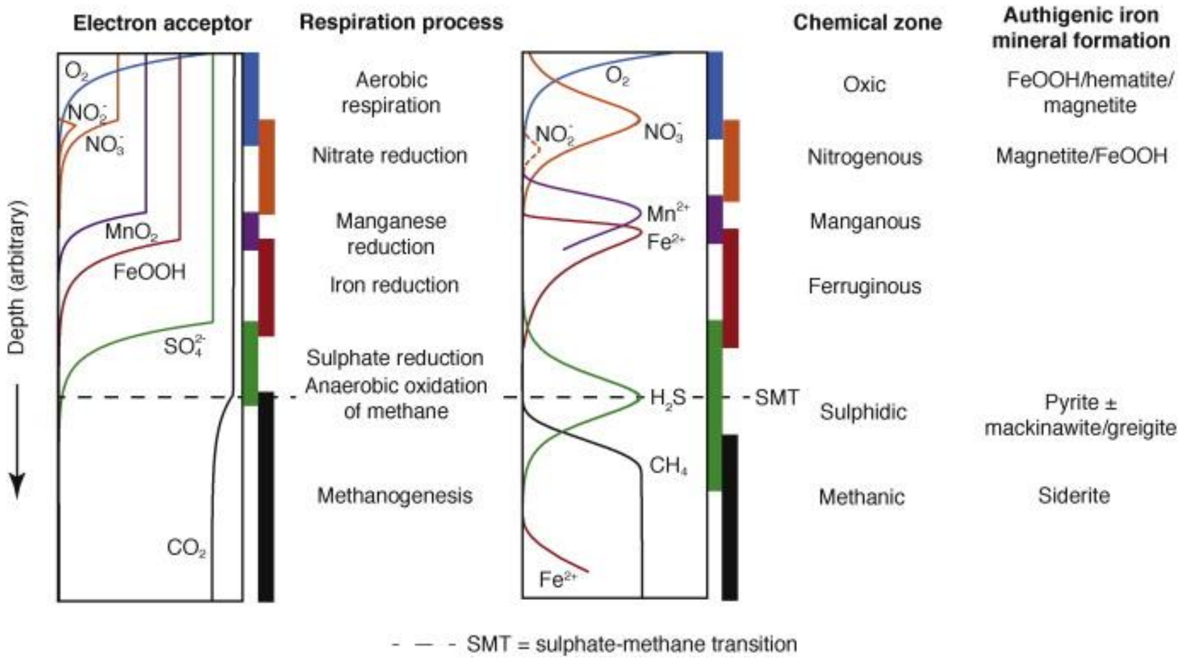

Figure 6: A schematic representation of the depth distribution of sedimentary redox-driven diagenetic zones. Electron acceptors and respiration processes by which reactants are consumed are indicated on the left. Idealised porewater profiles of reactants (O_2, NO_2^-, NO_3^-) and products (NO_3^-, N^{3-} , Mn^{2+} , Fe^{2+} , H_2S , CH_4) and associated chemical zones are shown on the right (Roberts, 2015).

Figure 7 presents the sulfur cycle of a marine sediment, illustrating key chemical reactions, microbially catalysed pathways, and a combination of both. Sulfate (SO_4^{2+}) reduction to sulfide (H_2S, HS^-, S^{2-}) is driven by the oxidation of buried organic carbon (C_{org}), supplemented by the anaerobic oxidation of methane (CH_4) at the subsurface sulfate-methane transition (SMT) (see Figure 6) (Jørgensen et al., 2019). Manganese and iron reduction are occur in the surface sediment, but Fe(III) can be buried and may act as an oxidant for sulfide in the deeper sediment layers where it may partly bind with produced sulfide forming FeS and pyrite (FeS_2) (Jørgensen et al., 2019). Pyrite formed by either (1) the polysulfide pathway, or (2) the H_2S pathway is a major sink for sulfur, as it is the end product of iron-sulfide mineralisation. Intermediate sulfur species [e.g. S^0, thiosulfate ($S_2O_3^{2-}$), tetrathionate ($S_4O_6^{2-}$), sulfite (SO_3^{2-})], are formed during the oxidation of sulfide [e.g. buried Fe(III)], and may be reduced back to sulfide, oxidised further to sulfate, or disproportionated to form both sulfide and sulfate (Jørgensen et al., 2019).

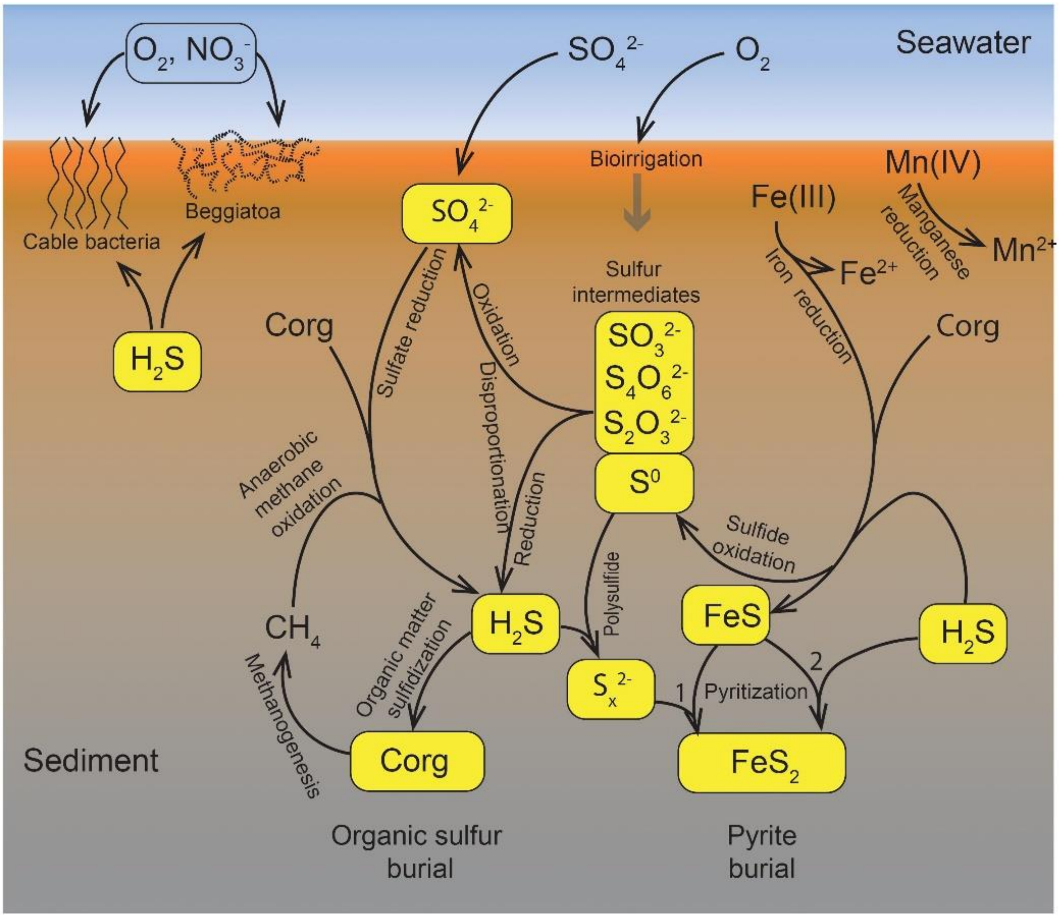

Figure 7: The biogeochemical sulfur cycle of marine sediments. Arrows indicate fluxes and pathways of key biological or chemical processes (Jørgensen et al., 2019).

SRB are ubiquitous in anoxic sediments, using sulfate (SO_4^{2-}) as their terminal electron acceptor during metabolism to produce sulfide. As discussed in Section 2.6, they have a major role in Hg methylation under anoxic environmental conditions. Therefore, sulfur cycling in sediment systems is likely to have implications in respect to net methylation.

2.8 Remediation

This section presents an overview of remedial approaches that have been applied *in situ* for Hg-contaminated soil and groundwater remediation and *ex situ* for soil and wastewater treatment at industrial sites linked to Hg pollution. Groundwater constitutes >97% of the world's unfrozen freshwater and is the major source for drinking water in certain countries (Weil et al., 2019). Regulatory drivers have made remediating Hg polluted soils, sediments, and water a primary concern of industry and government, to reduce potential risks associated with its toxicity. For example, the Minamata Convention requires signatory nations to phase out use of Hg in acetaldehyde and chlor-alkali production by 2018 and 2025, respectively (Phipps et al., 2013). Decommissioning of Hg-cell chlor-alkali plants and acetaldehyde factories worldwide, and the associated demolition activities, require reliable treatment technologies for Hg-contaminated soils and rubble as an alternative to disposal in underground repositories (Richter and Flachberger, 2010). Many efforts have been undertaken to develop remediation technologies to reduce and manage Hg-contamination in soils and water under both laboratory and field conditions (Mahbub et al., 2017; J. Wang et al., 2012). Soils contaminated with Hg have proved expensive and logistically challenging to remediate (McCarthy et al., 2017). Traditional soil excavation and off-site disposal approaches can produce large volumes of Hg-loaded wastes, with significant additional cost associated with its safe disposal (Phipps et al., 2013). Leaching from disposal sites can also cause additional environmental impacts (J. Wang et al., 2012).

Chlor-alkali plants which use elemental Hg(0) for the electrolytic production of chlorine and sodium hydroxide have been shown to be potential sources of Hg pollution (Neculita et al., 2005). The Hg-cell process utilises liquid elemental Hg(0) as a cathode in the electrolysis of a saturated sodium chloride (brine) solution. However, limitations associated with this process can allow Hg to be released to the environment via emissions to air, or the discharge of wastewaters and solid wastes to water bodies (USEPA, 1997).

The Network for Industrially Contaminated Land in Europe (NICOLE) document on ‘Risk-Based Management of Mercury Impacted Sites’ highlights key issues and remediation techniques being trialled at industrial sites. There are 8 case studies introduced, highlighting historic legacy issues, including several focusing on Hg legacy at chlor-alkali plants. Exact quantities of Hg released through atmospheric emissions to the environment, controlled discharges to the nearby aquatic systems, leakages in the cell plant, and contaminated sludge can be difficult to quantify (Guney et al., 2020). Variations in the environment surrounding each site can make risk assessment challenging, regulators and engineers must adapt to continuously evolving environmental conditions and tailor responses. Effective management of Hg-contaminated sites is dependent on site specific conditions, and includes more adaptive site investigation, remedy selection, and remedy implementation (Randall and Chattopadhyay, 2013).

2.8.1 Current Technologies

Excavation with off-site disposal has traditionally been the most common method for the remediation of Hg-contaminated sediment (Y. Wang et al., 2012). Alternative approaches have been developed and tested, which are becoming more commonly employed, these include: Solidification, stabilisation, amalgamation, soil washing, thermal desorption, and phytoremediation (Mahbub et al., 2017; Phipps et al., 2013; Y. Wang et al., 2012). Multiple management approaches can be combined as part of a remedial strategy, for more cost-effective treatment at a site (Phipps et al., 2013).

Stabilisation and solidification are immobilisation techniques that can be carried out either *in situ* or *ex situ*, although *ex situ* applications are more common. *In situ* mixing or injection is less established for environmental application, due to challenges associated with ensuring homogenous treatment (Phipps et al., 2013). Solidification reduces the mobility by physically binding contaminated soils enclosing contaminants within a stabilised mass, whereas stabilisation chemically converts Hg species into a less soluble form, reducing contaminant mobility by inducing chemical reactions with a stabilising agent (Mahbub et al., 2017; J. Wang et al., 2012). Soil or waste is mixed with a chemical binding agent such as cement, sulfide or phosphate binder, polyester resin, or polysiloxane compounds to create a semi-liquid state that eventually form a solid (J. Wang et al., 2012). Cement based immobilisation is of increasing importance for remediating contaminated sites because of its low costs (Y. Wang et al., 2012). Serrano *et al*. (2016) investigated the mechanism of Hg(II) immobilisation in tidal marsh sediments by sulfate-cement amendments, under salt and freshwater conditions. XAS data suggested that the primary immobilisation mechanism was physical encapsulation as a polynuclear chloro-Hg(II) salt (Serrano et al., 2012). Amalgamation is a subset of the wide range of immobilisation techniques, involving the dissolution of Hg in other metals (e.g. copper or zinc) and solidification to form a solid alloy, that can be used to supplement more traditional cement based techniques (Phipps et al., 2013).

Soil washing is an *ex situ* treatment for separating contaminants from soil via chemical extraction, physical separation or integrated approaches (Dermont et al., 2008). Chemical extraction is usually more effective at leaching contaminants in ionic form, whereas physical separation is more suited to separating particulate contaminants (J. Wang et al., 2012). Solvents proven effective for chemical extraction of Hg with limited impact on soil properties include ethylenediaminetetraacetic acid (EDTA), iodine and thiosulfate (Subirés-Muñoz et al., 2011). However, stronger chemicals shown to be more effective at removing Hg often substantially alter soil properties (Wasay et al., 1995). Soil washing plants upgraded by froth flotation enabled treatment of soils contaminated with greater than 1000 mg/kg Hg (Richter and Flachberger, 2010). Soil washing processes allow recovery of Hg and soil can later be returned to site, reducing financial and environmental costs associated with disposal (J. Wang et al., 2012).

Thermal desorption is an *in situ* and *ex situ* treatment that increases the volatility of the contaminant through heating, and the contaminant and sediment are separated without combustion (Phipps et al., 2013; J. Wang et al., 2012). Recalcitrant Hg content can be volatilised at high temperature with thermal desorption technologies (J. Wang et al., 2012). Hg species in soil, such as Hg(0), HgS, HgO and $HgCO_3$, can be transformed and captured as gaseous elemental mercury (GEM) at 600-800°C (J. Wang et al., 2012). Temperatures above 550°C have been shown to reduce Hg content from 1320 mg/kg to 6 mg/kg (Huang et al., 2011). Thermal treatment has proven a reliable technology for soils with 10 000 mg/kg of Hg reduced to the threshold value of 10 mg/kg following treatment (Richter and Flachberger, 2010). However, although effective at removing and recovering Hg, there are high energy costs associated with this process, and this approach can significantly alter the soil properties and can cause coexisting contaminants to transform and repartition (J. Wang et al., 2012).

Phytostabilisation and phytoextraction are phytoremediation techniques. Phytostabilisation harnesses biochemical processes in the rhizosphere of plant roots to prevent contaminant movement within the soil, whereas phytoextraction removes contaminants from soil by root uptake and transport to the above ground tissue (J. Wang et al., 2012). Phytovolatilisation can occur following phytoextraction in some plant species, where following uptake to plant tissue Hg evaporates to the atmosphere. Recent studies have engineered the *mer* operon microbial reduction resistance pathway into plant species enabling chloroplast transformations of Hg(II) to enhance phytovolatilisation of Hg(0) (Ruiz et al., 2003). Although, this approach can increase atmospheric contamination, unless Gaseous Elemental Mercury (GEM) capture mechanisms are incorporated. Phytoextraction techniques require a high proportion of mobile and bioavailable ionic and/or organic Hg in soil for effective removal, therefore Hg availability must be increased in soils with a limited mobility to facilitate the use of these methods (J. Wang et al., 2012).

Aquatic sediment sites pose more logistical challenges, as dredging is required for sediment excavation prior to disposal or additional treatment, which can be expensive and technically demanding. Dredging activities may resuspend buried contaminants, increasing their mobility and availability, creating more exposure within the system (Randall and Chattopadhyay, 2013). Subaqueous capping is an alternative technology that separates the sediment from the water column with lower financial and environmental costs (Randall and Chattopadhyay, 2013).

2.8.2 Emerging Approaches

Research continues into finding more cost-effective methods for treating Hg and reducing Hg-contamination in the environment, as there are many approaches that remain unexplored. Bioremediation approaches harnessing the mer operon in Hg-resistant microbes has shown promise in reducing Hg(II) to Hg(0). Also, nanomaterials are gaining ever increasing attention for the remediation of Hg in sediment, water, and flue gas, due to their high adsorption capacity, small dimension, large surface area, and additional unique properties. A range of nanomaterials [nanoparticles, nanosheets and nanocomposites (e.g. Carbo-Iron®)] have been tested for Hg remediation (Liuwei Wang et al., 2020).

Microbial Bioremediation

Bioremediation approaches are generally considered less costly, in both financial and environmental terms, than physico-chemical approaches (Mahbub et al., 2017). Transformation of the more toxic and mobile inorganic and organic forms of Hg to less toxic or less reactive Hg species which show less potential for bioaccumulation (e.g. Hg(0) or Hg sulfides) is becoming a more important approach for remediating Hg-contaminated sites (Mahbub et al., 2017). Bioremediation treatments may act through a complex combination of physico-chemical and biological processes effecting contaminant chemical speciation over time.

The bioremediation of Hg via the *mer* operon detoxification mechanism has undergone trials as both a wastewater treatment and as an *in situ* treatment for waters, soils and sediments (Nakamura et al., 1999; Saouter et al., 1995; von Canstein et al., 1999; Wagner-Döbler et al., 2003). As a wastewater treatment, a fixed bed bioreactor was employed for treating wastewater from chlor-alkali plants to reduce aqueous Hg(II) from the water and retain the Hg(0) precipitates within the reactor (von Canstein et al., 1999; Wagner-Döbler et al., 2003). Bioremediation options harnessing the enzymatic reduction of Hg(II) to water insoluble Hg(0) by Hg-resistant bacterial species, with the *mer* operon, have been widely applied in treating industrial wastewaters in pilot scale applications (von Canstein et al., 1999; Wagner-Döbler et al., 2003). Mabhub *et al.* (2017) identified that despite Hg-resistant bacteria being ubiquitous in terrestrial environments there is still limited knowledge about the application of these microbes as biocontrol agents for remediating Hg-contaminated soil.

Reductive transformation of contaminants by microbes has wide-reaching implications for controlling their mobility in the subsurface, resulting in the degradation of toxic organics or the reductive immobilisation of some toxic metals (e.g. Cr(VI), V(V), Co(III), U(VI), Tc(VII) and Np(V)) (Watts and Lloyd, 2012). These soluble toxic metal contaminants can be reduced directly, often being used as terminal electron acceptors during anoxic respiration by microbes, and removed from solution (Watts and Lloyd, 2012). Accelerating these natural processes as remediation applications has attracted much recent interest, studies have sought to understand these processes from the molecular level while applying them at field or industrial scale (Watts and Lloyd, 2012). However, technologies that attempt to reduce Hg(II) may require expensive GEM capture mechanisms due to the production of volatile Hg(0) (Mahbub et al., 2016)

Bio-functionalised zeolite with encapsulated *Pseudomonas veronii* has shown potential as a remediation option for Hg-contaminated mine tailing in a recent study (McCarthy et al., 2017). Microbial reduction increased the flux of gaseous Hg(0) by a magnitude of 10^4, in order to reduce emissions to the atmosphere a capture mechanism is under development (McCarthy et al., 2017). Hg sensitive microbial species without the *mer* operon have been found to reduce Hg(II) by non-mercuric reductase pathways (Mahbub et al., 2017). *Thiobacillus ferrooxidans,* an Fe(II)-oxidising bacteria, was reported to reduce Hg(II) by cytochrome *c* activity despite its sensitivity to Hg (Iwahori et al., 2000). Wiatrowski *et al.* (2006) reported that *Shewanella oneidensis* MR-1, *Geobacter sulfurreducens* PCA and *Geobacter metallireducens* GS-15 were able to reduced Hg(II) to Hg(0) under iron-reducing conditions in the presence of suitable electron donor and electron acceptor (Fe(III)-oxyhydroxide), without mercuric reductase (Wiatrowski et al., 2006). However, due to Hg sensitivity, these Hg(II) reduction pathways only occur at low Hg concentrations, therefore may only be useful for Hg remediation in anoxic sediments were Hg(II) concentrations are relatively low (Wiatrowski et al., 2006).

Iron-based Nanoparticles

Nanoparticle technology show much promise for applications in remediating soils, sediments, and water. Nanoparticles are characterised by enhanced intrinsic reactivity and a large surface area to volume ratio, and these properties accelerate sorption kinetics (J. Wang et al., 2012). NanoRem is a research project, funded through the European Commission, focusing on facilitating nanotechnology for *in situ* remediation. The project aims to unlock the potential of nanoscale remediation processes from laboratory scale to end user applications to restore land and water resources, alongside developing a better understanding of the environmental risk-benefit for the use of nanoparticles, market demand, overall sustainability, and stakeholder perceptions (http://www.nanorem.eu/). Conceptually, the key properties required for the use of any engineered nanoparticle for *in situ* remediation of polluted groundwater are: (1) high affinity for target contaminant; (2) long lasting reactivity, (3) sufficient mobility within media; and (4) low toxicity. Iron oxide (e.g. magnetite (Fe_3O_4), zero valent iron (ZVI), ZVI and activated carbon composites (e.g. Carbo-Iron®) and iron sulfides (e.g. FeS) nanoparticle treatments have shown potential as treatments for Hg-contaminated soils, sediments and water in recent studies, their magnetic properties can enhance recovery from treatment systems (Gong et al., 2012; Lewis et al., 2016; Wiatrowski et al., 2009; Yan et al., 2010). Particle size, size distribution and aggregation state are important parameters to evaluate before deploying ZVI in the subsurface environment to ensure efficient site remediation. Many studies have demonstrated that both the reactivity and mobility of metal nanoparticles can be dependent on their particle size (Chekli et al., 2016). Stabilising nanoparticles (e.g. FeS) with sodium carboxymethyl cellulose (CMC) stabiliser can enhance sorption and reduce Hg(II) leaching from soils and sediments (Gong et al., 2012; Gong et al., 2014; Xiong et al., 2009). Column tests have suggested that the stabilised nanoparticles can enhance mobility in sediments (Xiong et al., 2009).

Magnetite

Magnetite (Fe_3O_4), a naturally mixed oxidation state [Fe(II)/Fe(III)] iron oxide mineral, has been shown capable of reducing Hg(II) to volatile Hg(0) in water, under anoxic conditions (Wiatrowski et al., 2009). X-ray Photoelectron Spectroscopy (XPS) indicated that Hg(II) ions can adsorb onto the surface of magnetite, as Fe(II) in the magnetite structure donates electrons to Hg(II) (Wiatrowski et al., 2009). Magnetite is more common in iron-reducing sediments saturated with anoxic water, methylation of Hg(II) by DSRB and DIRB can also potentially occur under these condition, therefore Hg(II) reduction to Hg(0) by magnetite could potential reduce its availability for methylation (Wiatrowski et al., 2009).

Magnetite nanoparticles can be produced by abiotic chemical and mechanical methods, such as co-precipitation and ball mining (Byrne et al., 2013). However, these production methods can have significant financial and environmental costs due high energy requirements and the use of toxic materials (Byrne et al., 2013). Iron-reducing bacteria are an alternative biotic production pathway, *Shewanella oneidensis* and *Geobacter sulfurreducens* can reduce Fe(III) to Fe(II) in the presence of a suitable electron donor, soluble Fe(II) is able to recrystallize with solid phase Fe(III) to produce biogenic magnetite (biomagnetite) nanoparticles (Byrne et al., 2013). Byrne *et al.* (2011) reported that size of biomagnetite nanoparticles produced by *Geobacter sulfurreducens* could be controlled (within a range of 10 to 50 nm) by adjusting the total biomass used in the production, with higher bacterial concentrations producing smaller particles (Byrne et al., 2011). A follow up study demonstrated the ability to upscale production in a 50 L bioreactor, whilst still conserving magnetic properties and surface reactivity. This procedure was capable of producing up to 120 g of bio-magnetite, with particle size distribution maintained between 10 and 15 nm (Byrne et al., 2015). Figure 8 illustrates potential mechanisms for Fe(III) reduction during magnetite formation.

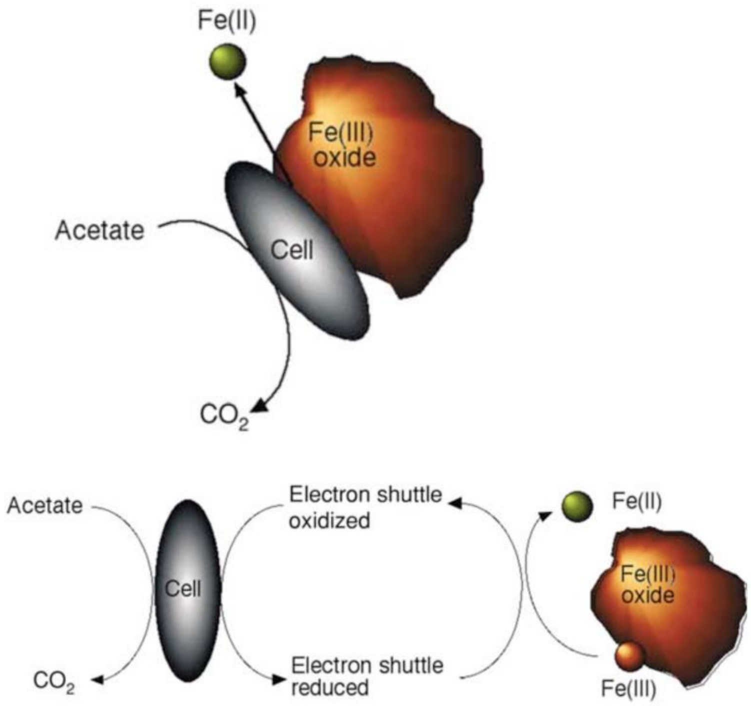

Figure 8: Biomagnetite synthesis process (Lloyd et al. 2003).

Coating magnetite particles may provide additional functionality, thiol-functionalised mesoporous silica-coated magnetite nanoparticles have shown promise as a treatment method for industrial wastewater in a recent study (Dong et al., 2008). However, the investigation focused on the sequestration of Hg by thiol-groups on the nanoparticle surface, rather than harnessing its reduction capacity, the loading capacity was reported to be 14 g/kg at pH 2. This technology has been principally developed for effluent stream remediation wastewater treatment prior to release into controlled waters. The magnetic properties of magnetite enable the particles to be recovered and re-used following Hg removal, recovery and reuse of nanoparticles allows for cost-effective treatment (Dong et al., 2008).

Zero Valent Iron (ZVI)

Zero valent iron nanoparticles (nZVI) have been widely tested and show significant promise for environmental remediation (Chekli et al., 2016; Mukherjee et al., 2016; Zhang, 2003). Mobility and reactivity of nZVI is dependent on particle size, surface chemistry and bulk composition (Chekli et al., 2016; Phenrat et al., 2007). In natural waters, the primary components available for corrosion reactions are dissolved oxygen (DO) [Equation 1 and Equation 3] and water {Equation 2 and Equation 4], under anoxic conditions the less thermodynamically favourable reactions proceeds (Crane & Scott 2012). Aqueous corrosion under anoxic conditions, forms hydrogen (H_2) gas and aqueous hydroxide

(OH^-). Hydroxide contributes to an increase in pH, inducing local conditions that are far from equilibrium and potentially favourable for contaminant removal (Crane and Scott, 2012).

$2Fe^0$ (s) + $4H^+$ (aq) + O_2 (aq) → $2Fe^{2+}$ + $2H_2O$ (l) $E^0 = +1.67$ V Equation 1

$2Fe^0$ (s) + $2H_2O$ (l) → $2Fe^{2+}$ + H_2(g) + $2OH^-$(aq) $E^0 = -0.39$ V Equation 2

Ferrous iron (Fe^{2+}) is a primary product from these reactions and, in turn, can undergo further oxidative transformation to ferric iron (Fe^{3+}).

$2Fe^{2+}$ (s) + $2H^+$ (aq) + ½O_2 (aq) → $2Fe^{3+}$ + H_2O (l) $E^0 = +0.46$ V Equation 3

$2Fe^{2+}$ (s) + $2H_2O$ (l) → $2Fe^{3+}$ + H_2 (g) + $2OH^-$ (aq) $E^0 = -1.60$ V Equation 4

Various iron oxide-hydroxide precipitates (e.g. $Fe(OH)_2$, $Fe(OH)_3$, Fe_3O_4, Fe_2O_3, FeOOH) and green rusts can form as ZVI corrosion products, alongside Fe^{3+} and H_2 (Crane and Scott, 2012). It should be noted that ZVI particles are encapsulated by a thin layer of porous surface oxide directly after synthesis, before introduction to a water treatment system (Crane et al., 2011). A core-shell structure (Figure 9) can be created during the initial stages of the reaction with both sorption by iron oxide-hydroxide shell and chemical reduction at the metallic Fe_0 / iron oxide-hydroxide interface able to occur simultaneously. However, increasing quantities of corrosion products can limit the porosity of the shell, and subsequently limit interaction between Fe^0 and H_2O, DO and contaminant interactions, and ultimately causing reduction the rate of reaction (Crane and Scott, 2012). A core-shell model for ZVI particles is shown in Figure 9.

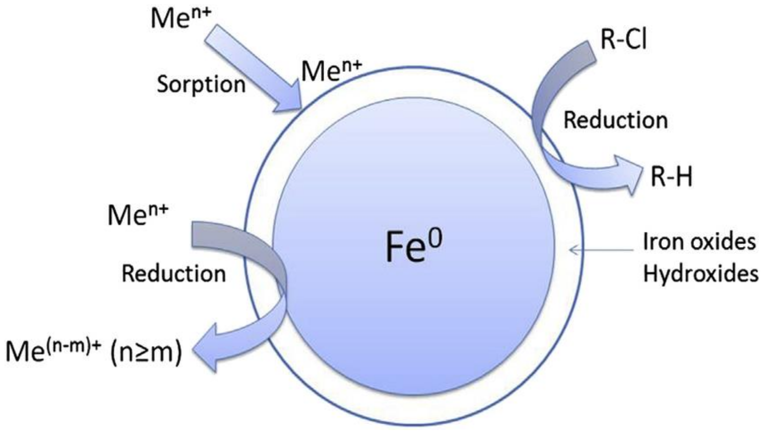

Figure 9: Core-shell model of ZVI particle (Chekli et al., 2016).

The difference in standard redox potential between Fe (E^o = -0.44 V) and Hg (E^o = +0.86 V) means that reduction of Hg(II) by Fe(0) is energetically favourable [25]. Equation 3 summarises the Hg(II) reduction reaction in anoxic systems containing ZVI.

$Hg^{2+} + Fe^0 (s) \rightarrow Hg^0 (l) + Fe^{2+}$ Equation 3

H_2 may act as an electron donor for microbial methanogens, stimulating beneficiary microbial processes (Conrad, 1999). H_2 may also act as an electron donor for IRB and SRB, stimulating the production of Fe(II) and sulfide, respectively (Fagerström and Jernelöv, 1971; Lovley et al., 1989; Nedwell and Banat, 1981). Small amounts of sulfide produced by SRB can precipitate with Hg(II) as insoluble HgS, minimising the adverse impacts of sulfide accumulation and free toxic metals on methanogenesis (Paulo et al., 2015).

Vernon and Bonzongo (2014) reported that the experimental and theoretical determination of adsorption capacities showed that nZVI has a higher adsorption capacity for ionic Hg than ZVI in wastewaters. Previous research has identified the amount of Hg volatilised in ZVI water treatment experiments is dependent on the system chemistry, as it only represented ∼1% of total Hg concentrations in a wastewater effluent, but up to 10% of total Hg dissolved in DIW (Vernon and Bonzongo, 2014).

ZVI nanoparticles has been shown capable of removing Hg(II) under aqueous conditions, XPS analysis of the reacted particles indicated that Hg(II) was sequestrated via chemical reduction to Hg(0) (Liu et al., 2014; Yan et al., 2010). Liu *et al*. (2014) reported that nZVI supported on pumice had a high capacity and efficiency for removing mercury from wastewater (Liu et al., 2014). Doping ZVI nanoparticles with a small amount of a second metal, such as Ag and Cu, which are known to from stable amalgam with Hg(0) could potentially increase the stability of mercury-nanoparticle binding, reducing the likelihood of transformation back to Hg(II) under environmental conditions (Yan et al., 2010). Innovations in nanoparticle synthesis and production have resulted in substantial cost reductions and increased availability of nZVI for large scale applications (Li et al., 2006).

Carbo-Iron®

Carbo-Iron® was developed with the goal to overcome shortcomings of nZVI for in-situ groundwater remediation (Mackenzie et al., 2016). It is a composite material consisting of a porous activated carbon colloid (ACC) framework with embedded clusters of nZVI. Combined effects theoretically enable effective targeting of multiple organic and inorganic contaminants, the reactivity of nZVI and the transport properties of the ACC should provide both better transport properties than nZVI and a higher affinity to non-aqueous phase liquids (NAPL). Enrichment of organic pollutants at the hydrophobic ACC carrier could be advantageous for their efficient degradation at neighbouring reactive centres (Mackenzie et al., 2012). Many contaminated sites have a wide range of pollutants (e.g. organics and metals), therefore any multi-contaminant solution (e.g. nZVI composite materials) would be very valuable. There is limited research into the effects of Carbo-Iron® and Hg, but a study results suggest that both granulated activated carbon and ZVI have the potential for reducing MeHg bioaccumulation in wetland sediment (Lewis et al., 2016).

The application of nanoparticle technology for *in situ* remediation of contaminated sediments is limited due the challenges associated with recovering the particles under environmental conditions. Insufficient groundwater flow or mechanical agitation, required to disperse the nanoparticles fully, can limit their movement through sediments and subsequently limit contact with target contaminants [e.g. Hg(II)]. There is limited knowledge of the fate and transport of nanoparticles in the environment and their potential toxic effects, which have the potential to increase mobility and bioavailability of non-target hydrophobic contaminants that could leach from sediment (Tungittiplakorn et al., 2004). Detailed scientific data from new treatment experiments could be used to determine the cost-effectiveness of new approach to remediation, and whether it may be feasible for them to be scaled up and applied to mitigate risk posed by Hg-contaminated sites and effluents from industrial processes.

3.0 Experimental Methods & Analytical Techniques

In this chapter the sampling, experimental and analytical techniques used to provide scientific data for this project thesis are outlined. The selection of appropriate experimental and analytical techniques for Hg-contaminated sediment and groundwater were dependent on the specific objectives for each phase of investigation. This chapter incudes the basic theory and scientific rationale for the methods and techniques applied during the project, more specific experimental details are provided for each individual research paper (Sections 4 – 6).

3.1 Safety

Planning experimental protocols that safely and effectively address research objectives is a crucial element of scientific research. Experimental protocols were planned carefully to ensure they were carried out within the limits of the Department of Earth and Environmental Sciences' resources and in line with the Control of Substances Hazardous to Health (COSSH) regulations. COSHH risk assessment forms were completed and authorised prior to (1) beginning any procedure or experiment involving hazardous substances and (2) submitting hazardous samples for analysis. Hg is categorised as a potential carcinogenic, mutagenic, reprotoxic (CMR) chemical for risk assessment, therefore an occupational health assessment was required prior to working with Hg chemicals, minerals and Hg-contaminated sediment and water. COSHH forms were completed and approved for all experimental procedures carried during this project.

3.2 Sampling

Sample collection for Hg analysis requires ultraclean sampling technique. Direct contact between sample media, equipment, field personnel and any other potential contamination sources should be prevented. Contamination of sampling equipment and containers is the largest source of error associated with low level Hg analysis (Olson and Dewild). Teflon containers should ideally be used (essential for aqueous samples) to minimise adsorption to container walls and eliminate gaseous exchange (Olson and Dewild). However, borosilicate glass containers are a viable alternative for sediment samples. Sampling equipment and storage containers should be subject to a rigorous cleaning protocol (acid washing in 5% v/v analytical grade 15.9 M HNO_3) prior to sample collection. Field personnel should wear Tyvek suits and arm length polypropylene gloves. Aqueous samples should be collected by decontaminated peristaltic pump or by grab technique. Surface sediment samples should be taken with a decontaminated stainless-steel trowel or plastic scoop.

Sediment samples from two sites were selected for experimental investigation. It was important to assess the effectiveness of treatment strategies on samples from environmental settings with varying biogeochemical matrix components. The variation in matrix composition of sediment from different environmental contexts was considered likely to influence changes in Hg chemical speciation during treatment experiments. Samples were selected based on the variation in their grain size and consistency and were gathered from sites in North-West England, UK.

3.2.1 Canal bed sediment (MLR)

Figure 10 shows a map and an aerial image of the area surrounding the sampling location at Weston Marsh Lock, Runcorn (UK).

Figure 10: (a) A map and (b) an aerial image of the area surrounding the MLR sampling location, marked by pin labelled 'Marsh Lock'.

Canal bed sediment, a sludge material, was collected from Weston Marsh Lock, Runcorn (MLR). The lock links the Weaver Navigation Canal to the River Weaver (Runcorn, North-West England, UK). The area surrounding the sampling site is highly Industrialised with multiple potential pollution sources, including a nearby chlor-alkali chemical plant. Samples were taken from the base of the Eastern lock gate by contractors whilst sediment was being dredged as part of remediation efforts. Dredging of the remaining MLR sediment for safe disposal was implemented at the site shortly after the time of sediment sampling to mitigate the ecosystem risk posed by potential Hg transformation. The sediment was characterised in work reported in Paper 1 (Section 4) and investigated in microcosm experiments reported in Paper 2 (Section 5).

3.2.2 Estuarine sediment (EST)

Estuarine (EST) sediment, a sandy material, was collected from the Ribble and Alt Estuaries, Southport. Faraaz Ahmed kindly collected the sediment that was used in microcosm experiments reported in Paper 2 (Section 5).

3.3 Treatment Materials

NanoFER 25S (a commercial nZVI product) was provided as a slurry by Nano Iron (Židlochovice, Czech Republic). The particle suspension contained ~20% (w/w) Fe, nZVI [(w/w) 14-18%] encased in a permeable magnetite shell [NanoFER 25S Safety Data Sheet (SDS)]. Carbo-Iron® was provided as a powder by Helmholtz Centre for Environmental Research (Leipzig, Germany), the particles were ~25% (w/w) nZVI embedded in ~75% (w/w) porous activated carbon colloid (ACC) framework. Biomagnetite particles were synthesised in the WRC laboratory, following the methodology for the procedure outlined in Section 3.4 and Section 5.2.2 (Paper 2). Organic electron donors, sodium acetate and sodium lactate, were purchased from Sigma Aldrich prior to application as a biostimulation treatment.

3.4 Biomagnetite Synthesis

Biomagnetite was synthesised from ferrihydrite by *Geobacter sulfurreducens* in closed anoxic systems containing an electron donor (sodium acetate) and a buffer (sodium bicarbonate). This method has previously been capable of large-scale production of biomagnetite, with control over particle size (Byrne et al., 2015; Byrne et al., 2011). Initially, 1L of Nutrient Broth Acetate Formate (NBAF) minimal growth medium was prepared for *Geobacter sulfurreducens* cultivation (Muhamadali et al., 2015). Serum bottles containing 100 mL NBAF were inoculated with an early stationary phase culture to give an optical density (OD) of ~0.02 at 600 nm. Figure 11 illustrates a microbial growth curve in a closed system and identifies the four stages of microbial growth [lag phase, exponential (log) phase, stationary phase, and death phase] (Willey et al., 2009). The full experimental method followed for biomagnetite production is described in Paper 2 (Section 5.2.2).

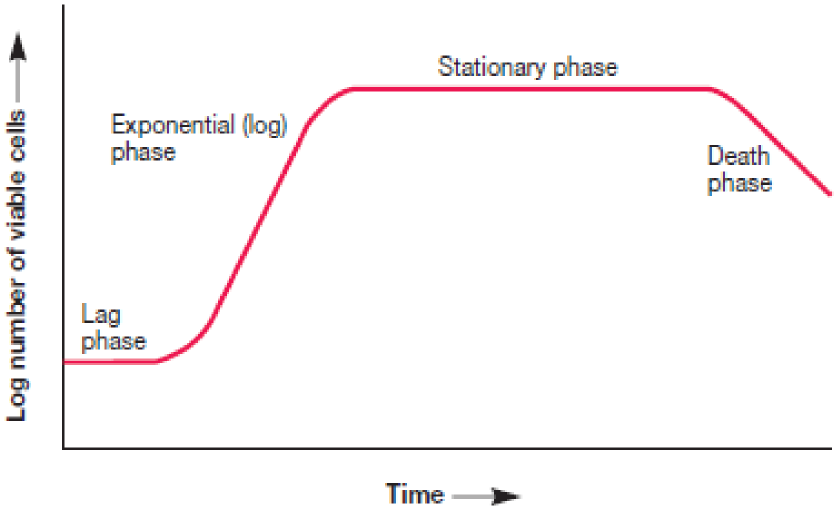

Figure 11: Microbial grow curve closed system, labels identify the four phases of microbial growth (Willey et al., 2009).

3.4 Chemical Extractions

3.4.1 Total Mercury (THg) Extraction

There was a broad spectrum of possible reagents identified in protocols used in previous experimental work, indicating a lack of consensus regarding the best reagents for completely extracting Hg from sediment for determining total Hg (THg) content (Issaro et al., 2009). A passive 18-hour aqua regia [3:1 ratio of concentrated hydrochloric acid (HCl) and concentrated nitric acid (HNO_3)] extraction protocol was selected, as this mixture of strong acids has been widely used to determine THg concentration in sediments (Issaro et al., 2009). This reagent can also be used as a final extraction step for residual Hg in a sequential extraction protocol (SEP) (Bloom et al., 2003; Issaro et al., 2009). Hg concentration in THg extracts were determined by inductively coupled plasma - mass spectroscopy (ICP-MS). The amount of Hg recovered in solid phase extractions was calculated based on recovery from a certified reference material (CRM) ERM-CC580, which is an estuarine sediment with a certified mass fraction (based on dry mass) of 132 ± 3 mg/kg and a MeHg concentration of 75 ± 3 µg/kg. ERM-CC580 was purchased from the European Commission Joint Research Centre Institute for Reference Materials and Measurements to assess the Hg extraction efficiency of the protocols. ERM-CC580 has a certified mass fraction (based on dry mass).

More detailed information for this experimental method can be found in Section 4.2.7 (Paper 1). A second aqua regia THg extraction method was applied by P S Analytical for sample analysis reported in Paper 2, further details on the experimental protocol can be found in Section 5.10.10. However, quantification of THg is insufficient for understanding the environmental and human health risk posed by the toxic metal, as is does not provide enough information to establish the potential mobility, reactivity, bioavailability, and toxicity of the Hg species present. Determining the mobility of Hg chemical species in sediment was considered essential for better understanding the biogeochemistry and potential risk to ecosystems. Sequential extraction procedures (SEPs) can provide more detailed information on the potential mobility of different portions of Hg in sediment by quantifying Hg in a various extractants (see Section 3.4.2). X-Ray Absorption Spectroscopy (XAS) can provide more detailed compound specific structural information to better understand Hg chemical speciation and the potential mobility of Hg in sediment (see Section 3.5.3).

3.4.2 Sequential Extraction Protocol (SEP) for Hg

A widely used laboratory-based SEP was applied to establish the potential mobility of Hg within contaminated sediment by accurately quantifying Hg in various extractants. SEPs are used to determine the partitioning of contaminants associated with different soil and sediment constituents, and the travel potential according to extractability by various solvents. Many established protocols that are commonly used to study trace metals are not appropriate for Hg due to the diverse range of Hg-species with unique physical and chemical properties (Bloom et al., 2003). However, *in situ* compound specific information can often be confounded and only operationally defined speciation determined (Bloom et al., 2003). There are a wide range of published SEP methodologies, a common theme in the literature relates to apparent contradictions with inter-comparison of results from different extraction procedures (Bloom et al., 2003; Issaro et al., 2009). Bloom *et al.* (2003) defines a widely used method that differentiates Hg compounds according to chemical reactivity, mobility, and potential bioavailability, to establish an understanding of their potential environmental behaviour. The procedure used five solvents to extract different Hg fractions: (F1) Water Soluble (DIW water); (F2) Weak Acid Soluble (pH 2, 0.1 M CH_3COOH + 0.01 M HCl); (F3) Organo-complexed (1 M KOH); (F4) Strongly Complexed (12 M HNO_3); (F5) Mineral Bound (aqua regia) (Phipps et al., 2013). The more mobile Hg portions found in SEP fractions F1, F2 and F3 typically drive the need for remediation, as Hg extracted in fractions F4 and F5 are considered relatively immobile (Phipps et al., 2013). More detailed information for this experimental method can be found in Section 4.2.6 (Paper 1). As multiple Hg species are often extracted in individual fractions (e.g. F3 may extract Hg sorbed to humics, MeHg or Hg_2Cl_2), a separate extraction procedure had to be applied for MeHg extraction and quantification (Section 3.4.3).

3.4.3 Methylmercury (MeHg) Extraction

A selective MeHg extraction with cold vapour atomic fluorescence spectroscopy (CV-AFS) method was adapted from Brombach et al. (2015) and Lancaster et al. (2019) (Brombach et al., 2015; Lancaster et al., 2019). It should be noted that the method applied here extracts all organometallic Hg. However, as ethyl-Hg (EtHg) and other forms of organomercury are rarely encountered, there is an assumption made that all organic Hg extracted is MeHg. Freeze dried powdered sediment samples (0.2 – 0.5g) were sent to P S Analytical (https://www.psanalytical.com/) for analysis. Full details of MeHg extraction techniques applied to solid phases can be found in Section 4.2.9 (Paper 1) and Section 5.2.9 (Paper 2). Shaun Lancaster (University of Aberdeen) kindly carried out the initial MeHg extraction with CV-AFS from MLR sediment described in Paper 1 (Section 4.2.8). A commercial arrangement was made with P S Analytical for the analysis of a batch of samples from microcosm experiments reported in Paper 2 (Section 5.2.9).

3.4.4 Total Iron Quantification

0.2 mL of sample suspension was digested in 9.8 mL analytical grade 15.9 M HNO_3 for 24 hours. Following dilution, triplicate 10 mL samples (2% (v/v) HNO_3) were filtered (0.4 µm) prior to analysis by inductively coupled plasma-atomic emission spectroscopy (ICP-AES).

3.5 Solid Phase Characterisation

3.5.1 X-Ray Fluorescence (XRF) & Loss on Ignition (LOI)

X-rays are a type of electromagnetic wave comparable to visible light rays but with much shorter wavelength (0.01 nm to 10 nm). XRF spectrometry is a technique for the elemental analysis of bulk specimens. The XRF effect is based on the excitation of atoms in the sample by a primary X-ray, typically generated in an X-ray tube (Spectro, 2021b). Interaction of this primary radiation with atoms making up the sample causes ionisation of discrete orbital electrons (Potts, 1987). During the subsequent electronic rearrangement the atom returns to the ground state, and fluorescence X-rays with energy characteristic of that element are emitted (Potts, 1987). Figure 12 is a diagram illustrating the production of fluorescent X-rays in an atom. The emission intensity of this characteristic radiation is measured with a suitable X-ray spectrometer, with a multi-channel analyser and compared with those from elemental standards, providing quantitative data for the elemental components of a sample (Potts, 1987; Spectro, 2021b).

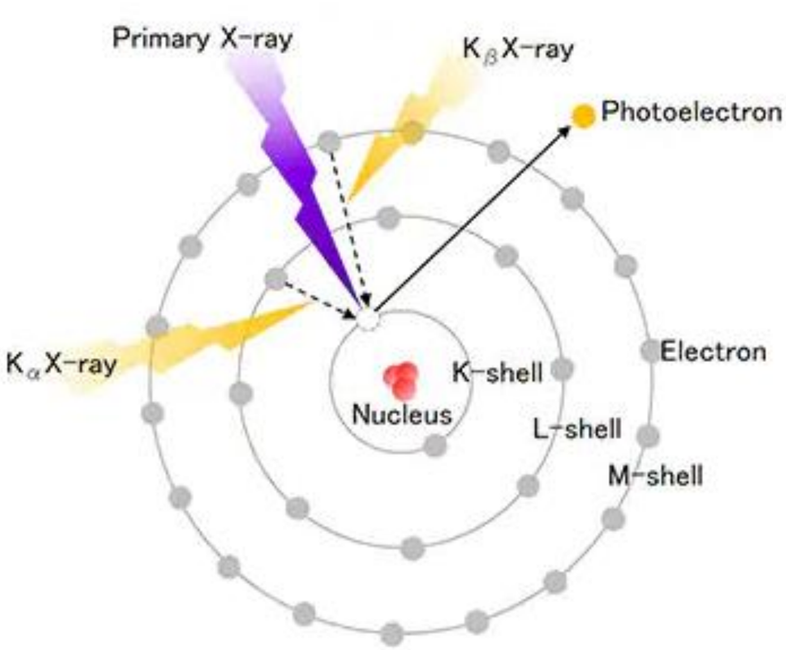

Figure 12: Fluorescent X-rays generation (Hitachi, 2021).

Elemental composition of sediments was determined by XRF and LOI techniques. XRF samples were prepared by drying and grinding samples into a fine powder using a grinding mill (Planetary Mono Mill Pulverisette 6, Fritsch). Ground sample (~12 g) was mixed with Hoechst Wax C Micropowder crystalline wax (~3 g) and pellets were pressed with a hydraulic press. Major and trace elemental composition of pelleted sediment samples was measured using XRF (Axios Sequential XRF Spectrometer, PANalytical).

LOI involved several steps, initially a porcelain crucible was weighed, and an aliquot of sediment (~1 g) was added to the crucible and heated in an oven for 1 hour at 100°C to evaporate any remaining H_20. The crucible and sample were reweighed after initial heating to determine H_20 content by mass loss. After this, the crucible and sample were heated for 1 hour at 1000°C in a furnace, to evolve CO_2 from organics and carbonate minerals, and reweighed to determine CO_2 evolution by mass loss.

3.5.2 X-Ray Diffraction (XRD)

XRD is a non-destructive technique capable of providing detailed information about the crystallographic structure and chemical composition of a solid phase. It was applied here to determine the mineral content of sediments and identify the crystal structure of laboratory synthesised nanoparticle treatments used in treatment experiments. The technique measures the average spacing between layers of atoms, because X-ray wavelengths (0.2 – 10 nm) are comparable to the interatomic spacing of crystalline solids (Kaliva and Vamvakaki, 2020). XRD can determine the orientation of a single crystal or grain and measure the size and shape of small crystalline regions (Salame et al., 2018). Crystalline materials have distinct atomic structures that generate a unique diffraction pattern, caused by a constructive and destructive interference of the scattered X-ray beam (Kaliva and Vamvakaki, 2020). Diffraction patterns for crystalline samples contain well-defined peaks at specific scattering angles. Bragg's law relating the wavelength of the X-rays to the interatomic spacing is given by the following equation:

$$2dsin\theta = n\lambda$$

Equation Bragg's Law

d is the perpendicular distance between pairs of adjacent planes, θ is the angle of incidence, λ is the wavelength of the beam, and n denotes an integer number referred to as the order of the reflection, and is the path difference between waves scattered by adjacent planes of atoms (Salame et al., 2018). Figure 13 shows a scheme for the deduction of Bragg's law from crystallographic planes.

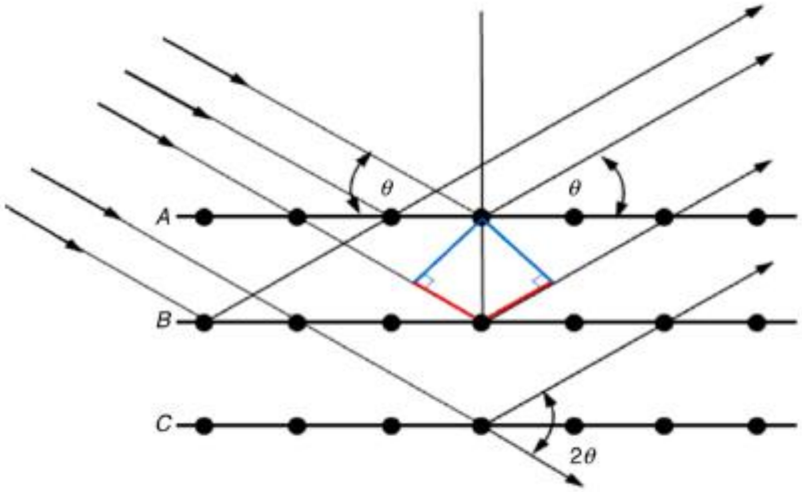

Figure 13: Scheme for the deduction of Bragg's law from crystallographic planes. Constructive interference occurs when the optical path difference of the different beams (marked in red) is equal to an integer number of wavelengths (nλ), from (Lamas et al., 2017).

Powdered dry sample (~0.1 g) was mounted on a glass slide and analysed on a Bruker D8 Advance X-ray Diffractometer to determine the mineral phases present. Phases were identified using the Bruker DIFFRAC.SUITE EVA software, and Bruker DIFFRAC.SUITE TOPAS software was used for their quantification.

3.5.3 X-Ray Absorption Spectroscopy (XAS)

XAS is particularly suited to studying metal chemical speciation, as it provides a non-destructive approach to determining Hg chemical speciation that is less likely to confound compound specific speciation than SEPs. X-ray energy is exploited to excite core electrons to unoccupied molecular orbitals or to eject electrons that produce unique wave patterns as they bounce off nearest neighbours to characterise the chemical speciation of the absorbing element (Cooke Andrews, 2006). X-ray absorption near edge structure (XANES) may resolve fine structural details that reveal the electronic and geometrical environment of the absorbing atom. Further from the edge, the extended X-ray absorption fine edge structure (EXAFS) can provide additional structural information revealing the local atomic environment to the element. Analysis of XANES and EXAFS regions of spectra can provide detailed molecular information such as inter-atomic distances, oxidation states, coordination number, nearest neighbour identity and degree of structural disorder in the sample (Kim et al., 2000). EXAFS spectra are unique for each compound enabling them to be used for identification of unknowns (Kim et al., 2000). However, methods capable of making accurate assertions concerning Hg-ligand binding (e.g. EXAFS) can often have high limits of detection (>100 ppm) making them unsuitable for analysis of most low level samples (Kim et al., 2000). EXAFS analysis was employed to determine the local molecular structure around Hg atoms and/or ions to identify specific Hg chemical species present. Figure 14 illustrates the three main regions of a Hg L_{III}-edge (12284 eV) spectrum, scanning from 12084 to 13000 eV.

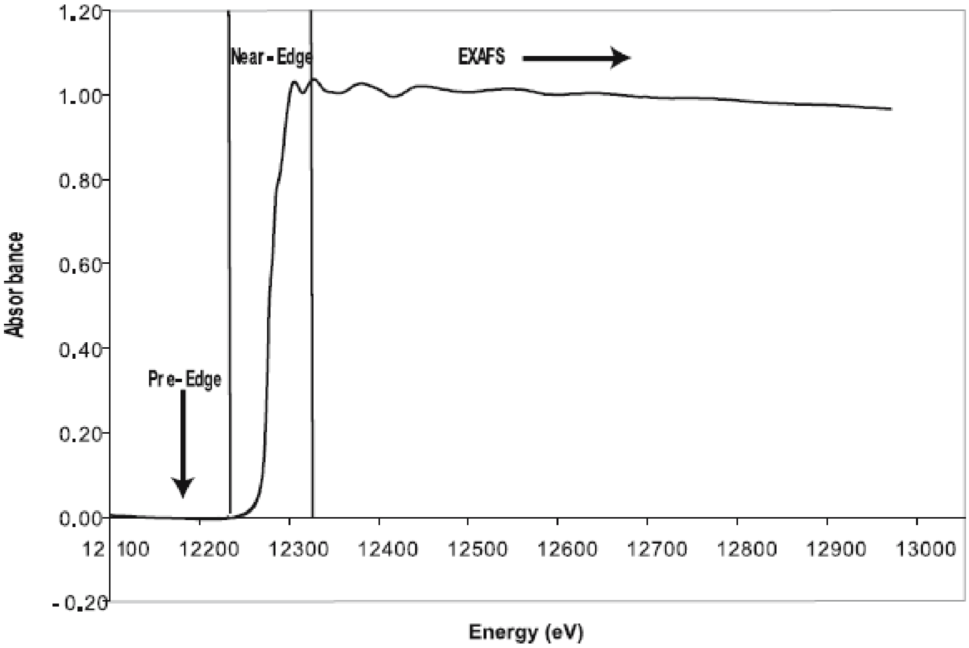

Figure 14: Hg L_{III}-edge spectrum (Pre-Edge [<12250 eV[, Near-Edge (or XANES) [12250–12350 eV] and EXAFS [12350–13000 eV] regions are labelled) from (Cooke Andrews, 2006).

Hg L_{III}-edge XAS was employed to resolve Hg chemical speciation in a range of samples and standards. Hg standards analysed on the I20 beamline are described in Table 2. Samples were scanned from 12084 to 13000 eV to resolve the Pre-edge, XANES and EXAFS spectral regions for the Hg L_{III}-edge at 12284 eV. Low temperature measurements were taken in a liquid nitrogen (77 k) or a helium (4 K) cryostat to ensure high quality data was collected from samples and standards. We managed to collect high quality XAS data from sediments with >60 mg/kg Hg with <10 scans on the I20 beamline at Diamond Light Source (DLS). Further details on the XAS methods applied in this research work can be found in Section 4.2.9 (Paper 1), Section 5.2.11 (Paper 2) and Section 6.2.9 (Paper 3). Figure 15 is an aerial photograph of the DLS synchrotron facility in Harwell, Oxfordshire (UK).

Figure 15: Diamond Light Source synchrotron (FireBird, 2018).

Table 2: List of Hg Standards made for XAS

Sample Reference	Description	Pellet / Disc
A	Cinnabar (α-HgS) 8.61mg / 100 mg Cellulose	Pellet
B	Meta-cinnabar (β-HgS) 8.61mg / 100 mg Cellulose	Pellet
C	Montroydite (HgO) 8.47mg / 100 mg Cellulose	Pellet
D	Calomel (Hg_2Cl_2) 8.97mg / 100 mg Cellulose	Pellet
E	Corderoite ($Hg_3S_2Cl_2$) 9.29mg / 100 mg Cellulose	Pellet
F	Hg sorbed to MLR sediment (~500 ppm)	Disc
G	Hg sorbed to EST sediment (~500 ppm)	Disc
H	Mercuric Chloride ($HgCl_2$) – 9.70mg $HgCl_2$ / 100 mg Cellulose	Pellet
J	Room temperature (RT) elemental Hg(0) – 7.60mg Hg(0) / 100 mg Cellulose	Pellet
K	Liquid nitrogen (LN) temperature (77 K) elemental Hg(0) – 7.60mg Hg(0) / 100 mg Cellulose	Pellet

3.5.4 Scanning Electron Microscopy (SEM) & Energy Dispersive X-Ray Spectroscopy (EDS)

SEM and EDS were employed for high resolution imaging of solid samples and visualisation of elemental components. SEM uses a focused electron beam to generate signals from electron-sample interactions at the surface of solid phases (Swapp, 2021). The signals reveal information about the sample including external morphology, crystalline structure, and orientation of sample components. Data are collected over a selected area of the sample surface generating a 2-dimensional image. Areas (1 cm – 5 µm) can be imaged in a scanning mode using conventional techniques. EDS can be applied at selected points on the sample to semi-quantitatively determining elemental compositions (Swapp, 2021).

100 mg aliquots of dried powdered solid samples were mounted on carbon pads (5 mm diameter) for analysis. Two different SEM and EDS systems were applied during this project. Analysis reported in Paper 1 (Section 4.3.1) used a Quanta 650 FEG, equipped with a Bruker X Flash 6 | 30 silicon drift detector, and utilised Bruker's ESPRIT EDS software to image physical topography and structure of particles in the sample via secondary electron emission, and establish their chemical composition. Samples were placed in a vacuum chamber at 0.5 mbar and the lens distance was set to the optimal distance of 10 mm for X-rays. Images presented in Paper 3 (Section 6.3.3) were taken during analysis

of samples under vacuum in ‘wet’ mode on an FEI XL30 ESEM-FEG (secondary electron or backscattered electron detectors). EDAX Gemini EDS system enabled elemental analysis of samples during imaging, automatically mapping and analysing components.

3.5.5 Transmission Electron Microscopy (TEM) & Energy Dispersive X-Ray Spectroscopy (EDS)

TEM is a technique that transmits a beam of electrons through a specimen to form an image. The interaction of the electrons with the sample as the beam is transmitted through the specimen forms a high-resolution image that can be magnified and focused onto an imaging device. TEM images were recorded using a FEI Talos F200X analytical scanning/transmission electron microscope (S/TEM) [operated at 200 kV] equipped with an integrated Super-X EDS system with 4 windowless silicon drift detectors (SDD), designed for precise and quantitative characterisation of nanomaterials. Holey-carbon Cu mesh TEM grids (200 mesh) were used to hold samples. TEM samples were prepared by directly pipetting sediment suspension onto the TEM grid followed by a few drops of isopropanol to wash off excess salt. Increased levels of Cu and C in EDS spectra are due to the use of holey-carbon Cu mesh grids.

3.5.6 X-ray Photoelectron Spectroscopy (XPS)

XPS analysis was applied to nanoparticles recovered following treatment of Hg-contaminated artificial groundwater (AGW) to investigate the surface speciation and mode of sequestration. XPS is a surface sensitive analytical technique that works due to the photoelectric effect, it is sensitive to the top 1 to 10 nm. Figure 16 is a simplified visual interpretation of the atomic layers at the surface of a material. The surface of a material is the point of interaction with the external environment, therefore better understanding the physical and chemical interactions that occur at the surface provide important information, such as elemental composition and oxidation state. The surface will influence factors such as corrosion rates, adhesive properties, and catalytic activity (XPSSimplified, 2021). XPS spectra are obtained by irradiating a solid surface with a beam of X-rays while simultaneously measuring the kinetic energy of electrons that are emitted from the surface layers of the material being analysed. A photoelectron spectrum is logged by counting ejected electrons over a range of kinetic energies. Spectral peaks are defined by atoms emitting electrons with specific characteristic energy (XPSSimplified, 2021). The energies and intensities of photoelectron peaks enable identification and quantification of surface elements

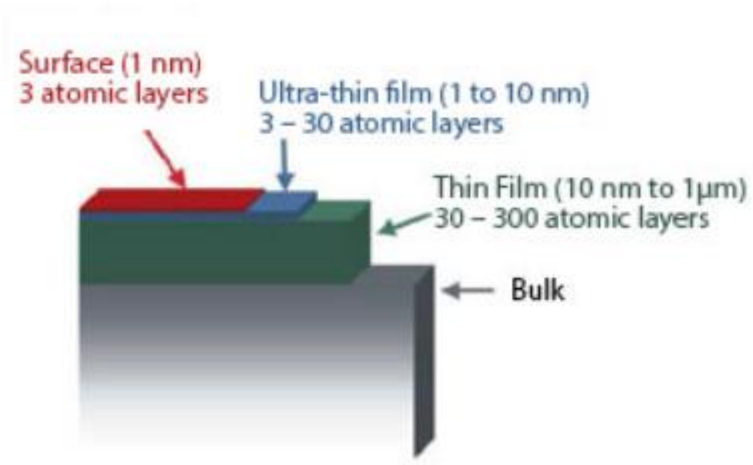

Figure 16: Schematic defining the atomic layers at the surface of a bulk material (XPSSimplified, 2021).

XPS was carried out using an ESCA2SR spectrometer (ScientaOmicron GmbH) using monochromated Al Kα radiation (1486.6 eV, 20 mA emission at 300 W, 1 mm spot size) under vacuum. Charge neutralisation was achieved using a low energy electron flood source (FS40A, PreVac). Binding energy scale calibration was performed using C-C in the C 1s photoelectron peak at 285 eV. Analysis and curve fitting was implemented using Voigt-approximation peaks using CasaXPS (Fairley, 2019).

3.6 Aqueous Geochemical Monitoring

3.6.1 pH and Oxidation Reduction Potential (ORP)

pH (hydrogen ion concentration) and ORP were measured from aqueous sample aliquots (>300 µL) with calibrated probes. pH was calibrated using pH 4, 7 and 10 buffer solutions before every 10 sample measurements. ORP was calibrated using standard solution of 220 mV relative to the standard hydrogen electrode potential.

3.6.2 Ion Chromatography (IC)

IC was utilised for aqueous phase anion analysis. The technique measures concentrations of ionic species by separating them according to interactions with a resin (Bruckner, 2021). Ionic species separate differently depending on species type and size, based on their affinity to the ion exchanger. Sample solutions pass through a pressurised chromatographic column where ions are absorbed by column constituents. An eluent runs through the column and extracts the absorbed ions, the retention time of different ionic species is used to determine their concentrations (Bruckner, 2021). 1 mL samples were stored at 4°C prior to anion analysis on a Dionex ICS-5000 Capillary HPIC^{TM} System.

Further details on specific sample preparation can be found in Section 4.2.4 (Paper 1) and Section 5.2.6 (Paper 2)

3.6.3 Inductively Coupled Plasma – Mass Spectrometry (ICP-MS)

Atomic elements from liquid samples are lead through a plasma source where they become ionised, and then ions are sorted and quantified on account of their mass. ICP-MS was applied for quantification of Hg and Cu in aqueous samples, with a detection limit of up to 0.001 ppb the technique in capable of determining ultra-trace levels (Passariello et al., 1996). The main functions of ICP-MS are: (1) producing ions and other species in a high temperature plasma; (2) extraction of ions from the plasma and attenuate polyatomic interferences; (3) separation of ions using a quadrupole mass filter according to mass charge ratio (MAGU, 2021). Polyatomic interferences are attenuated by means of a pressurised octopole reaction cell. Most elements in aqueous solutions can be analysed except for halides and some metals. Figure 17 is a schematic representation of and Agilent 7500 with a collision reaction cell.

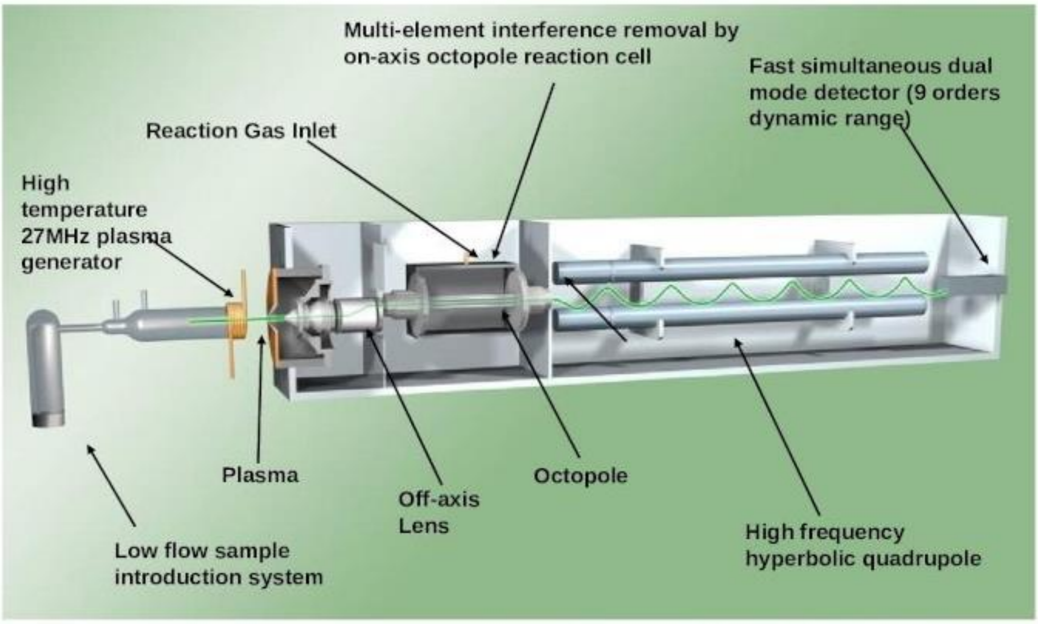

Figure 17: Agilent 7500 ICP-MS System with a collision reaction cell (Kusnadhi, 2015)(Ref)

Selecting an appropriate sample matrix is essential, as it can have a significant impact on the accuracy and precision of analytical data. The unique properties of Hg can cause a memory effect during ICP-MS analysis, and this has the potential to bias reported Hg concentrations during sequential sample analysis due to carryover between samples and calibration standards (Bloom et al., 2003). Amalgamation of Au and Hg has previously been reported to reduce the memory effects during Hg analysis (Chen, 2009), a 200 µg/L Au spike (from a 10 ppm elemental Au(0) in 2% in aqua regia stock solution) was added to a 2% aqua regia matrix for samples and calibration standards at the point of dilution to stabilise Hg in solution (Chen, 2009). An Agilent 7500 ICP-MS was operated in rapid sequential mode to detect and quantify Hg in samples, with detection limits that are typically 0.1 ppb under the standard operating conditions. Calibration standards (Blanks, 1, 5, 10, 50, 100 ppb) were run, followed by a wash, after every 10 samples. Further information on sample preparation can be found in Section 4.2.7 (Paper 1), Section 5.2.7 (Paper 2) and Section 6.2.7 (Paper 3).

3.6.4 Ferrozine Assay

Ferrozine assay measurements were taken from acid digests of microcosm sample suspensions (aqueous phase with suspended solids) on a Jenway 6715 series ultraviolet-visible (UV-vis) spectrophotometer at a wavelength of 562 nm to determine aqueous and bioavailable Fe(II) concentration (Lovley and Phillips 1987). Sample concentrations were interpolated by linear regression from the absorbance readings for Fe(II) standards. Figure 18 shows a standard calibration line for the ferrozine assay based on absorbance from a range of Fe(II) standards (0, 1, 5, 10, 20 mM). Further details of the methodology are described in Section 5.2.3 (Paper 2).

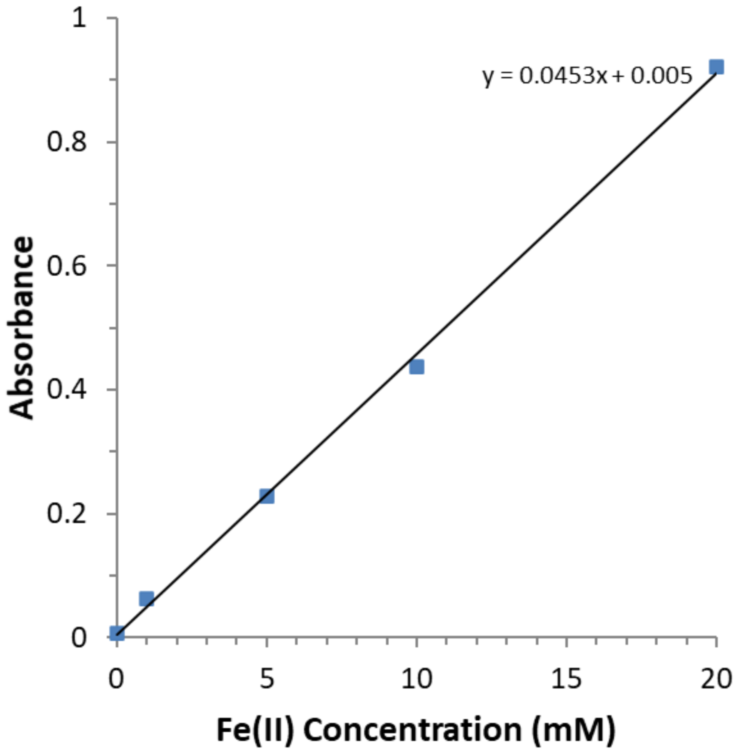

Figure 18: A standard calibration line for the ferrozine assay based on absorbance from a range of Fe(II) standards.

3.6.5 Inductively Coupled Plasma – Atomic Emission Spectrometry

ICP-AES is a technique that uses a plasma as a source and relies on optical emission for analysis. Liquid samples are turned into an aerosol and are then injected into the plasma. High temperatures in the plasma are sufficient to atomise the sample and provide the energy for ionisation and excitation (Spectro, 2021a). Electromagnetic radiation is emitted at wavelengths characteristic of a particular element, which can be used to quantify elemental components. The technique was used to determine concentrations of Fe in 10 mL samples (2% (v/v) HNO_3) from the aqueous phase of total Fe digests. The Perkin-Elmer Optima 5300 dual view ICP-AES was used for analysis, it has a detection range of 10 ppb – 50 ppm.

3.6.6 Optical Density

Optical density of biomass from *Geobacter sulfurreducens* cultures was determined by UV-Vis spectrophotometry at 600 nm (OD_{600}) on a Jenway 6715 series UV-vis spectrophotometer.

3.6.7 Cold Vapour - Atomic Fluorescence Spectroscopy (CV-AFS)

CV-AFS is analytical technique used in the measurement of trace amounts of volatile metals (e.g. Hg). No vaporisation step is required because the sample is volatile and a vapour at room temperature. The technique has high sensitivity without significant interferences, making it very applicable for trace analysis of water samples (Yap et al., 2010). UV light from a source is directed to the sample cell, atoms in the gaseous sample are excited by the UV light. Excited atoms reradiate the absorbed energy as omnidirectional fluorescence light. A detector is usually placed at a 90° angle to the UV light source to ensure that only the fluorescence light is detected. The detector is a photon-counting module, which will only detect the photons derived from the target atoms (Gasmet, 2021). Figure 19 is a simplified visual representation of an AFS instrument.

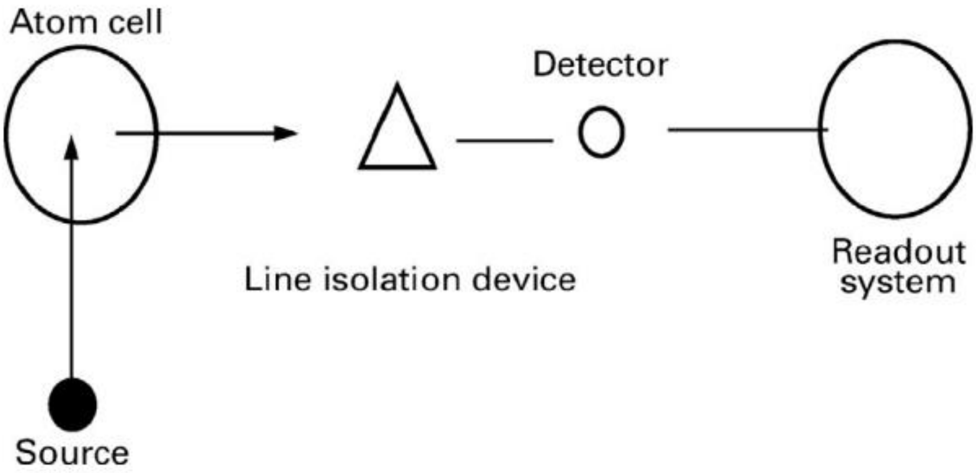

Figure 19: A schematic representation of AFS instrument (Hill and Fisher, 2017).

The technique was applied by P S Analytical (PSA) for quantification of Hg in MeHg extracts from solid samples reported in Paper 1 (Section 4.3.3) and Paper 2 (Section 5.3.2). PSA Millennium Merlin 10.025 Hg analyser combines the advantages of vapour generation techniques which removes most chemical interferences with the sensitivity and selectivity of AFS which allows Hg analysis down to sub ppt levels in all types of samples (PSAnalytical, 2021).

3.7 Bacterial Community Analysis

16S rRNA gene sequencing was applied for phylogenetic characterisation of the bacterial community in sediment samples. This technique can identify the phylogenetic and taxonomic composition of complex environmental samples by the sequencing of 16S ribosomal RNA genes. Sequencing of amplified 16S rRNA genes was applied to determine closest match phylotypes in samples and identify microbial metabolic pathways that could influence Hg chemical speciation under environmental conditions (e.g. Hg reduction, Hg sulfidation and Hg methylation).

This method entails the following steps: (1) extraction of genes from sediment; (2) amplification (replication) of 16s rRNA genes via a polymerase chain reaction (PCR); (3) separation via gel electrophoresis to target the specific base pair product; (4) sequencing of the PCR products using region of interest-specific forward and reverse primers; and (5) purification, cleaning, normalisation, and pooling of PCR products. Bioinformatic data analysis is required for characterisation via comparison to known 16S rRNA gene sequences. Figure 20 illustrates steps 1 to 4 of the 16S rRNA gene sequencing process. The specific methodology applied to sediment samples is described in Section 4.2.10 (Paper 1) and 5.2.12 (Paper 2).

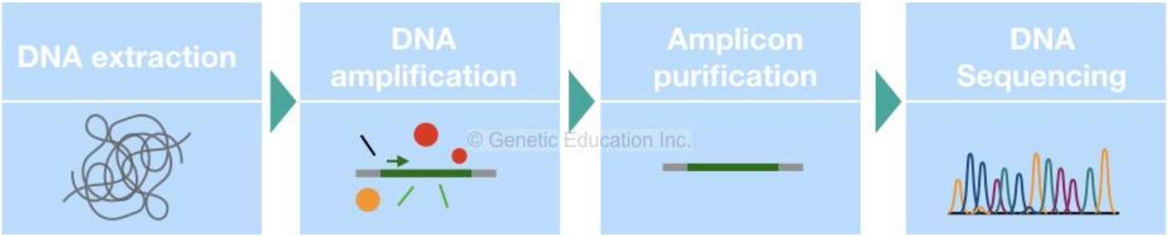

Figure 20: A broad overview of the 16S rRNA gene sequencing process (GeneticEducation, 2020).

3.8 Treatment Microcosm Experiments

Microcosm experiments were setup to investigate a portfolio of treatment strategies for Hg-contaminated sediment and groundwater systems utilising iron-based nanoparticle technologies and organic electron donor (biostimulation) of microbial communities. Papers 2 (Section 5.2.3) and Paper 3 (Section 6.2.3) provide detailed methods and scientific findings from microcosm experiments carried out as part of this research project. Figure 21 depicts the contents of a microcosm setup to investigate the impact of an iron-based particle treatment on biogeochemistry in a sediment and anoxic water systems implemented during experiments reported in Paper 2.

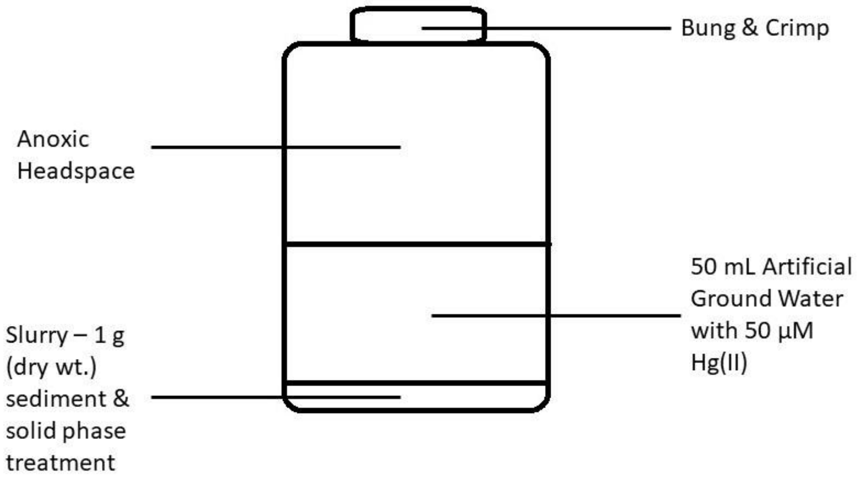

Figure 21: Diagram summarising the contents of microcosms setup for treatment experiments in Paper 2.

3.9 Experimental and Analytical Error

Methodologies were designed to ensure experiments and analysis were carried out to minimise experimental error to reduce the uncertainty associated with the difference between measured values and the true value. Experimental and analytical error was addressed using the following approaches:

1. Repeat sample analysis – most samples were analysed in duplicate, triplicate, or quadruple.
2. Standard error of mean was calculated from triplicate or quadruple measurements. Small standard errors highlighted consistency of experimental and analytical process, providing reassurance that averaged values were representative of true values.
3. Triplicate microcosm systems were setup for experiments where possible.
4. Application of aseptic laboratory technique was essential to mitigate against contamination of microcosm treatment systems from external micro-organisms in the environment (Siddiquee, 2017).
5. Accuracy and precision of Hg quantification by ICMPS values was ensured through calibration with Hg standards (1, 5, 10, 50, 100 ppb) after very 10 samples, blanks and washing between sample measurements. Memory effect of ‘sticky’ Hg was mitigated by addition of 200 ppb Au to samples prior to analysis to reduce carry over between samples (Chen, 2009).
6. Hg L_{III}-edge EXAFS linear combination fitting used residual values (R-value) and chi-squared and to inform the goodness of fit for quantitative compositions of Hg standard components. The residual can be interpreted as the amount of the spectrum that remains unfitted by the linear combination fitting procedure (Kim et al., 2000; Kim et al., 2004).

4.0 Paper 1: Chemical speciation and potential environmental mobility of mercury in a contaminated canal bed sediment.

Alexander Tait[a]*, Samuel Shaw[a], David Polya[a], Russell Thomas[b], Christopher Boothman[a], Jonathan R. Lloyd[a].

[a]Williamson Research Centre for Molecular Environmental Science, Department for Earth and Environmental Science, The University of Manchester, Manchester, M13 9PL, United Kingdom

[b]WSP, Kings Orchard, 1 Queen St, Bristol, BS2 0HQ, United Kingdom

*corresponding author e-mail address: alexander.tait@manchester.ac.uk

Keywords

Canal bed sediment

Hg mobility

Hg chemical speciation

Hazardous material risk assessment

Abstract

The speciation of Hg in a contaminated sediment from the Weaver Navigation Canal (Runcorn, UK) was investigated using a sequential extraction procedure, in combination with ICP-MS, and XAS to establish the potential mobility and bioavailability of the toxic metal. The mobility and chemical speciation of solid phase Hg at the site is crucial to understanding the environmental risk posed by contaminated sediment. Additional analytical techniques were employed to assist in other aspects of sediment characterisation. XRD indicated that the sediment mineralogy was dominated by calcite and brucite, which are key components of solid waste from Hg-cell chlor-alkali plants. Sequential extraction from sediment revealed the Hg to be recalcitrant, suggesting that it is predominantly strongly complexed or mineral bound, and therefore relatively immobile and less bioavailable. XAS was able to reveal that the bulk of the Hg (>85%) was present as beta-HgS, and the remaining ~15% was predominantly sorbed Hg(II). Methylmercury was detected and, although less than 0.1% total Hg, this potentially poses the largest risk due to its high toxicity and its tendency to bioaccumulate. Analysis of 16S rRNA gene sequencing data identified bacterial species capable of catalysing both sulfidation and methylation reactions in the sediment.

4.1 Introduction

Mercury (Hg) is a ubiquitous heavy metal that can pose a serious threat to human health and biota worldwide due to its toxicity, mobility and persistence in the environment (Mahbub et al., 2017). Anthropogenic activities contributing to release of Hg and contamination of the environment include fossil fuel combustion, Hg-mining, artisanal and small-scale gold mining, non-ferrous metal production, chlor-alkali chemical production, cement production and waste management (incineration and landfill) (J. Wang et al., 2012). Hg is recognized as a priority hazardous substance that can travel long distances via the atmosphere or in natural waters, following local release, leading to regional and global impacts (Brocza et al., 2019). In 2010, the global Hg emissions generated from industrial processes were estimated to be approximately 2,270 metric tons per year (Richter and Flachberger, 2010). Chlor-alkali plants which use elemental Hg(0) for the electrolytic production of chlorine and sodium hydroxide have been shown to be potential sources of environmental Hg pollution, of concern at the local to regional scales (Neculita et al., 2005). However, there is limited knowledge of the solid phase chemical speciation of Hg in environments impacted by the chlor-alkali industry. This needs to be better understood to establish the risk posed by potential remobilisation of Hg from contaminated soils and sediments on site, or off-site in river, lake, or sea sediments.

Brine solutions used in the Hg-cell process for chlorine and caustic soda production often contain calcium, magnesium, and sulphates, which are the main impurities (Hung et al., 2017). The solution is treated in a reactor with sodium carbonate (Na_2CO_3, soda ash) and sodium hydroxide (NaOH, caustic soda) to precipitate calcium carbonate ($CaCO_3$) and magnesium hydroxide ($Mg\ (OH)_2$), and therefore remove the impurities. Barium chloride can be added to precipitate sulphates as barium sulphate ($BaSO_4$, barite). Wash water containing Hg in aqueous solution is then transferred to a sulfide precipitation system, where soluble Hg(II) is immobilised as HgS in a solidification and stabilisation process (Hung et al., 2017). Precipitates are settled and the liquid effluent is discharged as wastewater to the sewage system, while the solid slurry can be stored as sludge in lagoons prior to offsite disposal. However, run off from solid waste storage lagoons can impact nearby water bodies (Brinkmann et al., 2014; Hung et al., 2017). Calcium carbonate, magnesium hydroxide, barium sulphate and mercuric sulfide (HgS) can all therefore be associated with solid phase waste from the precipitation processes used in Hg-cell production of chlorine and caustic soda.

Emission of Hg to air, land and water from chlor-alkali plants is a global issue. The UNEP estimated that 15.1 tonnes Hg emitted to air and 2.7 tonnes Hg emitted to the aquatic environment was linked to global chlor-alkali production in 2015 (UNEP, 2019). The chlor-alkali industry is the only sector for which emissions are estimated to have decreased significantly between 2010 and 2015, with an estimated 6 tonne decrease in emissions over this period. Total mercury (THg) emissions in Western Europe was estimated to be 9.5 tonnes in 1998, ranging from 0.2 – 3.0 g of Hg per tonne of chlorine production capacity at individual plants (Pirrone et al., 2010). This production process is gradually being phased out and replaced by cleaner technologies.

There is evidence to suggest wastewater and sludge produced in the Hg-cell process has been discharged directly into water bodies (Guney et al., 2020). However, despite implementation of wastewater treatment, Hg from legacy discharge could still potentially be remobilised under environmental conditions and bio-accumulate in the food chain (Randall and Chattopadhyay, 2013). Hg input from the chlor-alkali industry has been decreasing due to better waste management and process improvement associated with conversion to a membrane treatment process (Bernaus et al., 2006). Guney et al (2020) discusses the impacts of a former chlor-alkali plant site in Pavlodar (Kazakhstan) on Lake Balkyldak in North Kazakhstan, the most seriously contaminated receptor, with up to 617 mg/kg of Hg identified in sediments where the local population may be exposed to Hg due to fish consumption illegally caught from local rivers and reservoirs. The study makes comparison with five additional international cases of Hg pollution (in US, Spain, Portugal, Canada and Romania) resulting from former Hg-cell chlor-alkali plant activities, highlighting the global scale environmental hazard posed by these facilities (Guney et al., 2020).

The solubility, mobility, and potential bioavailability of Hg in the environment are controlled by numerous factors, including the environmental conditions (e.g. pH, redox potential) and Hg speciation. Hg generally exists in three forms in the environment, that have different properties and toxicity, these are inorganic (elemental and ionic) and organic. Inorganic Hg species are present in three oxidation states Hg(0), Hg(I) and Hg(II), although Hg(II) is much more common under environmental conditions (Morgan et al., 2009). These can be highly mobile and water-soluble ions (aqueous Hg(II)) and insoluble compounds (HgO, HgS, beta-HgS, Hg_2Cl_2). Mobile and bioavailable aqueous Hg(II) can be found in the hydrosphere, aqueous Hg(II) can sorb to minerals (e.g. Fe/Mn oxyhydroxides and clays) and organic matter under environmental conditions (O'Connor et al., 2019). Hg-contaminated sediments constitute complex systems where many interdependent factors, including the amount and composition of soil organic matter and clays, oxidized minerals (e.g. Fe/Mn oxides), reduced elements (e.g. S^{2-}), as well as sediment pH and redox conditions affect Hg speciation (O'Connor et al., 2019). Microbial reduction of sulphate to sulfide in anaerobic Hg contaminated sediments, can lead to the formation of HgS (O'Connor et al., 2019). HgS is a dimorphous mercuric compound found in two mineral forms (1) cinnabar (α-HgS) and (2) metacinnabar (β-HgS). Methylation is considered the most toxic transformation, in anoxic sediments, inorganic Hg(II) can be converted into the organic methylmercury (MeHg) species by anaerobic bacteria (Wiatrowski et al., 2009). Monomethyl- and dimethyl-Hg (MMeHg, DMeHg) are potent neurotoxins that can bio-accumulate in the food chain (Mahbub et al., 2017). Dissimilatory sulphate-reducing bacteria (DSRB) and dissimilatory iron-reducing bacteria (DIRB) are generally thought to drive this process (Kerin et al., 2006). However, recent research suggests that additional bacterial groups in the oxic zone of global oceans, such as *Nitrospina* species, may also play a role in environmental methylation (Gionfriddo et al., 2016; Tada et al., 2020; Villar et al., 2020).

Several previous studies have been published characterising Hg chemical speciation and mobility in soils and sediments impacted by activities at chlor-alkali plants (Bernaus et al., 2006; Biester et al., 2002; Biester and Scholz, 1997; Neculita et al., 2005; Santoro et al., 2010). Santoro et al (2000) identified amorphous Hg-S-Cl (34 - 56%), beta-HgS (20 - 33%), corderoite (6 - 26%), alpha-HgS (5 – 20%), by X-ray absorption near edge spectroscopy (XANES), in soil contaminated by Hg-containing wastes from a chlor-alkali plant in Italy. The proportion of Hg species was dependent on particle size, with the colloidal fraction (430 to 650 nm) considered to pose the most significant risk due to higher mobility (Santoro et al., 2010). Direct determination of Hg chemical speciation by XANES in soils collected from a chlor-alkali plant in the Netherlands identified HgS and corderoite ($Hg_3S_2Cl_2$) as the dominant Hg species, more soluble HgO and $HgSO_4$ were also identified (Bernaus et al., 2006). Hg(0) emitted from chlor-alkali plants could not be found in any of the soils studied (Bernaus et al., 2006; Biester et al., 2002; Santoro et al., 2010). A recent study investigating Hg concentrations in freshwater sediment from two Scottish canals, identified a significant inverse relationship between THg concentration and %MeHg (Cavoura et al., 2017). However there have been no studies investigating Hg chemical speciation and potential mobility of Hg in contaminated canal bed sediments directly impacted by Hg-cell chlor-alkali plants, such as the Marsh Lock site (Weston Point, Runcorn, UK) investigated in this study. Canals are often characterised by low flow, contributing to anoxic sediments with limited mobility. This type of waterway is used for transportation of goods between urban areas and industrial sites in close proximity could historically have been a source of pollutant input. Brine electrolysis at Weston Point, Runcorn started in 1897, the last remaining cell room was closed by the current operator in 2017 (INOVYN, 2016a; INOVYN, 2016b). However, historic practices and associated discharges and runoff may have contributed to Hg contamination in nearby waterways. In this study, we aimed to characterise contaminated canal bed sediment from the site, identify the solid phase Hg species present and establish Hg mobility to inform future risk assessment. The multidisciplinary approach included sequential extractions, augmented by X-Ray Absorption Spectroscopy and microbial profiling to characterise biogeochemical controls on Hg.

4.2 Methods

4.2.1 Sampling

The study site was located at Weston Marsh Lock, Runcorn (MLR), North-West England, UK (UK Grid reference: SJ 50582 79805). The site is located adjacent to multiple current and historic sources of pollution, which include a chlor-alkali plant. The Canal and River Trust, UK authorised site access during a period of maintenance works, which included dredging of sediment at the site. A sample of the MLR canal bed sediment, a wet sludge material, were collected in 5% (v/v) nitric acid (made up from analytical grade 15.9 M stock) washed 100 mL glass bottles. Canal bed sediment samples were collected from a single location at the base of the Eastern lock gate whilst sediment was being dredged as part of remediation efforts.

4.2.2 X-Ray Fluorescence (XRF) and Loss on Ignition (LOI)

XRF pellets were prepared from 12 g aliquots of powdered dry sediment (oven dried) and 3 g of wax. Sample pellets were subsequently analysed on an Axios Sequential XRF Spectrometer to determine their elemental composition. For LOI analysis, a porcelain crucible was weighed, and an aliquot of sediment (~1 g) was added to the crucible and heated in an oven at 100°C for 1 hour to evaporate any remaining water. The crucible and sample were reweighed after initial heating to determine water content by mass loss. Following this, the crucible and sample were heated in a furnace at 1000°C for 1 hour, to evolve CO_2 from organics and carbonate minerals, and reweighed to determine CO_2 evolution by mass loss.

4.2.3 X-Ray Diffraction (XRD)

A small aliquot (>0.1 g) of dried, powdered sediment sample was mounted on a glass slide and analysed on a Bruker D8 Advance X-ray Diffractometer to determine the mineral phases present. Phases were identified using the Bruker DIFFRAC.SUITE EVA software, and Bruker DIFFRAC.SUITE TOPAS software was used for their quantification.

4.2.4 Ion Chromatography (IC)

Aliquots (2 g) of sediment sample were transferred to 1.5 mL micro-centrifuge tubes and centrifuged at 14,000 g for 10 minutes to separate the solid phase from the water present in the sample. Supernatants were decanted into a 50 mL centrifuge tubes and filtered through a 0.2 µm pore diameter syringe filter. Triplicate 1 mL samples were stored at 4°C prior to anion analysis on a Dionex ICS-5000 Capillary HPIC^{TM} System.

4.2.5 Scanning Electron Microscopy (SEM) & Energy Dispersive X-Ray Spectroscopy (EDS)

100 mg aliquots of dried powdered sediment were mounted on carbon pads (5 mm diameter). An FEI/Thermofisher Quanta 650 FEG, equipped with a Bruker X Flash 6 | 30 silicon drift detector and utilises Bruker's ESPRIT Energy Dispersive X-Ray Spectroscopy (EDS) software (latest version 2.2), was used to image physical topography and structure of particles in the sediment sample via secondary electron emission, and establish their chemical composition. Samples were placed in a vacuum chamber at 0.5 mbar and the lens distance was set to the optimal distance of 10 mm for X-rays.

4.2.6 Transmission Electron Microscopy (TEM) & Energy Dispersive X-Ray Spectroscopy (EDS)

TEM images were recorded using a FEI Talos F200X analytical scanning/transmission electron microscope (operated at 200 kV) equipped with an integrated Super-X EDS system with 4 windowless silicon drift detectors (SDD). Holey-carbon Cu mesh TEM grids (200 mesh) were used to hold samples. TEM samples were prepared by directly pipetting sediment suspension onto the TEM grid followed by a few drops of isopropanol to wash off excess salt. Increased levels of Cu and C in EDS spectra are due to the use of holey-carbon Cu mesh grids.

4.2.7 Total Mercury (THg) Extraction Procedure

A passive THg extraction procedure was adapted from Bloom *et al*. (2003) (Bloom et al., 2003). Sediment sludge (~0.5 g, ~0.2 g dry wt.) and aqua regia (10 mL; 3:1 ratio of 12.1 M HCl and 15.9 M HNO_3) were added to 50 mL Nalgene™ Oak Ridge Centrifuge Tubes and left for an 18-hour extraction period. 80 mL DIW, 2 mL supernatant and 2 mL 10 ppm gold standard working solution (10 mg/L Au in 2% v/v aqua regia) were added to a 100 mL acid washed volumetric flask. The content of the flask was then made up to 100 mL with DIW, to create a 2% (v/v) aqua regia (with 200 ppb Au) sample matrix, and then transferred into a 100 mL acid washed bottle. Triplicate 10 mL aliquots were passed through 0.45 µm syringe filters into separate 10 mL tubes for ICP-MS analysis. THg extractions were carried out on duplicate MLR samples.

A certified reference material (CRM), ERM-CC580 Estuarine Sediment, was purchased from the European Commission's Joint Research Centre's Institute for Reference Materials and Measurements to assess the Hg extraction efficiency of the protocols. ERM-CC580 has a certified mass fraction (based on dry mass) for THg of 132 ± 3 mg/kg, and MeHg of 75 ± 4 µg/kg. THg extractions were carried out on ERM-CC580 to determine extraction and recovery efficiency of the protocol.

4.2.6 Mercury Sequential Extraction Procedure

The procedure uses five solutions to separate Hg species into fractions based on their extractability: (F1) Water Soluble (18.2 MΩ cm^{-1} deionised water); (F2) Weak Acid Soluble (pH 2, 0.1 M CH_3COOH +

0.01 M HCl); (F3) Organo-complexed (1 M KOH); (F4) Strongly Complexed (12 M HNO_3); and (F5) Mineral Bound (aqua regia) (Phipps et al., 2013). Table P1-3 identifies the Hg species typically found in each fraction.

Sediment/sludge (~0.5 g, ~0.2 g dry wt.) and 20 mL extractant 1 (F1) were added to 50 mL Nalgene™ Oak Ridge Centrifuge Tubes. Extraction vessels were then mixed on an orbital shaker at 200 rpm for 24 hours and centrifuged at 4000 g for 10 minutes with a Boeco C28A centrifuge. Supernatant was decanted off into 50 mL centrifuge tubes and the precipitate rinsed with 20 mL DIW by shaking vigorously and centrifuging at 4000 g for another 10 minutes. The rinse supernatant was decanted off and combined with the corresponding extractant supernatant.

After the rinse step (for F1 to F3), the next sequential extractant (F2 to F4) was added to sediment sample residue. 80 mL of DIW, 8 mL supernatant (1.34 mL for Fraction 4 to avoid excess HNO_3), 0.5 mL 15.9 M HNO_3 (0.75 mL for F3 to neutralise KOH; none for F4 to avoid excess), 1.5 mL 12.1 M HCl and 2 mL 10 ppm gold standard working solution (10 mg/L Au in 2% (v/v) aqua regia) were added to a 100 mL acid washed volumetric flask. The content of the flask was then made up to 100 mL with DIW, to create a 2% (v/v) aqua regia (with 200 ppb gold) sample matrix and transferred into a 100 mL acid washed bottle. Triplicate 10 mL aliquots were passed through 0.45 µm syringe filters into separate 10 mL tubes for ICP-MS analysis.

After the extractant 4 (F4) rinse step, the next sequential extractant (F5) was added to sediment sample residues following the methodology outlined in Section 2.5. Sequential Hg extractions were carried out in duplicate on ERM-CC580 to determine extraction and recovery efficiency of the protocol.

Table P1-3: Typical Hg compounds identified for extractants (F1 to F5) in the SEP (O'Connor et al., 2019; Phipps et al., 2013)

Fraction	Extractant	Description	Typical Compounds Extracted
F1	Deionised Water	Water soluble	$HgCl_2$
F2	HCl / CH_3COOH pH 2	Weak acid soluble	HgO / $HgSO_4$ / Hg sorbed to oxides (Fe, Mn)
F3	1M KOH	Organo complexed	Hg sorbed to humics / CH_3Hg^+ / Hg_2Cl_2
F4	12M HNO_3	Strongly complexed	Hg_2Cl_2 / Hg^0 / mineral lattice / beta-HgS (with impurities)
F5	Aqua regia	Mineral bound	HgS / beta-HgS / HgAu / HgSe

4.2.7 Inductively Coupled Plasma-Mass Spectroscopy (ICP-MS)

ICP-MS was used to determine concentrations of Hg in 10 mL samples from sediment extracts. An Agilent 7500 ICP-MS was operated in rapid sequential mode to detect and quantify Hg in samples.

Detection limits are typically 0.1 ppb under the standard operating conditions. A 200 µg/L gold spike (from a 10 ppm elemental Au(0) in 2% in aqua regia stock solution) was added to a 2% aqua regia matrix for samples and calibration standards at the point of dilution to stabilise Hg in solution, and minimise carryover between samples and calibration standards (Chen, 2009).

4.2.8 Methylmercury (MeHg) Analysis

A selective MeHg extraction and cold vapour atomic fluorescence spectroscopy (CV-AFS) method was adapted from Brombach et al. (2015) and Lancaster et al. (2019) (Brombach et al., 2015; Lancaster et al., 2019). ~500 mg of powdered dried sample was first extracted by acid leaching using 10 mL of 6 M hydrochloric acid and ultrasonicated for 10 min. Following the leaching process, samples were 0.45 µm filtered. Selective extraction of MeHg was carried out with the addition of 8 mL of 1.5 M KBr in 0.9 M sulphuric acid / 1.5 M $CuSO_4$ mixture (combined in a 2:1 ratio) and 10 mL dichloromethane (DCM) which was shaken on an automatic shaker for 2 hours followed by 30 seconds of mixing with a vortex mixer. A known volume of the DCM extract was removed and back extracted with 1 mL of 0.01 M sodium thiosulphate solution, with 30 minutes on an automatic shaker followed by 30 seconds of mixing with a vortex mixer. The thiosulphate layer was removed from the vial and the DCM layer was extracted again with another 1.5 mL of 0.01 M thiosulphate solution. The two thiosulphate extracts were combined and diluted with deionized water to 25 mL. MeHg was converted to inorganic Hg with the addition of 2.5 mL concentrated HCl and 3 mL of 0.1 N bromide/bromate solution and left to react for 30 minutes at ambient conditions. The samples were then decolourised with 12% (m/v) hydroxylamine solution and analysed by CV-AFS using PSA Millennium Merlin 10.025. Estuarine sediment CRM ERM-CC580 was used to assess the extraction and recovery efficiency of the protocol.

4.2.9 Hg L_{III}-edge X-Ray Absorption Spectroscopy

Hg L_{III}-edge XAS data were collected on the I20 Beamline at Diamond Light Source (Harwell, Oxfordshire). Samples were made from 50 to 100 mg aliquots of MLR sludge. The samples and Hg standards were analysed in X-ray fluorescence mode (64 element monolithic Ge detector with Xspress4) within a liquid nitrogen cryostat, at 77 K. Merges of data from less than 10 scans to k = 12 – 14 scans were sufficient for the collection of high-quality data from samples containing >80 mg/kg Hg. To quantify the Hg phases present in the MLR sample the K^3 weighted EXAFS spectra were linear combination fit with the spectra of various known standards (beta-HgS, alpha-HgS, Elemental Hg(0) 77K, HgO, $HgCl_2$, Hg_2Cl_2 $Hg_3S_2Cl_2$ and Hg(II) sorbed to MLR sediment) in Athena software from k = 3 to 12. Iterative linear combination fitting of various combination of Hg standards considered likely to exist under the geochemical conditions within the sediment enabled identification and proportionate quantification of these Hg chemical species in the solid phase samples.

4.2.10 Bacterial Population Analysis

DNA was extracted from 200 µL of sediment slurry using a DNeasy PowerLyzer PowerSoil Kit (Qiagen, Manchester, U.K). Sequencing of polymerase chain reaction (PCR) amplicons of 16S rRNA genes present in the samples was conducted with the Illumina MiSeq platform (Illumina, San Diego, CA, USA) targeting the V4 hyper variable region (forward primer, 515F, 5′-GTGYCAGCMGCCGCGGTAA-3′; reverse primer, 806R, 5′-GGACTACHVGGGTWTCTAAT-3′) for 2 × 250-bp paired-end sequencing (Illumina) (Caporaso et al., 2012; Caporaso et al., 2011). Polymerase Chain Reaction (PCR) amplification was performed using Roche FastStart High Fidelity PCR System (Roche Diagnostics Ltd, Burgess Hill, UK) in 50 µL reactions under the following conditions: initial denaturation at 95°C for 2 min, followed by 36 cycles of 95°C for 30 s, 55°C for 30 s, 72°C for 1 min, and a final extension step of 5 min at 72°C. The PCR products were purified and normalised to ~20 ng each using the SequalPrep Normalization Kit (Fisher Scientific, Loughborough, UK). The PCR amplicons from all samples were pooled in equimolar ratios. The run was performed using a 4 pM sample library spiked with 4 pM PhiX to a final concentration of 10% following the method of Schloss and Kozich (Kozich et al., 2013).

Raw sequences were divided into samples by barcodes (up to one mismatch was permitted) using a sequencing pipeline. Quality control and trimming was performed using Cutadapt (Martin, 2011), FastQC , and Sickle (Joshi and Fass, 2011). MiSeq error correction was performed using SPADes (Nurk et al., 2013). Forward and reverse reads were incorporated into full-length sequences with Pandaseq (Masella et al., 2012), and chimeras were removed using ChimeraSlayer (Haas et al., 2011). For the 16S sequences Operational Taxonomic Units (OTUs) were generated with UPARSE (Edgar, 2013). OTUs were classified by Usearch (Edgar, 2010) at the 97% similarity level, and singletons were removed. Rarefaction analysis was conducted using the original detected OTUs in Qiime (Caporaso et al., 2010). The taxonomic assignment was performed by the RDP naïve Bayesian classifier version 2.2 (Wang et al., 2007), used in combination with the Silva SSU 132 ribosomal RNA gene database (Quast et al., 2013). The OTU tables were rarefied to the sample containing the lowest number of sequences, all samples having less than 5,000 sequences were removed from analyses prior to the rarefaction step. The step size used was 2000 and 10 iterations were performed at each step.

4.3 Results and Discussion

4.3.1 Sediment Characterisation

To assess the fate of Hg from chlor-alkali wastes in Weston Marsh Lock, MLR canal bed samples (pH 10) were collected, and then characterised using a range of techniques. Calcite (84.7 ± 0.3%), Halite (11.7 ± 0.3%), Brucite (3.1 ± 0.2%) and Quartz (0.5%) were mineral phases identified and quantified by XRD in the MLR sediment (see Figure P1-28 in Supplementary Information).

The mineral composition is consistent with solid phase wastes from Hg-cell chlor-alkali plants, which are known to contain calcium carbonate (calcite) and magnesium hydroxide (brucite) due to precipitation processes used in brine purification (Brinkmann et al., 2014; O'Brien et al., 2005). The high calcite content may be due to historic precipitation due to carbonation of the alkaline fluids containing calcium from industrial wastewater (Serrano et al., 2016; J. Wang et al., 2012). Calcium carbonate is also associated with waste streams from the Solvay process used for soda ash production (Trypuć and Białowicz, 2011). Figure P1-22a presents an ESEM image of MLR sediment illustrating (a) brucite, (b) rhombohedral calcite particle (c) irregular calcite particles. Particles have been identified based on the EDS spectra (Figure P1-22b). TEM-EDS was used to further characterise the platy brucite particles (Figure P1-23). The image reveals hexagonal particles <200nm in size consistent with that expected for brucite.

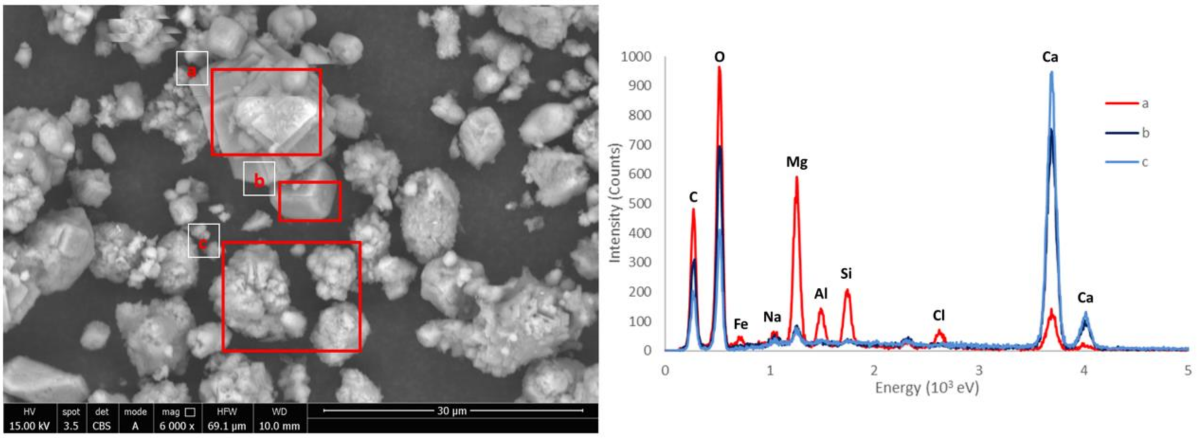

Figure P1-22: (Left) ESEM image of MLR sediment and (right) corresponding EDS spectra for particles (a, b, c).

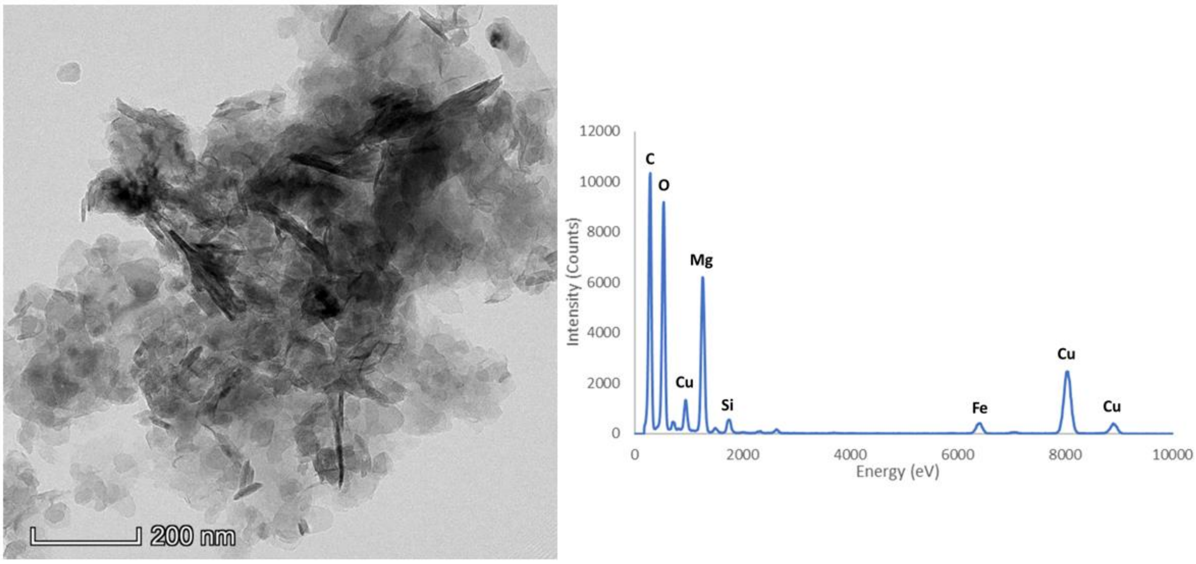

Figure P1-23: (Left) TEM Image of a particle in MLR sediment and (right) corresponding EDS spectra for the particle.

The presence of halite is consistent with high chloride levels identified in the sediment water. Brackish water entering the canal system from the River Mersey Estuary is likely to contribute the halite phase identified in the dried sediment, formed during the sample drying process.

Major and trace elemental content of dried MLR sediment was determined by XRF and LOI. Table P1-4 provides details relating to the major components contributing more than 0.1% of the total sediment mass.

Table P1-4: Major elemental components (>0.1% total mass) of MLR sediment determined by XRF and LOI analysis

Major Component	Percentage Total Mass (%)
SiO_2	2.30
Al_2O_3	0.96
Fe_2O_3	0.70
MgO	7.29
CaO	39.5
Na_2O	3.84
K_2O	0.11
P_2O_5	0.14
SO_3	1.11
Cl	3.14
F	0.12
LOI (H_2O)	1.20
LOI (CO_2)	39.4

CaO (39.5%) and CO_2 (39.4%) each accounted for almost 40% total mass, from degradation of carbonate and organic carbon. Other major components identified at levels greater that 2% total mass were MgO (7.3%), Na_2O (3.8%), Cl (3.1%), and SiO_2 (2.3%). Water content was 1.2% indicating that the drying process did not completely remove all the water. Overall, the XRF results are consistent with the XRD analysis, indicating the bulk of the sample is made of $CaCO_3$ (calcite) and $Mg(OH)_2$ (brucite). Mn (356 mg/kg), Ba (344 mg/kg), Sr (333 mg/kg), Cu (131 mg/kg) and Hg (131 mg/kg) were the most abundant trace components quantified by XRF. Barium and Hg can be associated with solid phase chlor-alkali waste due to Hg-cell waste precipitation processes. The full set of results for major and tracer elements detected by XRF and LOI analysis are presented as Tables P1-7 and P1-8 in the Supplementary Information.

The sludge had a water content equivalent to ~60% the total mass. Composition of sediment porewater separated from MLR sediment was analysed by IC. Chloride (Cl^-) was the dominant anion in the sediment water, present at a concentration of 0.17 g/L. Discharge from industrial processes and brackish water from the River Mersey entering the canal system are both potential sources. Sulphate and phosphate concentrations were 50 and 9 mg/L, respectively.

4.3.2 Total Mercury (THg) Extraction from Sediment

THg concentrations in MLR sediment were determined by ICP-MS analysis of sediment extracts and XRF analysis of the solid phase (see Figure P1-29 in Supplementary Information). Hg concentration calculated from the CRM extracts (120 ± 1 mg/kg) was less than the certified value (132 ± 3 mg/kg) suggesting ~90% Hg was effectively removed and recovered in the THg extraction process. Hg concentration in MLR sediment calculated from THg extracts was 77 ± 1 mg/kg (dry wt.). This value could be adjusted to ~86 ± 1 mg/kg (dry wt.), assuming 90% extraction and recovery during procedure.

Despite this, Hg concentration determined by XRF (131 ± 1 mg/kg dry wt.) is higher than that determined by ICP-MS (77 – 86 mg/kg dry wt.). XRF could potentially have overestimate the THg content as it was carried out on a standardless using Pro-Trace, alternatively residual Hg was not fully extracted in aqua regia, or the discrepancy was due to sample heterogeneity.

However, determining a THg concentration is insufficient for understanding the biogeochemical cycling of the metal, as is does not provide enough information to establish the mobility, reactivity, bioavailability, and toxicity of the Hg present. It does not, therefore, provide a good understanding of the potential risks that the Hg poses to human health or the environment, as the form of the Hg governs its toxicity and the pathway by which it may harm a receptor. Additional analysis of Hg chemical speciation is essential for further understanding the geochemistry of Hg in sediment. For this reason we applied sequential extraction procedures and XAS to further identify of chemical species present and constrain the potential mobility of the Hg fractions present (J. Wang et al., 2012).

4.3.3 Mercury Mobility as Determined by Sequential Extraction from Sediment

Concentrations of different operational Hg fractions in the sediment following sequential extraction are presented in Figure P1-24.

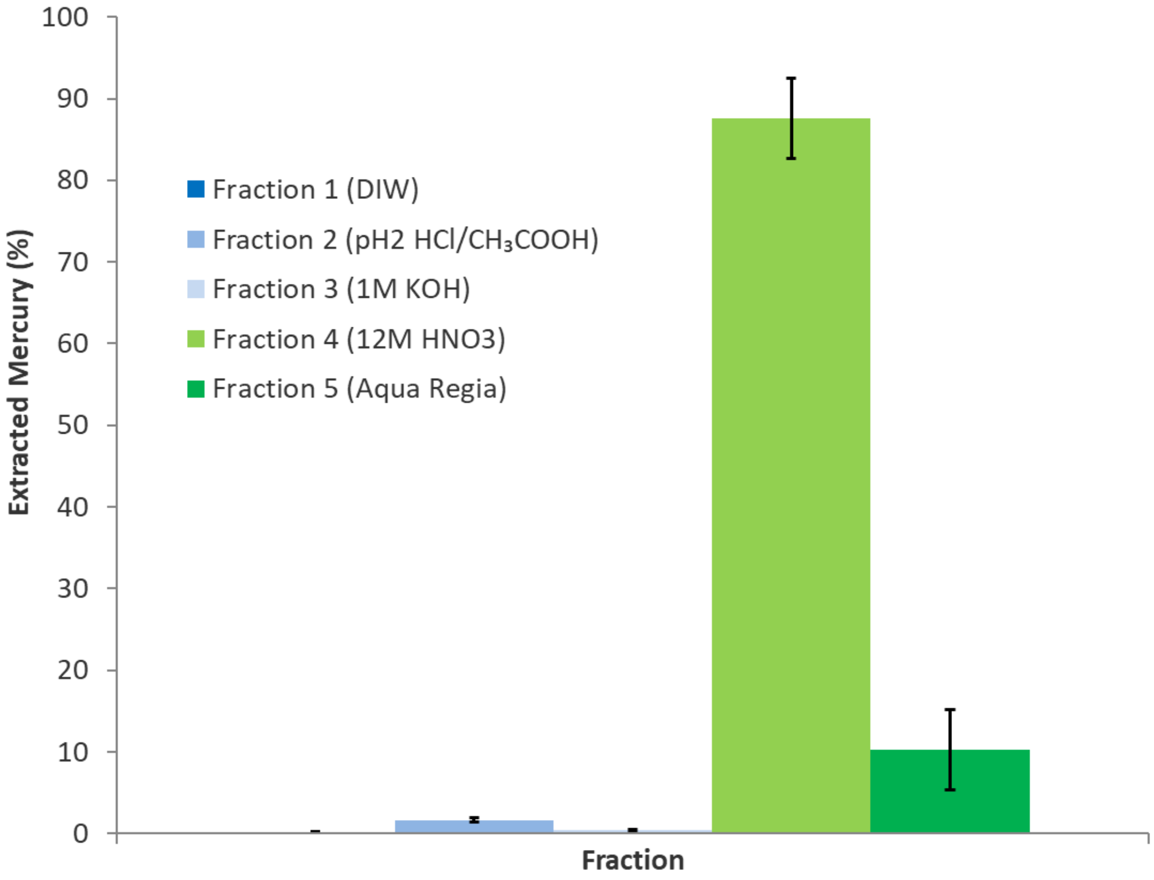

Figure P1-24: Hg extracted in each fraction as a percentage of total concentration in MLR sediment. Error bars represent the standard error of the mean (n=4).

The THg concentration calculated from the sum of individual fractions was 67 mg/kg (dry wt.), which is less than the value (77 mg/kg dry wt.) determined by the THg extraction procedure. As noted previously, heterogeneity of the sediment may be a factor contributing to variation in Hg content between sample aliquots, or alternatively reduced extraction and recovery efficiency of Hg during the sequential extraction process.

Hg concentration calculated from the CRM extracts (99 mg/kg) was less than the certified value (132 ± 3 mg/kg) suggesting that ~75% Hg was effectively extracted and recovered during the sequential extraction procedure. Assuming that the extraction and recovery is the same for MLR sediment, the THg concentration could be adjusted to ~89 mg/kg (dry wt.). This value is in line with the adjusted THg concentration (~86 mg/kg dry wt.) in the THg extraction procedure.

Table P1-5 shows the Hg concentration in the CRM sediment extracted in each sequential extract fraction alongside the percentage of total Hg extracted in each fraction.

Table P1-5: Hg extracted in each fraction CRM sediment with the standard error of the mean (n=4)

Extractant	Hg Concentration in Sediment (mg/kg)	Percentage of Total Hg Extracted (%)
Fraction 1 (DIW)	2 ± 0.5	2 ± 0.5
Fraction 2 (pH2 HCl/CH_3COOH)	1.9 ± 0.4	1.9 ± 0.4
Fraction 3 (1M KOH)	0.3 ± 0.1	0.3 ± 0.1
Fraction 4 (12M HNO_3)	71.3 ± 1.9	71.6 ± 1.9
Fraction 5 (Aqua Regia)	24.1 ± 0.7	24.2 ± 0.7
Total	99.5	100

Interpretation of ICP-MS data from the sequential extracts suggests that Hg was recalcitrant in the MLR sediment, as most is extracted in fraction 4 [Hg_2Cl_2, Hg_0, mineral lattice or beta-HgS with impurities] (~87%) and fraction 5 [HgS, beta-HgS, HgAu or HgSe] (~10%). These strong acid solutions thought to extract strongly complexed and mineral bound Hg species (e.g. HgS, beta-HgS or amalgamated HgAu), larger particles of pure HgS or beta HgS are likely to be more recalcitrant and extracted in aqua regia (fraction 5) (Bloom et al., 2003; Phipps et al., 2013). Less than 3% of Hg (~1.5 mg/kg) was extracted in fractions 1 to 3; Hg species extracted in these are usually considered more mobile in the environment (e.g. $HgCl_2$, HgO, $HgSO_4$, Hg(II) sorbed to humics, MeHg) and typically drive the need for remediation (Phipps et al., 2013). Any highly toxic MeHg should have been extracted in fraction 3 (~0.5%) along with any Hg sorbed to humics, therefore it cannot be assumed that all Hg extracted in this fraction is MeHg. Accurately determining and quantifying MeHg was crucial for better establish the risks associated with Hg-contaminated sediment. A selective MeHg extraction and CV-AFS established that the MeHg content of MLR sediment was 55 ± 1 µg/kg (dry wt.) adjusted for CRM recovery, less than 0.1% of the total Hg. MeHg concentration calculated from the CRM extracts (78.1 µg/kg) was very close to the certified value (75 ± 4 µg/kg.) suggesting efficient extraction and recovery during the extraction procedure.

Advances in our understanding of Hg biogeochemistry in relation to methylation have identified that even relatively immobile Hg species, such as HgS particles, may still be transformed to more mobile MeHg under certain environmental conditions, all be it at a slower rate than more mobile Hg(II) species (Zhang et al., 2012). More detailed compound specific information from XAS, confounded in results from the sequential extraction procedure, is therefore required to better guide any potential remediation strategy.

4.3.4 Compound Specific Mercury Speciation

XAS at the Hg L_{III}-edge (12,284 eV) allowed collection of high-quality data to k = 13 from the MLR sediment sample. X-ray absorption near edge structure (XANES) data for the MLR sample, metacinnabar (beta-HgS) standard and Hg(II) sorbed to MLR standard are presented in Figure P1-25.

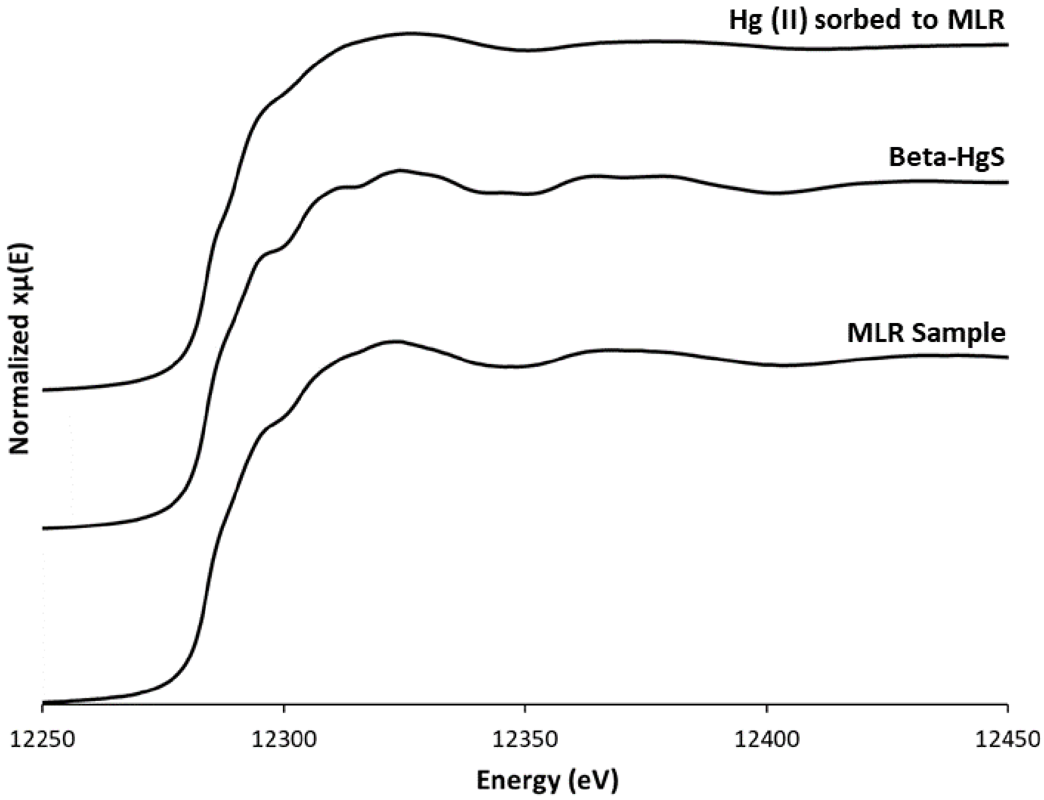

Figure P1-25: Hg L_{III}-edge XANES spectra for MLR sediment, beta-HgS and sorbed Hg(II).

EXAFS Linear Combination Fitting

The sample spectra were compared to multiple standards to establish Hg chemical species most likely to be present in the sample and their relative contribution to total Hg present. Linear combination fitting the Hg L_{III}-edge sample with various Hg chemical and mineral standards in Athena software suggested that 84.9 ± 2.5% is beta-HgS and 15.1 ± 2.5% is Hg(II) sorbed to MLR sediment (Ravel and Newville, 2005). More soluble Hg species likely diluted and dispersed leaving behind insoluble beta-HgS component. The values obtained for the statistical goodness-of-fit parameters, R-factor (R) and chi-square (χ^2), were 0.12 and 58.60, respectively. A K^3-weighted EXAFS spectrum for the MLR sample is presented alongside the linear combination fit spectrum, made up of relative contributions from beta-HgS and sorbed Hg(II) spectra, in Figure P1-26. The large proportion of beta-HgS is consistent with that expected in solid phase waste from the chlor-alkali Hg-cell process, following the sulfide precipitation process used to remove aqueous Hg from wastewaters (Hung et al., 2017). High pH and high chloride conditions are favourable for Hg(II) sorption and potentially enhance sorption of Hg(II) in aqueous phase under environmental conditions (Barrow and Cox, 1992).

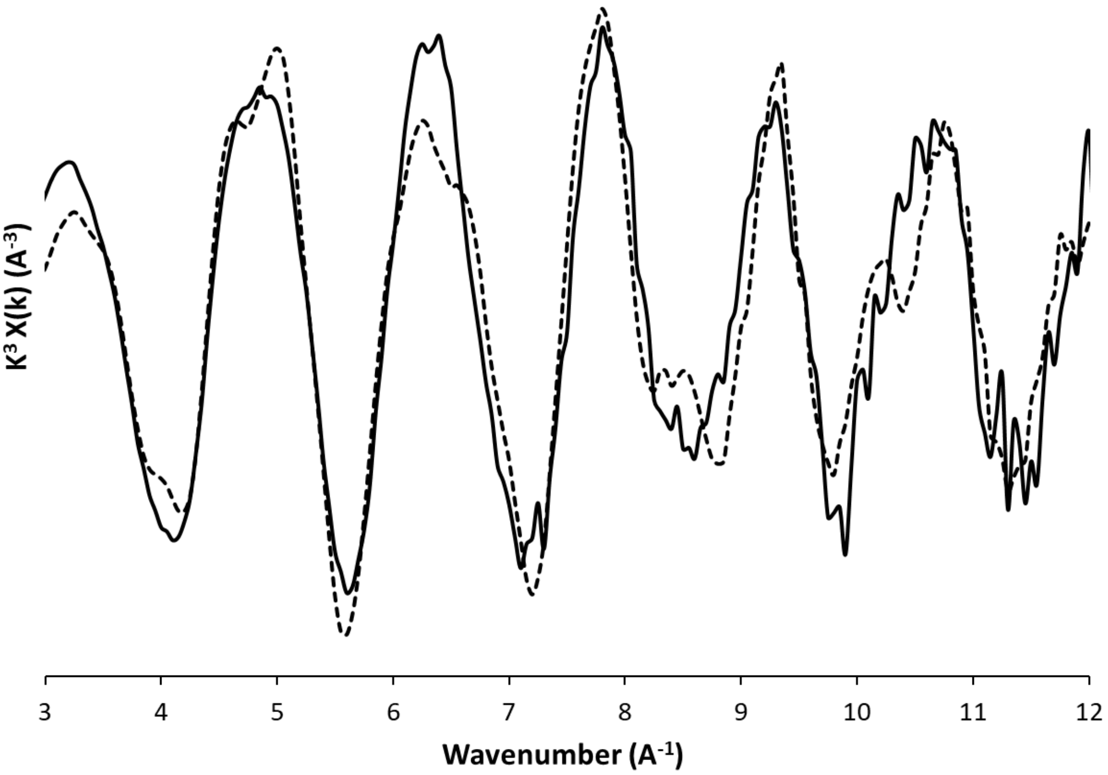

Figure P1-26: Hg L_{III}-edge K^3-weighted EXAFS spectra for MLR sediment (solid line) and a linear combination model fit (dashed line).

Model Fits for XAS data from Hg Standards

Hg L_{III}-edge EXAFS spectra for beta-HgS and Hg(II) sorbed to MLR standards, as well as corresponding Artemis model fits and fitting parameter are presented in Figure P1-27 and Table P1-6.

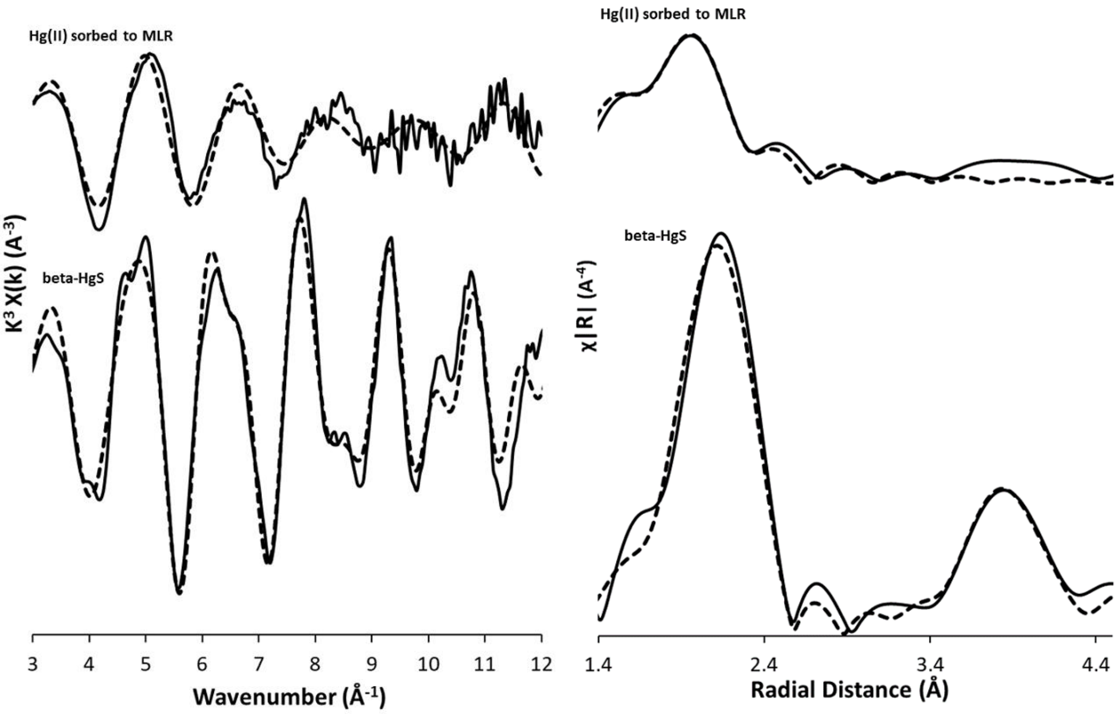

Figure P1-27: Hg L_{III}-edge XAS spectra for Hg standards (left) K^3-weighted EXAFS spectra, and (right) Fourier transform of K^3-weighted EXAFS spectra for Hg standard data (solid lines) and their corresponding model fit data (dashed line).

Table P1-6: Fitting parameters for K^3-weighted EXAFS model fits for Hg standards shown in Figure P1-27. CN denotes the coordination number; R denotes the atomic distances; σ^2 denotes the Debye-Waller factor; S_0^2 denotes the amplitude factor, E_0 denotes the shift in energy from the calculated Fermi level.

Standard	Path	CN	R (Å)	σ^2 (Å^2)	E_0	S_0^2	Reduced χ^2	R-factor
Beta-HgS	S1	4	2.5300	0.0086	8.576 ± 0.818	0.8	2181.0	0.0188
(R = 1.5 to 4.5)	Hg1	12	4.1363	0.0113				
	S2	12	4.7756	0.0144				
Sorbed Hg(II) to	O1	0.9	2.1022	0.0073	9.407 ± 1.357	1	41.8	0.0049
MLR sediment	Cl1	0.5	2.4064	0.0007				
(R = 1.4 to 3.4)	Cl2	0.3	2.5749	0.0005				

4.3.5 Bacterial Population in Sediment

The microbial communities within the sediment sample were analysed by 16S rRNA gene sequencing to identify the range of organisms present, including those with the potential to impact on Hg speciation (Figure P1-30 in the SI). 111 unique OTUs were identified from the PCR amplified gene sequences, of these 21 made up >1% of the population identified. Gammaproteobacteria (45.5%) dominated the sediment, although the most heavily represented family of organisms detected was the Betaproteobacterial-affiliated Burkholderiaceae (20.8% total sequences). This group is phenotypically, metabolically, and ecologically diverse and includes both strict aerobic and facultatively anaerobic chemoorganotrophs, as well as obligate and facultative chemolithotrophs (Coenye, 2014). Previous studies have shown *Burkholderia* species can tolerate Hg-contaminated soils, and species resistant to toxic metals (lead and cadmium) have been isolated and characterised from contaminated soils (Jiang et al., 2008; Lei Wang et al., 2020). In addition to the potential to mediate the reduction of Hg(II) to less toxic Hg(0) via the *mer* operon, which is widespread in bacterial groups identified (Barkay et al., 2010). 16S rRNA gene sequencing also identified *Desulfovibrio* species (~0.9%) and *Geobacte*r species (~1.8%) in MLR sediment. These deltaproteobacteria are known to produce the HgcA and HgcB proteins, via hgcAB gene pathways, which are essential for Hg methylation (Kerin et al., 2006). The presence of these DSRB and DIRB may explain the formation of existing MeHg identified in the sediment, thus suggesting that there may be a risk of future methylation in this sediment were it under anoxic environmental conditions. The ability of these organisms to produce sulfide from sulfate (*Desulfovibrio*) and sulfur (*Geobacte*r) also gives the potential to mediate Hg sulfidation, consistent with the dominance of HgS in the sediments.

4.4 Conclusion

Mineral and elemental components identified can be associated with solid phase waste from chlor-alkali plants utilising the Hg-cell process. Mercury concentration in brine muds from mercury cell plants varies from 13 to 1000 ppm, with an average concentration of 200 ppm. Insoluble mercury sulfide compounds (e.g. HgS or beta-HgS) can form in waste sludge treated with sodium sulfide following treatment and filtration in a sulfide precipitation system (Hung et al., 2017). Alternatively, mercury sulfides could have formed via biological processes in the sediment following deposition (Manceau et al., 2015). Total extractable Hg concentration in MLR sediment, as determined by ICP-MS following aqua regia extraction and adjusted for recovery, is 86 ± 1 mg/kg. Sequential extraction procedures revealed that most Hg appears to be immobile in the sediment as ~97% requires strong acids (12 M HNO_3 or aqua regia) to be extracted from the sediment, suggesting that it is predominantly strongly complexed or mineral bound. XAS analysis was applied to reveal more detailed compound specific information providing greater insight into the chemical speciation of Hg present. Comparison of the Hg L_{III}-edge EXAFS spectrum with spectra from mineral standards using linear combination fitting suggested that most is likely to be beta-HgS (~85%), along with Hg(II) sorbed to MLR sediment (~15%).

A selective MeHg extraction and CV-AFS technique established there was 55 ± 1 µg/kg (dry wt.) of highly toxic MeHg in the sediment, although less than 0.1% total Hg it is likely to contribute significantly to the overall toxicity of Hg in the sediment due to its tendency to bioaccumulate. The small proportion of Hg in methyl form and the large proportion of immobile HgS could lead to the conclusion that there is a relatively low risk posed by Hg in this sediment. However, Deltaproteobacteria capable of methylation were identified through analysis of 16S rRNA sequencing data. Therefore, were this sediment still in place at the site, continued monitoring would be required. Recent publications point to the importance of HgS particle size in determining bioavailability of Hg for potential methylation, and suggest that HgS nanoparticles may be more bioavailable for uptake and potential methylation by microbial cells than larger HgS particles (Poulin et al., 2017).

Typically, when a site is being investigated for the presence of potential contamination, the analysis scheduled may only include THg if its previous use on the site has not been identified. If the previous use of Hg on the site is known, then the analysis of elemental Hg(0), inorganic ionic Hg and organomercury (e.g. MeHg) may also be scheduled. The resulting risk assessment undertaken would usually consider the form of Hg and likely pathways of exposure to human health and the environment in the form of the conceptual site model. The techniques applied in this work, allows a more detailed identification and quantification of the various forms of Hg present, and thus establishes a better understanding of whether it is likely to pose a risk to the wider environment and/or human health. This tiered approach to sediment risk assessment could be useful for deciding whether disturbing a material through remediation may pose more potential risks than leaving *in situ* if stable and immobile.

This sediment was collected during remedial dredging of the lock, and Hg in this material does not pose additional risk to the surrounding area, as it is no longer in place. However, the characterisation techniques used in this study could be applied at similar sites during risk assessment studies. Further work could also be done to establish the particle size distribution of HgS in the sediment and whether that could affect additional Hg methylation. Long term monitoring is required to better establish the risks posed by Hg in contaminated sediments and guide decision making regarding potential remediation options if required.

Acknowledgements

We thank EPRSC, WSP and Akzo Nobel for funding under a PhD CASE award. We acknowledge beamtime awarded at the Diamond Light Source for XANES and EXAFS on the I20 beamline under proposals SP18794 and SP21441. We thank Shu Hayama and Frederick Mosselmans for their assistance at Diamond Light Source.

We thank Karen Jackson (Canals and Rivers Trust) for arranging site access for MLR sediment sample collection. We thank Paul Lythgoe and Alastair Bewsher (Manchester Analytical Geochemistry Unit, University of Manchester) for ICP-MS, XRF, LOI and IC analysis. We thank Heath Bagshaw (Mineral Analysis Facility, University of Manchester) for his assistance with SEM and TEM analysis. We thank Shu Hayama for his assistance on I20 at Diamond Light Source. We thank Shaun Lancaster (Trace Element Speciation Laboratory, University of Aberdeen and PS Analytical) for MeHg analysis.

4.5 Paper 1: Supporting Information

4.5.1 Section 1: X-ray Diffraction Spectrum

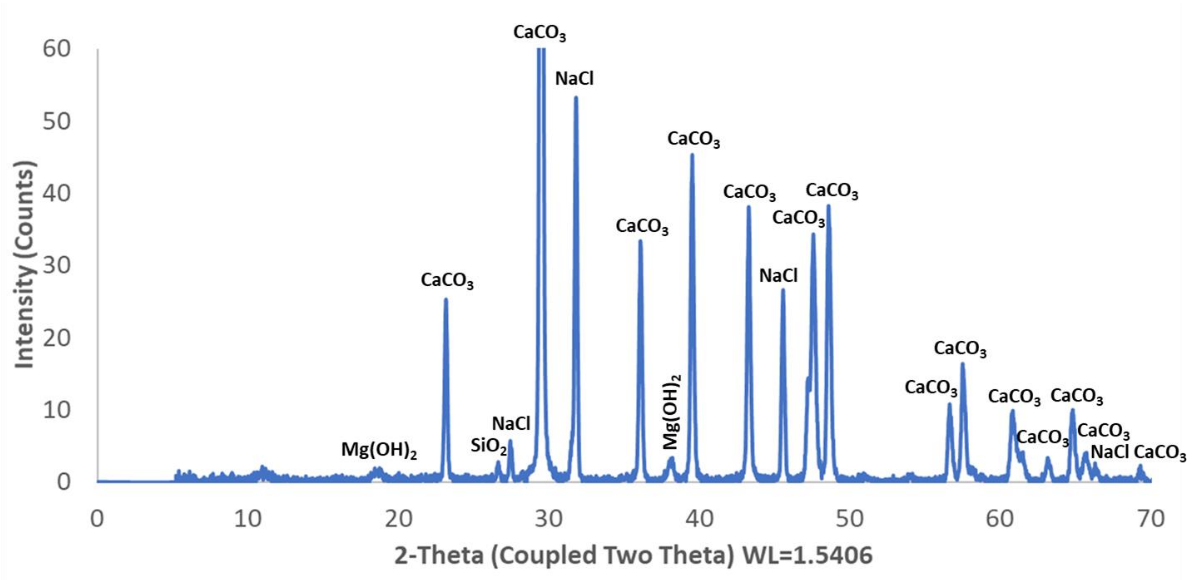

Figure P1-28: Mineral phases identified in MLR sediment by XRD (labels identify mineral associated with each peak).

4.5.2 Section 2: Total Mercury (THg) Concentration in MLR samples

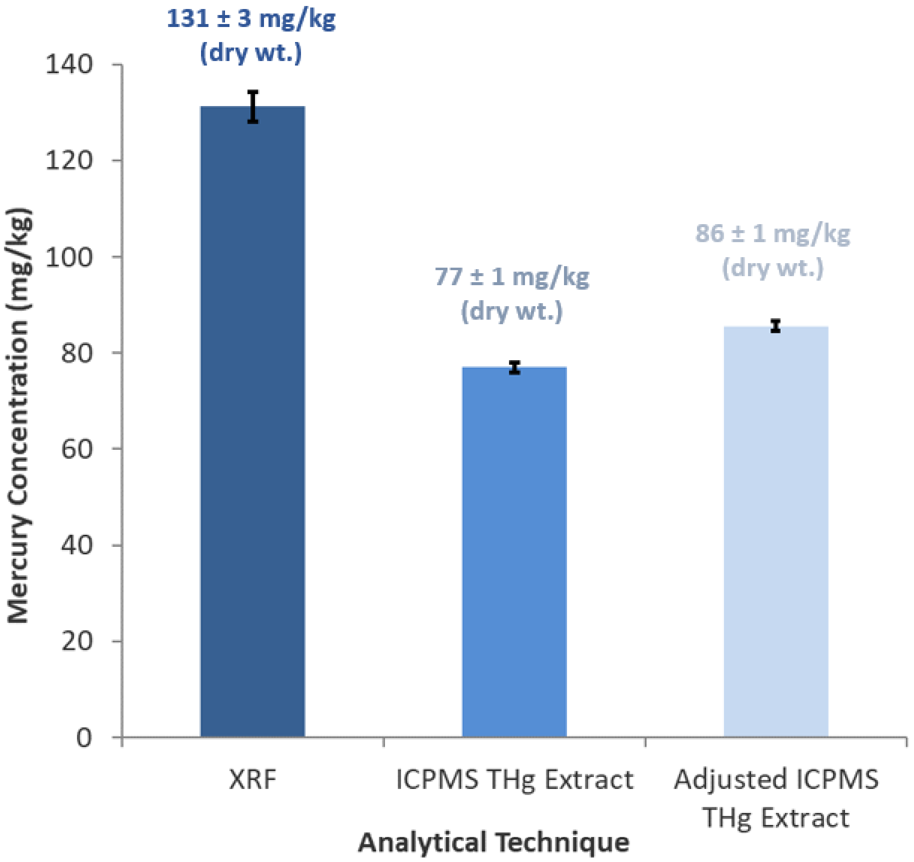

Figure P1-29: THg concentrations in sediment calculated from ICP-MS data from MLR sediment extracts and XRF analysis of an MLR sediment sample. Error bars represent the standard error of the mean (n=4).

4.5.3 Section 3: Bacterial Phyla in MLR sediment

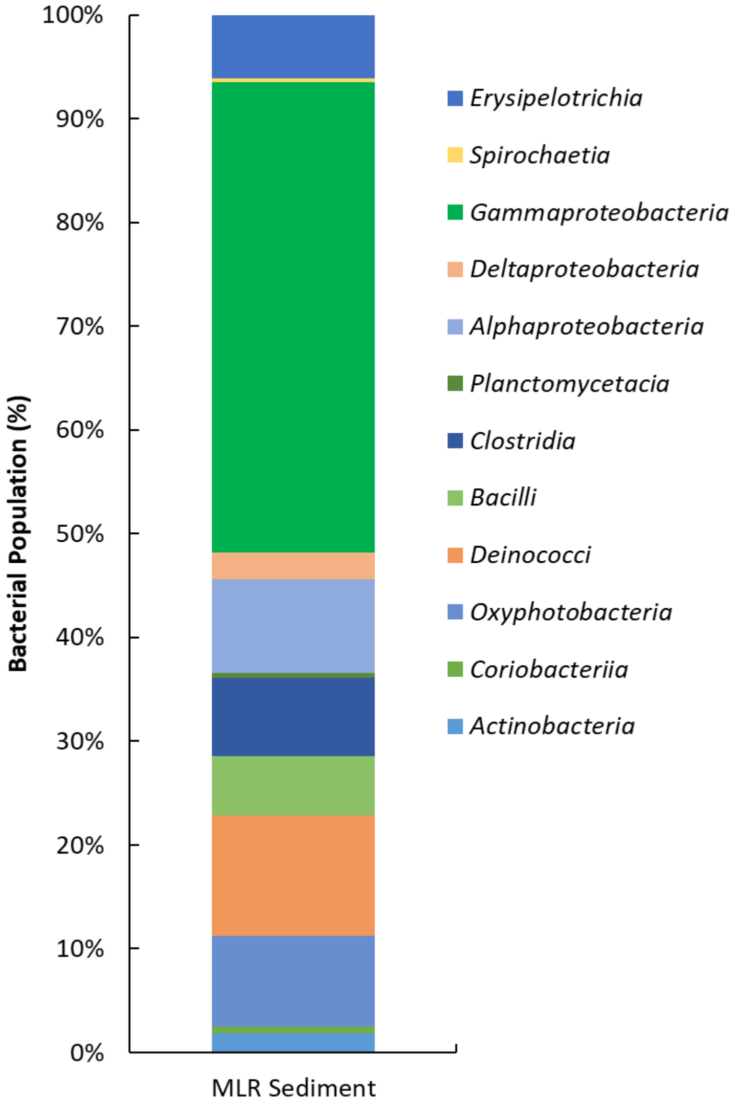

Figure P1-30: Bacterial phyla identified in sediment, by 16S rRNA sequencing, conributing >0.1% total population.

4.5.4 Section 4: X-ray Fluorescence and Loss on Ignition Major Components

Table P1-7: Major elemental components of MLR sediment determined by XRF and LOI.

Major Component	Percentage Total Mass (%)
SiO_2	2.30
Al_2O_3	0.96
Fe_2O_3	0.70
MgO	7.29
CaO	39.5
Na_2O	3.84
K_2O	0.11
TiO_2	0.03
P_2O_5	0.14
MnO	0.04
SO_3	1.11
Cl	3.14
F	0.12
LOI (H_2O)	1.20
LOI (CO_2)	39.4

4.5.5 Section 5: X-ray Fluorescence Trace Components

Table P1-8: Minor elemental components of MLR sediment determined by XRF.

Trace Component	Concentration (mg/kg)
As	0.6
Ba	344.1
Bi	1.4
Br	66.4
Cd	0.3
Ce	6.2
Co	2.5
Cr	29.2
Cs	12.5
Cu	131.3
Ga	1.1
Ge	0.7
Hf	3.4
Hg	131.2
I	1.9
La	11.2
Mn	366.8
Mo	0.6
Nb	0.2
Nd	7.0
Ni	28.8
Pb	35.9
Rb	6.9
Se	0.4
Sn	1.6
Sr	333.6
Ta	0.6
The	53.4
Th	1.2
Tl	1.7
U	8.6
V	5.6
W	1.7
Y	1.5
Yb	1.3
Zn	69.5
Zr	2.4

5.0 Paper 2: Investigating the impacts of iron-based nanoparticle and biostimulation treatments on biogeochemistry and mercury chemical speciation in anoxic sediment and artificial groundwater systems.

Alexander Tait[a]*, Samuel Shaw[a], Christopher Boothman[a], Dominic Mulroy[a], David Polya[a], Russell Thomas[b], Jonathan R. Lloyd[a].

[a]Williamson Research Centre (WRC) for Molecular Environmental Science, Department for Earth and Environmental Science, The University of Manchester, Manchester, M13 9PL, United Kingdom

[b]WSP, Kings Orchard, 1 Queen St, Bristol, BS2 0HQ, United Kingdom

*corresponding author e-mail address: alexander.tait@manchester.ac.uk

Keywords

Contaminated sediment

Hg remediation

Hg chemical speciation

Hazardous material treatment

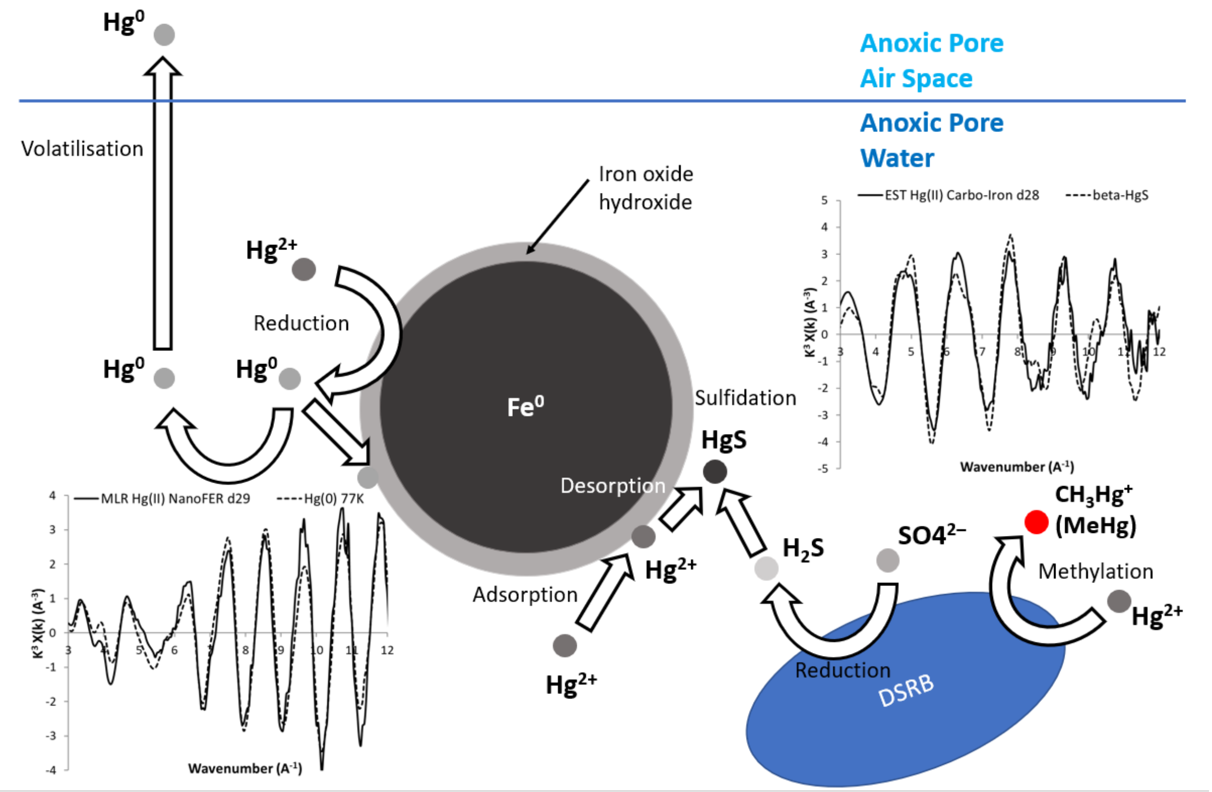

Figure P2-31: Graphical abstract illustrating potential impacts of treatments containing nZVI (NanoFER 25S and Carbo-Iron) on Hg transformation in anoxic sediment and pore water.

Abstract

Iron-based nanoparticles and biostimulation via slow-release electron donor based organic substrates have previously shown capacity for the immobilisation of mobile contaminant metals, such as Tc (VII) and Cr (VI), in anoxic subsurface water and sediment. Here we primarily focused on investigating the impacts of four treatments [NanoFER 25S (nZVI), Carbo-Iron® (nZVI and activated carbon)], biogenic magnetite and organic electron donor biostimulation) on solid phase Hg chemical speciation, in batch microcosm systems containing anoxic Hg-contaminated artificial groundwater (AGW) and either Marsh Lock Runcorn (MLR) or estuarine (EST) sediment, in the context of changes to key biogeochemical parameters. Solid phase Hg transformations appeared to be influenced by the type of treatment, the unique geochemical characteristics of sediment matrices and their respective microbial populations. Impacts on Hg reduction, sulfidation and methylation pathways appear crucial in establishing the effectiveness of treatments in anoxic subsurface systems. Treatments containing nZVI (NanoFER 25S and Carbo-Iron®) appeared to pose the greatest risk in respect to reductive mobilisation and methylation of Hg. NanoFER 25S was capable of inducing and maintaining reducing conditions for the duration of the experiment independent of sediment type, capable of not only reducing sorbed Hg(II) to volatile Hg(0), but also immobile beta-HgS. Net Hg methylation increased following addition

of Carbo-Iron® to both sediments. Biomagnetite and biostimulation with organic electron donors (acetate and lactate) both accelerated Hg immobilisation, via sulfidation, in estuarine sediment, but appeared to inhibit sulfidation in canal bed sediment when compared to no treatment systems. Natural attenuation of Hg by sulfidation appeared the most effective at immobilising Hg(II) as beta-HgS irrespective of sediment type. This work highlights the importance of taking in account not only the type of treatment, but also the individual site conditions (e.g. chemical composition of a sediment matrix, physical conditions, microbial community diversity, presence of additional contaminants) when considering applying treatments *in situ*. Application of remedial treatments should be undertaken with caution, despite potential beneficial immobilising effects in respect to one contaminant (e.g. Cr (VI)) under specific site conditions, intervention may have potentially adverse effects in respect to mobilisation of other contaminants [e.g. Hg(II)].

5.1 Introduction

Mercury (Hg) is a highly toxic trace metal, considered as one of the top ten chemicals or groups of chemicals of major public health concern by the World Health Organisation (WHO, 2017). Globally, there are numerous sites with Hg contamination linked to historic and ongoing industrial activities (Kocman et al., 2013; Phipps et al., 2013; Turner and Southworth, 1999). These sites and contributing industrial sources have now become the focus of remediation efforts (He et al., 2015; Otto and Bajpai, 2007; Liuwei Wang et al., 2020). Major mechanisms involved in Hg remediation are outlined in Figure P2-32. There has been increased research focused on the development of novel materials and their application to investigate their potential as remediation solutions at Hg-contaminated sites (Mackenzie et al., 2012; Liuwei Wang et al., 2020). The most widely adopted immobilisation techniques are stabilisation and containment, which prevent Hg migration by chemical complexation or physical trapping, respectively (Liuwei Wang et al., 2020). The NanoRem project (http://www.nanorem.eu/index.aspx) was setup to examine the development and optimisation of a range of nanoparticles for treatment of various contaminants in the subsurface. Nanoparticles are defined as particles that are ≤100 nm in at least one dimension, they are highly reactive due to their large surface area, and have the potential to increase the rate and extent of contaminant treatment compared to traditional materials (Newsome et al., 2019). Their size means they may be easily transported in groundwater, making them amenable to treating large areas of the subsurface (Newsome et al., 2019).

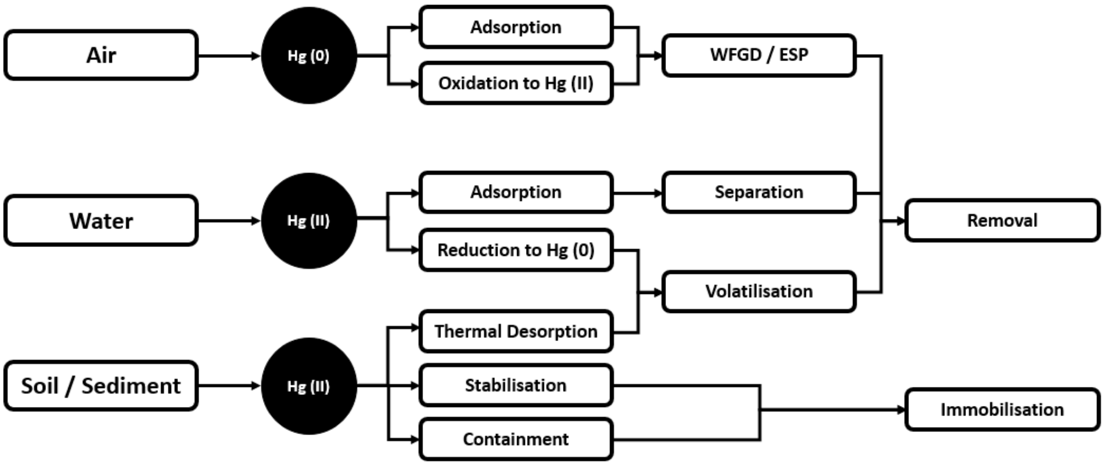

Figure P2-32: Major mechanisms involved in Hg remediation, adapted from (Liuwei Wang et al., 2020). [Acronyms: wet flue gas desulfurization (WFGD); electrostatic precipitation (ESP)].

Groundwater is essential for the provision of drinking water in many areas around the world (Giordano, 2009). The performance of groundwater bearing aquifers relies on the ecosystem services provided by groundwater-related microorganisms (Weil et al., 2019). The potential environmental risk posed by a remedial agent needs to be assessed prior to application into an aquifer, and a remediation method must only be considered suitable if the environmental risk after application is considered to be less than before the treatment application (Lemming et al., 2009). If remediation of contaminated groundwater and subsurface sediment is considered necessary, the remediation method must be carefully selected to avoid trade-offs that might impact these ecosystems (Weil et al., 2019). This paper investigates the impacts of four potential remediation options on Hg chemical speciation, in anoxic artificial groundwater (AGW) and sediment batch systems, in the context of changes to key biogeochemical parameters. The remediation mechanisms of the treatments would theoretically involve adsorption of aqueous Hg(II) and stabilisation of sorbed Hg(II) associated with sediment and/or particle solid phase. However, potential reduction of aqueous Hg(II) to Hg(0), may potentially inhibit stabilisation pathways due to the challenges related to the containment of volatile Hg(0).

The ability of microbes to reductively transform various contaminant metals has wide-reaching implications for controlling their mobility in the subsurface (Watts and Lloyd, 2012). Soluble toxic metals, including Cr (VI), Hg(II), V(V), Co(III), U(VI), Tc(VII) and Np(V) can be reduced directly and removed from solution by enzymatic processes, often being used as terminal electron acceptors during anoxic respiration (Watts and Lloyd, 2012). The bioremediation of Hg via the mer operon detoxification mechanism has undergone trials as both a wastewater treatment and as an *in situ* treatment for waters and sediments (Nakamura et al., 1999; Saouter et al., 1995; von Canstein et al., 1999; Wagner-Döbler et al., 2003). Recent research found that *Pseudomonas veronii* cells grown to stationary phase could be immobilised and encapsulated in a biopolymer and coated onto natural zeolite granules (McCarthy et al., 2017). The microbial strategy involved application of coated zeolite to contaminated sediments *in situ*, where Hg(II) was taken into cells and reduced intracellular to volatile Hg(0), which passively diffused from the cell (McCarthy et al., 2017). They proposed that emitted gaseous elemental mercury (GEM) could be captured and transformed back into metallic Hg for appropriate storage or reuse (McCarthy et al., 2017). Previous work has highlighted large-scale use of Hg volatilising bacteria to clean up Hg-contaminated waters (Mahbub et al., 2017). However, the costs associated with capturing GEM may make *in situ* bioaugmentation of Hg-contaminated soils less cost-effective in comparison to alternative physical and chemical approaches.

Hg chemical speciation in the subsurface, critical to establishing risk, is directly linked to its surrounding geochemical and microbial environment (Hellal et al., 2015). Aqueous Hg(II) can sorb to minerals (e.g. Fe/Mn oxide-hydroxides and clays) and organic matter (OM) under environmental conditions (O'Connor et al., 2019). Many interdependent factors, including the quantity and composition of soil OM and clays, oxidised minerals (e.g. Fe/Mn oxides), reduced elements (e.g. S^{2-}), pH and redox conditions affect Hg chemical speciation in complex sediment systems, and therefore its mobility and bioavailability (O'Connor et al., 2019). Microbial reduction of sulphate in anoxic Hg sediments, can lead to the formation of mercuric sulfide (HgS) (O'Connor et al., 2019). However, sulphate reducing bacteria (SRB) can also play a role in methylation of Hg to methylmercury (MeHg) compounds (Gilmour et al., 1992).

Methylation is considered the most toxic transformation, by which inorganic Hg(II) can be converted into organic MeHg species, these are potent neurotoxins that can bioaccumulate in the food web (Mahbub et al., 2017; Wiatrowski et al., 2009). MeHg is produced mainly in anoxic sediments and soils, primarily intracellularly by dissimilatory sulfate- and iron-reducing bacteria (DSRB and DIRB) belonging to the Deltaproteobacteria (Gilmour et al., 1992; Graham et al., 2012a; Kerin et al., 2006). Gilmour (2013) identified methylation in two methanogens, and in a wide variety of Firmicutes, extending scientific knowledge of Hg-methylating microorganisms outside of the Deltaproteobacteria for the first time (Gilmour et al., 2013). Furthermore, recent research suggests that additional bacterial groups in the oxic zone of global oceans, such as *Nitrospina* species, may also play a role in environmental methylation (Gionfriddo et al., 2016; Tada et al., 2020; Villar et al., 2020). Methylation rates are reduced when Hg is sequestered in crystalline sulfides or bound to thiol groups in macromolecular natural organic matter (NOM) (Manceau et al., 2015). The presence of H_2S in sediments of lakes can reduce the rate of Hg methylation, due to the formation of HgS, which is methylated much more slowly than $HgCl_2$ (Fagerström and Jernelöv, 1971). High Hg(II) concentrations (>500 mg/kg) can decrease the amount of MeHg formed due to the toxic effects of inorganic Hg(II) on the methylating organisms (Jensen and JernelÖV, 1969). It has been proposed that disordered nanocolloidal metacinnabar-like species, bioavailable to Hg-methylating bacteria, may form in sulfidic systems containing dissolved organic matter (DOM) (Gerbig et al., 2011; Graham et al., 2012a).

Iron nanoparticles shown capacity for the immobilisation of mobile contaminant metals, such as Tc(VII) and Cr(VI), in subsurface anoxic water and sediment (Newsome et al., 2019; Watts et al., 2015). Zero valent iron nanoparticles (nZVI) have been widely tested and show significant promise for environmental remediation (Chekli et al., 2016; Mukherjee et al., 2016; Zhang, 2003). NanoFER 25S is a nZVI [Fe(0)] product, containing ~20% Fe(w/w). The core-shell model for nZVI is presented in Figure P2-33, particles have characteristics of iron oxide-hydroxides (e.g. sorbent) and Fe(0) (e.g. reductant), the iron oxide-hydroxide coat forms during aqueous corrosion of the Fe(0) core (Chekli et al., 2016). Mobility and reactivity of nZVI is dependent on particle size, surface chemistry and bulk composition

(Chekli et al., 2016; Phenrat et al., 2007). However, due to their magnetic properties, nZVI particles have a natural tendency to aggregate which reduces reactivity and decreases environmental mobility.

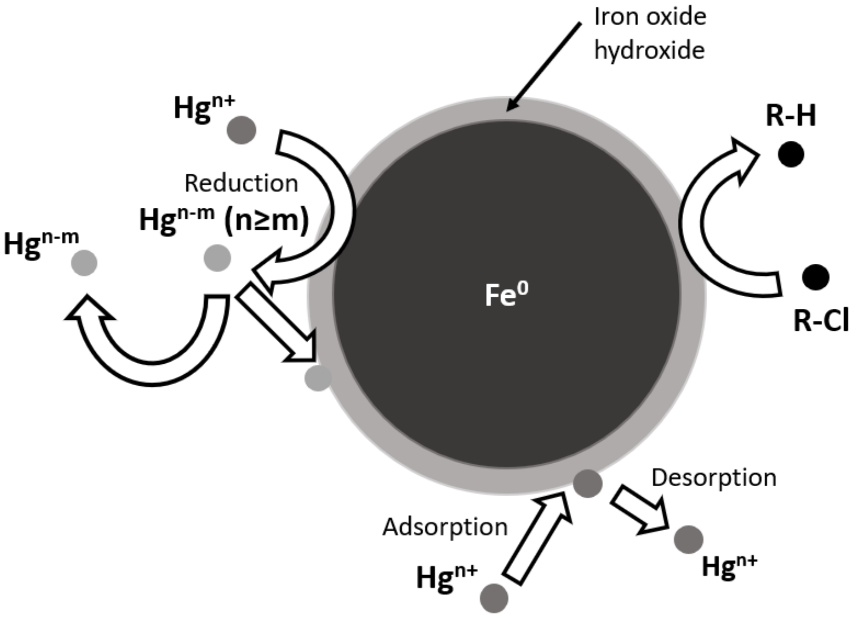

Figure P2-33: Core shell model for ZVI nanoparticles, adapted from (Li et al., 2006).

Carbo-Iron® is a composite material consisting of a porous activated carbon colloid (ACC) framework [~75% (w/w)] with embedded clusters of nZVI [~25% (w/w)]. Figure P2-34 illustrates how nZVI particles are associated with the carbon framework in Carbo-Iron®. Combined effects theoretically enable effective targeting of multiple organic and inorganic contaminants, the reactivity of nZVI and the transport properties of the ACC should provide both better transport properties than nZVI and a higher affinity to non-aqueous phase liquids (NAPL). Enrichment of organic pollutants at the hydrophobic ACC carrier could be advantageous for their efficient degradation at neighbouring reactive centres (Mackenzie et al., 2012). Many contaminated sites can have a broad range of pollutants, including organic compounds, organic complexes, and inorganic metals, therefore a treatment solution (e.g. nZVI composite materials) that can target multiple contaminants would be of great value.

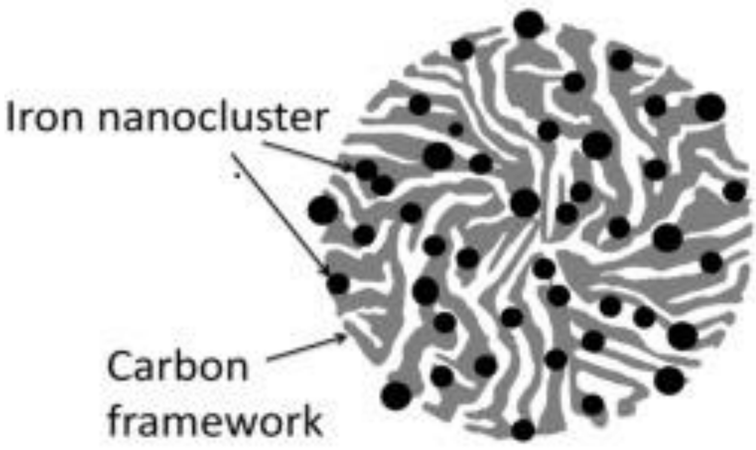

Figure P2-34: Carbo-Iron® particle structure (Mackenzie et al., 2016).

Magnetite (Fe_3O_4), a common naturally occurring mineral that contains both Fe(II) and Fe(III), is widely deposited in soils and aquatic sediments. Its magnetic properties attract toxic trace metals and make collection and detection easier. Previous research has demonstrated that magnetite can remove toxic metals and organic compounds from wastewater either through adsorption and/or direct reduction (Liu and Wiatrowski, 2018). Magnetite can be produced via geologic processes or microbial activity (Bazylinski et al., 2007; Karlin et al., 1987; Liu and Wiatrowski, 2018). *Geobacter sulfurreducens* has proven capable of largescale biological synthesis of biomagnetite (Byrne et al., 2015).

In this study, we explored the impact of four potential treatments on biogeochemistry in anoxic batch microcosm systems containing sediments and contaminated artificially groundwater (AGW), containing Hg(II), to assess their suitability as potential *in situ* remediation solutions. This research aimed to investigate and compare the effectiveness of emerging treatment options (1) NanoFER 25S (nZVI), (2) Carbo-Iron® (nZVI with ACC), (3) biogenic magnetite (biomagnetite), and (4) biostimulation with organic electron donors (acetate and lactate). Microcosm experiments were monitored to determine changes in: (1) Sediment and pore-water chemistry and mineralogy, (2) solid phase chemical speciation of Hg, and (3) the microbial community.

5.2 Materials and Methods

5.2.1 Materials

Sediment samples were gathered from sites in North-West England, UK. Canal bed sediment, a wet sludge material, was collected from Weston Marsh Lock, Runcorn (MLR). Samples were taken at the base of the Eastern lock gate whilst sediment was being dredged as part of remediation efforts. Estuarine (EST) sediment was collected from the Ribble and Alt Estuaries, Southport. Samples were selected due to the variation in their grain size and major component consistency, MLR sediment is carbonate rich industrial waste material, whereas EST is a silicate rich sandy sediment.

NanoFER 25S was provided as a slurry by Nano Iron (Czech Republic), the particle suspension contained ~20% (w/w) Fe, nZVI encased in a permeable iron oxide-hydroxide shell. Carbo-Iron® was provided in powder form by Helmholtz Centre for Environmental Research (Germany), the particles were ~25% (w/w) nZVI embedded in ~75% (w/w) ACC framework. Biomagnetite particles were produced in the WRC laboratory, the methodology for the synthesis process in outlined in Section 2.2. Organic electron donors, sodium acetate and sodium lactate, were purchased from Sigma Aldrich for application as a biostimulation treatment.

5.2.2 Biomagnetite (Fe_3O_4) Synthesis

Biomagnetite was synthesised from ferrihydrite, an Fe(III) oxide-hydroxide (Fe(III)O(OH)), by *Geobacter sulfurreducens* in a three-step procedure (Schwertmann and Cornell, 2000).

Ferrihydrite ($Fe_2O_3 \bullet 0.5H_2O$) synthesis

1 L of 0.67 M $FeCl_3$ solution was prepared, and pH adjust to 6.9 with 10 M NaOH. As a wash step, $FeCl_3$ solution was centrifuged at 5000 g for 20 minutes, and the resulting Fe(III) gel re-suspended in deionised water DIW [18.2 MΩ]. The wash step was repeated 5 times and Fe(III) gel was re-suspend in 1 L DIW for storage (Schwertmann and Cornell, 2000).

Geobacter sulfurreducens cultivation

1 L of Nutrient Broth Acetate Formate (NBAF) minimal growth medium was prepared for *Geobacter sulfurreducens* cultivation (Muhamadali et al., 2015). Pre-sterilised serum bottles containing 100 mL NBAF were inoculated with an early stationary phase culture to give an optical density (OD) of ~0.02 at 600 nm. Inoculated serum bottles were incubated at 30°C for 5 days. Under anoxic conditions, Geobacter cell cultures were decanted into centrifuge tubes, cells were pelleted by centrifugation at 5000 g for 20 minutes at 4°C. Cells were then resuspended in sterile anoxic 30 mM sodium bicarbonate ($NaHCO_3$) buffer and centrifuged at 5000 g for 20 minutes, wash step was repeated twice, before cells

were resuspended in anoxic sterile 30 mM $NaHCO_3$ and transfer to a sterile serum bottle for storage at 4°C (Byrne et al., 2015; Byrne et al., 2011; Coker et al., 2010; Coker et al., 2008).

Biomagnetite formation

To produce the biomagnetite, *G. sulfurreducens* cells were added to anoxic sterile serum bottles ~95 mL reaction medium containing, 30 mM $NaHCO_3$, 20 mM sodium acetate (CH_3COONa), 40 mM amorphous ferrihydrite. The reaction proceeded as serum bottles were incubated at 30°C for 72 hours with a starting *G. sulfurreducens* cell OD of ~0.2 at 600 nm. After synthesis, the biomagnetite was recovered using a magnet, washed in anoxic water to remove residual biomass, and resuspended in anoxic sterile 30 mM $NaHCO_3$. 0.2 mL of biomagnetite suspension was digested in 9.8 mL analytical grade 15.9 M HNO_3 for 24 hours. Following 50-fold dilution, triplicate 10 mL samples (2% (v/v) HNO_3) were filtered (0.4 µm) prior to analysis by inductively coupled plasma-atomic emission spectroscopy (ICP-AES). Biomagnetite structure was verified by XRD (Figure P2-42).

5.2.3 Treatment Microcosm Setup

Sediment microcosms were setup to investigate the interactions between Hg and solid phase (sediment and/or treatment particles) in systems representative of an anoxic canal sediment or subsurface aquifer. Aliquots of anoxic sludge (~1 g dry wt. sediment) were added to sterile 120 mL serum bottles [~2.5 g MLR sludge (x5) and ~2 g EST sludge (x5)]. 1 L of sterile anoxic AGW [0.066 g/L KCl, 0.242 g/L $NaHCO_3$, 0.081 g/L $MgCl_2$, 0.0976 g/L $MgSO_4$, 0.1672 g/L $CaCO_3$, 0.0275 g/L $NaNO_3$, 0.0094 g/L NaCl in DIW] was prepared for use in microcosm treatment systems. Anoxic pre-treatment microcosm systems were sealed and incubated at to 20°C for 18 hours following addition of 46 mL AGW containing ~54 µM $HgCl_2$.

Day 1 (pre-treatment) samples (1 mL) were taken by needle and syringe degassed with nitrogen. 0.05 mL aliquots of sample suspension were allocated for Fe(II) and total Fe determination by ferrozine assay, prior to centrifugation at 14000 g for 5 minutes. Duplicate 0.1 mL and 0.2 mL aliquots of aqueous phase were allocated for inductively coupled plasma-mass spectroscopy (ICP-MS) and ion chromatography (IC) analysis respectively, whilst 0.3 mL was allocated for pH and oxidation reduction potential (ORP) measurement with calibrated probes, remaining aqueous and solid phases were frozen at -20°C.

8 mL treatment dispersions or solutions were made up: (1) 1 g NanoFER 25S, (2) 0.8 g Carbo-Iron®, (3) 0.8 g biomagnetite, (4) 0.125 M acetate and 0.125 M lactate (biostimulation). Following day 1 sampling, 4 mL aliquots of respective treatment dispersions or solutions were added to a serum containing MLR sediment and a serum bottle EST sediment (4 mL DIW was added to no treatment

controls). Serum bottles were resealed and incubated at 20°C for the duration of the experiment. The contents of each individual treatment microcosms system, including controls, at day 1 (post-treatment addition) are summarised in Table P2-9.

Table P2-9: Contents of sediment treatment microcosm at day 1 (following addition of treatments).

Microcosm	Sediment Mass (dry wt.) and Sediment Type	Concentration $HgCl_2$	Treatment and Concentration in AGW	Volume AGW after treatment addition
A	~1 g MLR	~50 µM	NanoFER 25S (~10 g/L) [~2 g/L Fe]	50 mL
B	~1 g MLR	~50 µM	Carbo-Iron® (~8 g/L) [~2 g/L Fe]	50 mL
C	~1 g MLR	~50 µM	Biogenic Magnetite (2 g/L) [~2 g/L Fe]	50 mL
D	~1 g MLR	~50 µM	Bio-stimulation: Acetate (~10 mM) and Lactate (~10 mM)	50 mL
E	~1 g MLR	~50 µM	No Treatment	50 mL
F	~1 g EST	~50 µM	NanoFER 25S (~10 g/L) [~2 g/L Fe]	50 mL
G	~1 g EST	~50 µM	Carbo-Iron® (~8 g/L) [~2 g/L Fe]	50 mL
H	~1 g EST	~50 µM	Biogenic Magnetite (~2 g/L) [~2 g/L Fe]	50 mL
I	~1 g EST	~50 µM	Bio-stimulation: Acetate (~10 mM) and Lactate (~10 mM)	50 mL
J	~1 g EST	~50 µM	No Treatment	50 mL

Post-treatment samples (1 mL) were taken on days 5, 15, 29, 43, 57, 71, 169, 358 and 911, using aseptic technique by needle and syringe degassed with nitrogen. As with the pre-treatment samples, post-treatment sample aliquots were allocated Fe(II) and total Fe determination by ferrozine assay, pH, ORP, ICP-MS and IC. Solid phase from days 29 and 358 (except EST) samples were allocated for XAS analysis. Solid phase from days 5, 29 and 358 (except EST) samples were allocated for 16S rRNA sequencing. Following final sampling (day 911), the remaining contents of each microcosm were centrifuged at 4000 g for 15 minutes, and solid phases were allocated for total Hg (THg) and MeHg analysis.

5.2.3 Bioavailable Iron Quantification - Ferrozine Assay

1 g/L ferrozine solution [1 g ferrozine ($C_{20}H_{12}N_4Na_2O_6S_2$) and 11.96 g HEPES in 1 L DIW] was made up for ferrozine assays. 50 mL Fe(II) standard solutions (0, 1, 5, 10, 20 mM) were compiled from iron(II) sulphate heptahydrate ($FeSO_4{\cdot}7H_2O$) and DIW. Sample suspensions (0.05 mL) were digested for 3 hours in 0.5 M HCl (2.45 mL) to dissolve bioavailable Fe. Sample digests and standards were added to ferrozine solution, and absorbance was determined at 520 nm. Sample concentrations were interpolated by linear regression from the absorbance reading for Fe standards.

5.2.4 X-Ray Diffraction (XRD)

Powdered dry sample (~0.1 g) was mounted on a glass slide and analysed on a Bruker D8 Advance X-ray Diffractometer to determine the mineral phases present. Phases were identified using the Bruker DIFFRAC.SUITE EVA software, and Bruker DIFFRAC.SUITE TOPAS software was used for their quantification.

5.2.5 X-Ray Fluorescence (XRF) and Loss on Ignition (LOI)

XRF pellets (12 g powdered dry sediment and 3 g wax) were analysed on an Axios Sequential XRF Spectrometer to determine their elemental composition. For LOI analysis, sediment (1 g) was added to a crucible (of known mass) and oven heated to 100°C for 1 hour, to evaporate any remaining water, and crucible was reweighed to determine water content by mass loss. Following this, the crucible and sample were furnace heated to 1000°C for 1 hour, to evolve CO_2 from organics and carbonate minerals, and reweighed to determine CO_2 evolution by mass loss.

5.2.6 Ion Chromatography (IC)

Following storage at -20°C, duplicate 0.2 mL aliquots of aqueous phase from each treatment microcosm sample were defrosted, and five-fold diluted with DIW in 1 mL glass IC vials. Duplicate 1 mL samples were stored at 4°C prior to anion analysis (SO_4^{2-}, S_2O^{2-}, NO_3^-, NO_2^-, PO_4^{3-}, Cl^-, Br^-) on a Dionex ICS-5000 Capillary HPIC^{TM} System.

5.2.7 Inductively Coupled Plasma-Mass Spectroscopy (ICP-MS)

ICP-MS was used to determine concentrations of Hg in 10 mL samples (2% aqua regia with 200 µg/L gold matrix) from duplicate 100-fold diluted 0.1 mL aqueous phase aliquots from microcosm samples. An Agilent 7500 ICP-MS was operated in rapid sequential mode to detect and quantify Hg in samples. Detection limits are typically 0.1 ppb under the standard operating conditions. A 200 µg/L gold spike (from a 10 ppm elemental Au (0) in 2% in aqua regia stock solution) was added to a 2% aqua regia matrix for samples and calibration standards at the point of dilution to minimise carryover between samples and calibration standards (Chen, 2009).

5.2.8 Inductively Coupled Plasma-Atomic Emission Spectroscopy (ICP-AES)

ICP-AES was used to determine concentrations of Fe in 10 mL samples (2% (v/v) HNO_3) from aqueous phase of total iron digests. The Perkin-Elmer Optima 5300 dual view ICP-AES was used for analysis, it has a detection range of 10 ppb – 50 ppm.

5.2.9 Solid Phase Methylmercury (MeHg) Analysis

0.2 g of sample was weighed into 50 mL sample vials. The samples were first extracted by acid leaching using 10 mL of 6 M HCl and ultrasonicated for 30 min. Following the leaching process, samples were filtered through a 0.45 µm filter disk. Selective extraction of MeHg was carried out with the addition of 8 mL of acidified KBr/$CuSO_4$ mixture (combined in a 2:1 ratio) and 10 mL dichloromethane (DCM), which was then shaken on an automatic shaker for 2 hours followed by 30 seconds of mixing with a vortex mixer. A known volume of the DCM extract was removed and back extracted with 1.5 mL of sodium thiosulphate solution with 30 minutes on an automatic shaker followed by 30 seconds of mixing with a vortex mixer. The thiosulphate layer was removed from the vial and the DCM layer was extracted again with another 1.5 mL of thiosulphate solution. The two thiosulphate extracts were combined then 1 mL pipetted into 50 mL sample digestion vial and diluted with DIW to 25 mL. The MeHg was converted to inorganic Hg with the addition of 2.5 mL concentrated HCl and 3 mL of bromide/bromate solution and left to react overnight at ambient conditions. Calibration standards and reagent blank were also brominated. The samples were then de-colourised with hydroxylamine solution and analysed by CV-AFS using PSA Millennium Merlin 10.025. The limit of detection for this method analysis was 0.0012 ng/ml equating to a method detection limit of 0.0006 mg/kg in the sediment.

5.2.10 Solid Phase Total Mercury (THg) Analysis

0.1 g of sample was taken and digested in a 10 mL aqua regia (3:1 HCl: HNO_3) by heating at 120°C for 3 hours. Once cooled, the samples were diluted to 100 mL with DIW then filtered through Grade 41 Fast Ashless Filter Paper, 90 mm circle, 20 µm. Samples were further diluted in 10% (v/v) Aqua Regia then analysed using the PSA 10.025 Millennium Merlin system. The method detection limit for THg was found to be 0.015 mg/Kg in the sediment.

5.2.11 Hg L_{III}-edge X-Ray Absorption Spectroscopy

Hg L_{III}-edge XAS data were collected on the I20 Beamline at Diamond Light Source (Harwell, Oxfordshire). Samples were made from 50 to 100 mg aliquots of MLR sludge. The samples were analysed in x-ray fluorescence mode and Hg standards were analysed in x-ray transmission mode (64 element monolithic Ge detector with Xspress4) within a liquid nitrogen cryostat, at 77 K. Merges of data from less than 10 scans (to k = 12 – 14 scans) in Athena was sufficient for producing high quality data in samples containing >80 mg/kg Hg. Whereas merges of data from less than 5 scans to k = 12 – 14 were sufficient for good quality data from samples containing >450 mg/kg Hg. To quantify the Hg phases present in the samples the relevant K^3 weighted EXAFS spectra were linear combination fit with the spectra of various known standards (beta-HgS, alpha-HgS, Elemental Hg(0) 77K, HgO, $HgCl_2$, Hg_2Cl_2 $Hg_3S_2Cl_2$ and Hg(II) sorbed to sediment) in Athena software from k = 3 to 12 (Ravel and Newville, 2005). The elemental Hg(0) was prepared by slowly cooling liquid elemental Hg(0) to 77K by initially freezing at 193K for 4 hours to form a defined crystal structure. Figure P2-35 shows the difference in

K^3 weighted EXAFS spectra between Hg(0) analysed at room temperature and liquid nitrogen temperature, and this illustrates the importance the slow cooling in order to identify Hg(0) by XAS linear combination fitting. A similar method has only been published in one previous research paper (Jew et al., 2011). Iterative linear combination fitting of various combination of standards considered likely to exist under the physicochemical conditions within the microcosms enabled identification and proportionate quantification of these Hg chemical species in the solid phase samples. Spectra from Hg standards identified in samples were fit in Artemis software to determine their structure (Ravel and Newville, 2005).

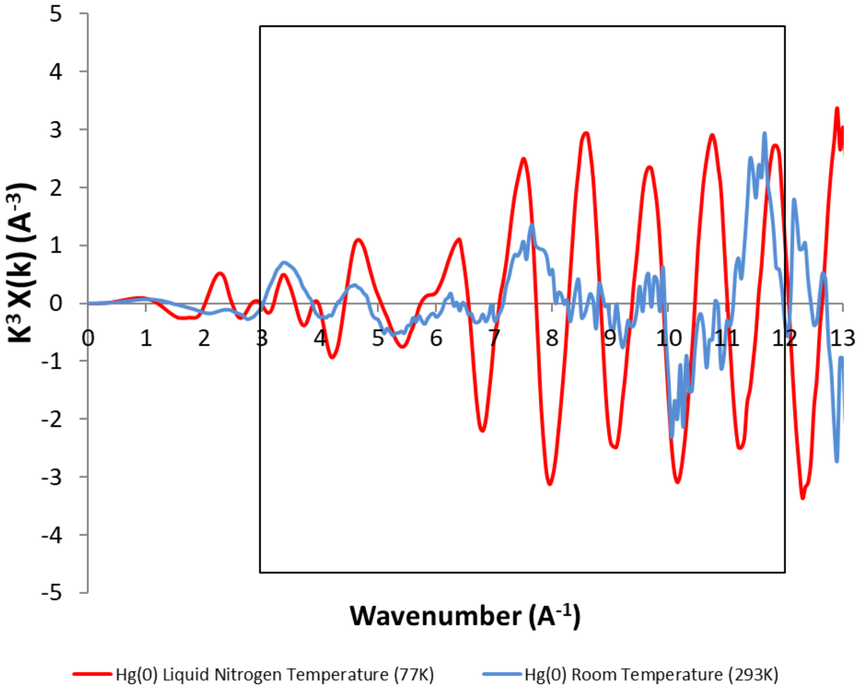

Figure P2-35: Hg L_{III}-edge K^3-weighted EXAFS spectra for Hg(0) standard at 77K (red) and 293K (blue).

5.2.12 Bacterial Population Analysis

DNA was extracted from 200 µL of sediment slurry using a DNeasy PowerLyzer PowerSoil Kit (Qiagen, Manchester, UK). Sequencing of polymerase chain reaction (PCR) amplicons of 16S rRNA genes present in the samples was conducted with the Illumina MiSeq platform (Illumina, San Diego, CA, USA) targeting the V4 hyper variable region (forward primer, 515F, 5′-GTGYCAGCMGCCGCGGTAA-3′; reverse primer, 806R, 5′-GGACTACHVGGGTWTCTAAT-3′) for 2 × 250-bp paired-end sequencing (Illumina) (Caporaso et al., 2012; Caporaso et al., 2011). Polymerase Chain Reaction (PCR) amplification was performed using Roche FastStart High Fidelity PCR System (Roche Diagnostics Ltd, Burgess Hill, UK) in 50 µL reactions under the following conditions: initial denaturation at 95°C for 2 min, followed by 36 cycles of 95°C for 30 s, 55°C for 30 s, 72°C for 1 min, and a final extension step of 5 min at 72°C. The PCR products were purified and normalised to ~20 ng each using the SequalPrep

Normalization Kit (Fisher Scientific, Loughborough, UK). The PCR amplicons from all samples were pooled in equimolar ratios. The run was performed using a 4 pM sample library spiked with 4 pM PhiX to a final concentration of 10% following the method of Schloss and Kozich (Kozich et al., 2013).

Raw sequences were divided into samples by barcodes (up to one mismatch was permitted) using a sequencing pipeline. Quality control and trimming was performed using Cutadapt (Martin, 2011), FastQC , and Sickle (Joshi and Fass, 2011). MiSeq error correction was performed using SPADes (Nurk et al., 2013). Forward and reverse reads were incorporated into full-length sequences with Pandaseq (Masella et al., 2012), and chimeras were removed using ChimeraSlayer (Haas et al., 2011). For the 16S sequences Operational Taxonomic Units (OTUs) were generated with UPARSE (Edgar, 2013). OTUs were classified by Usearch (Edgar, 2010) at the 97% similarity level, and singletons were removed. Rarefaction analysis was conducted using the original detected OTUs in Qiime (Caporaso et al., 2010). The taxonomic assignment was performed by the RDP naïve Bayesian classifier version 2.2 (Wang et al., 2007), used in combination with the Silva SSU 132 ribosomal RNA gene database (Quast et al., 2013). The OTU tables were rarefied to the sample containing the lowest number of sequences, all samples having less than 5,000 sequences were removed from analyses prior to the rarefaction step. The step size used was 2000 and 10 iterations were performed at each step.

5.3 Results and Discussion

5.3.1 Sediment Characteristics

MLR sediment was calcite rich, and major elemental components >3% total mass as determined by XRF and LOI analysis were CaO (39.5%), MgO (7.3%), Na_2O (3.8%), Cl (3.1%), and LOI (CO_2) (39.4%) (Table P2-14 in the Supplementary Information (SI) for all major elemental components detected at >0.1% total mass). Recent research identified that the elemental and mineral components, as well as bulk Hg chemical speciation (~85% beta-HgS, ~15% Hg(II) sorbed to sediment) were consistent with solid phase waste from the chlor-alkali industry [Paper 1(Section 4)]. THg was determined to be ~86 mg/kg [~73 mg/kg beta-HgS, ~13 mg/kg Hg(II) sorbed to sediment components] and the MeHg concentration was ~55 µg/kg (see Section 3 Paper 1). EST sediment was silicate rich, major elemental components >3% total mass as determined by XRF and LOI analysis were SiO_2 (52.4%), Al_2O_3 (13.1%), CaO (6.8%), Fe_2O_3 (5.3%), Mg0 (3.0%), and LOI (CO_2) (10.4%) (Table P2-15 in the SI reports all major elemental components detected at >0.1% total mass). There was no detectable Hg in EST sediment, EST sediment (Fe_2O_3 5.3%) had significantly higher Fe content than MLR sediment (Fe_2O_3 0.7%), and that MLR sediment (SO_3 1.1%) had a greater sulfur content than EST Sediment (SO_3 0.6%), as determined by XRF.

5.3.2 Mercury Chemical Speciation and Fate

Hg(II) Sorption

Figures P2-36a and P2-36b show the aqueous Hg concentration in samples from MLR and EST treatment systems, respectively. Hg(II) sorbed rapidly to EST sediment and appeared to remain associated with the solid phase for the remainder of the experiment, as Hg was not detected in the day 1 (pre-treatment addition), or any later, aqueous phase samples. Hg(II) did not seem to sorb as quickly to MLR sediment, 75 – 80 % sorbs in the first 24 hours. Addition of iron particle treatments (NanoFER 25S, Carbo-Iron® and biomagnetite) all enhanced sorption capacity in MLR sediment microcosms, removing the remaining Hg(II) from solution before day 5 (first post-treatment sampling time point). ~5% and ~2% remain in the aqueous phase of the biostimulation and no treatment control systems at day 5 and day 15 respectively, most Hg (>99%) had been removed from the aqueous phase by day 29, likely sorbed to the solid phases. Most Hg appeared to remain associated with the solid phase for the remainder of the experiment, <1% can be detected in aqueous phase samples after day 29. However, considering potential Hg(0) volatilisation to the gaseous phase, it is difficult to confirm whether gaseous Hg(0) was present within the systems at any time point as headspace gases were not monitored.

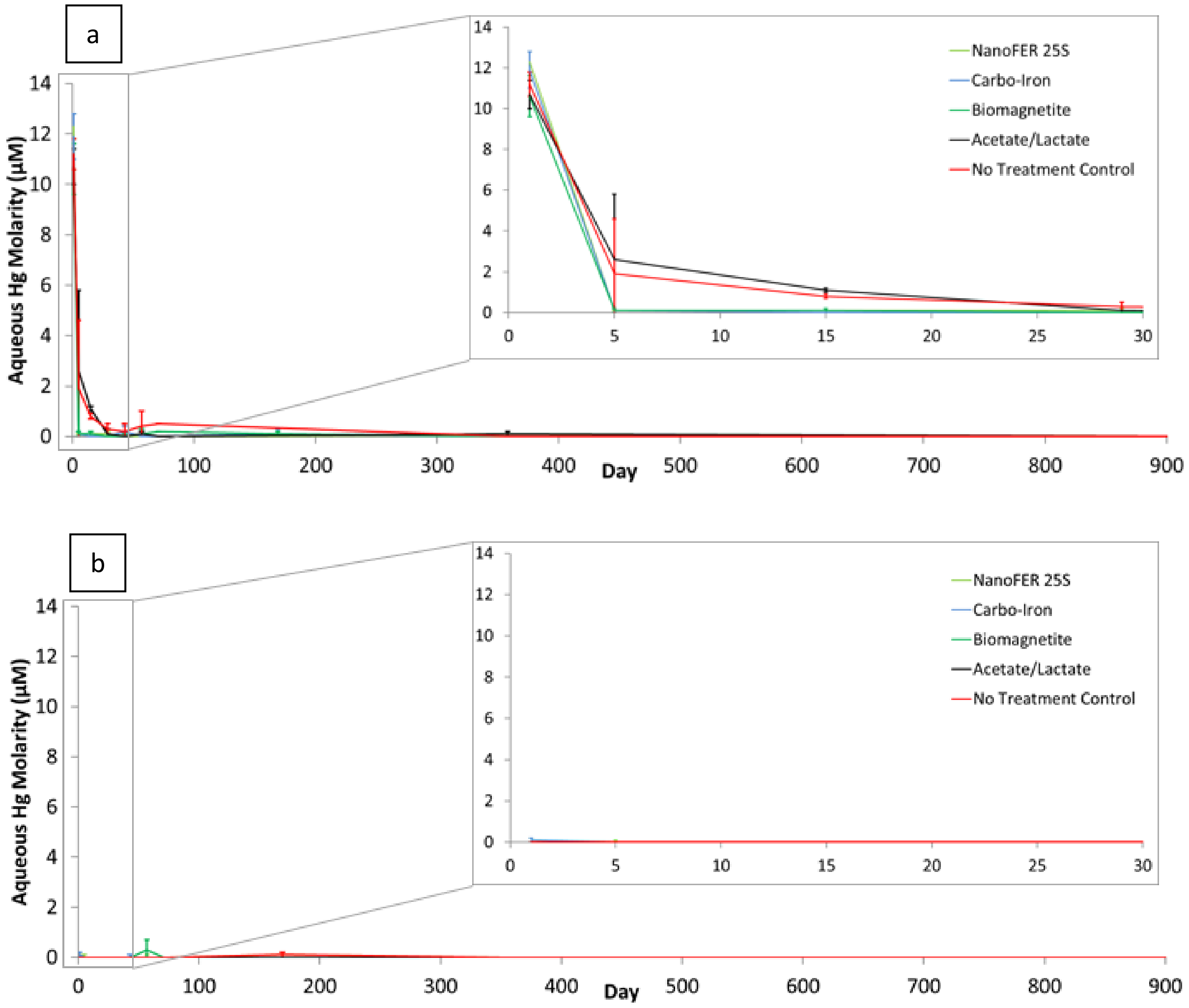

Figure P2-36: Aqueous Hg concentration in (a) MLR and (b) EST treatment systems (n=2).

Compound Specific Mercury Speciation

Hg L_{III}-edge EXAFS spectra and corresponding Fourier transforms for Hg standards, determined to be present in samples by linear combination fitting, are presented in Figures P2-47 and P2-47b (in the SI). EXAFS spectra fit results for beta-HgS, Hg(II) sorbed to MLR, Hg(II) sorbed to EST and Hg(0) standards, determined using in Artemis software, are shown in Table P2-10 (in the SI) (Ravel and Newville, 2005). Figure P2-37 is a summary of the linear combination fit results for day 29 and day 358 solid phase samples from the four treatment systems and a no treatment control system containing MLR sediment, illustrating the relative contribution of various Hg standards to total solid phase Hg. Iterative linear combination fittings highlighted varying contributions from Hg(II) sorbed to MLR, beta-HgS and Hg(0) to Hg L_{III}-edge EXAFS spectra for day 29 and day 358 solid phase samples (A – E). The K^3-weighted Hg L_{III}-edge EXAFS spectra for the MLR treatment system sample are presented alongside the corresponding linear combination fit spectra in Figures P2-48 and P2-49 (in the SI). The values obtained for the statistical goodness-of-fit parameters, R-factor (R) and chi-square (χ^2), are reported in Tables P2-11 and P2-12 (in the SI).

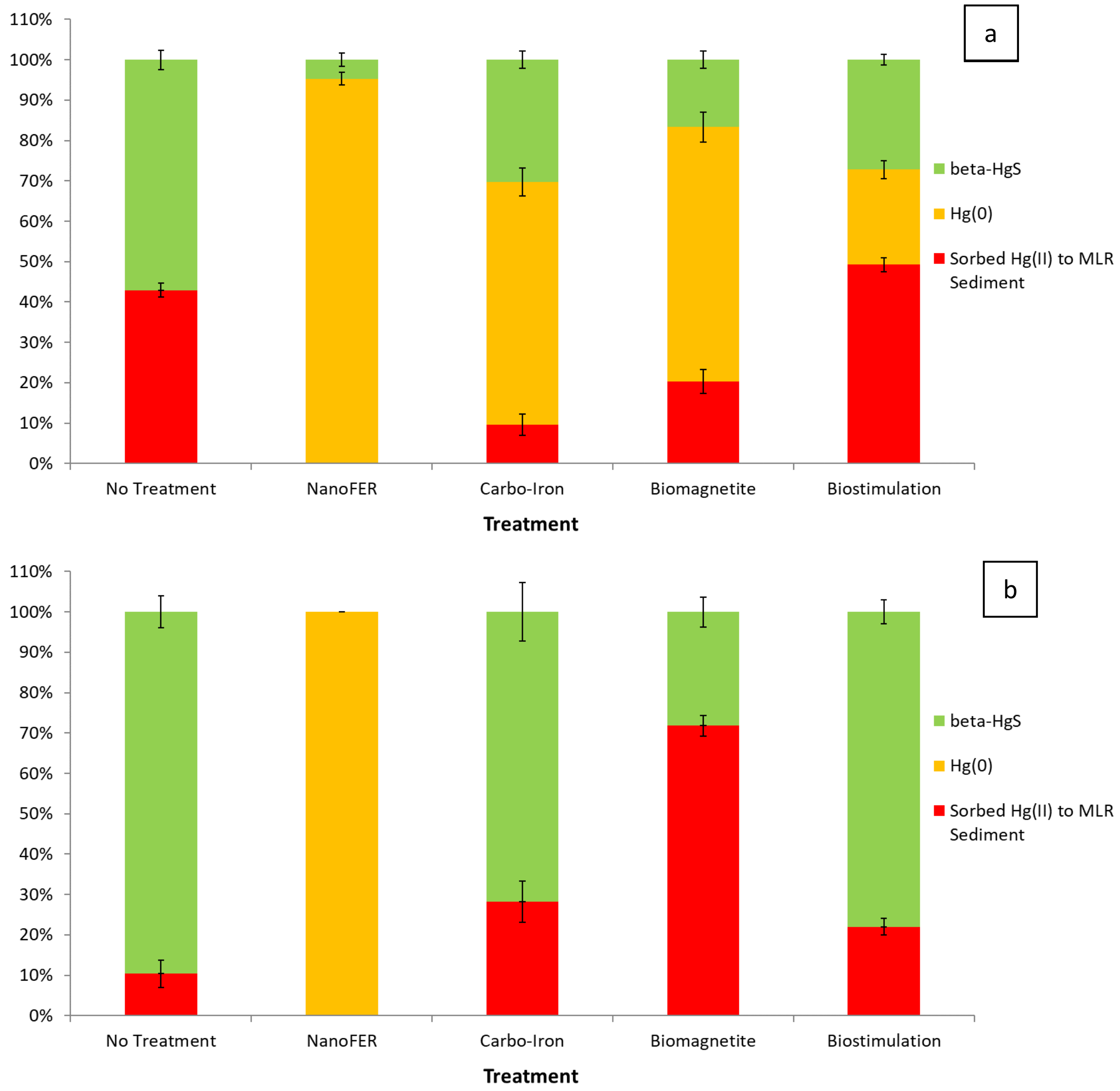

Figure 37: Hg L$_{III}$-edge EXAFS spectra (K^3) linear combination fit results for solid phase samples from MLR treatment systems (a) day 29 (b) day 358.

Sorbed Hg(II) is mobile and bioavailable, hence poses the greatest environmental risk after highly toxic organic MeHg species. >95% Hg(II) was reduced to Hg(0) in day 29 samples from MLR system containing NanoFER 25S. >99% Hg in day 358 solid samples was elemental Hg(0), suggesting the nZVI in the system was able to reduce almost all the existing immobilised Hg(II) in beta-HgS particles to Hg(0), these highly reducing conditions were maintained for at least a year. In day 29 solid phase samples, ~60% Hg(II) was reduced to Hg(0) in the MLR system containing Carbo-Iron®, whilst ~30% was present as beta-HgS, suggesting a competing sulfidation process. nZVI in NanoFER 25S and Carbo-

Iron® systems, a powerful reducing agent, is likely to have stimulated the reduction of Hg(II) in both these systems. However, microbial Hg(II) reduction via the mer operon pathway may also have contributed to the formation of Hg(0). Bacterial population data presented in Section 3.4 identified *Sphingobium,* a highly Hg-resistant bacterial strain, made up ~5% total identified population at day 5, day 71 and day 358 in the Carbo-Iron® MLR system, and could have contributed to Hg(II) reduction (Mahbub et al., 2016). However, Hg(0) was not detected in day 358 solid phase samples from the Carbo-Iron® MLR system, ~70% was beta-HgS, suggesting that sulfidation transformation pathways have become more dominant over time in this system or potentially significant loss via volatilisation of Hg(0) from solid and aqueous phases.

ZVI forms hydrogen (H_2) gas and aqueous hydroxide (OH^-) during aqueous corrosion under anoxic conditions (Equations 1 and 2) (Crane and Scott, 2012).

$2Fe^0 (s) + 4H_2O (l) \rightarrow 2Fe^{2+} (s) + 2H_2 (g) + 4OH^- (aq)$ $E^0 = -0.39$ V Equation 1

$2Fe^{2+} (s) + 2H_2O (l) \rightarrow 2Fe^{3+} (s) + H_2 (g) + 2OH^- (aq)$ $E^0 = -1.60$ V Equation 2

The difference in standard redox potential between Fe ($E^o = -0.44$ V) and Hg ($E^o = +0.86$ V) means that reduction of Hg(II) by Fe(0) is energetically favourable [25]. Equation 3 summarises the Hg(II) reduction reaction in anoxic systems containing ZVI at room temperature (Vernon and Bonzongo, 2014).

$Hg^{2+} + Fe^0 \rightarrow Hg^0 + Fe^{2+}$ Equation 3

Previous work has reported that almost 100% HgS was obtained in anoxic systems under alkaline conditions in the presence of elemental sulphur after ~2 years (Svensson et al., 2006). Highest yields were observed for the samples containing S(0), elemental Hg(0) was transformed into HgS, S(0) may disproportionate into S(-II) and S(VI) under anaerobic conditions leading to more efficient sulphide generation (Svensson et al., 2006). Hydroxide contributed to an increase in pH (see Figure P2-40), whilst H_2 may have acted as an electron donor for microbial hydrogenotrophic methanogens (Conrad, 1999). H_2 can stimulate beneficiary microbial processes, acting as an electron donor to generate additional ferrous iron [Fe(II)] from microbial ferric iron [Fe(III)] reduction (Lovley et al., 1989); and stimulating the production of sulfide [H_2S or HS^-] via sulfate-reducing bacteria (SRB) which may cause HgS minerals to precipitate (Fagerström and Jernelöv, 1971; Nedwell and Banat, 1981).

Linear combination fit data for day 29 samples from the biomagnetite MLR system suggested that ~60% Hg(II) was reduced to Hg(0). Biomagnetite has a single Fe(II), with an electron available for reduction of Hg(II). ~20% Hg was identified as metacinnabar (beta-HgS), most likely the original beta-HgS in the MLR sediment as this was the same percentage identified in the untreated baseline MLR sample used for comparison, alongside ~20% Hg(II) sorbed to MLR sediment components. Day 358 samples did not contain any Hg(0), ~40% total Hg was present as beta-HgS, alongside ~60% sorbed Hg(II), suggesting Hg(0) may be being oxidised at some point prior to day 358 samples being taken. Biostimulation of an MLR system with acetate and lactate also identified Hg(II) reduction over the first 29 days, ~25% Hg(II) was reduced to Hg(0) suggesting potential microbial reduction pathways harnessing the mer operon. Bacterial population data presented in Section 3.4 identified *Thermus* species, one of the earliest Hg-resistant bacterial strains identified, made a significant contribution to total identified population at day 5 (16.8%) and day 71 (20.4%) in the biostimulation MLR system, and could have contributed to Hg(II) reduction (Wang et al., 2009). ~25% was present as beta-HgS, most is probably from existing beta-HgS in the sediment, but some additional sulfidation may have been stimulation, the bulk of the Hg remained as sorbed Hg(II) in day 29 samples. However, sulfidation appeared to become a more dominant process over the next 11 months, as ~80% Hg was identified as beta-HgS in day 358 samples, alongside ~20% sorbed Hg(II). ~60% Hg was identified as beta-HgS in the no treatment MLR system in day 29 samples, with ~40% present as sorbed Hg(II), suggesting sulfidation was occurring during the first month. Sulfidation processes appear to continue over the next 11 months, as almost all Hg (~80%) was identified as beta-HgS in day 358 samples, alongside ~20% sorbed Hg(II). Less Hg was identified as Hg(0) in MLR sediment at day 358 than at day 29 with biomagnetite, Carbo-Iron® and bio-stimulation treatment – suggesting there was less Hg reduction potential over the longer term in MLR systems with these treatments. Biomagnetite, Caro-Iron® and biostimulation all seemed to reduce the amount of sulfidation in MLR sediment when compared to the no treatment control system, whilst NanoFER 25S appeared to inhibit Hg sulfidation completely, even desulfurising and reducing Hg(II) in existing beta-HgS.

Figure P2-38 is a summary of the linear combination fit results for day 29 solid phase samples from the four treatment systems and no treatment control system containing EST sediment, illustrating the relative contribution of various Hg standards to solid phase Hg. Varying contributions from Hg(II) sorbed to EST, beta-HgS and Hg(0) were identified from linear combination fitting Hg L_{III}-edge EXAFS spectra for day 29 solid phase samples from microcosm treatment systems containing EST sediment (F – J). The values obtained for the statistical goodness-of-fit parameters, R-factor (R) and chi-square (χ^2), are presented alongside Hg L_{III}-edge EXAFS sample spectra and respective fit spectra (Hg standard component contributions) in Section 7 of the SI. We were unable to collect XAS data for day 358 solid phase samples and are unable to confirm Hg chemical speciation one-year post-treatment.

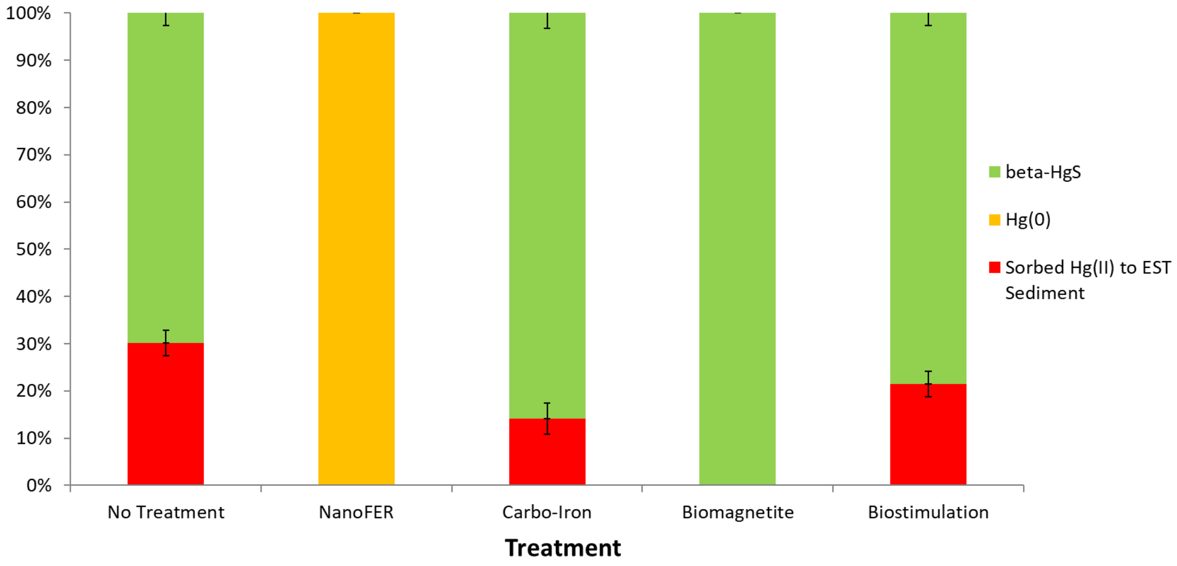

Figure P2-38: Hg L_{III}-edge EXAFS spectra (K^3) linear combination fit results for day 29 solid phase samples from EST treatment systems.

>99% Hg in day 29 solid phase samples for EST systems containing NanoFER 25S was determined to be elemental Hg(0), suggesting the bulk of Hg(II) was reduced by nZVI. Almost all Hg in day 29 solid phase samples from EST system treated with biomagnetite was identified as beta-HgS. Beta-HgS formation was also significantly enhanced in Carbo-Iron® and biostimulation EST systems, >80% of Hg was present as beta-HgS 28 days following treatment addition, more than the ~70% HgS identified in the no treatment control, with the bulk of the remaining fraction present as sorbed Hg(II) in these three systems. Bacterial population data presented in Figure P2-41 shows the contribution of SRB to total population increased notable between day 5 (1.3 – 6.4%) and day 71 (8.7% – 15.6%) in all treatment and no treatment systems with EST sediment. The contrasting impacts of Carbo-Iron®, biomagnetite and biostimulation on Hg in the MLR and EST systems over the first month highlight the importance of the different sediment components (e.g. geochemical characteristics, microbial community) on controlling processes determining Hg chemical speciation.

Figure P2-39 highlights the increase in organic MeHg concentrations from baseline (before microcosm setup) values (Table P2-16 in the SI) over the duration of the experiment (911 days) in MLR and EST treatment systems. The results suggested that there was net methylation in all treatment systems, as there is more MeHg in solid phase day 911 samples from all treatment systems. NanoFER 25S treatment systems have the least net methylation, as there is <10 µg/kg increase in MeHg in both MLR and EST day 911 samples. There is less net methylation in all MLR treatments systems than comparable EST systems, apart from Carbo-Iron®, despite MLR (34 µg/kg) sediment having more existing MeHg than EST (0 µg/kg) at baseline. Bacterial population data presented in Figure P2-41 shows all EST sediment systems had a greater proportion of SRB and iron-reducing bacteria (IRB), known to methylate Hg, than MLR systems. Sediment composition and origin (EST is natural estuarine sediment, whereas MLR is a calcite rich waste material), and pH (EST pH ~8, whereas MLR pH ~10) will all be major factors contributing to the increased prevalence of IRB and SRB in EST sediment. Carbo-Iron® was the only treatment to increase MeHg levels more than the no treatment systems, with levels increasing from 34 to 218 µg/kg (>600%) in MLR sediment and increasing from 0 to 121 µg/kg in EST sediment, suggesting Carbo-Iron® was having an adverse effect in respect to stimulating net methylation in the MLR and EST systems. In section 3.4 we assess changes in 16S rRNA data (day 5, day 70 and day 358) and attempt to link to changes in Hg chemical speciation discussed here. However, we were unable to obtain 16s rRNA data from day 911, therefore we are unable to provide evidence to identify potential methylators (and demethylators) present at that time point.

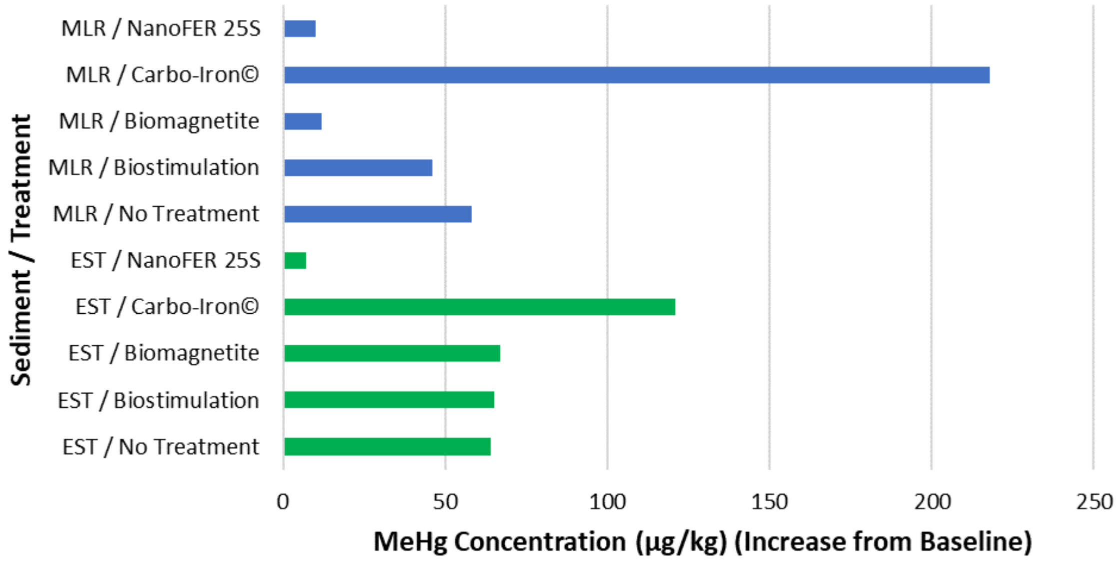

Figure P2-39: Change in MeHg concentration from baseline value in solid phase from MLR and EST treatment systems.

5.3.3 Geochemical Monitoring

Changes in key geochemical parameters (pH, ORP, bioavailable Fe(II), nitrate and sulphate concentrations) monitored for the duration of the experiment are presented for MLR and EST treatment systems in Figures P2-40a and P2-40b, respectively.

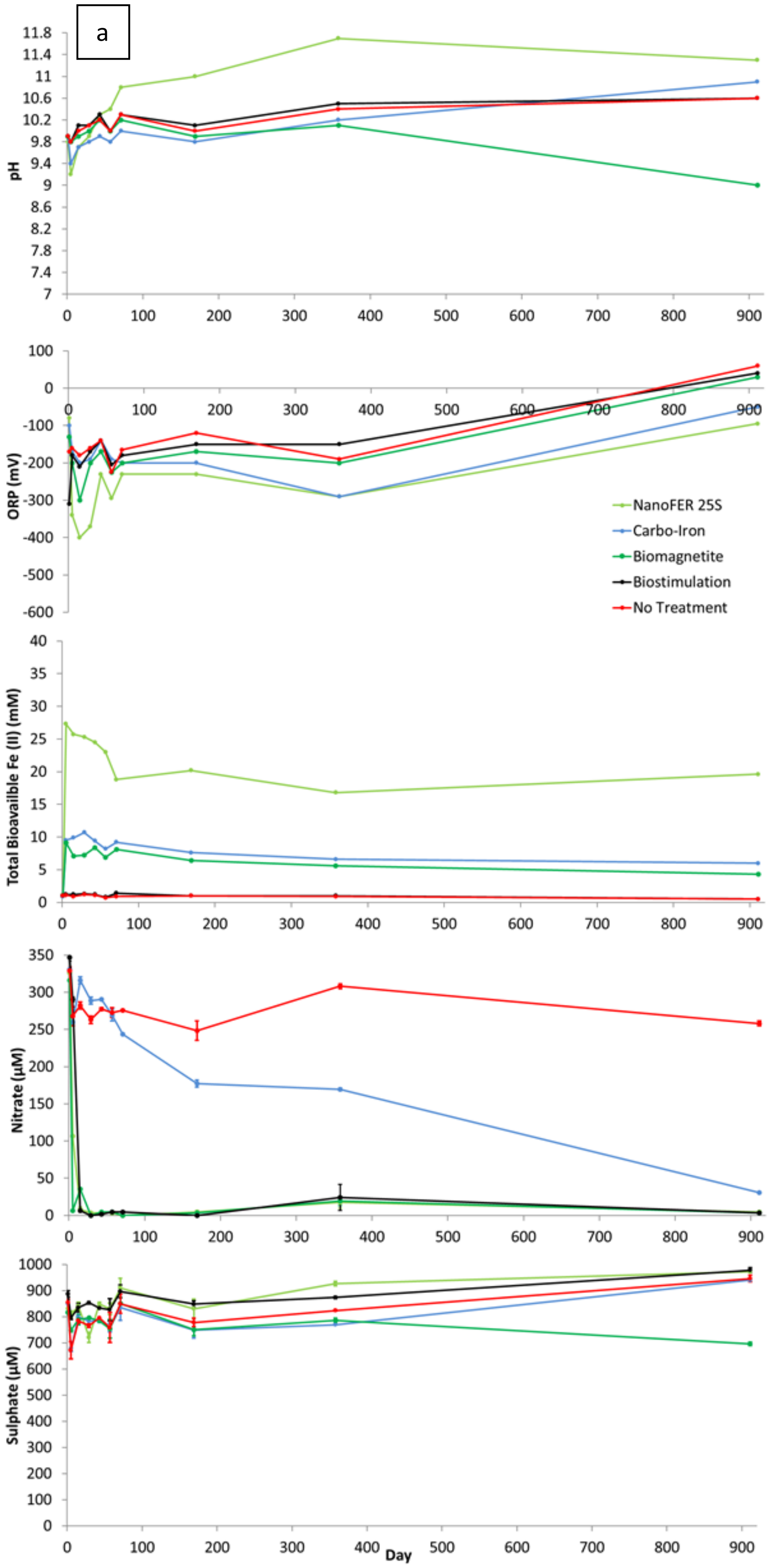
a
pH
11.8
11.4
11
10.6
10.2
9.8
9.4
9
8.6
8.2
7.8
7.4
7
0
100
200
300
400
500
600
700
800
900
100
0
-100
-200
-300
-400
-500
-600
ORP (mV)
NanoFER 25S
Carbo-Iron
Biomagnetite
Biostimulation
No Treatment
Total Bioavailble Fe (II) (mM)
40
35
30
25
20
15
10
5
0
Nitrate (µM)
350
300
250
200
150
100
50
0
Sulphate (µM)
1000
900
800
700
600
500
400
300
200
100
0
Day

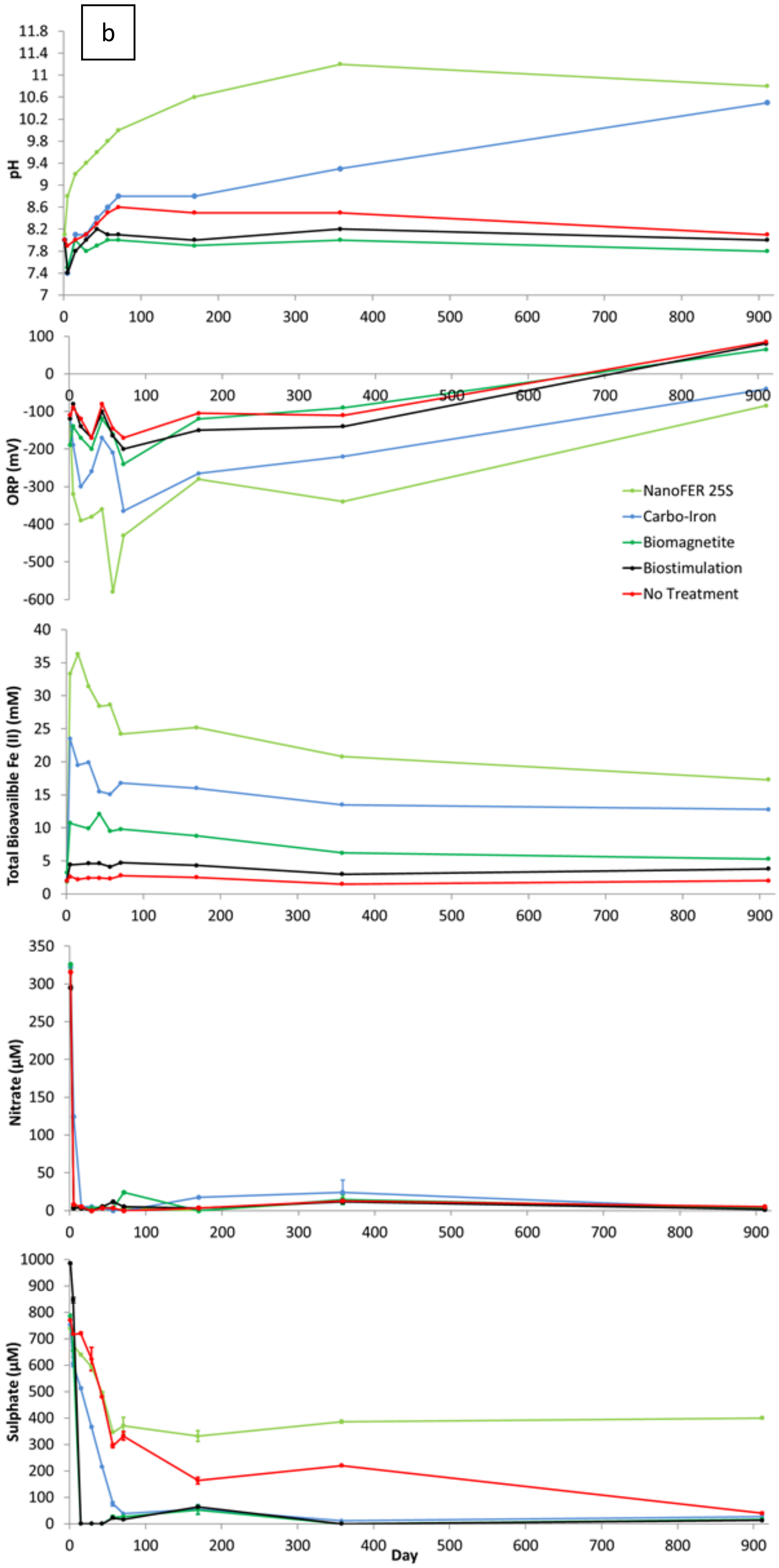

Figure P2-40: pH, ORP, bioavailable Fe(II) concentration, aqueous nitrate (NO_3^-) concentration (n=2) and aqueous sulphate (SO_4^{2-}) concentration (n=2) in (a) EST and (b) MLR treatment systems.

MLR systems had a higher pre-treatment (day 1) pH (~9.9) than EST systems (~8.0), due to the alkaline nature of the MLR sediment material. Addition of treatments initially caused a decrease in pH in all treatment systems, due to a dilution effect, except the NanoFER 25S EST system. Despite an initial decrease in pH most systems recovered to original day 1 values by day 15 sampling and were maintained in the vicinity of their original levels (day 1 value +/- 0.6) over the first 2 months, except the NanoFER 25S EST system which continued to increase to 9.8 by day 57, reaching a peak (11.2) at day 358. NanoFER 25S MLR system started to increase in pH more significantly after 2 months, peaking (11.7) at day 358. Carbo-Iron® EST system started to significantly increase from day 70, reaching a peak (10.5) at day 911. However, Carbo-Iron® MLR system only started to significantly increase from one-year post-treatment, reaching a peak (10.9) at day 911. NanoFER 25S and Carbo-Iron® were the only two treatments to notably change pH from pre-treatment values, both caused pH to increase over the duration of the experiment. Increase in pH is likely due to the production of hydroxide during the anoxic aqueous corrosion of nZVI. NanoFER 25S appeared to corrode more rapidly and had potentially lost reactivity by day 911, in contrast Carbo-Iron® seemed to be slower reacting, with the most significant pH increases occurring between day 358 and day 911. This is in congruence with the theory that Carbo-Iron® is a slow-release treatment with longer acting reducing effects due to its slower anoxic degradation (Mackenzie et al., 2012).

ORP remained below zero for all samples from MLR and EST systems during the first year, suggesting reducing conditions had been maintained in the anoxic systems over this period. However, by day 911 biomagnetite, biostimulation and no treatment systems had become slightly oxidising (30 – 90 mV), Carbo-Iron® and NanoFER 25S systems remained reducing for the duration of the experiment, most likely due to the continued anoxic degradation of nZVI in both materials. NanoFER 25S created and maintained the most reducing conditions and reached a minimum ORP at day 15 (-400 mV) in MLR systems and day 57 (-580 mV) in EST systems.

Bioavailable Fe(II) was highest in NanoFER 25S systems for both sediments peaking shortly after addition of the nZVI treatment. However, the EST peak (36 mM) at day 15, was slightly higher than the MLR peak (27 mM) at day 5. Initial XRF analysis highlighted that EST sediment (5.3 g/kg) had a higher Fe content than MLR sediment (0.7 g/kg), prior to treatment addition, likely contributing the higher bioavailable Fe(II) values in EST systems. Bioavailable Fe(II) decreased between day 15 (36 mM) and day 71 (24 mM), continuing to decrease gradually until day 911 (17 mM) in the NanoFER 25S EST system. Nevertheless, in the NanoFER 25S MLR system, bioavailable Fe(II) decreased from day 5 (27 mM) until day 71 (19 mM), fluctuating slightly over subsequent sampling time points. Addition of Carbo-Iron® treatment caused a rapid increase in bioavailable Fe(II) between day 1 (pre-treatment) and day 5 in MLR (10 mM) and EST (24 mM) systems. Bioavailable Fe(II) levels continued to increase to a peak (11 mM) at day 29 in Carbo-Iron® MLR system, before decreasing to 6 mM by day 911. However, in the Carbo-Iron® EST system bioavailable Fe(II) levels decreased from the day 5 peak (24 mM) to 13 mM at day 911. Bioavailable Fe(II) peaked at day 5 following addition biomagnetite in both MLR (9 mM) and EST (11 mM) systems and continued to decrease for the duration of the experiment. It is difficult to gauge the contribution of microbial Fe reduction taking place in treatment systems containing Fe particles due to the anoxic degradation of the treatment itself.

Biostimulation and no treatment systems containing MLR sediment had the lowest bioavailable Fe(II) concentration with little change (+/- 0.5 mM) in concentration from day 1 (1 mM) over the duration of the experiment, suggesting biostimulation had little impact on this parameter in MLR systems. The equivalent systems with EST sediment had a higher bioavailable Fe(II) concentration at day 1 (2 mM) due to higher sediment Fe content. Bioavailable Fe(II) peaks at day 5 (3 mM) in no treatment EST system and fluctuated between 2 and 3 mM for the duration of the experiment. An increase in bioavailable Fe(II) concentration was observed at day 5 (4 mM) in biostimulation EST system following treatment addition and continued to increase to a peak of 5 mM at day 71. Bacterial population data (Figure P2-41) shows that IRB made up ~12% total population identified at day 5 in both biostimulation and no treatment EST systems.

Rapid nitrate decrease was observed in biomagnetite, biostimulation and NanoFER 25S MLR systems, most nitrate (>99%) was removed from the aqueous phase by day 29, suggesting there is rapid nitrate reduction in these systems. Highly efficient reduction of nitrate by ZVI-based materials has previously been reported across a range of operational parameters (Liu and Wang, 2019). However, Carbo-Iron® (nZVI and ACC composite) did not appear to degrade nitrate as efficiently as NanoFER 25S, markedly in the MLR systems, suggesting potential sediment matrix effects. Nitrate concentration decreased steadily from day 15 (316 µM) until day 357 (169 µM) in the Carbo-Iron® MLR system, >90% was removed by day 911 (31 µM), suggesting nitrate reduction increased later in the experiment.

Nitrate removal was fastest in the biomagnetite MLR system, ~98% nitrate was absent from the aqueous phase by day 5. Recently published work found that nitrate reduction to nitrogen gas (N_2) was only completed in microbial microcosms containing nitrate polluted groundwater and magnetite nanoparticles, likely due to an increased Fe(II) availability from nano-sized compared to micro-sized magnetite particles (Margalef-Marti et al., 2020). Aqueous nitrate concentration increased slightly in the biomagnetite MLR system between day 5 (7 µM) and day 15 (36 µM), before being almost completely removed by day 29. There were slight fluctuations in nitrate concentration in the no treatment MLR system, but concentration remained around ~270 µM. Rapid nitrate removal was observed in all EST treatment systems, with >97% removed from aqueous phase in four systems by day 5, decrease in nitrate concentration was slower in the Carbo-Iron® EST system with ~40% still in solution at day 5 (124 µM). Day 15 samples contained >5 µM in all EST systems, aqueous nitrate concentrations remained below this value at subsequent sampling points, except for one-year samples in which nitrate concentration increased in all EST systems (11 – 24 µM).

There were slight fluctuations in aqueous sulphate concentrations across all MLR systems, but average concentration remained at ~820 µM for the duration of the experiment, suggesting limited sulphate reduction was taking place. XRF analysis at baseline revealed that MLR sediment (SO_3 1.1% total mass) had a higher sulfur content than EST sediment (SO_3 0.6% total mass). Figure P2-41 reveals that SRB were present at notable levels (>1% total population) at day 71 in NanoFER 25S system and at day 358 in NanoFER 25S, biomagnetite and biostimulation. However, only the biomagnetite MLR system appeared to show a notable decrease in sulphate concentration between day 71 (851 µM) and day 911 (696 µM), suggesting alternative sulfur intermediates may be electron acceptors for SRB in MLR sediment.

Biomagnetite and biostimulation had a rapid impact on sulphate levels in EST systems, with almost complete removal from the aqueous phase by day 15, despite SRB only representing 1.3% and 1.8% of the microbial community at day 5. Carbo-Iron® was slightly slower acting with a gradual decrease in sulphate concentration between day 5 (602 µM) and day 71 (75 µM). SRB contribution to total microbial community identified increased from 6.4% to 8.7% over this period. 15 – 38 µM sulphate was identified in aqueous phase of EST systems containing biomagnetite, biostimulation and Carbo-Iron® systems at day 71. NanoFER 25S exhibited a similar, less pronounced, reduction in aqueous phase sulphate over this period reaching a minimum (346 µM) on day 57, levels remained relatively constant from this point onward. No treatment EST system exhibited a similar decrease in sulphate levels over the first two months, but aqueous concentrations continue to decrease between day 57 (395 µM) and day 911 (40 µM). Figure P2-41 highlights the significant role SRB played at various time points over the first year in all the EST systems, making up >12% total microbial population identified at day 71 and/or day 358.

5.3.4 Bacterial Population in Sediment

The bacterial communities within the sediment were analysed by 16S rRNA gene sequencing to identify the organisms present, including those with the potential to impact on Hg speciation. However, recent studies have identified weak correlations between Hg-methylating bacteria and soil Hg concentrations in environmental samples, with overall total Hg and MeHg concentrations poorly correlated with Hg-cycling genes (Christensen et al., 2019). Bacterial phyla identified at baseline in unamended sediments are presented alongside those identified in samples at three time points (day 5, day 71 and day 358) from each treatment system for MLR (Figure P2-51a in the SI) and EST (Figure P2-51b in the SI) sediments. Detailed discussion and figures relating to change in contribution of bacterial phyla in the treatment systems are presented in Section 10 of the SI.

Baseline data highlighted a significant variation in diversity between MLR and EST sediment, 111 unique OTUs were identified from the PCR amplified gene sequences extracted from MLR sediment, of these 21 made up >1% of the population identified. Gammaproteobacteria (45.5%) dominated the sediment, although the most heavily represented family of organisms detected was the Betaproteobacterial-affiliated Burkholderiaceae (~24% total sequences). Whereas EST sediment had a much more diverse microbial population, with 779 unique OTUs, of these 14 made up >1% of the population identified. Gammaproteobacteria (19.2%), Deltaproteobacteria (14.6%), Oxyphotobacteria (12.8%) and Planctomycetacia (10.7%) were the most abundant phyla identified in the EST sediment control.

IRB and SRB contribution to the total bacterial population for each 16S rRNA sequencing time point (day 5, day 71 and day 358) from all MLR and EST systems are presented in Figure P2-41. IRB and SRB can be capable of Hg methylation or reduction under anoxic conditions, therefore changes to their communities may have significance in relation to potential impacts on Hg chemical speciation. Microbial methylation and demethylation are two competing processes controlling the net production and bioaccumulation of neurotoxic methylmercury (MeHg) in natural ecosystems. Research findings have indicated a cycle of Hg methylation and demethylation (e.g. IRB *Geobacter bemidjiensis*) among anaerobic bacteria, thereby influencing net MeHg production in anoxic water and sediments (Lu et al., 2016). Considering this information, the influence of IRB on production of MeHg cannot be determined without more detailed phylogenetic analysis.

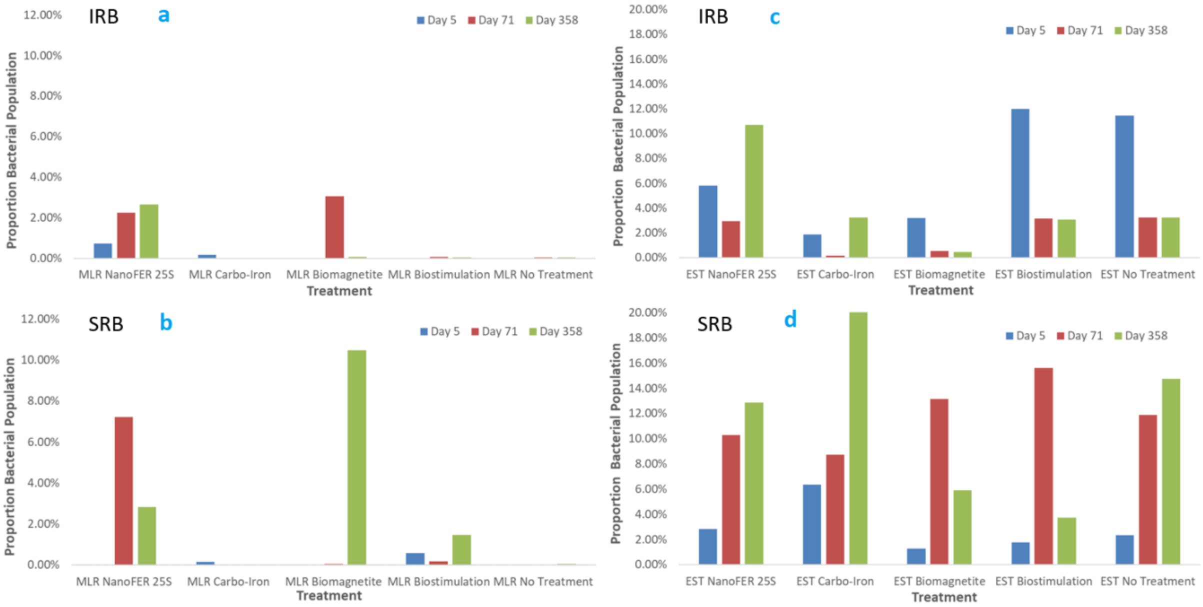

Figure P2-41: Proportion of bacterial population that are [1] IRB in MLR (a) and EST (c) treatment systems [2] SRB in MLR (b) and EST (d) treatment systems.

There were a limited number of IRB identified in MLR systems, suggesting that there was minimal microbial iron reduction taking place. NanoFER 25S MLR system was the only microcosm that showed a consistent increase in IRB population from day 5 (0.8%) to day 358 (2.6%). *Shewanella putrefaciens strain Hammer 95* was the most abundant IRB identified present at 1.9% and 2.1% total population in day 71 and day 358 samples, respectively. *Shewanella putrefaciens* strains are facultative anaerobic bacteria and have been shown to be resistant to high concentration of Hg(II), the mer operon gives them the capability of reducing Hg(II) (Barkay et al., 2003; Jiang et al., 2012). IRB seemed to play a much more significant role in EST systems, making up >10% of total identified microbial community at day 5 in biostimulation (12.0%) and no treatment (11.5%) systems, becoming much less prevalent by day 71 (< 3% total population) An increase in bioavailable Fe(II) between day 1 and day 5 (Figure P2-40b), is likely due to microbial iron reduction in the early stages of the experiment. Changes in bioavailable Fe(II) can be more easily attributed to the microbial community in these two treatment systems, as there was no additional Fe added to systems, as with the iron particle treatment systems. The NanoFER 25S EST system showed a dynamic shift in IRB contribution to total population over the duration of the experiment, decreasing between day 5 (5.8%) and day 71 (2.9%), before increasing notably by day 358 (10.7%), suggesting that they may have had a more significant influence at this time point. However, as with the equivalent MLR system, it is difficult to attribute changes in bioavailable Fe(II) to IRB activity due to the impact of the anoxic dissolution of Fe(0) from the NanoFER 25S treatment.

SRB only made up a notable portion (>2%) of the population in day 71 (6.9%) and day 358 (2.8%) samples from the NanoFER 25S MLR system, and at day 358 (10.5%) in biomagnetite MLR system. A decrease in aqueous sulphate concentration from day 358 to day 911 (Figure P2-40a) suggests there may be limited sulphate reduction in biomagnetite system from day 358. However, it is a little more ambiguous in relation to the NanoFER 25S treatment, as there was not a clear decrease in sulphate levels at day 71 despite SRB making up >5% total community identified at this time point, therefore SRB may utilising alternative sulfur compounds as electron acceptors.

SRB played a much more obvious role in EST systems, with a decrease in sulphate levels observed in all treatment systems over the duration of the experiment (Figure P2-40b). Biostimulation and biomagnetite systems showed a rapid decline in aqueous sulphate concentration between day 5 and day 15 and had the highest number of SRB at day 71, making up between 11.9% and 13.2% of the total population. *Desulfomicrobium baculatum DSM 4028* and *Desulfobulbus elongatus strain FP* (closely matched) contributed significantly to the SRB community in day 71 samples from these two treatment systems. SRB made up >8.7% of the total microbial population identified in all treatment systems at this time point, their impact on sulphate levels is apparent, as >50% aqueous sulphate had been transformed in all EST systems by day 71 (Figure P2-40b). Whereas SRB contribution to the total bacterial community decreased from day 71 to day 358 in biostimulation and biomagnetite systems, it continued to increase in all other treatment systems, reaching a maximum in day 358 samples for no treatment (14.8%), NanoFER 25S (12.8%) and Carbo-Iron® (20.4%) systems.

Despite SRB making up >12% of the total community at day 358 in the NanoFER 25S EST system, they did not appear to have a notable impact on aqueous sulphate levels which are maintained at ~350 µM from day 57 until day 911. In contrast sulphate levels continued to decrease from day 358 to day 911 in the no treatment system. Aqueous sulphate concentration remained <80 µM from day 57 in all other EST systems, including the Carbo-Iron® system in which SRB continued to proliferate to day 358, suggesting they may be using an alternative electron acceptor as with the SRB in the NanoFER 25S system. SRB are known to predominantly methylate Hg in freshwater and estuarine sediments under reducing conditions, but this is usually only limited by the availability of sulfate in freshwater sediments (Compeau and Bartha, 1985; Hellal et al., 2015). HgS particles are known to nucleate in anoxic zones, by reaction of thiol-bound Hg with biogenic sulfide (Manceau et al., 2015). Figure P2-42 proposes potential Hg reduction, sulfidation and methylation pathways in an anoxic subsurface / groundwater system treated with nZVI, such as in NanoFER25S and Carbo-Iron®.

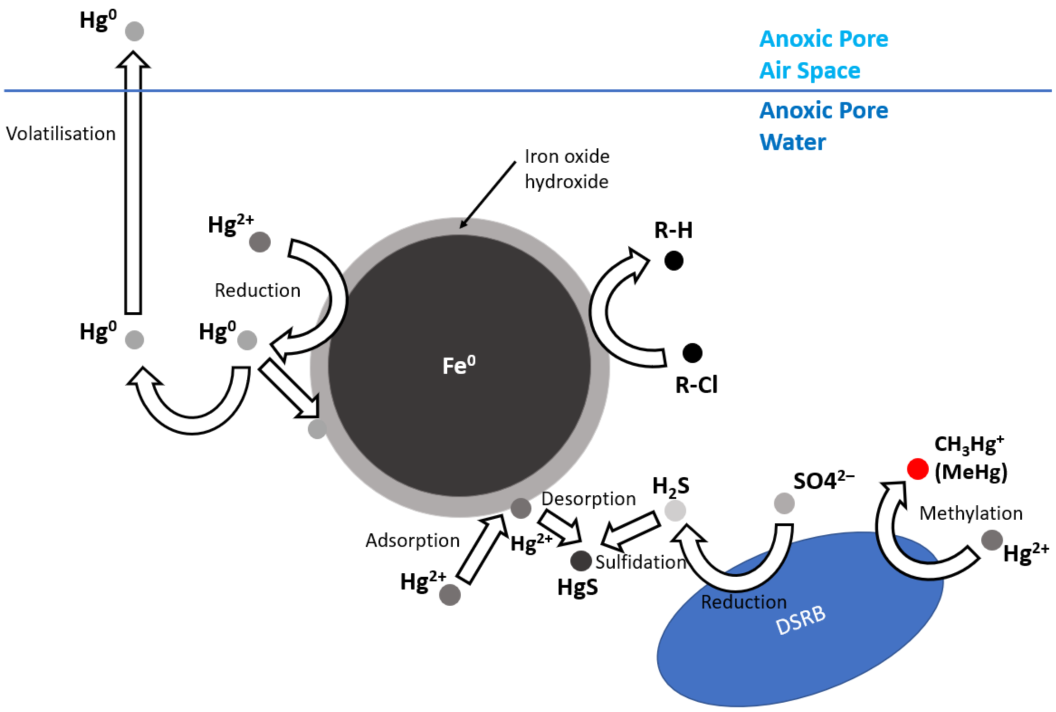

Figure P2-42: Potential Hg reduction, sulfidation and methylation pathways in an anoxic subsurface / groundwater system treated with nZVI (NanoFER25S and Carbo-Iron® treatments).

Desulfomicrobium baculatum DSM 4028 was the most common SRB in NanoFER 25S and Carbo-Iron® EST systems at day 358, making up 4% and 7.5% of the total microbial communities identified, respectively. *Desulfovibrio sulfodismutans strain ThAc* (5.1%) also contributed significantly to the microbial community in the Carbo-Iron® EST system. Previous research has shown *Desulfomicrobium baculatum and Desulfovibrio sulfodismutans* strains to be a Hg-methylating SRB, and they could have influenced the notable net methylation in the Carbo-Iron® EST system (Gilmour et al., 2013; Graham et al., 2012b). *Desulfomicrobium baculatum* may have contributed to the increased MeHg levels in EST treatments system, as it makes up >1% total identified population at day 71 and day 358 in all EST systems. Due to the limited IRB and SRB communities in MLR systems, there is uncertainty regarding potential microbial methylation pathways contributing to net methylation in these systems.

5.4 Conclusion

Experimental work presented here provides insight into the complex biogeochemical interactions between four treatments, in two contrasting anoxic sediment systems, and their impact on solid phase Hg chemical speciation. Geochemical characteristics of sediment matrices appeared to influence Hg(II) sorption capacity, MLR had a lower affinity for Hg(II) than EST sediment. However, addition of iron particle treatments (NanoFER 25S, Carbo-Iron® and biomagnetite) seemed to enhance Hg(II) sorption capacity, notably in MLR sediment systems. Solid phase Hg transformations appeared to be influenced by the type of treatment, sediment matrix characteristics and microbial populations. NanoFER 25S systems reduced >95% Hg(II) to Hg(0) over 28 days in both MLR and EST sediment systems. Hg L_{III}-edge EXAFS linear combination fitting identified that the bulk of solid phase Hg remained reduced for over a year post-treatment. NanoFER 25S was effective at reducing Hg(II) to Hg(0) and maintaining reduced chemical form over longer term. Reduction products may sorb to Fe particle phase, but this may not be a desirable end point given Hg(0) tendency to volatilise to atmosphere. Hg(II) was reduced to Hg(0) in MLR systems with Carbo-Iron® (60%), biomagnetite (60%) and biostimulation with organic electron donors (25%) over the first 28 days post-treatment, with potential chemical and microbial pathways identified. The remainder of the solid phase Hg was either Hg(II) sorbed to sediment components (10 - 50 %) or beta-HgS (20 - 30 %) in these three treatment systems.

However, despite minimal SRB activity, after one year >70% solid phase Hg was identified as beta-HgS in MLR systems treated with Carbo-Iron® and biostimulation, with the bulk of the remaining fraction present as Hg(II) sorbed to sediment. Biomagnetite MLR system was stimulating beta-HgS formation as effectively over one year, ~30% was present as beta-HgS and ~70% mobile sorbed Hg(II). Furthermore, the SRB population had proliferated significantly (>10% total population) by this time point, therefore continued monitoring of inorganic Hg chemical speciation may have revealed more beta-HgS in day 911 samples. Almost 60% solid phase Hg was present as beta-HgS at day 29 in the no treatment MLR system, most of the remaining fraction was Hg(II) sorbed to MLR. 16S rRNA analysis did not detect a significant SRB population (<0.05% total), suggesting beta-HgS was formed without direct influence SRB in the unamended system. >90% Hg had reached the most desirable beta-HgS endpoint after one year in untreated MLR systems, suggesting most Hg(II) added to the anoxic MLR sediment is naturally attenuated as immobile beta-HgS without treatment.

Sulfidation appeared to be a more competitive process than reduction in 4 of 5 EST systems over 28 days following treatment. NanoFER 25S was the only treatment to induce an observable reducing effect in respect to solid phase Hg transformation, almost all (>99%) the Hg(II) was reduced to Hg(0) in day 29 samples. In contrast, almost all (>99%) Hg in day 29 solid phase samples from biomagnetite EST system was beta-HgS. Beta-HgS formation was also significantly enhanced in Carbo-Iron® and biostimulation EST sediment systems, >80% of Hg was present as beta-HgS 28 days following treatment addition, slightly more than the ~70% HgS identified in the no treatment control, with the bulk of the remaining fraction identified as sorbed Hg(II) in these three systems. EST sediment had a much more diverse microbial population than MLR sediment, SRB communities proliferated between day 5 and day 71 in all EST systems, suggesting microbial pathways may play a significant role in HgS sulfidation. The contrasting impacts of Carbo-Iron®, biomagnetite and biostimulation on Hg chemical speciation in the MLR and EST systems over the first month highlights the influence of unique sediment properties, sorbed Hg(II) species were more likely to be reduced in MLR sediment than EST sediment during the early phase of treatment.

Biomagnetite seemed to have to most contrasting effects on Hg chemical speciation in the two sediment systems over the early phase of treatment, reducing >60% Hg(II) in MLR system, but enhancing beta-HgS (>99%) formation in EST system. Natural attenuation seemed to have a consistent beneficial effect independent of sediment type, significant amounts of Hg was transformed to beta-HgS in both no treatment systems. In respect to net Hg methylation, all systems exhibited an increase in MeHg concentration from baseline. However, only Carbo-Iron® seemed to have a notable adverse impact when compared to no-treatment. Microbial activity can often have positive and negative effects in respect to Hg transformation and ecosystem health. SRB may drive HgS formation, as well as stimulate MeHg formation. However, sulfide may induce iron oxide reduction that may mobilise Hg, that is subsequently immobilised as HgS or sorbed to FeS (Poulton, 2003). IRB may drive iron oxide dissolution, not only mobilising sorbed Hg species, but also stimulating MeHg formation.

Previously iron nanoparticles and biostimulation with organic electron donors have been considered suitable for application in saturated groundwater zones and have been used to remediate organic contaminants and redox active metals, such as Cr (VI), in field or pilot-scale projects (Newsome et al., 2019). However, prospective remediation treatments may have an adverse impact – potentially inhibiting Hg immobilisation (e.g. sulfidation) or remobilising Hg (e.g. reduction) in some sediments. Iron nanoparticles should be applied to anoxic groundwater and lagoons with caution in systems containing mobile Hg(II) due to their ability to reduce to volatile Hg(0), atmospheric release could cause further contamination on a regional to global scale. NanoFER 25S seemed to pose the greatest risk, capable of inducing and maintaining reducing condition over a long period independent of sediment type, capable of not only reducing mobile sorbed Hg(II), but also existing immobile beta-HgS in MLR sediment.

Longer term monitoring of Hg chemical speciation (incl. MeHg) is required to better establish cost-benefit of treatments. Future work should be done to investigate the stability of solid phase Hg and better understand phase portioning of elemental Hg(0) within the system by including headspace monitoring of GEM. Column experiments may also help better establish particle mobility through a subsurface sediment system, and subsequent impacts on Hg chemical speciation and biogeochemical parameters at different depths. This research highlights the importance of considering not only the type of iron nanoparticle or biostimulation treatment, but also the individual site conditions (e.g. chemical composition of a sediment matrix, physical conditions, microbial community diversity, presence of additional contaminants) when considering applying treatments *in situ*. Despite potential beneficial immobilising effects in respect to one contaminant under specific site conditions, intervention may have potentially adverse effects in respect to (re)mobilisation of other contaminants. This highlights the importance of tailoring approaches during site risk assessment and remediation efforts, any intervention should be carefully monitored to ensure adverse effects are not being stimulated over the longer term.

Acknowledgements

We thank EPRSC, WSP and Akzo Nobel for funding under a PhD CASE award. We acknowledge beamtime awarded at the Diamond Light Source for XANES and EXAFS on the I20 beamline under proposals SP18794 and SP21441. We thank Shu Hayama and Frederick Mosselmans for their assistance on I20 at Diamond Light Source.

We thank the Karren Jackson (Canals and Rivers Trust) for allowing access to the site for collection of MLR sediment samples. We thank Faraaz Ahmed for collection of EST sediment. We thank Paul Lythgoe and Alastair Bewsher (Manchester Analytical Geochemistry Unit, University of Manchester) for ICP-MS, XRF, LOI and IC analysis. We thank John Waters (Mineral Analysis Facility, University of Manchester) for his assistance with XRD analysis. We thank PS Analytical for their assistance with MeHg analysis.

5.5 Paper 2: Supplementary Information

5.5.1 Section 1: Biomagnetite Characterisation by XRD

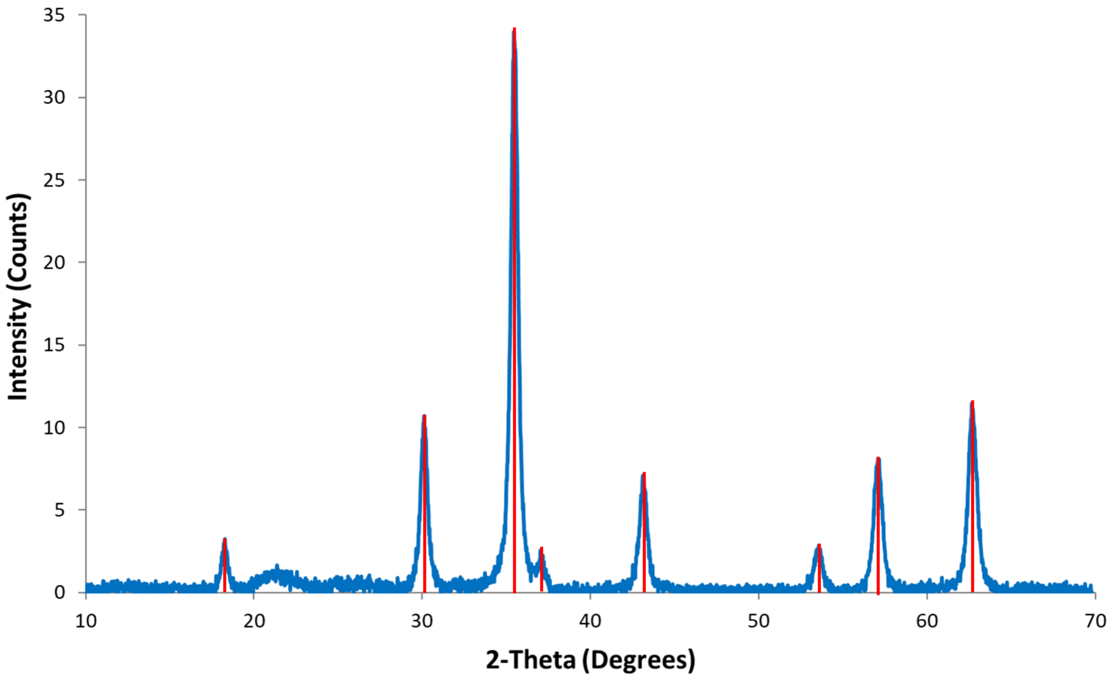

Figure P2-43: XRD spectra and biomagnetite peak fit [major peaks at 18.3, 30.1, 35.4, 37.1, 43.2, 53.4, 56.9, 62.5 degrees]

5.5.2 Section 2: Hg L_{III}-edge XANES Spectra for Hg Standards

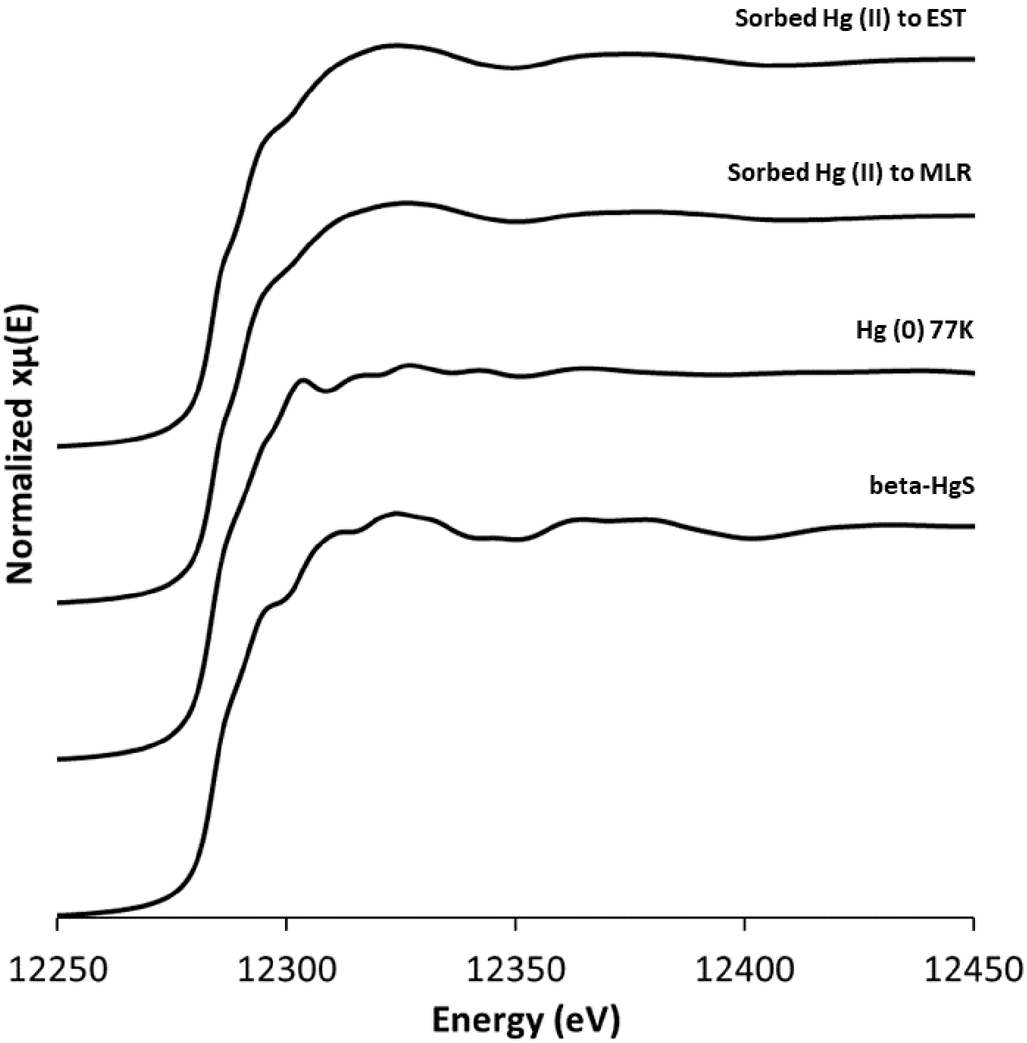

Figure P2-44: Hg L_{III}-edge XANES spectra for Hg standard materials used for linear combination fitting,

5.5.3 Section 3: Hg L_{III} Edge XANES Spectra for Solid Phase Samples from MLR Treatment Systems

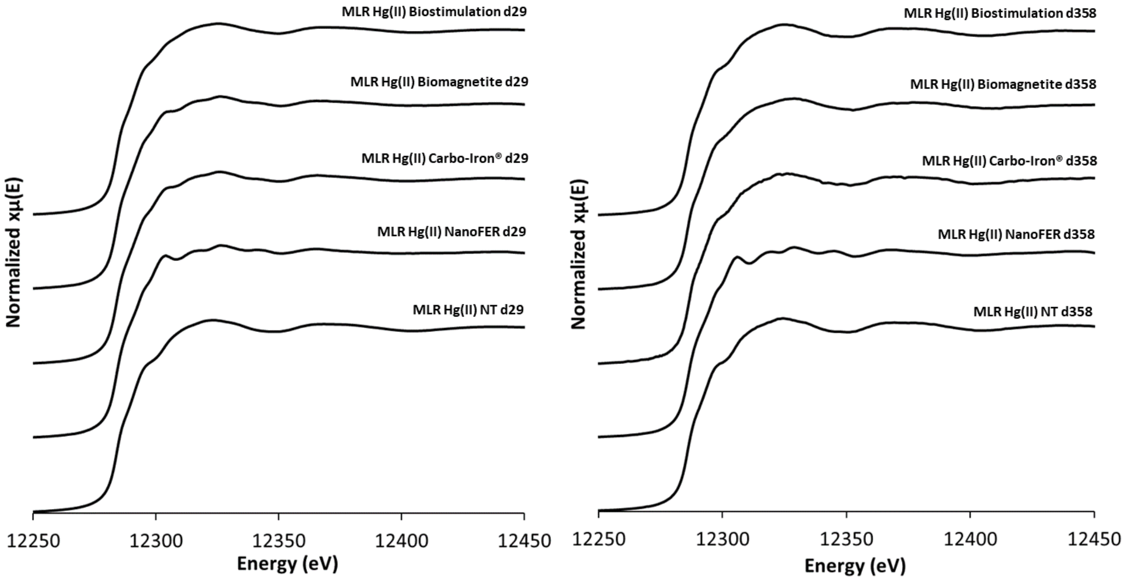

Figure P2-45: Hg L_{III}-edge XANES spectra for solid samples from MLR treatment system at (a) day 29 and (b) day 358.

5.5.4 Section 4: Hg L_{III} Edge XANES Spectra for Solid Phase Samples from EST Treatment Systems

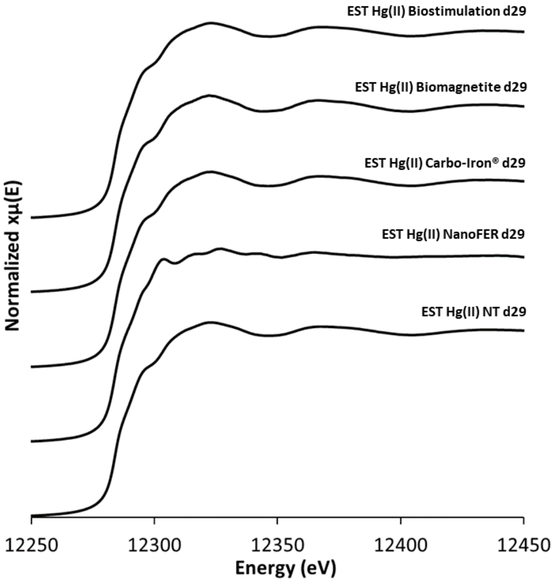

Figure P2-46: Hg L_{III}-edge XANES spectra for solid samples from EST treatment systems at day 29.

5.5.5 Section 5: Hg L_{III}-edge EXAFS Spectra for Hg Standards and Structural Model Fits

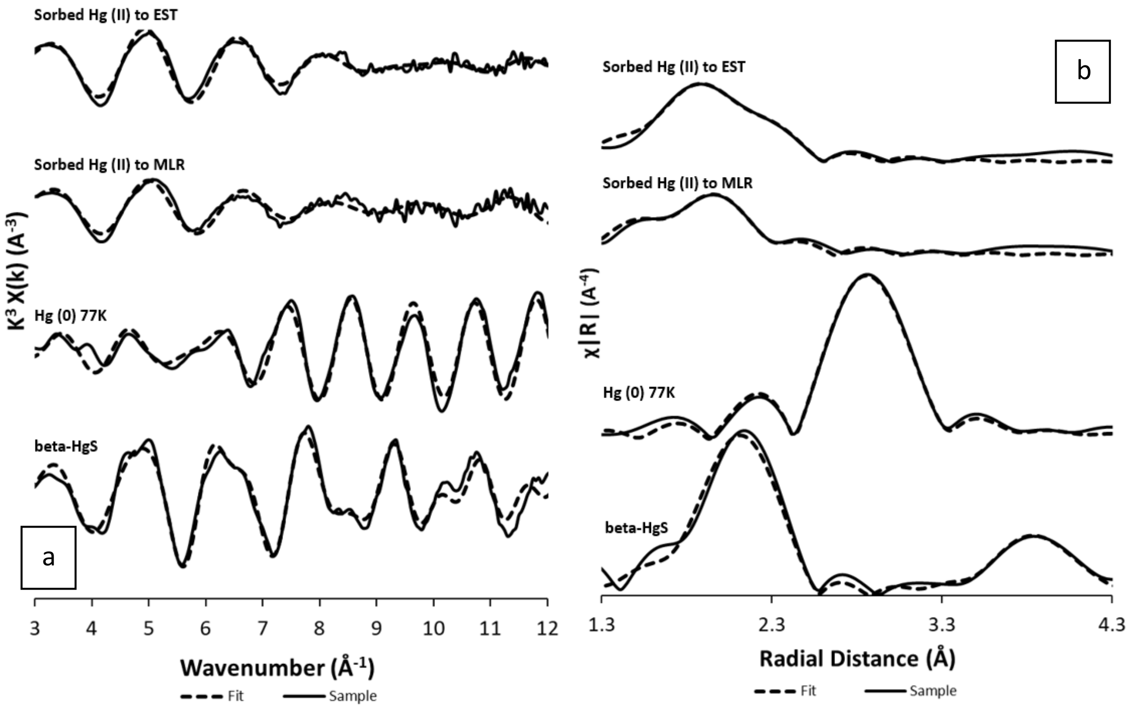

Figure P2-47: Hg L_{III}-edge XAS spectra for Hg standard materials used for linear combination fitting (a) K^3-weighted EXAFS spectra, and (b) Fourier transform of K^3-weighted EXAFS spectra for Hg standard data (solid lines) and their corresponding model fit data (dashed line).

Table P2-10: Fitting parameters for the EXAFS data for Hg Standards shown in Figure P2-47. CN denotes the coordination number; R denotes the atomic distances; σ^2 denotes the Debye-Waller factor; S_0^2 denotes the amplitude factor, E_0 denotes the shift in energy from the calculated Fermi level.

Standard	Path	CN	R (Å)	σ^2 (Å^2)	E_0	S_0^2	Reduced χ^2	R-factor
Sorbed Hg(II) to	O1	1.1	2.17	0.0123	9.68 ± 1.02	1	48.6	0.0014
EST sediment	Cl1	0.9	2.41	0.0056				
(R = 1.5 to 3.5)	S1	0.5	2.58	0.0018				
Sorbed Hg(II) to	O1	0.9	2.10	0.0073	9.41 ± 1.36	1	41.8	0.0049
MLR sediment	Cl1	0.5	2.41	0.0007				
(R = 1.4 to 3.4)	Cl2	0.3	2.57	0.0005				
Hg(0) 77 K	Hg1	2.0	2.81	0.0237	2.14 ± 1.07	0.9	71.2	0.0014
(R = 1.9 to 3.9)	Hg2	5.0	2.97	0.0061				
Beta-HgS	S1	4.0	2.53	0.0086	8.58 ± 0.82	0.8	2181.0	0.0188
(R = 1.5 to 4.5)	Hg1	12	4.14	0.0113				
	S2	12	4.78	0.0144				

XAS at the Hg L_{III}-edge (12,284 eV) allowed collection of high-quality data to k = 13 from most solid phase samples (sediment and treatment) taken from MLR (day 1, day 29, day 358) and EST (day 1, day 29) treatment systems. Day 1 samples were taken 24 hours after microcosm setup (prior to treatment addition), and therefore could be considered representative of a natural system such as a lagoon or a canal which has had a recent input from a highly contaminated groundwater plume. At this point, we assumed that the bulk of the added Hg(II) had sorbed to components of the sediments and had not undergone any significant chemical changes (e.g. sulfidation, reduction and volatilisation), therefore day 1 (pre-treatment) samples from respective systems have been used as a proxy for Hg(II) sorbed to MLR and Hg(II) sorbed to EST standards. MLR sediment contained existing Hg(~73 mg/kg beta-HgS, ~13 mg/kg sorbed Hg(II), ~75 µg/kg MeHg), whereas EST sediment did not contain any detectable Hg. The bulk of the solid phase Hg in day 1 MLR samples (~420 mg/kg) is sorbed Hg(II), alongside ~73 mg/kg beta-Hg, therefore we must assume that ~15% Hg in Hg(II) sorbed to MLR standard is from the existing beta-HgS contribution. However, we can assume that all the solid phase Hg (~460 mg/kg) in day 1 EST samples is sorbed Hg(II), therefore the Hg(II) sorbed to EST standard does not have any significant contribution from other Hg species.

5.5.6 Section 6: Hg L_{III}-edge EXAFS Spectra for Solid Phase Samples from MLR Treatment Systems and Corresponding Linear Combination Fits

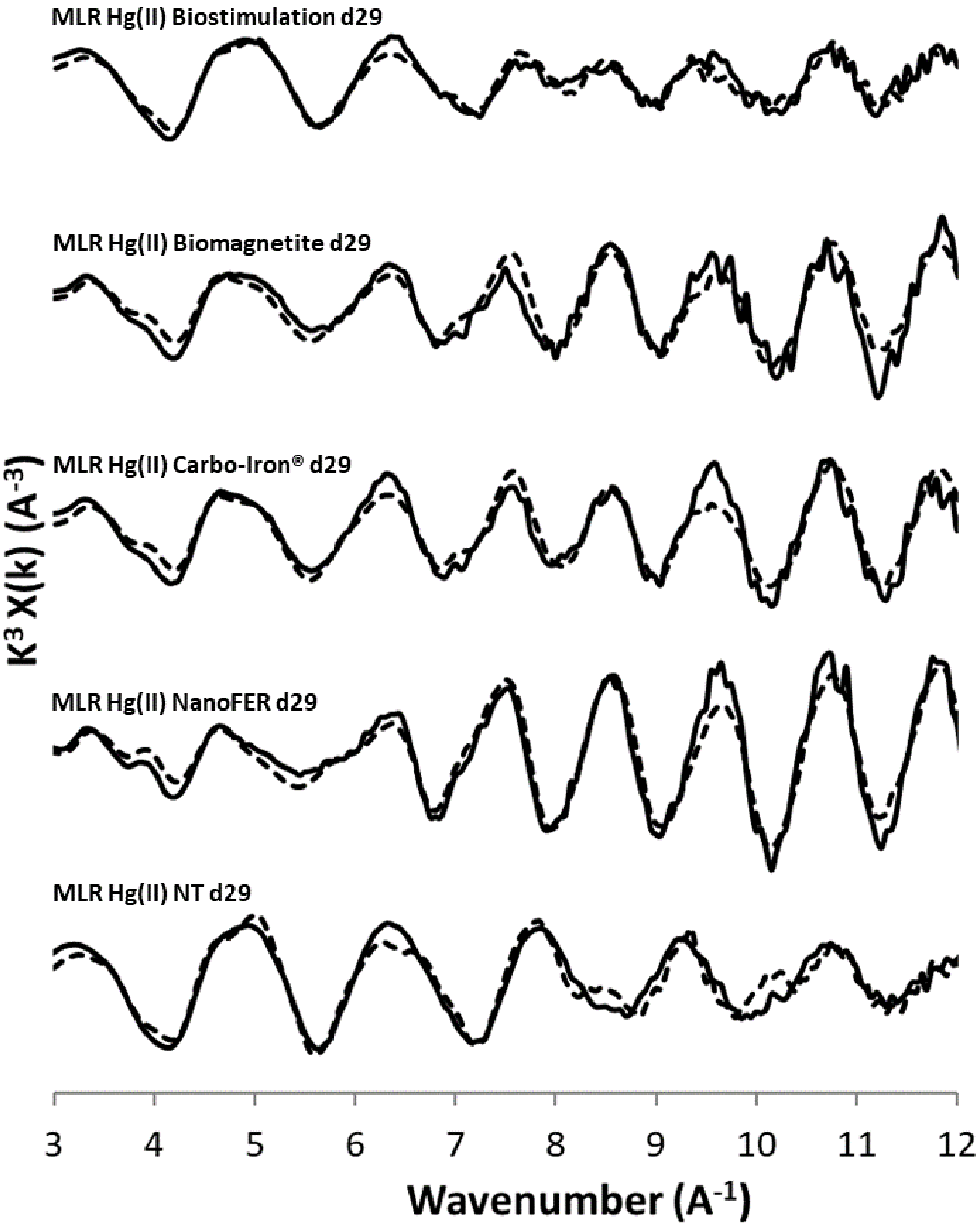

Figure P2-48: Hg L_{III}-edge EXAFS spectra for solid samples from MLR treatment system at day 29 (solid line) and the corresponding linear combination fit spectra (dashed line) (K = 3 – 12).

Table P2-11: Statistical goodness-of-fit parameters for linear combination fits (K = 3 – 12) of Hg L_{III}-edge EXAFS spectra for solids from MLR treatment systems at day 29.

Treatment System	Time Point	R-factor (R)	Chi-square (χ^2)	Reduced chi-square
MLR Hg(II) No Treatment (NT)	Day 29	0.0996	27.25	0.1514
MLR Hg(II) NanoFER 25S	Day 29	0.0797	41.65	0.2314
MLR Hg(II) Carbo-Iron	Day 29	0.1366	39.61	0.2213
MLR Hg(II) Biomagnetite	Day 29	0.1639	46.38	0.2591
MLR Hg(II) Biostimulation	Day 29	0.1109	15.97	0.0892

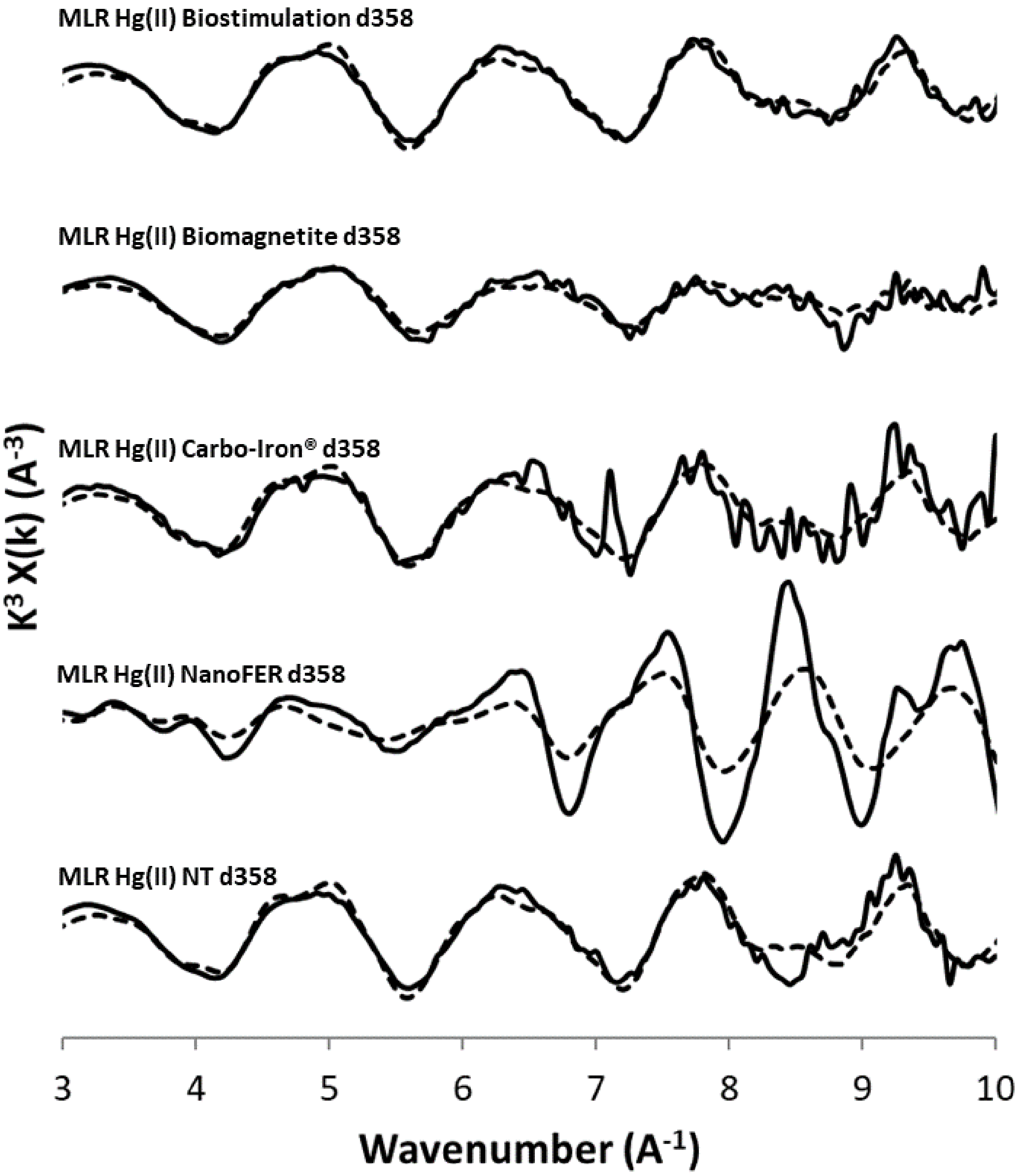

Figure P2-49: Hg L_{III}-edge EXAFS spectra for solid samples from MLR treatment system at day 358 (solid line) and the corresponding linear combination model fit (dashed line) (K = 3 – 10).

Table P2-12: Statistical goodness-of-fit parameters for linear combination fits (K = 3 – 10) of Hg L_{III}-edge EXAFS spectra for solids from MLR treatment systems at day 358.

Treatment System	Time Point	R-factor (R)	Chi-square (χ^2)	Reduced chi-square
MLR Hg(II) No Treatment (NT)	Day 358	0.1380	66.93	0.4781
MLR Hg(II) NanoFER 25S	Day 358	0.3839	425.48	3.0610
MLR Hg(II) Carbo-Iron	Day 358	0.3379	156.02	1.11
MLR Hg(II) Biomagnetite	Day 358	0.2081	39.32	0.2808
MLR Hg(II) Biostimulation	Day 358	0.0677	24.94	0.1781

5.5.7 Section 7: Hg L_{III}-edge EXAFS Spectra for Solid Phase Samples from EST Treatment Systems and Corresponding Linear Combination Fits

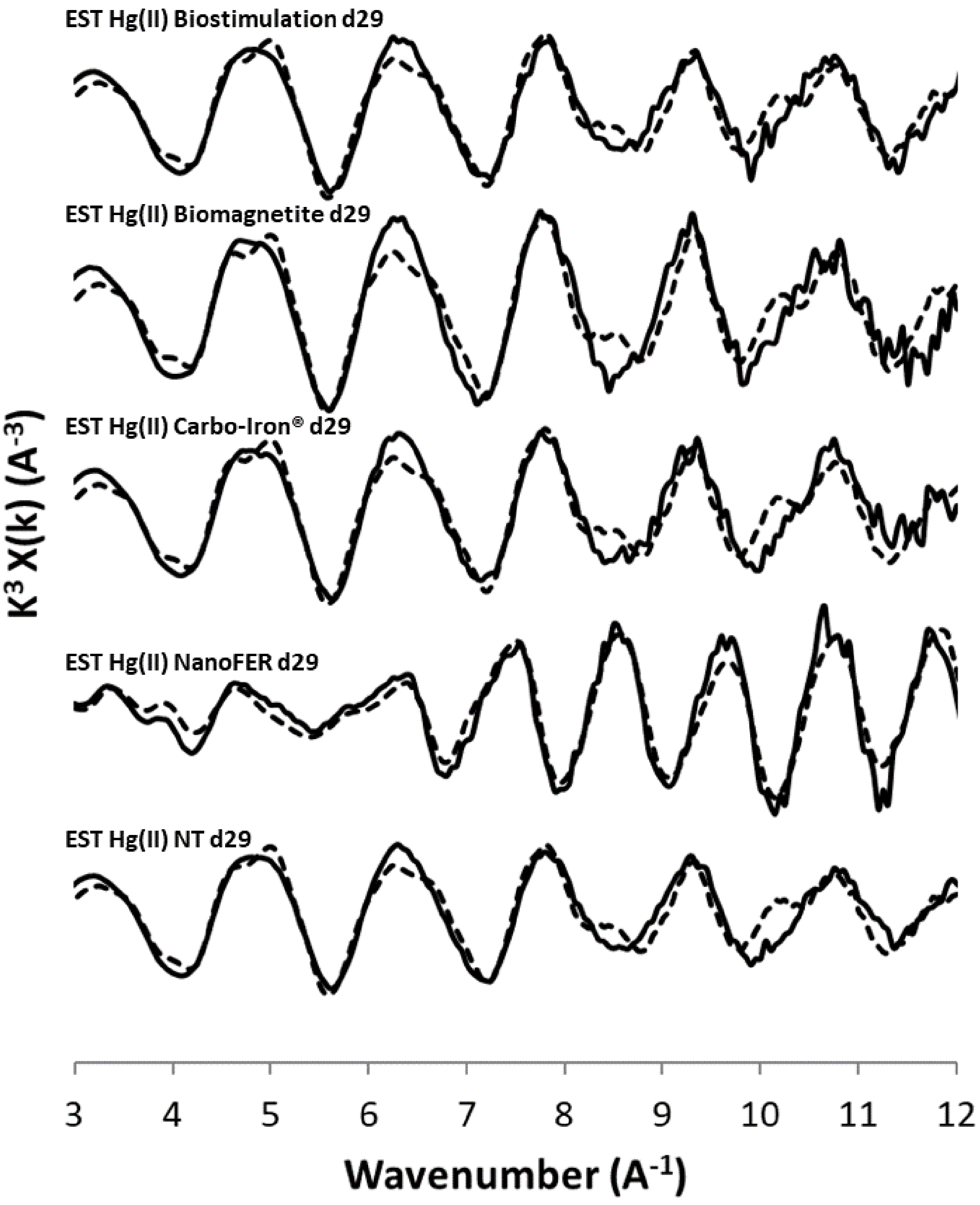

Figure P2-50: Hg L_{III}-edge spectra for solid samples from EST treatment system at day 358 (solid line) and the corresponding linear combination model fit (dashed line) (K = 3 – 12).

Table P2-13: Statistical goodness-of-fit parameters for linear combination fits (K = 3 – 12) of Hg L_{III}-edge EXAFS spectra for solids from EST treatment systems at day 29.

Treatment System	Time Point	R-factor (R)	Chi-square (χ^2)	Reduced chi-square
EST Hg(II) No Treatment (NT)	Day 29	0.1210	51.51	0.2862
EST Hg(II) NanoFER 25S	Day 29	0.0985	58.45	0.3266
EST Hg(II) Carbo-Iron	Day 29	0.1328	74.88	0.4160
EST Hg(II) Biomagnetite	Day 29	0.1544	124.18	0.6937
EST Hg(II) Biostimulation	Day 29	0.1035	50.56	0.2809

5.5.8 Section 8: XRF and LOI Sediment Major Components

Table P2-14: Major elemental components (>0.1% total mass) of MLR sediment determined by XRF and LOI analysis.

Major Component	Percentage Total Mass (%)
SiO_2	2.30
Al_2O_3	0.96
Fe_2O_3	0.70
MgO	7.29
CaO	39.51
Na_2O	3.84
K_2O	0.11
P_2O_5	0.14
SO_3	1.11
Cl	3.14
F	0.12
LOI (H_2O)	1.20
LOI (CO_2)	39.39

Table P2-15: Major elemental components (>0.1% total mass) of EST sediment determined by XRF and LOI analysis.

Major Component	Percentage Total Mass (%)
SiO_2	52.39
Al_2O_3	13.14
Fe_2O_3	5.33
MgO	3.03
CaO	6.77
Na_2O	1.87
K_2O	2.73
TiO_2	0.74
P_2O_5	0.34
MnO	0.21
SO_3	0.55
Cl	1.24
LOI (H_2O)	1.11
LOI (CO_2)	10.37

5.5.9 Section 9: THg and MeHg in Baseline Sediment and Endpoint Solid Phase Samples from Treatment System

Table P2-16: THg and MeHg concentrations at baseline (before microcosm setup) and in endpoint solids from treatment systems.

Microcosm	Solid Phase Sample (Sediment / treatment)	Day	MeHg (µg/kg)	THg (mg/kg)	THg Percentage Recovery (%)
N/A	MLR Baseline [Before addition of treatment and Hg(II)]	0	34	81	N/A
A	MLR NanoFER 25S	911	44	183	48
B	MLR Carbo-Iron®	911	252	319	89
C	MLR Biomagnetite	911	46	263	67
D	MLR Biostimulation	911	80	385	75
E	MLR No Treatment	911	92	500	98
N/A	EST Baseline [Before addition of treatment and Hg(II)]	0	0	0	N/A
F	EST NanoFER 25S	911	7	39	11
G	EST Carbo-Iron®	911	121	85	27
H	EST Biomagnetite	911	67	294	82
I	EST Biostimulation	911	65	284	60
J	EST No Treatment	911	64	399	87

5.5.10 Section 10: Changes to the Bacterial Population in Treatment Systems

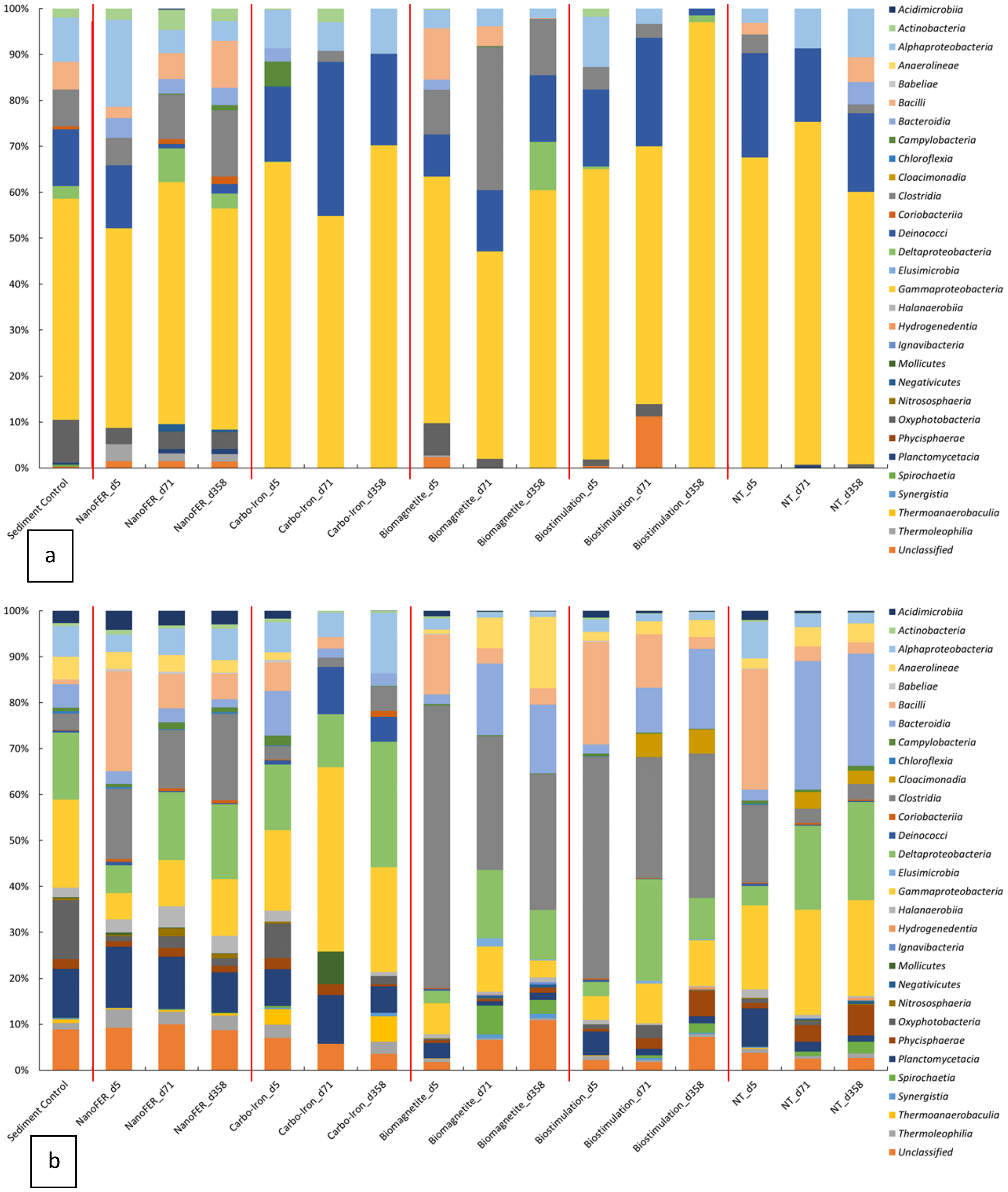

Figure P2-51: Proportions of bacterial phyla identified (>0.1% total population) in sediment by 16S rRNA sequencing in EST control and day 5, day 71 and day 358 samples from (a) MLR and (b) EST treatment systems.

Gammaproteobacteria was the most abundant phylum at all sampling time points in all MLR treatment systems, varying between 43.2% (NanoFER 25S day 5) and 96.0% (Biostimulation day 358) of the total population identified. The Burkholderiaceae family dominated the community identified in samples throughout MLR no treatment system, increasing in dominance from day 5 (44.4%) to day

71 (71.1%) before reducing in dominance by day 358 (42.8%). Similarly, Burkholderiaceae were the most prevalent family identified in samples from MLR Carbo-Iron® treatment system [day 5 (62.2%), day 71 (53.3%), day 358 (54.5%)], making up over the half the identified population in all samples. In MLR NanoFER 25S treatment systems Burkholderiaceae were the most common family identified in day 5 samples. However, at day 71 the population was dominated by organisms from the Halomonadaceae (22.0%) and Pseudomonadaceae (22.6%) families, which continued to be the most prevalent families identified in day 358 samples, with Pseudomonadaceae and Halomonadaceae making up 18.8% and 9.6% of the identified population, respectively. Halomonadaceae were the most widespread family of microorganisms identified in day 5 (37.9%) samples from MLR biomagnetite treatment systems, Burkholderiaceae were most prevalent in day 71 (37.9%) and day 358 (47.6%) samples. Burkholderiaceae dominated the population at day 5 (52.6%) and day 71 (29.1%) in biostimulation treatment system, halophilic Halomonadaceae were most prevalent by day 358 (82.1%).

Deltaproteobacteria and Gammaproteobacteria were the most abundant phyla in EST Carbo-Iron® treatment systems. Clostridia dominated biomagnetite treatment systems at day 5 (61.4% of total population identified), dominance decreased over time as population became more diverse, Deltaproteobacteria and Bacteroidia became more prevalent in day 71 and day 358 samples. Similarly, Clostridia dominated biostimulation treatment systems at day 5 (48.1% of total population identified). However, despite a reduction in contribution to total population at later time points, it continued to be the most abundant phylum in day 71 (26.2%) and day 358 (31.2%) samples. EST NanoFER 25S treatment system appeared to have most clear shift in community dominance over the duration of the experiment. Bacilli were the most prevalent phylum at day 5 (21.8%), Deltaproteobacteria were most abundant at day 71 (14.8%), and by day 358 (18.8%) Clostridia made up the largest portion of the population. Bacilli were most abundant in EST no treatment system at day 5 (26.2%), Bacteroidia made up largest portion of population at day 71 (27.9%) and day 358 (24.4%). Gammaproteobacteria represented a significant portion (18.3% – 22.8%) of the population at all sampling time points of EST no treatment system.

Family XII [Order Bacillales] organisms were the most prevalent at day 5 (13.0%) in EST no treatment system, Flavobacteriaceae became more widespread at later time points, making up 20.2% and 12.3% total population identified in day 71 and day 358 samples, respectively. Clostridiaceae dominated the microbial community at day 5 (30.6%) in EST biostimulation systems. However, in day 71 samples Family XII [Order Clostridiale] (10.3%), Paenibacillaceae (9.1%) and Desulfobulbaceae (9.2%) made up similar portions of the total population. Day 358 sample from EST biostimulation system identified another shift in the population, Bacteroidetes vadinHA17 (11.4%), Peptococcaceae (11.0%) and Clostridiaceae (9.9%) were the most extensive families of organisms identified. Carnobacteriaceae and Family XII [Order Bacillales], despite only representing 3% and 2.8% of the total population respectively, were the most abundant family identified in Carbo-Iron® day 5 samples. However, at day 71, Burkholderiaceae (17.2%) and Thermaceae (10.3%) had become more dominant in the population. Despite a reduction in proportion of the total population, Burkholderiaceae (7.7%) remained the most highly represented family identified in day 358 samples, Desulfomicrobiaceae (7.5%), Desulfovibrionaceae (5.1%) and Thermoanaerobaculaceae (5.6%) were also well represented at this time point. Family XII [Order Bacillales] (13.2%) made up the greatest proportion of the population at day 5 in EST NanoFER 25S system. Halanaerobiaceae (4.0%), Family XII [Order Bacillales] (3.7%) and Desulfomicrobiaceae (3.2%) were the most abundant families identified in day 71 samples. Day 358 samples identified another shift in the community, with SRB2 [Order Thermoanaerobacterales] (6.7%) becoming the most represented family, along with Desulfomicrobiaceae (4.0%) and Bacillaceae (3.7%). Clostridiaceae were dominant at day 5 (36.3%) in EST biomagnetite systems, they continued to constitute a significant portion of the community at day 71 (12.1%) and at day 358 (16.3%). Bacteroidetes vadinHA17 also made up a major portion of the population at day 71 (12.1%) and at day 358 (12.7%).

6.0 Paper 3: Investigating the impacts of Cu-coated iron-based nanoparticles on chemical speciation and potential mobility of Hg in artificial groundwater.

Alexander Tait[a]*, Rick Kimber[a], Samuel Shaw[a], Yue Wang[a], David Polya[a], Russell Thomas[b], Jonathan R. Lloyd[a].

[a]Williamson Research Centre for Molecular Environmental Science, Department for Earth and Environmental Science, The University of Manchester, Manchester, M13 9PL, United Kingdom

[b]WSP, Kings Orchard, 1 Queen St, Bristol, BS2 0HQ, United Kingdom

*corresponding author e-mail address: alexander.tait@manchester.ac.uk

Keywords

Mercury amalgamation

Hg remediation

Hg chemical speciation

Contaminated water treatment

Abstract

This research aimed to produce a refractory Cu-Hg amalgam ($HgCu_{AM}$) from reduction of Cu(II) and Hg(II) in batch artificial groundwater (AGW) microcosms. Iron-based nanoparticles [biomagnetite and nZVI (NanoFER 25S)] and Cu-coated iron based-nanoparticles (Cu-biomagnetite and Cu-NanoFER 25S) were added to anoxic AGW contaminated with Hg(II) [and Cu(II) in treatment systems not containing Cu-coated particles]. Hg chemical speciation and potential mobility of Hg and Cu in endpoint solids were investigated. Hg and Cu were rapidly removed from aqueous phase following addition of all particle treatments. Hg L_{III}-edge EXAFS revealed that a solid phase $HgCu_{AM}$ formed following addition of Cu-coated NanoFER 25S or Cu-coated biomagnetite to AGW contaminated with aqueous Hg(II) [Cu-NanoFER 25S Hg(II) or Cu-biomagnetite Hg(II) systems], or NanoFER 25S to AGW containing aqueous Hg(II) and Cu(II) [Cu-NanoFER 25S Hg(II) Cu(II)]. Sequential extraction recovery data suggested $HgCu_{AM}$ formed in Cu-biomagnetite Hg(II) microcosms may be less stable than that formed in the Cu-NanoFER 25S Hg(II) and NanoFER 25S Hg(II) Cu(II) systems. SEM imaging and EDS mapping of Cu-biomagnetite Hg(II) samples revealed that the $HgCu_{AM}$ phase may not be associated with the Fe particle surface. Extraction and imaging data suggested that multiple Cu species may have formed in Cu-biomagnetite microcosms. Hg and Cu recovery was lowest in extracts from $HgCu_{AM}$ formed in Cu-containing NanoFER 25S systems. Moreover, recovery was lowest for both Hg [50%] and Cu [43%] from endpoint solid phase extracts from the Cu-NanoFER 25S Hg(II) systems, likely due to the formation of a more

stable and immobile $HgCu_{AM}$ phase. However, due to the volatility of Hg(0) there is some uncertainty regarding whether the bulk of residual Hg is associated with Cu as a recalcitrant alloy or whether some gaseous Hg(0) may have been emitted to the headspace. SEM and EDS revealed there may be an interaction between Hg, Cu and Fe at the particle surface in endpoint solids from the Cu-NanoFER 25S Hg(II) systems. There are concerns over the long-term fate and eco-toxicity of nanoscale treatment technologies in environmental systems. Therefore, these newly developed Cu-biomagnetite and Cu-NanoFER25S particles maybe more easily applied as treatment for Hg-contaminated wastewater in the shorter term.

6.1 Introduction

There is concern regarding the potential health implications associated with the anthropogenic release of highly toxic mercury (Hg) into the environment. Many industrial activities contribute to release of Hg into the environment, these include fossil fuel combustion, Hg-mining, artisanal and small-scale gold (Au) mining, chlor-alkali chemical production via Hg electrolysis, cement manufacture, waste management, and additional non-ferrous metal production (J. Wang et al., 2012). Due to its widespread application, Hg is frequently encountered in polluted soils in industrial areas and hazardous waste sites (Huttenloch et al., 2003). Mitigating the adverse environmental and human health impacts associated with Hg-contamination through increased investment into research and development of cost-effective remediation options is essential. Globally, releases of Hg directly to water may be the largest contributor to freshwater Hg levels (UNEP, 2019). There are strong regulatory drivers that require Hg removal as part of the wastewater treatment prior to discharge (Hargreaves et al., 2016). This has created demand for the innovation of novel effluent treatment techniques to reduce release of Hg into the environment from industrial activities and immobilise Hg associated with legacy environmental contamination. Development and evaluation of new materials for the removal of Hg from contaminated water remains a focus for application in water treatment and groundwater remediation technologies (Huttenloch et al., 2003).

Iron-based nanomaterials have received broad attention as potential remediation technologies for controlling Hg pollution via sorption mechanisms, as they are low cost, more environmentally friendly, have high reactivity, and they are controllable through modulating particle morphology and surface properties (Gong et al., 2019). Iron and iron mineral particles [e.g. Zero Valent Iron (ZVI), iron oxides (e.g. Fe_3O_4) and iron sulphides (e.g. FeS)] have previously shown capacity for Hg removal from water and immobilisation in sediment (Gong et al., 2019; Lewis et al., 2016; Vélez et al., 2016; Vernon and Bonzongo, 2014; Xiong et al., 2009). Iron-based nanoparticles with magnetic properties can make particle and contaminant recovery from treatment systems more straight forward (Kimber et al., 2019; Phenrat and Kumloet, 2016; Zargoosh et al., 2013). Particle size distribution and aggregation state are important parameters to evaluate before deploying nanoparticles for remediation. Previous work found that nanoscale ZVI particles (nZVI) has a higher adsorption capacity for ionic Hg than ZVI in wastewaters (Vernon and Bonzongo, 2014).

Ferrous [Fe(II)] and ferric [Fe(III)] formed during the dissolution of Fe(0) can form an iron oxide-hydroxide shell around the Fe(0) core, supporting the idea that there is a core-shell model for ZVI particles (see Section 2.10.2). Products of ZVI corrosion contribute to the reductive transformation and/or physical removal (sorption or enmeshment) of contaminant chemical species (see Section

2.10.2). Aqueous corrosion of ZVI under anoxic conditions can enhance contaminant immobilisation as there can be significant destabilisation of equilibrium conditions, due to the formation of gaseous H_2 and aqueous OH^- (Crane and Scott, 2012). Equation 1 summarises the Hg(II) reduction reaction in anoxic systems containing ZVI.

$Hg^{2+} (s) + Fe^0 (s) \rightarrow Hg^0 (l) + Fe^{2+} (s)$ Equation 1

Magnetite (Fe_30_4) is a common naturally occurring mineral, containing both Fe(II) and Fe(III), that is widely deposited in soils and aquatic sediments (Liu and Wiatrowski, 2018). Biogenic magnetite (biomagnetite) can be synthesised by a range of bacterial species, these include *Geobacter sulfurreducens*, which has been proven capable of large-scale biomagnetite production with control over nanoparticle size (Byrne et al., 2015; Byrne et al., 2011).

A potential reaction mechanism for the successively reduction of Hg(II) to Hg(I) and Hg(II) by Fe(II) in magnetite is shown in Equation 2 and Equation 3 (Raposo et al., 2000).

$Hg^{2+} + Fe^{2+} \rightarrow Hg^+ + Fe^{3+}$ Equation 2

$Hg^+ + Fe^{2+} \rightarrow Hg^0 + Fe^{3+}$ Equation 3

Newly developed Fe_3O_4-Ag^0 nanocomposites were more effective than Fe_3O_4 at removing Hg(II) from water in recent research. The complex removal mechanism involved Hg(II) adsorption and reduction, Fe(II) and Ag(0) oxidation accompanied with reactions of Cl^- with Hg(I) and Ag(I) (Inglezakis et al., 2020)..

However, there are still knowledge gaps relating to long-term stability of the immobilised Hg and the molecular-level reaction mechanisms between iron-based particles and Hg (Gong et al., 2019). Existing technologies that attempt to reduce Hg(II) often require costly gaseous capture mechanisms due to the atmospheric risk posed by volatile Hg(0) (Mahbub et al., 2016). Batch studies have shown that Hg volatilisation rates were faster for Hg-contaminated deionised water (DIW) containing nZVI than those with ZVI. The amount of Hg volatilised was the same from more chemically complex Hg-contaminated wastewater treated with both ZVI and nZVI (Vernon and Bonzongo, 2014). Nevertheless, the amount of Hg volatilised from wastewater represented ~1% of total Hg (THg), but up to 10% of THg dissolved in DIW (Vernon and Bonzongo, 2014). These observations were of importance, as they showed that Hg volatilisation is influenced by both water chemistry and particle surface area.

Previous work has revealed the formation of colloidal metallic Cu particles containing Hg under low sulfate conditions or prior to the onset of sulfate-reduction, structural analysis suggested that Hg had substituted for Cu in the metallic Cu nanoparticles (Hofacker et al., 2013). There are two naturally occurring morphologies of the intermetallic alloy Cu_7Hg_6, these are Belendorffite and Kolymite (Bernhardt and Schmetzer, 1992; Markovo, 1982).

Novel bimetallic Cu-Fe nanoparticles have been developed previously for us as a recoverable heterogeneous catalyst for the azide-alkyne ‘click chemistry’ reaction in water (Hudson et al., 2012). Recently, nanoscale biomagnetite particles were applied to recover Cu from whiskey distillery waste and subsequently support Cu catalysed azide-alkyne cycloaddition, magnetic recovery made separation for reuse and recycling simpler (Kimber et al., 2019). Figure P3-52 shows a mechanism for the selective formation of high value Cu(0)-bearing nanoparticles from acidic wastewater treated with nZVI [Equation 4], with potential application as an upscaled process for Cu(II) in wastewater (Crane and Sapsford, 2018).

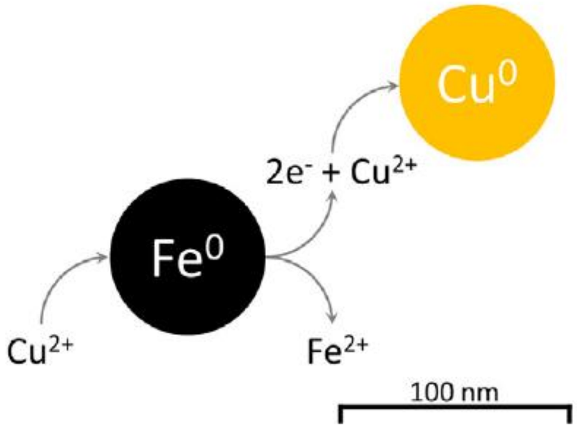

Figure P3-52: Diagrammatic representation for the reaction between aqueous Cu^{2+} and Fe^0 in ZVI nanoparticles (Crane & Slapsford 2018).

$Fe^0 + Cu^{2+} \rightarrow Fe^{2+} + Cu^0$ $E^0 = 0.78$ V Equation 4

Huttenloch et al. (2003) used elemental Cu(0), in the form of shavings, to remove Hg(II) from aqueous solution via adsorption, reduction and amalgamation processes. Cu(0) was able to build a stable intermetallic alloy with toxic Hg(0), formed by reduction of Hg(II) at the Cu(0) particle surface [Equation 5] (Huttenloch et al., 2003). Alloys containing Hg are commonly referred to as amalgams, and they have historically been widely used in dentistry to form resistant solid materials to fill teeth cavities. Aqueous Hg(II) can be reduced to Hg(0) by Cu(0), which forms a Cu-Hg amalgam ($CuHg_{AM}$) with additional Cu(0) atoms [Equation 6], the amount of Cu(II) released corresponds to amount of Hg(0) bound to the Cu(0) particles (Huttenloch et al., 2003).

$Hg^{2+} + Cu^0 \rightarrow Hg + Cu^{2+}$ $E^0 = 0.51$ V Equation 5

$Hg^0 + Cu^0 \rightarrow CuHg_{AM}$ Equation 6

This research work has the aim of producing a $CuHg_{AM}$ from Fe(0)- and Fe(II)-mediated reduction of Cu(II) and Hg(II) at the particle surface. Batch treatment systems were setup to investigate the impact of iron-based nanoparticles (biomagnetite and nZVI) and Cu-coated nanoparticles on Hg chemical speciation and potential mobility of Hg and Cu, in anoxic artificial groundwater (AGW) containing aqueous Hg(II) [and Cu(II)].

6.2 Materials and Methods

6.2.1 Materials

NanoFER 25S (nZVI product) was provided as a slurry for research purposes by Nano Iron (Czech Republic). Suspension contained ~20% (w/w) Fe, a nZVI core encased in a permeable iron oxide-hydroxide shell (NanoFER 25S SDS). Biomagnetite (Fe_3O_4) particles were produced in the Williamson Research Centre (Manchester, UK) laboratories, the methodology for the synthesis process is outlined in Paper 2 (Section 5.2.2). Previous characterisation of particle size revealed an average particle size of 13.3 ± 0.6 nm (Byrne et al., 2011). Biomagnetite structure was confirmed by XRD, a spectrum for the biomagnetite used in the treatment experiments is presented in Figure P3-59 (in the SI). Cu-coated NanoFER 25S (Cu-NanoFER 25S) and Cu-coated biomagnetite (Cu-biomagnetite) particles were prepared prior to addition to treatments systems following the methodology outlined in Section 6.2.2.

6.2.2 Cu-coating Iron-based Particles

Under anoxic conditions, $CuSO_4*5H_20$ was added to 25 mL Fe particle suspension in degassed DIW to prepare a 16 g/L Fe particle suspension in 12.6 mM Cu solution. 25 mL of anoxic 0.325 M NaOH solution was made up. 25 mL of 160 mM $NaBH_4$ 0.325 M NaOH was formulated by adding $NaBH_4$ to 25 mL of 0.325 M NaOH solution in an anaerobic chamber. Under anoxic conditions, 160 mM $NaBH_4$ 0.325 M NaOH solution was slowly added to the Fe particle suspension, containing added Cu(II), to create 50 mL of 80 mM $NaBH_4$ 0.163 M NaOH solution. The mixture was left for 12 hours to allow Cu(II) to be reduced to Cu(0) by $NaBH_4$ and coat the Fe particles. Cu-coated Fe particles were washed with degassed DIW to remove excess $NaBH_4$ and left suspended in degassed DIW. Biomagnetite nanoparticles and NanoFER 25 were coated independently to produce Cu-biomagnetite and Cu-NanoFER 25S.

6.2.3 Treatment Microcosm Setup

Triplicate aqueous NanoFER 25S and biomagnetite treatment systems were setup in 50 mL glass serum bottles with 30 mL AGW: (1) NanoFER 25S with 0.5 mM Hg(II) and 1.58 mM Cu(II), (2) Cu-NanoFER 25S with 0.5 mM Hg(II), (3) NanoFER 25S with 0.5 mM Hg(II) [Hg only control], (4) Biomagnetite with 0.5 mM Hg(II) and 1.58 mM Cu(II), (5) Cu-Biomagnetite with 0.5 mM Hg(II), and (6) Biomagnetite with 0.5 mM Hg(II) [Hg only control]. Hg(II) was added as $HgCl_{2,}$ and Cu(II) was added as $CuSO_4*5H_20$. Following day 1 (pre-treatment) sampling, treatments were added as a 1 mL suspension to give a final microcosm concentration of 2 g/L Fe. Duplicate no treatment control systems were setup with (1) 0.5 mM Hg and 1.58 mM Cu, and (2) 0.5 mM Hg, alongside single treatment only control systems without added Hg(II) or Cu(II), to effectively assess the geochemical changes influenced in treatment systems. Table P3-17 summarises the contents of each system following treatment addition.

Anoxic sampling, with degassed needle and syringe, was carried out at six time points from each system (day 1 (pre-treatment), day 1 plus 1-hour (post-treatment), day 1 plus 2-hours, day 1 plus 4-hours, day 2, day 26). 1 mL samples were taken from treatment systems, from which 100 µL of particle suspension was allocated from XPS, prior to centrifugation at 14000 g for 5 minutes. 300 µL of aqueous phase was allocated for pH and ORP measurement with a calibrated probe, 100 µL was allocated for ICP-MS, remaining solid and aqueous phases were stored at -18°C. Following anoxic sampling at the endpoint (day 26), serum bottles were opened and centrifuged under anoxic conditions. Solid phase was dried under anoxic conditions in a desiccator, ~30 mg was allocated for a two-step sequential extraction and the remaining solid phase was pressed into pellets for XAS analysis.

Table P3-17: Contents of water treatment microcosm at day 1 (following addition of treatments)

Microcosm	Replicates	Concentration $HgCl_2$	Concentration $CuSO_4$	Volume AGW after treatment addition	Treatment & Concentration in AGW
A	Triplicate	~0.5 mM	~1.58 mM	30 mL	NanoFER 25S (~10 g/L) [~2 g/L Fe]
B	Triplicate	~0.5 mM	N/A	30 mL	NanoFER 25S (~10 g/L) [~2 g/L Fe]
C	Triplicate	~0.5 mM	N/A	30 mL	Cu-NanoFER 25S (~10 g/L) [~2 g/L Fe]
D	Triplicate	~0.5 mM	~1.58 mM	30 mL	Biomagnetite (~2 g/L) [~2 g/L Fe]
E	Triplicate	~0.5 mM	N/A	30 mL	Biomagnetite (~2 g/L) [~2 g/L Fe]
F	Triplicate	~0.5 mM	N/A	30 mL	Cu-Biomagnetite (~2 g/L) [~2 g/L Fe]
G	Single	N/A	N/A	30 mL	Cu-NanoFER 25S (~10 g/L) [~2 g/L Fe]
H	Single	N/A	N/A	30 mL	Cu-Biomagnetite (~2 g/L) [~2 g/L Fe]
I	Duplicate	~0.5 mM	~1.58 mM	30 mL	No treatment
J	Duplicate	~0.5 mM	N/A	30 mL	No Treatment

6.2.4 Total Iron Quantification

0.2 mL of biomagnetite suspension was digested in 9.8 mL analytical grade 15.9 M HNO_3 for 24 hours. Following 50-fold dilution, triplicate 10 mL samples (2% (v/v) HNO_3) were filtered (0.4 µm) prior to analysis by inductively coupled plasma-atomic emission spectroscopy (ICP-AES).

6.2.5 Sequential Extraction Procedure

The procedure used two solvents to separate Hg and Cu fractions based on their extractability: (F1) weak acid soluble (pH 2, 0.1 M CH_3COOH + 0.01 M HCl) and (F2) strongly complexed (12 M HNO_3). Dried sediment from particle treatment systems (~30 mg dry wt.) were added to 10 mL centrifuge tube and mixed with 10 mL of extractant 1 (F1). Extraction vessels were then mixed on an orbital shaker at 200 rpm for 24 hours and centrifuged at 4000 g for 10 minutes with a Boeco C28A centrifuge.

The extract supernatant was decanted off into 50 mL centrifuge tubes and the precipitate was rinsed with 10 mL DIW. The rinse supernatant was separated by centrifugation and combined with the corresponding extractant supernatant. After the rinse step, 10 mL of extractant 2 (F2) was added to sediment sample residue following same process as for the F1 extraction. Extract solution were 500-fold diluted prior to analysis by ICP-MS.

6.2.6 X-Ray Diffraction (XRD)

Powdered dry sample (~0.1 g) was mounted on a glass slide and analysed on a Bruker D8 Advance X-ray Diffractometer to determine the mineral phases present. Phases were identified using the Bruker DIFFRAC.SUITE EVA software, and Bruker DIFFRAC.SUITE TOPAS software was used for their quantification.

6.2.7 Inductively Coupled Plasma-Mass Spectroscopy (ICP-MS)

ICP-MS was used to determine Hg and Cu concentrations in 10 mL samples (2% (v/v) aqua regia with 200 µg/L gold (Au) matrix), 100-fold diluted from aqueous microcosm samples and 500-fold diluted from sequential extract solutions. An Agilent 7500 ICP-MS was operated in rapid sequential mode to detect and quantify Hg and Cu. Detection limits are typically 0.1 ppb under the standard operating conditions. A 200 µg/L Au spike (from a 10 ppm elemental Au(0) in 2% in aqua regia stock solution) was added to a 2% aqua regia matrix for samples and calibration standards to minimise carryover between samples and calibration standards (Chen, 2009).

6.2.8 Inductively Coupled Plasma-Atomic Emission Spectroscopy (ICP-AES)

ICP-AES was used to determine concentrations of Fe in 10 mL samples (2% (v/v) HNO_3) from aqueous phase of total iron digests. The Perkin-Elmer Optima 5300 dual view ICP-AES, with a detection range of 10 ppb – 50 ppm, was employed for analysis.

6.2.9 Hg L_{III}-edge X-Ray Absorption Spectroscopy

Hg L_{III}-edge XAS data were collected on the I20 Beamline at Diamond Light Source (Harwell, Oxfordshire, UK). Hg sample pellets were analysed in X-ray transmission mode (64 element monolithic Ge detector with Xspress4) within a liquid helium cryostat, at 4 K. Merging spectra from 4 scans (to k – 14) was sufficient for producing high quality data with improved signal to noise ratio. Background subtraction, normalisation and averaging of spectra from multiple sample scans was carried out in Athena, prior to fitting in Artemis to establish the crystal structure (Ravel and Newville, 2005).

6.2.10 X-ray Photoelectron Spectroscopy (XPS)

XPS was performed using an ESCA2SR spectrometer (ScientaOmicron GmbH) using monochromated Al Kα radiation (1486.6 eV, 20 mA emission at 300 W, 1 mm spot size) under vacuum. Sample suspensions were dropped onto carbon stubs and dried under anoxic conditions prior to analysis. Charge neutralisation was achieved using a low energy electron flood source (FS40A, PreVac). Binding energy scale calibration was performed using C-C in the C 1s photoelectron peak at 285 eV. Analysis and curve fitting was performed using Voigt-approximation peaks in CasaXPS (Fairley, 2019).

6.2.11 Scanning Electron Microscopy (SEM) and Energy Dispersive X-Ray Spectroscopy (EDS)

Samples mounted on carbon pads were imaged under vacuum in ‘wet’ mode on an FEI XL30 ESEM-FEG (secondary electron or backscattered electron detectors). EDAX Gemini EDS system enabled elemental analysis of samples during imaging, automatically mapping and analysing components.

6.3 Results and Discussion

6.3.1 Geochemistry in Hg-amended Microcosms

Figure P3-53 illustrates changes in redox potential (ORP), as well as aqueous Hg and Cu concentrations in NanoFER 25S (Left) and biomagnetite (Right) treatment systems over the duration of the experiment.

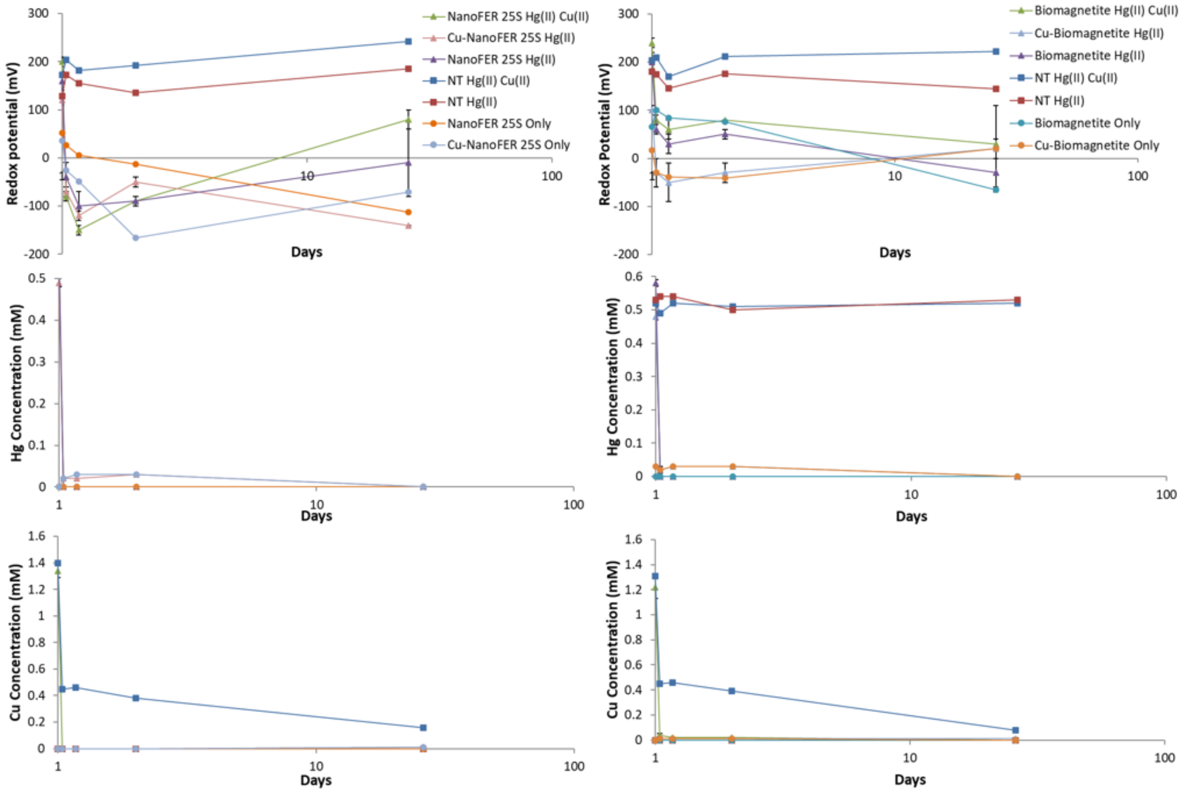

Figure P3-53: Redox Potential (ORP), Cu concentration (aq) and Hg concentration (aq) in NanoFER 25S (Left) and biomagnetite (Right) treatment systems (NT refers to no treatment control systems, x-axis is a log scale).

NanoFER 25S induced more reducing conditions in treatment systems, causing a notable decrease in ORP (190 – 280 mV) between day 1 (pre-treatment) and 1-hour post treatment samples. ORP in NanoFER 25S Hg(II) Cu(II) and NanoFER 25S Hg(II) systems started to increase from 4-hours post treatment, with systems becoming more oxidising by day 26. Despite fluctuations over the duration of the experiment, ORP was lowest at day 26 (-140 mV) in Cu-NanoFER 25S Hg(II) systems. This observation could suggest that the Cu-coating may increase the duration of reactivity of nZVI in NanoFER 25S. Biomagnetite caused a decrease in ORP (130 – 160 mV) between day 1 (pre-treatment) and 1-hour (post-treatment) in both biomagnetite Hg(II) Cu(II) and biomagnetite Hg(II) systems. However, only Cu-biomagnetite induced reducing conditions capable achieving a negative ORP value that lasted at least 24-hours following treatment addition, reaching a minimum at 4-hours post-treatment (-50 mV). Nonetheless, by day 26, Cu-biomagnetite Hg(II) systems had become more oxidising, whereas ORP in uncoated biomagnetite systems had continued to decrease, with notable variability across the triplicate. Reducing conditions were achieved in biomagnetite Hg(II) systems, with average ORP reaching a low (-30 mV) at day 26, suggesting that the adsorption of aqueous Hg(II) had not decreased the reactivity of Fe(II) in the particles.

Hg and Cu were removed rapidly from aqueous phase by uncoated iron-based particles in relevant treatment systems containing aqueous Hg(II) and/or Cu(II). NanoFER 25S removed Cu slightly more effectively than biomagnetite, with 0 and 40 µM identified in 1-hour post-treatment samples, respectively. However, Hg removal was equally as effective in uncoated biomagnetite and NanoFER 25S treatment systems, Hg was not detected in any post-treatment samples. Cu-coating slightly reduced the Hg sorption capacity of biomagnetite and NanoFER 25S with 20 – 30 µM Hg detected in samples taken during the first 24-hours following treatment addition. However, Hg was not detected in day 26 aqueous phase samples from either Cu-NanoFER 25S Hg(II) or Cu-Biomagnetite Hg(II) systems. As expected, Hg(II) remained in the aqueous phase of no treatment systems. Although, Cu(II) appeared to precipitate from solution, aqueous phase Cu(II) concentration decreased rapidly, >65% was removed from solution during the first hour, and <12% was detected in aqueous phase by day 26. Cu precipitation from solutions, similar to AGW, containing sulfate and natural calcium carbonates has previously been observed (Zhizhaev et al., 2007).

6.3.2 Mercury and Copper chemical speciation and fate

Hg L_{III}-edge EXAFS spectra from day 26 (endpoint) samples from six particle treatment systems and the corresponding model fit data are presented in Figure P3-54a. Figure P3-54b shows Fourier transform of K^3-weighted EXAFS spectra for sample data and the corresponding model fit data. Table P3-18 contains information on the fitting parameters used in the respective model to fits for EXAFS spectra for, providing structural information for Hg in samples from each treatment system.

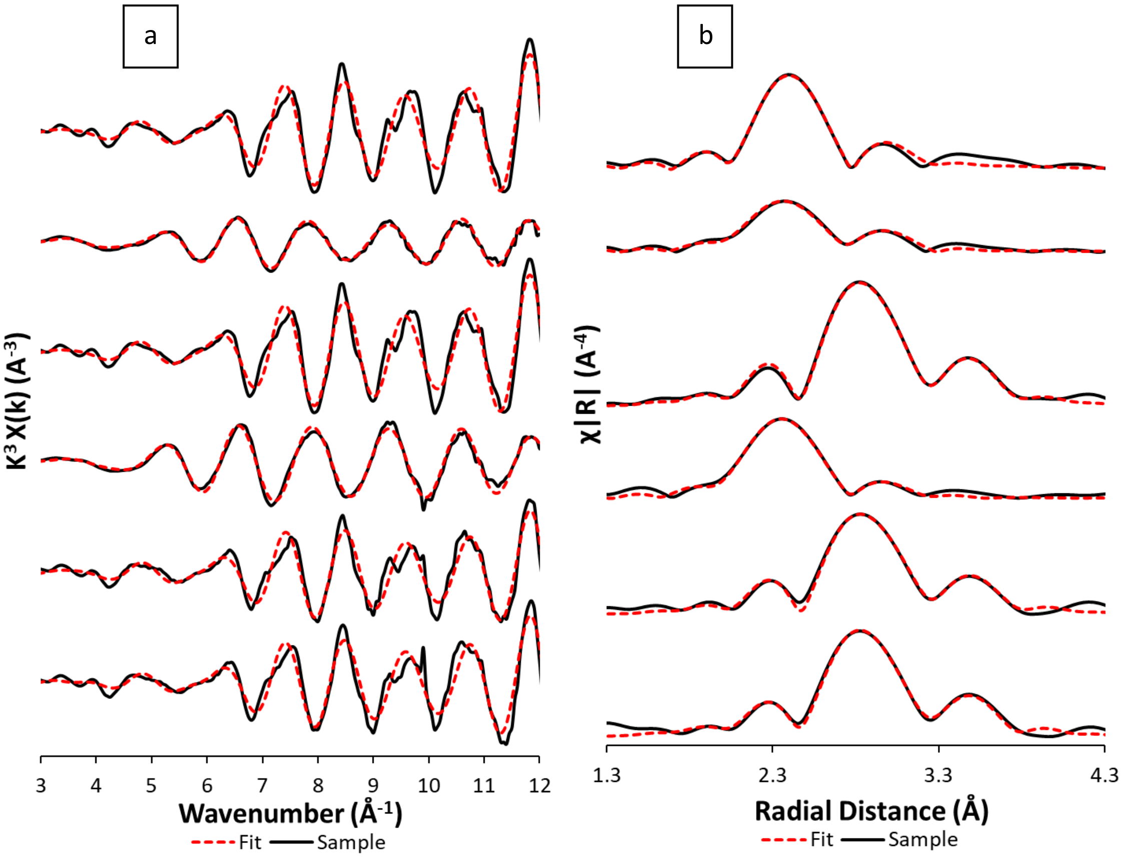

Figure P3-54: Hg L_{III}-edge XAS spectra for day 26 samples (a) k^3-weighted EXAFS spectra, and (b) Fourier transform of k^3-weighted EXAFS spectra for sample data (solid lines) and their corresponding model fit data (dashed line).

Table P3-18: Fitting parameters for the EXAFS data for samples shown in Figure P3-54. CN denotes the coordination number; R denotes the atomic distances; σ^2 denotes the Debye-Waller factor; S_0^2 denotes the amplitude factor, E_0 denotes the shift in energy from the calculated Fermi level (R = 1.7 to 3.8).

Standard	Path	CN	R (Å)	σ^2 (Å^2)	E_0	S_0^2	Reduced χ^2	R-factor
Cu-NanoFER 25S Hg(II)	Cu1	2	2.6568	0.0108	0.316 ± 2.628	1	383.85	0.013
	Cu2	3	2.7534	0.00337				
	Hg1	3	2.9390	0.00668				
Cu-Biomagnetite Hg(II)	Cu1	3	2.6842	0.04875	3.637 ± 1.216	1.1	148.18	0.013
	Cu2	3	2.7193	0.00754				
	Hg1	3	2.9643	0.00816				
NanoFER 25S Hg(II)	Hg1	5	2.9773	0.0020	4.796 ± 0.373	1	41.16	0.002
	Hg2	5	3.4447	0.0061				
NanoFER 25S Hg(II) Cu(II)	Cu1	4	2.7015	0.00591	5.118 ± 1.337	1	91.82	0.005
	Cu2	2	2.8216	0.00932				
	Hg1	3	2.9820	0.00985				
Biomagnetite Hg(II)	Hg1	5	2.9802	0.0025	6.344 ± 1.036	0.9	144.89	0.015
	Hg2	5	3.4504	0.0066				
Biomagnetite Hg(II) Cu(II)	Hg1	4	2.9742	0.0014	4.536 ± 1.079	0.9	104.07	0.012
	Hg2	6	3.4428	0.0077				

Model fit data for the Hg L_{III}-edge EXAFS spectra for endpoint samples from Cu-containing microcosms suggested that $HgCu_{AM}$ may have formed 3 treatments systems [Cu-NanoFER 25S Hg(II), Cu-Biomagnetite Hg(II) and NanoFER 25S Hg(II) Cu(II)]. Initial visual analysis suggested that Hg in biomagnetite Hg(II) Cu(II) and biomagnetite Hg(II) systems was most likely elemental Hg(0) in endpoint samples. However, most Hg in the Cu-biomagnetite Hg(II) systems appeared to be a different chemical speciation, potentially an amalgamation of elemental Hg(0) and Cu(0) on the particle surface [$HgCu_{AM}$]. EXAFS model fits (Table P3-18) supported this observation, the best fit for solid phase Hg from Cu-biomagnetite Hg(II) included 3 Cu backscatterers at 2.68 Å, 3 Cu backscatterers at 2.72 Å, 3 Hg backscatterers at 2.96 Å (Table P3-18). These coordination numbers and interatomic distances were consistent with previously published crystal structure data for Cu_7Hg_6, with 6 Cu backscatters <2.85 Å from the absorbing Hg atom and 3 Hg backscatterers between 2.9 and 3.0 Å (Bernhardt and Schmetzer, 1992). Pre-coating biomagnetite particles with reduced Cu seemed to be a key factor in the process, as the reduction potential of unamended particles alone does not seem capable of achieving the same endpoint in the Biomagnetite Hg(II) Cu(II) systems. Here, the best fit for solid phase Hg included 4 Hg backscatterers at 2.97 Å and 6 Hg backscatterers at 3.44 Å (see Table 2). The best fit for solid phase Hg in endpoint samples from the biomagnetite Hg(II) systems included 5 Hg backscatterers at 2.98 Å and 5 Hg backscatterers at 3.45 Å (Table P3-18).

Initial visual analysis suggested that Hg in NanoFER 25S Hg(II) Cu(II) and Cu-NanoFER 25S Hg(II) systems had a similar endpoint speciation to Hg in the Cu- NanoFER 25S Hg(II), potentially forming $HgCu_{AM}$.

EXAFS model fit data (Table P3-18) supported this observation, the best fit for day 26 solid phase Hg from Cu- NanoFER 25S Hg(II) systems included 2 Cu backscatterers at 2.66 Å, 3 Cu backscatterers at 2.75 Å, 3 Hg backscatterers at 2.94 Å (Table P3-18). However, this did not seem to be dependent on the pre-coating step in these systems, the reduction potential of nZVI (NanoFER 25S) alone seemed capable of achieving a similar $HgCu_{AM}$ endpoint, with only slight structural differences in the modelled data fits. The best fit for solid phase Hg in endpoint samples from the NanoFER 25S Hg(II) systems included 4 Cu backscatterers at 2.70 Å, 2 Cu backscatterers at 2.82 Å, 3 Hg backscatterers at 2.98 Å (Table P3-18). Interatomic distances and coordination numbers for endpoint samples from Cu-containing NanoFER 25S systems were similar to crystal structure data for Cu_7Hg_6, with 5 or 6 Cu backscatters <2.85 Å from the absorbing Hg atom and 3 Hg backscatterers between 2.9 and 3.0 Å (Bernhardt and Schmetzer, 1992). In the absence of Cu, the NanoFER 25S Hg(II) system appeared to reduce most Hg(II) to Hg(0). Here, the best fit for solid phase Hg included 5 Hg backscatterers at 2.98 Å and 5 Hg backscatterers at 3.44 Å (Table P3-18).

Copper Oxidation State

Characterisation of Cu oxidation state in the endpoint samples from systems containing Cu was performed using XPS. A Cu $2p_{3/2}$ peak at 934.2 eV is characteristic of Cu(II) whereas a peak at 932.8 eV suggests the presence of reduced Cu [Cu(I) or Cu(0)] (Kimber et al., 2019). This technique is not considered accurate for distinguishing between Cu(I) and Cu(0) (Biesinger et al., 2010). Interestingly, initial XPS analysis identified a peak at 933.8 eV see (Figure P3-60c in the SI) in solids from Cu-NanoFER 25S Hg(II), suggesting that some Cu reduced during the coating process may have later oxidised to Cu(II). However, a peak at 91.8 eV (Figure P3-60a in the SI) from NanoFER 25S Hg(II) Cu(II) systems, could indicate the presence of more reduced Cu species, potentially due to reduction at the interface with the Fe(0) core of NanoFER 25S particles. Endpoint solids from Cu-containing biomagnetite microcosms exhibited peaks at 933.2 eV and 933.6 eV (see Figure P3-60b and P3-60d in the SI), suggesting there may a range of Cu species with varying oxidation state. The chemical speciation of Cu and the surface could be better resolved using Cu k-edge XAS and/or hard X-ray photoelectron spectroscopy (HAXPES).

Stability & Mobility Testing

A two-step sequential extraction was done to assess the relative stability of Hg and Cu in relevant treatment systems, in order to establish whether co-treatment of Cu(II) and Hg(II) or coating particles with reduced Cu has the potential to form a more recalcitrant endpoint. Figures P3-55 and P3-56 show the proportions of total Hg and total Cu extracted in each fraction of the mini-SEP applied to day 26 samples. Hg(0) is not soluble in water, but will readily dissolve in lipids, and is considered extractable in 12 M HNO_3 (Bloom et al., 2003; O'Connor et al., 2019). Under normal conditions Cu(0) is not soluble in water, but oxygen and oxidising acids such as HNO_3 can induce corrosion of Cu(0) (Huttenloch et al., 2003). Cu(I) and Cu(II) compounds can be more soluble depending on the ligand. Table P3-19 shows percentage recovery of total Hg and total Cu added to treatment systems, as calculated by mass balance.

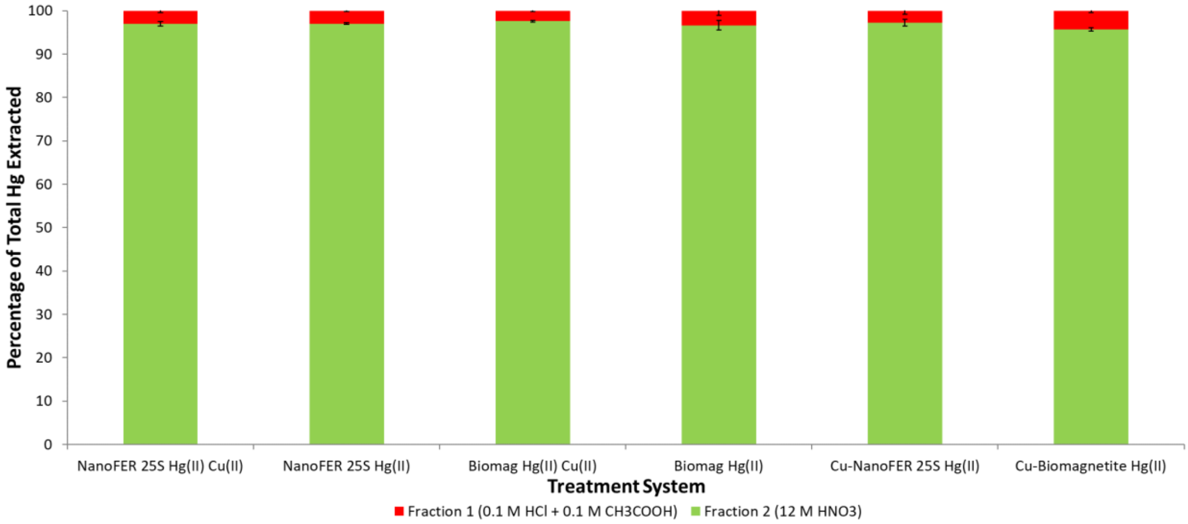

Figure P2-55: Percentage of total Hg extracted in sequential extraction fractions in treatment systems containing Hg

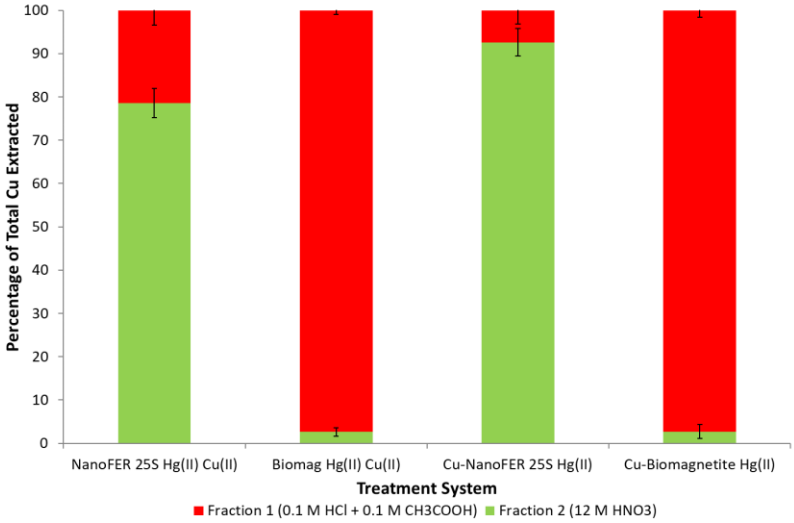

Figure P3-56: Percentage of total Cu extracted in sequential extraction fractions in treatment systems containing Cu.

Table P3-19: Total extracted solid phase Cu and Hg in treatment systems and percentage recovery based on expected total concentrations given complete recovery.

Treatment System	Extracted Solid Phase Cu Concentration (mg/g)	% Recovery	Extracted Solid Phase Hg Concentration (mg/g)	% Recovery
NanoFER 25S Hg(II) Cu(II)	26.1 ± 2.3	57	32 ± 3.6	70
NanoFER 25S Hg(II)	0.8 ± 0	N/A	44.3 ± 3.4	93
Biomagnetite Hg(II) Cu(II)	20.6 ± 1.2	61	25 ± 1.3	74
Biomagnetite Hg(II)	0 ± 0	N/A	33.1 ± 1.7	92
Cu-NanoFER 25S Hg(II)	22.8 ± 1.8	50	19.4 ± 1.8	43
Cu-Biomagnetite Hg(II)	24.1 ± 1.8	69	34.5 ± 5	99
NanoFER 25S Only	0.7	N/A	0.2	N/A
Biomagnetite Only	0	N/A	0	N/A
Cu-NanoFER 25S Only	26	55	0	N/A
Cu-Biomagnetite Only	24.1	67	0	N/A

>95% of Hg extracted from all systems was in fraction 2, suggesting Hg was predominantly immobile and strongly complexed. However, the percentage recovery was assessed (Table P3-19) to establish whether Hg could have formed a more recalcitrant species not extractable in Fractions 1 and 2 (e.g. HgS, HgAu, HgSe, HgCu) or whether Hg(0) may have volatilised to headspace. Cu recovery was relatively low (50 – 67%) in extractants from all Cu-containing systems, with slightly better recovery from endpoint solids in biomagnetite systems (61 – 67%). Notably, >95% extractable Cu was recovered in the weak acid fraction from endpoint solid phases in Cu-Biomagnetite Hg(II) and Biomagnetite Hg(II) Cu(II) systems. In contrast >75% extractable Cu was removed in 12 M HNO_3 extractant in day 26 solids from Cu-NanoFER 25S Hg(II) and NanoFER 25S Hg(II) Cu(II) microcosms, suggesting Cu is more recalcitrant following treatment with NanoFER 25S. However, more detailed scientific information is needs to establish Cu chemical speciation in relevant treatment systems.

>90% of Hg was recovered in solid phase extracts from NanoFER 25S Hg(II), Biomagnetite Hg(II) and Cu-Biomagnetite Hg(II) systems, predominantly in the second fraction, which would suggest the bulk was Hg(0). EXAFS model fits (Figure P3-54) identified Hg crystal structure as Hg(0) in NanoFER 25S Hg(II) and Biomagnetite Hg(II) in endpoint samples, which is extractable in 12 M HNO_3. However, high Hg recovery [99%] from Cu-Biomagnetite Hg(II) endpoint samples suggested the $HgCu_{AM}$ solid phase, identified by EXAFS model fit, may not be any more recalcitrant than Hg(0), as Hg was slightly more extractable when compared to the endpoint Hg(0) identified in samples from NanoFER 25S Hg(II) and Biomagnetite Hg(II) systems.

Recovery from was lower from NanoFER 25S Hg(II) Cu(II) [70%] and biomagnetite Hg(II) Cu(II) [74%] systems. Cu-NanoFER 25S Hg(II) systems had the lowest Hg recovery [43%], residual Hg maybe immobilised as a recalcitrant solid phase $HgCu_{AM}$, identified by EXAFS model fits. Interestingly, Cu recovery was also lowest from the Cu-NanoFER 25S Hg(II) system. $HgCu_{AM}$ was also identified in endpoint solid phase from NanoFER 25S Hg(II) Cu(II), but there was slightly less residual Hg. However, there is uncertainty regarding whether Hg that has not been accounted for is residual in the solid or has volatilised to headspace. Amalgamated forms of Hg (e.g. HgAu and HgSe) often require stronger acids, such as aqua regia, for dissolution and extraction of Hg. Further investigation is required to establish whether Hg and Cu that have not been recovered in the two-step sequential extraction are residual in the solid phase.

6.3.3 High Resolution Imaging of Cu-coated Particles

Figures P3-57 and P3-58 shows a high-resolution SEM image of the solid phases from Cu-biomagnetite and Cu-NanoFER 25S systems at endpoint (day 26) and the EDS component mapping of Cu, Fe and Hg for the corresponding regions of the samples.

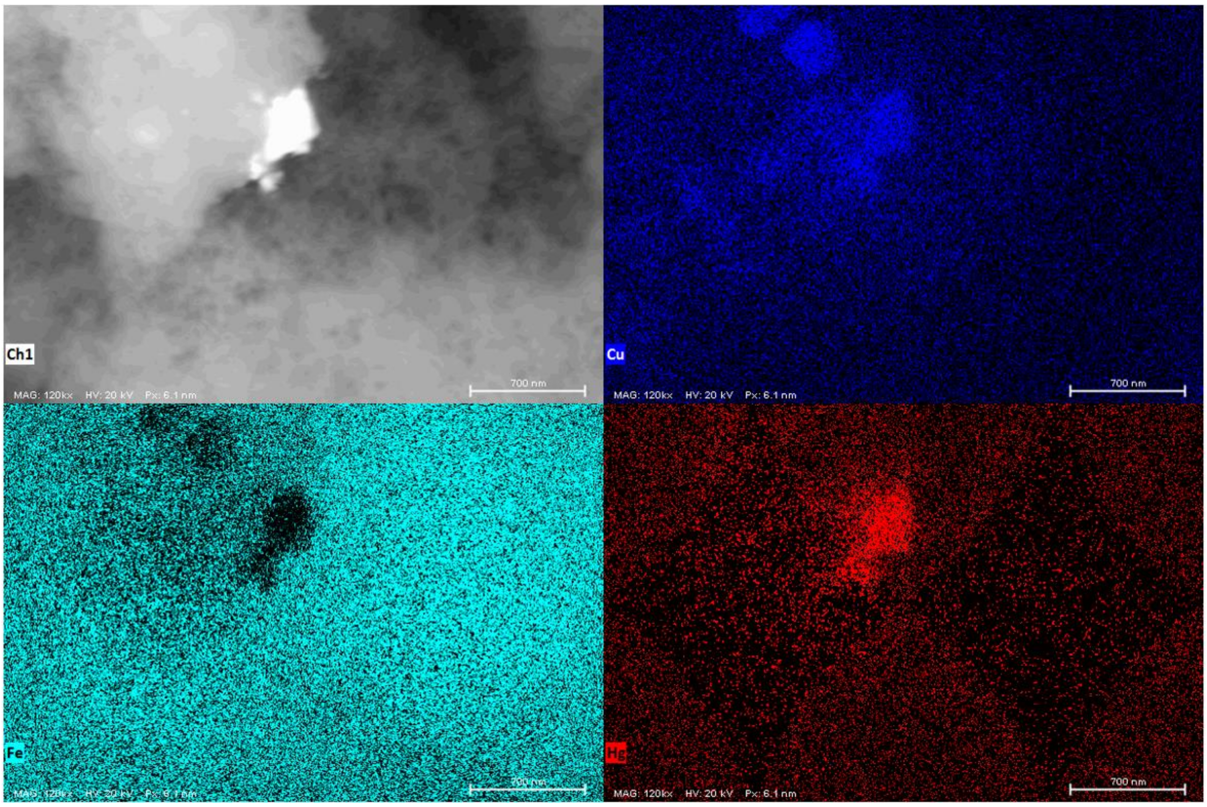

Figure P3-57: (a) an SEM image of a particle from the Cu-biomagnetite Hg(II) system and EDS surface component mapping for (b) Cu, (c) Fe, and (d) Hg.

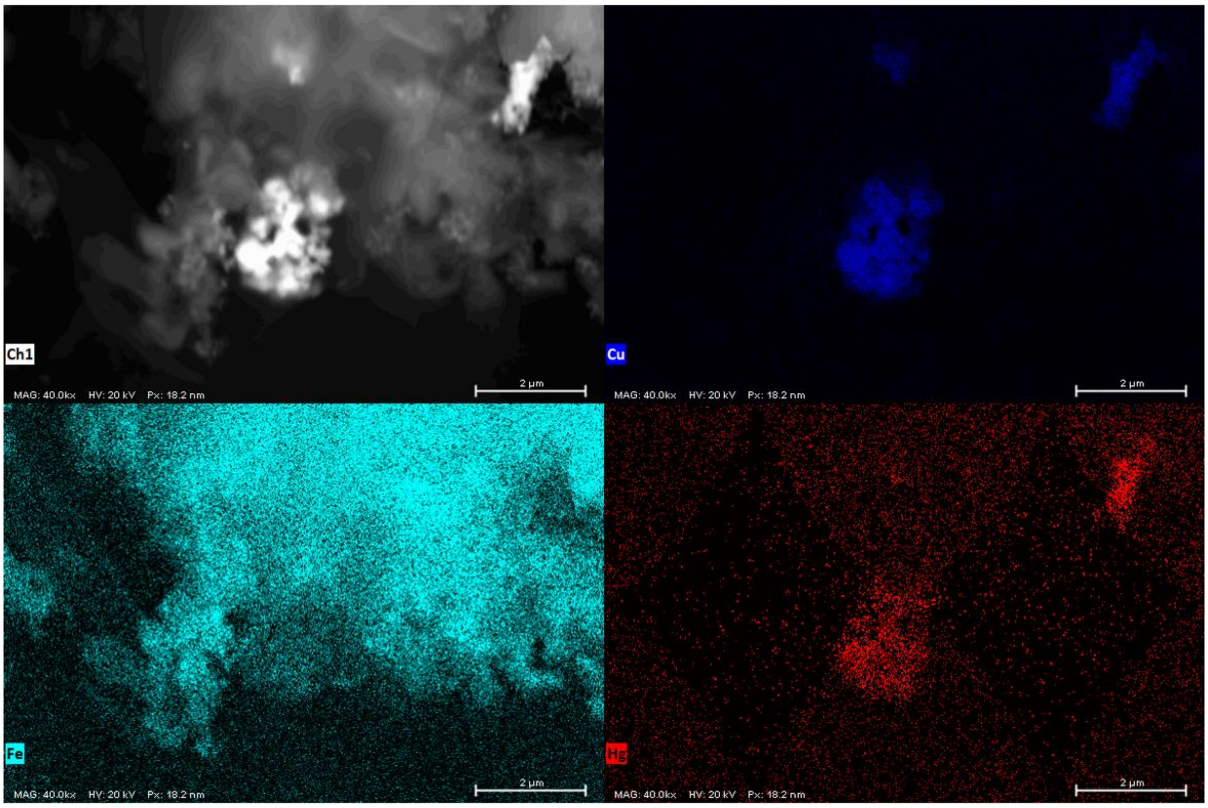

Figure P3-58: (a) an SEM image of a particle from the Cu-NanoFER 25S Hg(II) system and EDS surface component mapping for (b) Cu, (c) Fe, and (d) Hg.

Fe, Cu and Hg components are distributed across the image area in Figure P3-57. However, there appears to be a dense agglomeration of Cu and Hg phases in a zone (200 x 600 nm) in the centre of the image, with notable absence of Fe. This zone is a much lighter shade (white) in the grey-scale SEM image. The close association of Cu and Hg in the agglomeration zone supports the XAS modelled data fit (Table P3-19) that suggested formation of $HgCu_{AM}$ in the Cu-biomagnetite Hg(II) system. However, limited Fe signal in suggests the $HgCu_{AM}$ phase may not be associated with the Fe particle surface.

Fe signal is generally strongest at the top-right, but weakens the bottom-left, of the image in Figure P3-58. Cu and Hg are more sparsely distributed than Fe, but there appears to be an agglomeration of Cu and Hg phases in a zone (~2 µm x ~2 µm) in the centre of the image. The lighter shade of this zone in the grey-scale SEM image makes it visually prominent. The association of Hg and Cu in this section of the image series supports the Hg L_{III}-edge EXAFS spectra fit for endpoint samples from the Cu-NanoFER 25S systems that identified a crystal structure suggesting formation of $HgCu_{AM}$. EDS mapping revealed a relatively strong Fe signal in the areas of the image with an association of Cu and Hg, suggesting there may be an interaction between Hg, Cu and Fe at the particle surface.

6.4 Conclusion

Hg and/or Cu were rapidly removed from AGW treatment systems following addition of all particle treatments. Hg L_{III}-edge EXAFS model fits revealed that a solid phase $HgCu_{AM}$ may have formed in 3 treatment systems [Cu-NanoFER 25S Hg(II), Cu-Biomagnetite Hg(II) and NanoFER 25S Hg(II) Cu(II)], with the bulk of endpoint solid phase Hg determined to be Hg(0) in the other treatment batches [NanoFER 25S Hg(II), Biomagnetite Hg(II) and Biomagnetite Hg(II) Cu(II)]. Hg recovery data from the two-step sequential extraction suggested $HgCu_{AM}$ formed in Cu-Biomagnetite Hg(II) microcosms was less recalcitrant than that formed in the Cu-NanoFER 25S Hg(II) and NanoFER 25S Hg(II) Cu(II) systems. SEM and EDS imaging revealed an agglomeration of Hg and Cu in a region of the image that had less Fe signal, suggesting the $HgCu_{AM}$ phase may not be associated with the Fe particle surface. There were also, separate areas with high Cu signal but limited Hg signal, suggesting there could be additional Cu species present, this would be supported by extraction data that identified that a significant amount of the extractable Cu was weak acid soluble in biomagnetite systems. Additional analysis (e.g. Cu k-edge XAS, HAXPES and advanced-TEM) will be needed to better understand Cu chemical speciation in these systems and improve visualisation of interaction(s) between Hg, Cu and Fe at the particle surface interface. Further investigation will assist in establishing how these interactions may be influencing Hg mobility.

Hg and Cu recovery was low in extracts from $HgCu_{AM}$ formed in Cu-containing NanoFER25S systems. Furthermore, recovery was lowest for both Hg [50%] and Cu [43%] from endpoint solids in Cu-NanoFER 25S systems, likely due to the formation of more stable refractory $HgCu_{AM}$ phases. However, due to the volatility of Hg(0) there is some uncertainty regarding whether the bulk of residual Hg is associated with Cu as a more recalcitrant alloy or whether some GEM may have been emitted from the solid and aqueous phases. EDS mapping revealed a relatively strong Fe signal in the areas of the image with an association of Cu and Hg, suggesting that there may be an interaction between Hg, Cu and Fe at the particle surface. Advanced-TEM may be able to provide higher resolution imaging capable of resolving interactions the particle surface interface. Further experimental work is needed to better assess stability of solid phase end products in treatment system, such as application of a more thorough five-step SEP including an aqua regia digest. Gaseous headspace monitoring in batch microcosms would enable GEM quantification and establish the proportion of THg volatilising to the headspace. Hg(0) was not monitored in the headspace during the experiment as our research laboratory did not have the analytical capability. Experimental and theoretical determination of sorption kinetics and maximum loading in the aqueous systems would provide additional important scientific information.

Better understanding the timescale required for $HgCu_{AM}$ formation is essential, as should these new approaches to remediation be scaled up as a wastewater treatment, it would be much more cost-effective for industry to use fast acting treatment technologies. Investigating a wide-range of natural and wastewaters with varying chemical compositions will be needed to provide greater insight into the suitability of using Cu-NanoFER25S and Cu-biomagnetite for treatment of Hg-contaminated waters (Vernon and Bonzongo, 2014). There are concerns over the long-term fate, transformation, and eco-toxicity of novel nanoscale treatment solution in environmental systems (Crane and Scott, 2012). Therefore, these newly developed Cu-biomagnetite and Cu-NanoFER25S particles maybe more easily applied as treatment for Hg-contaminated effluent wastewater from industrial processes in the shorter term. As this does not involve *in situ* application and treats Hg at point source prior to discharge to the environment these potential solutions could be brought to market faster. Reduction of toxic wastewater discharge that can harm ecosystems and human health is vital. Column experiments could be setup to simulate *in situ* treatment of anoxic real-world subsurface sediments, contaminated with both Cu(II) and Hg(II), to establish whether stable refractory $HgCu_{AM}$ could form in sediments. Biogeochemical monitoring and itrack mapping could be applied to monitor metal migration and accumulation in different zones and link changes in metal speciation to local biogeochemistry.

Acknowledgements

We thank EPRSC, WSP and Akzo Nobel for funding under a PhD CASE award. We acknowledge beamtime awarded at the Diamond Light Source for XANES and EXAFS on the I20 beamline under proposals SP18794 and SP21441. We thank Shu Hayama and Frederick Mosselmans for their assistance at Diamond Light Source.

We thank Paul Lythgoe (Manchester Analytical Geochemistry Unit, University of Manchester) for ICP-MS and ICP-AES analysis. We thank Lewis Hughes for his assistance with SEM analysis. We thank Ben Spencer for his assistance with XPS analysis (Henry Royce Institute, University of Manchester funded through EPSRC grants EP/R00661X/1, EP/P025021/1 and EP/P025498/1).

6.5 Paper 3: Supplementary Information

6.5.1 Section 1: Biomagnetite XRD Spectra Characterisation

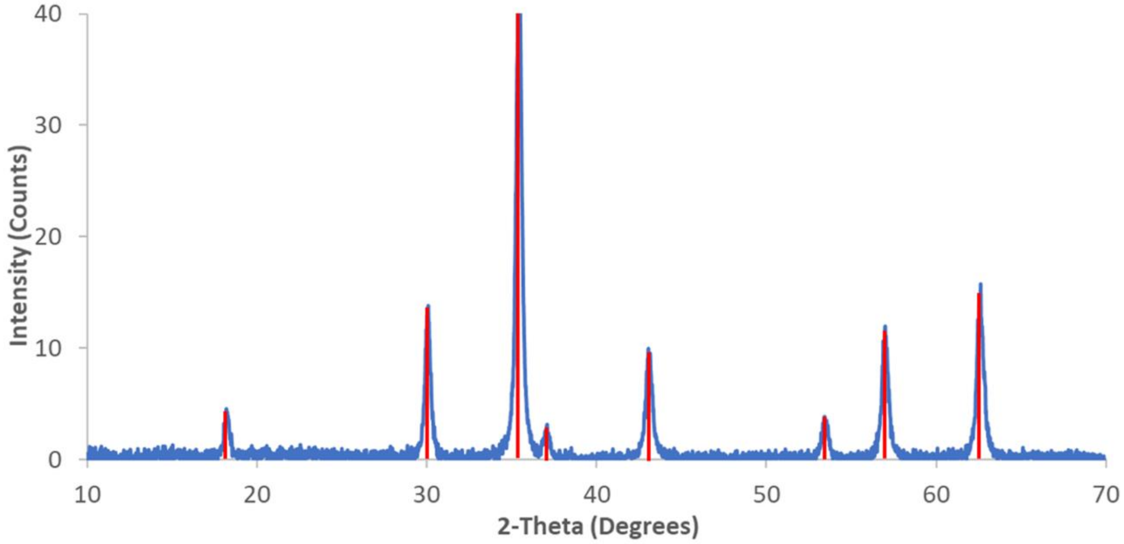

Figure P3-59: Biomagnetite XRD spectrum and peak fit (major peaks at 18.3, 30.1, 35.4, 37.1, 43.2, 53.4, 56.9, 62.5 degrees)

6.5.2 Section 2: XPS Spectra Fits for Cu-containing Samples

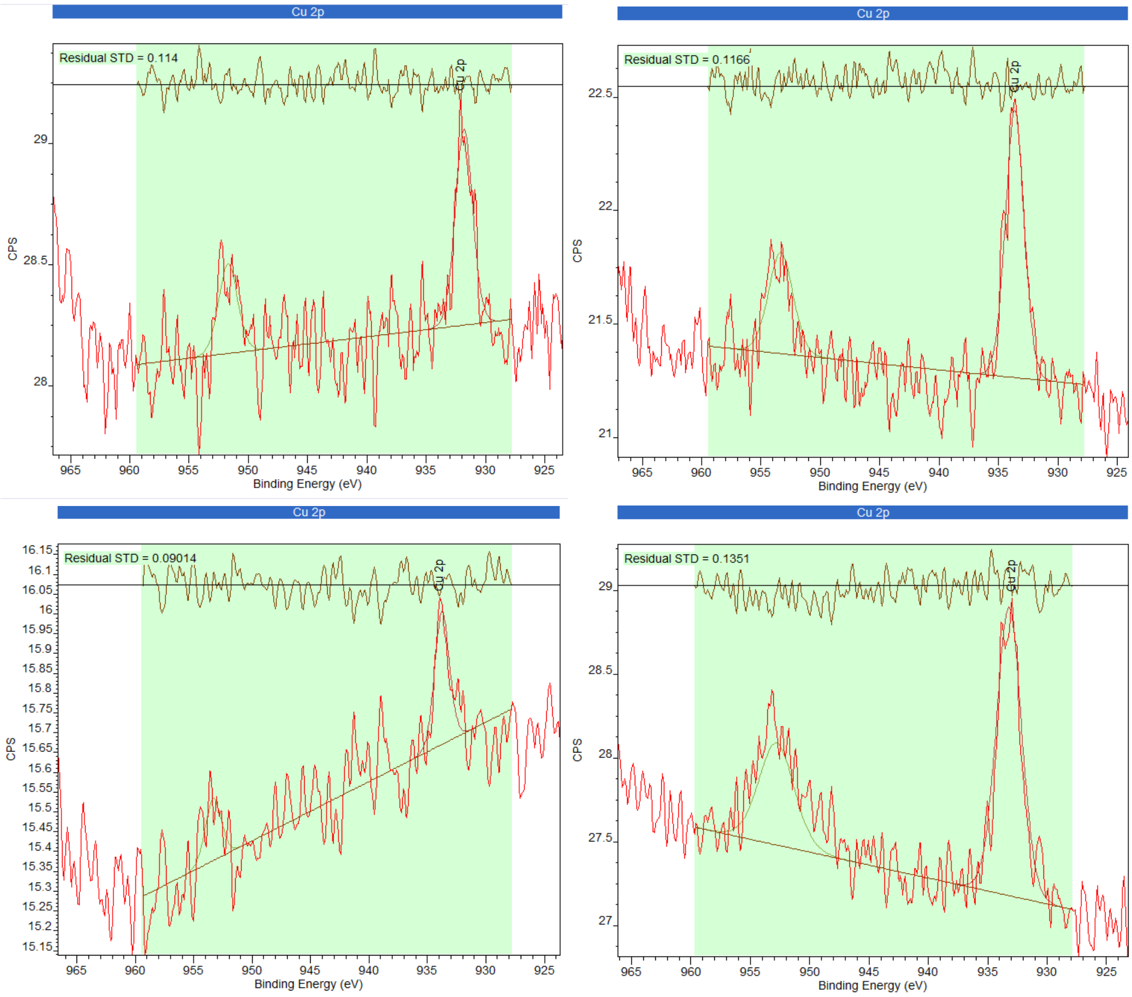

Figure P3-60: XPS component fitting for endpoint samples from (a) NanoFER 25S Hg(II) Cu(II), (b) Biomagnetite Hg(II) Cu(II), (c) Cu-NanoFER 25S Hg(II), and (d) Cu-Biomagnetite Hg(II) treatment systems.

7.0 Conclusions & Future Work

This research work provides further insight into the biogeochemical behaviour of Hg in contaminated sediments and groundwater. Hg poses a significant risk to ecosystems and human health due to ongoing and legacy release from waste-streams at industrial sites (e.g. chlor-alkali chemical plants). Determining the chemical speciation, mobility, and bioavailability of toxic metals (e.g. Hg) is essential for effective risk assessment. Paper 1 (Section 4) presented experimental and analytical data carried out in the first phase of work, investigating the chemical speciation and potential environmental mobility of Hg in a contaminated canal bed sediment. Mineral components (e.g. brucite and carbonate) identified in Hg-contaminated canal bed (MLR) sediment adjacent to an industrial area can be linked to alkaline solid waste from chlor-alkali plants utilising the Hg-cell process, identifying legacy discharge from a nearby facility as a potential source of pollution. Total extractable Hg in MLR sediment was estimated to be 86 ± 1 mg/kg. Sequential extraction from the solid phase revealed that most Hg was immobilised in the sediment, ~97% required strong acids (12 M HNO_3 or aqua regia) to be applied for extraction, suggesting that it was likely to be strongly complexed or mineral bound, and therefore likely limited in its bioavailability. XAS data revealed more detailed compound specific information, providing greater insight it to the local coordination environment. Iterative linear combination fitting the Hg L_{III}-edge EXAFS spectra from MLR samples to Hg standards suggested that most is likely to be beta-HgS (~85%), with the bulk of the remaining portion Hg(II) sorbed to MLR sediment components (~15%).

CV-AFS analysis of selective MeHg extracts revealed that there was 55 ± 1 µg/kg (dry wt.) of highly toxic MeHg in the sediment. However, despite the relatively low contribution to THg (< 0.1%), it may have a significant contribution to the overall toxicological risk posed by the Hg-contaminated sediment, due to its tendency to bioaccumulate. Deltaproteobacteria capable of Hg methylation were identified in 16S rRNA sequencing data. Recent publications point to the importance of HgS particle size in determining bioavailability of Hg for potential methylation, and suggest that HgS nanoparticles may be more bioavailable for uptake and potential methylation by microbial cells than larger HgS particles (Poulin et al., 2017). Therefore, were this sediment still in place at the site, continued monitoring of Hg chemical speciation would be required, to ensure MeHg levels were not increasing. Further work could also be done to establish the particle size distribution of HgS in the sediment and whether that could influence net Hg methylation. Long-term monitoring is required to better establish the risks posed by Hg in contaminated sediments and guide decision making regarding potential remediation options if required, as the unregulated deposition of metal-based nanoparticles in terrestrial ecosystems has been shown to threaten the sustainability of the environment and diversity of beneficial microbial populations such as soil bacteria and fungi (Ameen et al., 2021).

This sediment was collected during remedial dredging of the lock, and Hg in this material does not pose additional risk to the surrounding area, as it is no longer in place. However, the characterisation techniques used in this study could be applied at similar sites during risk assessment studies. Typically, when a site is being investigated for the presence of potential ground contamination, the analysis scheduled may only include THg if its previous use at the site has not been identified. If the previous use of Hg on the site is known, then the analysis of elemental, inorganic ionic and MeHg may also be scheduled. The resulting risk assessment undertaken would usually consider the form of Hg and likely pathways of exposure to human health and the environment in the form of the conceptual site model. The techniques applied in this work, allows a more detailed identification and quantification of the various forms of Hg present, and thus establish a better understanding of whether it is likely to pose a risk to the wider environment and/or human health. This tiered approach to sediment risk assessment could be useful for deciding whether disturbing a material through remediation may pose more potential risks than leaving *in situ* if stable and immobile.

Recent research has focused on reductive immobilisation of toxic metal pollutants with electron donor substrates, including iron-nanoparticles (e.g. magnetite, nZVI and Carbo-Iron®), both in situ and at the point of pollution. Experimental work presented in Paper 2 (Section 5) provided insight into the complex biogeochemical interactions between four treatments, in two contrasting anoxic sediment systems, and their impact on solid phase Hg chemical speciation. Geochemical characteristics of the sediment matrices appeared to influence their affinity for Hg(II), aqueous Hg(II) sorbed to MLR sediment more slowly than to EST sediment. Addition of iron-based particle treatments enhanced Hg(II) sorption capacity, notably in MLR sediment systems. Hg transformations in the solid phase seemed to be influenced by multiple factors, including treatment type, sediment matrix characteristics and microbial population. Linear combination fitting of Hg L_{III}-edge EXAFS spectra was able to provide insight into the influence of treatments on Hg chemical speciation over time. NanoFER 25S reduced >95% Hg(II) to Hg(0) over 4 weeks in both MLR and EST systems, and most Hg remained reduced for over one year post-treatment. Hg(0) may not be a desirable endpoint, as although it may initially be associated with the Fe particle surface following reduction processes, its tendency to volatilise poses a risk of atmospheric emission. Hg(II) was reduced to Hg(0) in MLR Carbo-Iron® (60%), MLR biomagnetite (60%) and MLR organic electron donor (25%) systems during the 4 weeks following treatment. It is easier to link Hg(0) formation to microbial pathways in the MLR organic electron donor as there is no influence from added Fe(II) and Fe(0). The remainder of the solid phase Hg was either Hg(II) sorbed to sediment components (10 - 50 %) or beta-HgS (20 - 30 %) in these three systems.

One-year post treatment, >70% solid phase Hg was beta-HgS in MLR systems treated with Carbo-Iron® and organic electron donors, despite minimal SRB activity. Hg sulfide formation was slower in MLR biomagnetite systems over the first year, ~30% was identified as beta-HgS and ~70% more mobile sorbed Hg(II). Furthermore, the SRB population had proliferated significantly (>10% total population) by this time point, therefore continued monitoring of Hg chemical speciation may have revealed more beta-HgS in endpoint samples. Almost 60% solid phase Hg was present as beta-HgS at day 29 in the no treatment MLR system, most of the remaining fraction was Hg(II) sorbed to MLR components. 16S rRNA analysis did not identify many SRB (<0.05% total), suggesting beta-HgS may have formed without the influence of SRB. >90% Hg was more desirable beta-HgS after one year in untreated MLR systems, highlighting that Hg(II) added to anoxic MLR sediment can be naturally attenuated as immobile beta-HgS without the need for treatment.

Hg reduction was not observed in most EST systems over 28 days following treatment, sulfidation appeared to be a more competitive process in 4 systems. NanoFER 25S was the only treatment to induce an observable reducing effect in respect to solid phase Hg transformation over the 4 weeks post-treatment addition, >99% Hg(II) was reduced to Hg(0). In contrast, >99% solid phase Hg from the biomagnetite EST system was beta-HgS in day 29 samples. Beta-HgS formation was also enhanced in the 28 days following addition of Carbo-Iron® and organic electron donors to EST sediment, >80% of solid phase Hg was determined to be beta-HgS in both treatment systems, which is only slightly more than the ~70% HgS identified in the EST no treatment control. The bulk of the remaining Hg was identified as sorbed Hg(II) in these three systems.

EST sediment exhibited much greater microbial diversity than MLR sediment. SRB communities proliferated between day 5 and day 71 in all EST systems, suggesting microbial pathways may play a role in HgS sulfidation. Interestingly, Carbo-Iron®, biomagnetite and biostimulation had contrasting impacts of on Hg chemical speciation in the MLR and EST systems over the first month. These observations highlight the influence of unique sediment characteristics (e.g. pH, elemental composition, and microbial population) on Hg transformation, as sorbed Hg(II) was more likely to be reduced in MLR sediment than EST sediment during the early phase of treatment. More detailed sediment characterisation (e.g. OM content, particle size analysis, EST minerology) could provide a better understanding of the factors contributing to the contrasting impacts of the treatments. Although costly, longer-term monitoring of Hg chemical speciation in EST (one-year and endpoint) and MLR (endpoint) systems would provide greater insight into the fate of Hg, and whether they reach an equilibrium during the experiment.

Biomagnetite seemed to exhibit the most disparity in respect to its influence over Hg chemical speciation in the two sediments, over the early phase of treatment, reducing >60% Hg(II) in the MLR system, but enhancing sulfidation in EST system (>99% beta-HgS). Natural attenuation seemed to have a consistent beneficial effect independent of sediment type, as most Hg was transformed to beta-HgS in both unamended sediment systems. In respect to net Hg methylation, all systems exhibited an increase in MeHg concentration from baseline. However, only Carbo-Iron® seemed to have a notable adverse impact in respect to net methylation, when compared to no treatment systems, which was independent of sediment type. Microbial activity may often have both positive and negative effects in respect to Hg transformation and ecosystem health. SRB may drive HgS formation, as well as stimulate MeHg formation. However, sulfide may also induce iron oxide reduction that could mobilise Hg, that is subsequently immobilised as HgS or sorbed to FeS (Poulton, 2003). IRB may drive iron oxide dissolution, not only mobilising sorbed Hg species, but also stimulating MeHg formation. Throughout this work the identification of key microbial groups focused on 16S rRNA gene sequencing. This is useful in identify organisms likely to reduce sulfate and iron, and also having the potential to transform Hg species directly. The role of the organisms in transformation could be clarified by: (1) using metagenomic data to look for methylation genes, ideally look to see where the genes are (via bins i.e. individual genomes); (2) additional microcosm studies to see if Hg is methylated under a wider range of conditions; (3) seeing if the methylation genes are expressed using metatranscriptomics and correlate with Hg analyses (following on from 1), then; and (4) by looking for mRNA for the genes of interest.

Previously iron-based nanoparticles and biostimulation with organic electron donors have been considered suitable for application in saturated groundwater zones and have been used to remediate organic contaminants and redox active metals, such as Cr (VI), in field or pilot-scale projects (Newsome et al., 2019). However, prospective remediation treatments may have an adverse impact, potentially enhancing formation of more toxic organometallic Hg (e.g. methylation), inhibiting Hg immobilisation (e.g. sulfidation) or (re)mobilising Hg (e.g. reduction and volatilisation) in subsurface sediments. Iron-based nanoparticles should be applied to anoxic groundwater and lagoons with caution in systems containing Hg due to their ability to reduce Hg(II) to volatile Hg(0) under certain conditions, atmospheric release could cause further contamination on a regional to global scale. As previously mentioned, observations suggested that NanoFER 25S was able to induce and maintaining reducing condition over a long period independent of sediment type, capable of not only reducing sorbed Hg(II), but also existing immobile beta-HgS in MLR sediment.

Longer term monitoring of Hg chemical speciation (incl. MeHg) is required to better establish cost-benefit of prospective remediation solutions. Future work should be done to investigate the endpoint stability of solid phase Hg and better understand phase partitioning of Hg (0) within the system by including headspace monitoring of GEM. GEM could be monitored by flushing headspace (e.g. flushing Hg vapour from the gas phase into an acidified $KMnO_4$ trapping solution) or with a gaseous trap monitoring system (e.g. gold coated bead trap) (Bu et al., 2018; Zheng et al., 2007). Column experiments may also help better establish particle mobility through a subsurface sediment system, and subsequent impacts on Hg chemical speciation and biogeochemical parameters at different depths. This research highlights the importance of considering not only the treatment type, but also the individual site conditions (e.g. elemental composition of matrices, local geochemical conditions, microbial community diversity, additional contaminants) when considering *in situ* application of remediation agents. Despite potential beneficial immobilising effects in respect to one contaminant under specific site conditions, intervention may have potentially adverse effects in respect to (re)mobilisation of other contaminants. This highlights the importance of tailoring approaches during site risk assessment and remediation efforts, any intervention should be carefully monitored to ensure that adverse impacts are not being stimulated over the longer term.

A multi-contaminant approach to risk assessment and pollutant mitigation is crucial to developing cost-effective remediation technologies. Valuable new scientific data for experiments reported in the second research paper (Section 5) highlighted the potential risks posed by *in situ* technologies (e.g. nZVI) in relation to potential (re)mobilisation of Hg. As mentioned previously, reduction of Hg(II) to Hg(0), does not necessarily have an immobilising effect due to its volatility, and poses increased risk in respect to atmospheric release of GEM. Existing technologies that attempt to reduce Hg(II) often require costly gaseous capture mechanisms (Mahbub et al., 2016). This led to the consideration of alternative approaches attempting to mitigate these risks through amalgamation of Hg with other metals during treatment. Hg amalgams have historically been widely used in dentistry. Hg(0) has unique properties (including volatility), but alloying reactions with other metals (e.g. Ag and Cu) can form refractory solid amalgams end members that could reduce the tendency of Hg(0) to volatilise to atmosphere in the environment. Previous research has identified the formation of Hg-Cu amalgams in subsurface sediment systems (Hofacker et al., 2013), highlighting a tendency for this type of material to form under certain environmental conditions. Cu(II) is often a co-contaminant of Hg(II) in environmental systems and industrial waste, therefore alloy formation could potential be promoted by addition of nanoparticle treatments capable of simultaneously sorbing and reducing both metals to their elemental form at the particle surface.

The focus of the third research paper (Section 6) was the investigation of the potential for commercial nZVI, biogenic magnetite and Cu-coated iron-based nanoparticles [NanoFER 25S, biomagnetite, Cu-coated NanoFER 25S (Cu-NanoFER 25S) and Cu-coated biomagnetite (Cu-biomagnetite)] to reduce aqueous Hg(II) [and Cu(II)] and form stable immobile $HgCu_{AM}$ phases in batch microcosm experiments. Scientific information from this work acts as 'proof of concept' for a novel remediation solution that may reduce risk posed by volatile Hg(0). Hg and/or Cu was rapidly removed from the aqueous phase of AGW treatment systems following addition of all particle treatments. Hg L_{III}-edge EXAFS model fits revealed that a solid phase $HgCu_{AM}$ likely formed in three treatment systems [Cu-NanoFER 25S with aqueous Hg(II), Cu-Biomagnetite with aqueous Hg(II) and NanoFER 25S with aqueous Hg(II) and Cu(II)], with the bulk of endpoint solid phase Hg determined to be Hg(0) in the additional treatment batches. Hg recovery data from the mini-SEP suggested $HgCu_{AM}$ formed in Cu-biomagnetite Hg(II) microcosms was less recalcitrant than that formed in the Cu-NanoFER 25S Hg(II) and NanoFER 25S Hg(II) Cu(II) systems. SEM and EDS imaging revealed an agglomeration of Hg and Cu in a region of the image that had lower Fe signal, suggesting that the $HgCu_{AM}$ phase may not be associated with the Fe particle surface. There were also, separate areas with high Cu signal but limited Hg signal, suggesting that there may be additional Cu species present, this would be supported by data in the mini-SEP that identified that a large proportion of Cu in biomagnetite systems was the extractable in weak acid. Additional analysis (e.g. Cu k-edge XAS, HAXPES and advanced-TEM) will be needed to better understand Cu chemical speciation in these systems and improve visualisation of interaction(s) between Hg, Cu and Fe at the particle surface interface. Further investigation will assist in establishing how these interactions may be influencing Hg mobility.

Hg and Cu recovery was lower in extracts from $HgCu_{AM}$ phases formed in Cu-containing NanoFER25S systems. Furthermore, recovery was lowest for both Hg [50%] and Cu [43%] from endpoint solid phase extracts from the Cu-NanoFER 25S Hg(II) systems, likely due to the formation of a more stable $HgCu_{AM}$ phase. However, due to the volatility of Hg(0) there is some uncertainty regarding whether the bulk of residual Hg is associated with Cu as a more recalcitrant alloy or whether some GEM may have been emitted from the solid and aqueous phases. EDS imaging revealed a relatively strong Fe signal in the areas of the image with an association of Cu and Hg, signifying that there may be an interaction between Hg, Cu and Fe at the particle surface. Employing advanced-TEM may be able to provide higher resolution imaging capable of resolving interactions at the particle surface interface. Further experimental work is requited to better assess stability of solid phase end products in treatment system, such as application of a more thorough five-step SEP including an aqua regia digest. Gaseous headspace monitoring in batch microcosms would enable GEM quantification and establish the proportion of THg volatilising to the headspace. Experimental and theoretical determination of sorption kinetics and maximum loading in the aqueous systems would also provide additional important scientific information that could be useful for optimising the process.

Better understanding the timescale required for the formation of recalcitrant $HgCu_{AM}$ is essential, as should these new approaches to remediation be scaled up as an industrial wastewater treatment, it would be much more cost-effective for industry to use fast acting treatment technologies. Investigating a wide-range of natural and wastewaters with varying chemical compositions will be needed to provide greater insight into the suitability of using Cu-NanoFER25S and Cu-biomagnetite for treatment of Hg-contaminated waters, as previous work has revealed that water chemistry can influence performance of ZVI (Vernon and Bonzongo, 2014). There are concerns over the longer term fate, transformation, and eco-toxicity of novel nanoscale treatment solution in environmental systems (Crane & Scott 2012). Therefore, these newly developed Cu-biomagnetite and Cu-NanoFER25S particles maybe more easily applied as treatment for Hg-contaminated wastewater in the shorter term. Reduction of toxic wastewater discharge that can harm ecosystems and human health is vital. Column experiments could be setup to simulate *in situ* treatment of anoxic real-world subsurface sediments, contaminated with both Cu(II) and Hg(II), to establish whether stable recalcitrant $HgCu_{AM}$ can form in sediments following addition of nZVI. Biogeochemical monitoring and iTrack mapping could be applied to monitor metal migration and accumulation in different zones and link changes in metal chemical speciation to local biogeochemistry.

In summary, despite potential environmental benefits, *in situ* application of iron-based particle and organic electron donor remedial treatments should be undertaken with caution, despite potential beneficial immobilising effects in respect to one contaminant [e.g. Cr (VI)] under specific site conditions, intervention may have potentially adverse effects in respect to mobilisation of other contaminants [e.g. Hg(II)]. Due to additional concerns over the long-term fate, transformation, and eco-toxicity of nanoparticles, treatments maybe more easily applied at point of pollution source with GEM capture mechanism (e.g. treatment for Hg-contaminated industrial wastewater). Co-treatment of aqueous Hg(II) and Cu(II), which are often co-contaminants associated with industrial wastewaters (e.g. Hg-cell chlor-alkali chemical plants), with nZVI may provide a solution that reduces the need for GEM capture through formation $CuHg_{AM}$. Cu-coated nZVI has also exhibited capacity for the formation of stable $CuHg_{AM}$ phases. However, further stability testing of $CuHg_{AM}$ is needed prior to any future scale-up for industrial application. Information from this research work could contribute to the development of a more bio-geochemically integrated conceptual model for Hg remediation in contaminated environments. Building a comprehensive conceptual model would require collaboration between research laboratories, industry, and policy makers to integrate data from multiple laboratory and field-scale studies globally. The GMOS-Train programme (https://www.gmos-train.eu/) has been created with the purpose of better understanding the global exchange of Hg between atmosphere, hydrosphere, lithosphere, and biosphere, through the implementation of 9 work packages. Researchers will gain expertise through a network with strong inter-sectorial collaboration involving academic and non-academic partners, NGOs and international organisations. The network-based, highly interdisciplinary research training programme includes atmospheric chemistry and physics, aquatic chemistry, ecology, analytical chemistry, multimedia modelling, and the use of science results for policy making. This is the type of large-scale project that is currently ongoing that will integrate data from a range of studies globally including this research and help inform decision making in relation to Hg contaminated land and remediation options if required.

8.0 Personal Development

A summary of events and activities not directly related to my experimental work that have contributed to my personal development.

8.1 Conferences

Manchester Green Summit (March 2018)

Andy Burnham's Greater Manchester Green Summit, at the Manchester Central Convention Complex, provided an opportunity to engage with stakeholders from a wide range of backgrounds in discussions focused on setting a new environmental vision for Greater Manchester. The summit has given me confidence that my research into better understanding the potential of new remediation approaches for Hg could have a positive impact on my local community. A full review of my experience, written for the Geomicro Group blog (web link is below).

https://manchestergeomicro.wordpress.com/2018/04/19/greater-manchester-green-summit/

Contaminated Land and Groundwater - Resources Past and Future (July 2018)

The Geological Society conference explored the role of the contaminated land specialists in management of risk to, and sustainable use of, our increasingly valuable land and groundwater resources.

Society of Brownfield Risk Assessment Conference (December 2018)

This was the first opportunity for me to present some of my initial research finding to an audience working as brownfield risk assessors or providing laboratory or technical services.

Society of Environmental Geochemistry and Health Conference (July 2019)

This provided a fantastic opportunity to present my work on characterising Hg-contaminated canal bed sediment to an audience with an interest in the overlap between geochemistry and health.

International Conference on Mercury as a Global Pollutant (July 2017 and September 2019)

I attended this unique conference focus on Hg pollution as a learning experience in 2017, and then returned to present some of my work investigating the impacts on iron-based nanoparticles on Hg chemical speciation in 2018

Royal Society of Chemistry (RSC) Chemistry of the Whole Environment (25th June 2021)

I had the opportunity to present some of my work investigating the impacts on iron-based nanoparticles via ZOOM at the online event. The conference was one of the best I've attended in the online format, with an interesting range of work relating to environmental chemistry exhibited

8.2 Professional Affiliations

My previous role as an Environmental Consultant required membership of the Institute of Environmental Sciences and the Institute of Air Quality Management. However, I have also recently supplemented my existing professional affiliations by become a member of the Royal Society of Chemistry and the Microbiology Society. Being a member of these professional bodies will provide the opportunity to knowledge share across a network of peers, as well as attend bespoke events, and access cutting edge science relevant to the respective fields.

8.3 Outreach

I have taken part in two outreach events with other members of the Geomicro Group. The group have developed interactive games built around the 'Life at the Extremes' theme to help showcase the importance of our core research work and inspire the next generation of scientists. The first event was the annual Community Festival held at the University of Manchester (UoM) on Saturday 16th June, where research groups from across the university provided an opportunity for members of the community to find out all about our work and get hands-on with a variety of exciting activities. We also took the 'Life at the Extremes' learning experience to Bluedot Festival at Jodrell Bank (Friday 20th July to Sunday 22nd July), where festival goers had the opportunity to explore the realms of music, science, art and culture. I designed an interactive game focused on seven microbial processes that can be used to recover resources from waste – composting, anaerobic digestion, microbial fuel cells, microbial immobilisation, microbial degradation, microbial metal reduction and fermentation. These two events have been valuable experiences, it was very rewarding trying to get children and adults interested in the scientific research work we do, how it provides an understanding of the world around us, and its technological applications.

8.4 Project Mentoring

I designed two 60 credit MSc research projects and mentored two students through their projects from March 2019 to September 2019. Both students were studying for an MSc in Pollution and Environmental Control. Both students wrote high quality dissertations for their projects, achieving a Distinction and a Merit.

8.5 Geomicro Group Blog Editor

I took on responsibility for managing the Geomicro group blog (web link is below) from July 2017 to September 2020. The blog includes profiles for group members and summaries of publications from researchers. Contributions also include short reports on an activity relating to research work done group members (e.g. specialist analysis, conferences, society meetings, outreach events, and field trips). URL: https://manchestergeomicro.wordpress.com/

9.0 References

Author *FastQC*.Available at: https://www.bioinformatics.babraham.ac.uk/projects/fastqc/.

Mindat: Belendorffite. Available at: https://www.mindat.org/min-608.html (Accessed: 16th July).

Mindat: Kolymite. Available at: https://www.mindat.org/min-2244.html (Accessed: 16th July).

Adediran, G. A., Liem-Nguyen, V., Song, Y., Schaefer, J. K., Skyllberg, U. & Björn, E. (2019). 'Microbial Biosynthesis of Thiol Compounds: Implications for Speciation, Cellular Uptake, and Methylation of Hg(II)', *Environmental Science & Technology,* 53(14), pp. 8187-8196.

Allard, B. & Arsenie, I. (1991). 'Abiotic reduction of mercury by humic substances in aquatic system — an important process for the mercury cycle', *Water Air & Soil Pollution,* 56(1), pp. 457-464.

Ameen, F., Alsamhary, K., Alabdullatif, J. A. & Alnadhari, S. (2021). 'A review on metal-based nanoparticles and their toxicity to beneficial soil bacteria and fungi', *Ecotoxicology and Environmental Safety,* 213, p. 112027.

Amos, H. M., Jacob, D. J., Streets, D. G. & Sunderland, E. M. (2013). 'Legacy impacts of all-time anthropogenic emissions on the global mercury cycle', *Global Biogeochemical Cycles,* 27(2), pp. 410-421.

AnglianWater (2018). *Drinking Water Standards*. Available at: https://www.anglianwater.co.uk/siteassets/household/services/dwq-standards.pdf.

Association, S. (Unknown). *The Electrolysis of Brine*: Salt Association. Available at: https://www.saltassociation.co.uk/education/salt-history/salt-the-chemical-revolution/electrolysis-of-brine/ (Accessed: 16th July).

ATSDR (2019). *Substance Priority List*: Agency for Toxic Substances and Disease Registry. Available at: https://www.atsdr.cdc.gov/spl/index.html (Accessed: 16th July).

Barkay, T., Kritee, K., Boyd, E. & Geesey, G. (2010). 'A thermophilic bacterial origin and subsequent constraints by redox, light and salinity on the evolution of the microbial mercuric reductase', *Environmental Microbiology,* 12(11), pp. 2904-2917.

Barkay, T., Miller, S. M. & Summers, A. O. (2003). 'Bacterial mercury resistance from atoms to ecosystems', *FEMS Microbiology Reviews,* 27(2-3), pp. 355-384.

Barkay, T. & Wagner-Döbler, I. (2005). 'Microbial Transformations of Mercury: Potentials, Challenges, and Achievements in Controlling Mercury Toxicity in the Environment', *Advances in Applied Microbiology*: Academic Presspp. 1-52.

Barnett, M. O., Harris, L. A., Turner, R. R., Stevenson, R. J., Henson, T. J., Melton, R. C. & Hoffman, D. P. (1997). 'Formation of Mercuric Sulfide in Soil', *Environmental Science & Technology,* 31(11), pp. 3037-3043.

Barrow, N. J. & Cox, V. C. (1992). 'The effects of pH and chloride concentration on mercury sorption. I. By goethite', *Journal of Soil Science,* 43(2), pp. 295-304.

Bazylinski, D. A., Frankel, R. B. & Konhauser, K. O. (2007). 'Modes of Biomineralization of Magnetite by Microbes', *Geomicrobiology Journal,* 24(6), pp. 465-475.

Benoit, J. M., Mason, R. P. & Gilmour, C. C. (1999). 'Estimation of mercury-sulfide speciation in sediment pore waters using octanol—water partitioning and implications for availability to methylating bacteria', *Environmental Toxicology and Chemistry,* 18(10), pp. 2138-2141.

Bernaus, A., Gaona, X., van Ree, D. & Valiente, M. (2006). 'Determination of mercury in polluted soils surrounding a chlor-alkali plant', *Analytica Chimica Acta,* 565(1), pp. 73-80.

Bernhardt, H. J. & Schmetzer, K. (1992). 'Belendorffite, a new copper amalgam dimorphous with kolymite', *Neues Jahrbuch für Mineralogie. Monatshefte,* 1992(1), p. 21.

Biesinger, M. C., Lau, L. W. M., Gerson, A. R. & Smart, R. S. C. (2010). 'Resolving surface chemical states in XPS analysis of first row transition metals, oxides and hydroxides: Sc, Ti, V, Cu and Zn', *Applied Surface Science,* 257(3), pp. 887-898.

Biester, H., Müller, G. & Schöler, H. F. (2002). 'Binding and mobility of mercury in soils contaminated by emissions from chlor-alkali plants', *Science of The Total Environment,* 284(1), pp. 191-203.

Biester, H. & Scholz, C. (1997). 'Determination of Mercury Binding Forms in Contaminated Soils: Mercury Pyrolysis versus Sequential Extractions', *Environmental Science & Technology,* 31(1), pp. 233-239.

Bloom, N. S., Preus, E., Katon, J. & Hiltner, M. (2003). 'Selective extractions to assess the biogeochemically relevant fractionation of inorganic mercury in sediments and soils', *Analytica Chimica Acta,* 479(2), pp. 233-248.

Brinkmann, T., Giner-Santonja, G., Schorcht, F., Roudier, S. & Sancho, L. (2014). *Best Available Techniques (BAT) Reference Document for the Production of Chlor-alkali*.

Brocza, F. M., Biester, H., Richard, J.-H., Kraemer, S. M. & Wiederhold, J. G. (2019). 'Mercury Isotope Fractionation in the Subsurface of a Hg(II) Chloride-Contaminated Industrial Legacy Site', *Environmental Science & Technology,* 53(13), pp. 7296-7305.

Brombach, C.-C., Gajdosechova, Z., Chen, B., Brownlow, A., Corns, W. T., Feldmann, J. & Krupp, E. M. (2015). 'Direct online HPLC-CV-AFS method for traces of methylmercury without derivatisation: a matrix-independent method for urine, sediment and biological tissue samples', *Analytical and Bioanalytical Chemistry,* 407(3), pp. 973-981.

Bruckner, M. (2021). *Ion Chromatography*. Available at: https://serc.carleton.edu/microbelife/research_methods/biogeochemical/ic.html (Accessed: 30th July).

Bu, X., Zhang, H., Lv, G., Lin, H., Chen, L., Yin, X., Shen, G., Yuan, W., Zhang, W., Wang, X. & Tong, Y. (2018). 'Comparison of Reactive Gaseous Mercury Collection by Different Sampling Methods in a Laboratory Test and Field Monitoring', *Environmental Science & Technology Letters,* 5(10), pp. 600-607.

Byrne, J. M., Coker, V. S., Moise, S., Wincott, P. L., Vaughan, D. J., Tuna, F., Arenholz, E., van der Laan, G., Pattrick, R. A. D., Lloyd, J. R. & Telling, N. D. (2013). 'Controlled cobalt doping in biogenic magnetite nanoparticles', *Journal of The Royal Society Interface,* 10(83).

Byrne, J. M., Muhamadali, H., Coker, V. S., Cooper, J. & Lloyd, J. R. (2015). 'Scale-up of the production of highly reactive biogenic magnetite nanoparticles using Geobacter sulfurreducens', *Journal of The Royal Society Interface,* 12(107).

Byrne, J. M., Telling, N. D., Coker, V. S., Pattrick, R. A. D., Laan, G. v. d., Arenholz, E., Tuna, F. & Lloyd, J. R. (2011). 'Control of nanoparticle size, reactivity and magnetic properties during the bioproduction of magnetite by Geobacter sulfurreducens', *Nanotechnology,* 22(45), p. 455709.

Caporaso, J. G., Kuczynski, J., Stombaugh, J., Bittinger, K., Bushman, F. D., Costello, E. K., Fierer, N., Peña, A. G., Goodrich, J. K., Gordon, J. I., Huttley, G. A., Kelley, S. T., Knights, D., Koenig, J. E., Ley, R. E., Lozupone, C. A., McDonald, D., Muegge, B. D., Pirrung, M., Reeder, J., Sevinsky, J. R., Turnbaugh, P. J., Walters, W. A., Widmann, J., Yatsunenko, T., Zaneveld, J. & Knight, R. (2010). 'QIIME allows analysis of high-throughput community sequencing data', *Nature Methods,* 7(5), pp. 335-336.

Caporaso, J. G., Lauber, C. L., Walters, W. A., Berg-Lyons, D., Huntley, J., Fierer, N., Owens, S. M., Betley, J., Fraser, L., Bauer, M., Gormley, N., Gilbert, J. A., Smith, G. & Knight, R. (2012). 'Ultra-high-throughput microbial community analysis on the Illumina HiSeq and MiSeq platforms', *The ISME Journal,* 6(8), pp. 1621-1624.

Caporaso, J. G., Lauber, C. L., Walters, W. A., Berg-Lyons, D., Lozupone, C. A., Turnbaugh, P. J., Fierer, N. & Knight, R. (2011). 'Global patterns of 16S rRNA diversity at a depth of millions of sequences per sample', *Proceedings of the National Academy of Sciences,* 108(Supplement 1), p. 4516.

Cavoura, O., Brombach, C. C., Cortis, R., Davidson, C. M., Gajdosechova, Z., Keenan, H. E. & Krupp, E. M. (2017). 'Mercury alkylation in freshwater sediments from Scottish canals', *Chemosphere,* 183(Supplement C), pp. 27-35.

Chekli, L., Bayatsarmadi, B., Sekine, R., Sarkar, B., Shen, A. M., Scheckel, K. G., Skinner, W., Naidu, R., Shon, H. K., Lombi, E. & Donner, E. (2016). 'Analytical characterisation of nanoscale zero-valent iron: A methodological review', *Analytica Chimica Acta,* 903, pp. 13-35.

Chen, J. (2009). Determination of Mercury in Wastewater by Inductively Coupled Plasma-Mass Spectrometry. Available at: http://www.perkinelmer.com/pdfs/downloads/APP_MercuryinWastewaterbyICPMS.pdf (Accessed:

Christensen, G. A., Gionfriddo, C. M., King, A. J., Moberly, J. G., Miller, C. L., Somenahally, A. C., Callister, S. J., Brewer, H., Podar, M., Brown, S. D., Palumbo, A. V., Brandt, C. C., Wymore, A. M., Brooks, S. C., Hwang, C., Fields, M. W., Wall, J. D., Gilmour, C. C. & Elias, D. A. (2019). 'Determining the Reliability of Measuring Mercury Cycling Gene Abundance with Correlations with Mercury and Methylmercury Concentrations', *Environmental Science & Technology,* 53(15), pp. 8649-8663.

CL:AIRE (2018). *Withdrawal of the SGV and associated reports for Mercury*. Available at: https://www.claire.co.uk/home/news/1118-withdrawal-of-the-sgv-and-associated-reports-for-mercury (Accessed: 27th July).

Cleckner, L. B., Gilmour, C. C., Hurley, J. P. & Krabbenhoft, D. P. (1999). 'Mercury methylation in periphyton of the Florida Everglades', *Limnology and Oceanography,* 44(7), pp. 1815-1825.

Coenye, T. (2014). 'The Family Burkholderiaceae', in Rosenberg, E., DeLong, E. F., Lory, S., Stackebrandt, E. & Thompson, F. (eds.) *The Prokaryotes: Alphaproteobacteria and Betaproteobacteria*. Berlin, Heidelberg: Springer Berlin Heidelbergpp. 759-776.

Coker, V. S., Bennett, J. A., Telling, N. D., Henkel, T., Charnock, J. M., van der Laan, G., Pattrick, R. A. D., Pearce, C. I., Cutting, R. S., Shannon, I. J., Wood, J., Arenholz, E., Lyon, I. C. & Lloyd, J. R. (2010). 'Microbial Engineering of Nanoheterostructures: Biological Synthesis of a Magnetically Recoverable Palladium Nanocatalyst', *ACS Nano,* 4(5), pp. 2577-2584.

Coker, V. S., Pearce, C. I., Pattrick, R. A. D., Laan, G. v. d., Telling, N. D., Charnock, J. M., Arenholz, E. & Lloyd, J. R. (2008). 'Probing the site occupancies of Co-, Ni-, and Mn-substituted biogenic magnetite using XAS and XMCD', *American Mineralogist,* 93(7), pp. 1119-1132.

Compeau, G. C. & Bartha, R. (1985). 'Sulfate-reducing bacteria: principal methylators of mercury in anoxic estuarine sediment', *Applied and environmental microbiology,* 50(2), pp. 498-502.

Conrad, R. (1999). 'Contribution of hydrogen to methane production and control of hydrogen concentrations in methanogenic soils and sediments', *FEMS Microbiology Ecology,* 28(3), pp. 193-202.

Cooke Andrews, J. (2006). 'Mercury Speciation in the Environment Using X-ray Absorption Spectroscopy', in Atwood, D. A. (ed.) *Recent Developments in Mercury Science*. Berlin, Heidelberg: Springer Berlin Heidelbergpp. 1-35.

Crane, R. A., Dickinson, M., Popescu, I. C. & Scott, T. B. (2011). 'Magnetite and zero-valent iron nanoparticles for the remediation of uranium contaminated environmental water', *Water Research,* 45(9), pp. 2931-2942.

Crane, R. A. & Sapsford, D. J. (2018). 'Selective formation of copper nanoparticles from acid mine drainage using nanoscale zerovalent iron particles', *Journal of Hazardous Materials,* 347, pp. 252-265.

Crane, R. A. & Scott, T. B. (2012). 'Nanoscale zero-valent iron: Future prospects for an emerging water treatment technology', *Journal of Hazardous Materials,* 211-212, pp. 112-125.

Deonarine, A. & Hsu-Kim, H. (2009). 'Precipitation of Mercuric Sulfide Nanoparticles in NOM-Containing Water: Implications for the Natural Environment', *Environmental Science & Technology,* 43(7), pp. 2368-2373.

Dermont, G., Bergeron, M., Mercier, G. & Richer-Laflèche, M. (2008). 'Soil washing for metal removal: A review of physical/chemical technologies and field applications', *Journal of Hazardous Materials,* 152(1), pp. 1-31.

Dong, J., Xu, Z. & Wang, F. (2008). 'Engineering and characterization of mesoporous silica-coated magnetic particles for mercury removal from industrial effluents', *Applied Surface Science,* 254(11), pp. 3522-3530.

Driscoll, C. T., Mason, R. P., Chan, H. M., Jacob, D. J. & Pirrone, N. (2013). 'Mercury as a Global Pollutant: Sources, Pathways, and Effects', *Environmental Science & Technology,* 47(10), pp. 4967-4983.

EC (2010). *European Comission: EU Mercury Strategy*. Available at: http://ec.europa.eu/environment/chemicals/mercury/strategy_en.htm (Accessed: 16th July).

EC (2016). *European Comission: Ratification of the Minamata Convention on Mercury by the EU*. Available at: http://ec.europa.eu/environment/chemicals/mercury/ratification_en.htm (Accessed: 16th July).

EC (2017). *European Comission: Mercury*: European Comission. Available at: http://ec.europa.eu/environment/chemicals/mercury/index_en.htm (Accessed: 16th July).

Edgar, R. C. (2010). 'Search and clustering orders of magnitude faster than BLAST', *Bioinformatics,* 26(19), pp. 2460-2461.

Edgar, R. C. (2013). 'UPARSE: highly accurate OTU sequences from microbial amplicon reads', *Nature Methods,* 10(10), pp. 996-998.

EEA (2018). 'Mercury in Europe's environment: A priority for European and global action'.

Fagerström, T. & Jernelöv, A. (1971). 'Formation of methyl mercury from pure mercuric sulphide in aerobic organic sediment', *Water Research,* 5(3), pp. 121-122.

Author (2019). *CasaXPS*.Available at: casaxps.com.

Feng, X., Li, P., Qiu, G., Wang, S., Li, G., Shang, L., Meng, B., Jiang, H., Bai, W., Li, Z. & Fu, X. (2008). 'Human Exposure To Methylmercury through Rice Intake in Mercury Mining Areas, Guizhou Province, China', *Environmental Science & Technology,* 42(1), pp. 326-332.

Figueiredo, N., Serralheiro, M. L., Canário, J., Duarte, A., Hintelmann, H. & Carvalho, C. (2018). 'Evidence of Mercury Methylation and Demethylation by the Estuarine Microbial Communities Obtained in Stable Hg Isotope Studies', *International journal of environmental research and public health,* 15(10), p. 2141.

FireBird (2018). *Case Study: Diamond Light Source*. Available at: http://www.firebirdpr.co.uk/case-studies/diamond-light-source.html (Accessed: 30th July).

Francis, A. J. (1990). 'Microbial dissolution and stabilization of toxic metals and radionuclides in mixed wastes', *Experientia,* 46(8), pp. 840-851.

Gadd, G. M. (2000). 'Bioremedial potential of microbial mechanisms of metal mobilization and immobilization', *Current Opinion in Biotechnology,* 11(3), pp. 271-279.

Gadd, G. M. (2010). 'Metals, minerals and microbes: geomicrobiology and bioremediation', *Microbiology,* 156(3), pp. 609-643.

Gasmet (2021). *CVAF – Cold Vapor Atomic Fluorescence*. Available at: https://www.gasmet.com/products/cvaf-cold-vapor-atomic-fluorescence/ (Accessed: 30th July).

GeneticEducation (2020). *16S rRNA: Gene, Sequencing and Importance*. Available at: https://geneticeducation.co.in/16s-rrna-gene-sequencing-and-importance/ (Accessed: 30th July).

Gerbig, C. A., Kim, C. S., Stegemeier, J. P., Ryan, J. N. & Aiken, G. R. (2011). 'Formation of Nanocolloidal Metacinnabar in Mercury-DOM-Sulfide Systems', *Environmental Science & Technology,* 45(21), pp. 9180-9187.

Gfeller, L., Weber, A., Worms, I., Slaveykova, V. I. & Mestrot, A. (2021). 'Mercury mobility, colloid formation and methylation in a polluted Fluvisol as affected by manure application and flooding–draining cycle', *Biogeosciences,* 18(11), pp. 3445-3465.

Gilmour, C. C., Henry, E. A. & Mitchell, R. (1992). 'Sulfate stimulation of mercury methylation in freshwater sediments', *Environmental Science & Technology,* 26(11), pp. 2281-2287.

Gilmour, C. C., Podar, M., Bullock, A. L., Graham, A. M., Brown, S. D., Somenahally, A. C., Johs, A., Hurt, R. A., Bailey, K. L. & Elias, D. A. (2013). 'Mercury Methylation by Novel Microorganisms from New Environments', *Environmental Science & Technology,* 47(20), pp. 11810-11820.

Gionfriddo, C. M., Tate, M. T., Wick, R. R., Schultz, M. B., Zemla, A., Thelen, M. P., Schofield, R., Krabbenhoft, D. P., Holt, K. E. & Moreau, J. W. (2016). 'Microbial mercury methylation in Antarctic sea ice', *Nature Microbiology,* 1(10), p. 16127.

Giordano, M. (2009). 'Global Groundwater? Issues and Solutions', *Annual Review of Environment and Resources,* 34(1), pp. 153-178.

Gong, Y., Huang, Y., Wang, M., Liu, F. & Zhang, T. (2019). 'Application of Iron-Based Materials for Remediation of Mercury in Water and Soil', *Bulletin of Environmental Contamination and Toxicology,* 102(5), pp. 721-729.

Gong, Y., Liu, Y., Xiong, Z., Kaback, D. & Zhao, D. (2012). 'Immobilization of mercury in field soil and sediment using carboxymethyl cellulose stabilized iron sulfide nanoparticles', *Nanotechnology,* 23(29), p. 294007.

Gong, Y., Liu, Y., Xiong, Z. & Zhao, D. (2014). 'Immobilization of Mercury by Carboxymethyl Cellulose Stabilized Iron Sulfide Nanoparticles: Reaction Mechanisms and Effects of Stabilizer and Water Chemistry', *Environmental Science & Technology,* 48(7), pp. 3986-3994.

Graham, A. M., Aiken, G. R. & Gilmour, C. C. (2012a). 'Dissolved Organic Matter Enhances Microbial Mercury Methylation Under Sulfidic Conditions', *Environmental Science & Technology,* 46(5), pp. 2715-2723.

Graham, A. M., Bullock, A. L., Maizel, A. C., Elias, D. A. & Gilmour, C. C. (2012b). 'Detailed Assessment of the Kinetics of Hg-Cell Association, Hg Methylation, and Methylmercury Degradation in Several Desulfovibrio Species', *Applied and Environmental Microbiology,* 78(20), p. 7337.

Gregoire, D. S. & Poulain, A. J. (2014). 'A little bit of light goes a long way: the role of phototrophs on mercury cycling', *Metallomics,* 6(3), pp. 396-407.

Guney, M., Akimzhanova, Z., Kumisbek, A., Beisova, K., Kismelyeva, S., Satayeva, A., Inglezakis, V. & Karaca, F. (2020). 'Mercury (Hg) Contaminated Sites in Kazakhstan: Review of Current Cases and Site Remediation Responses', *International Journal of Environmental Research and Public Health,* 17(23), p. 8936.

Gustin, M. S., Biester, H. & Kim, C. S. (2002). 'Investigation of the light-enhanced emission of mercury from naturally enriched substrates', *Atmospheric Environment,* 36(20), pp. 3241-3254.

Haas, B. J., Gevers, D., Earl, A. M., Feldgarden, M., Ward, D. V., Giannoukos, G., Ciulla, D., Tabbaa, D., Highlander, S. K., Sodergren, E., Methé, B., DeSantis, T. Z., Petrosino, J. F., Knight, R. & Birren, B. W. (2011). 'Chimeric 16S rRNA sequence formation and detection in Sanger and 454-pyrosequenced PCR amplicons', *Genome Res,* 21(3), pp. 494-504.

Han, Y., Kingston, H. M., Boylan, H. M., Rahman, G. M. M., Shah, S., Richter, R. C., Link, D. D. & Bhandari, S. (2003). 'Speciation of mercury in soil and sediment by selective solvent and acid extraction', *Analytical and Bioanalytical Chemistry,* 375(3), pp. 428-436.

Hargreaves, A. J., Vale, P., Whelan, J., Constantino, C., Dotro, G. & Cartmell, E. (2016). 'Mercury and antimony in wastewater: fate and treatment', *Water, Air, & Soil Pollution,* 227(3), p. 89.

He, F., Gao, J., Pierce, E., Strong, P. J., Wang, H. & Liang, L. (2015). 'In situ remediation technologies for mercury-contaminated soil', *Environmental Science and Pollution Research,* 22(11), pp. 8124-8147.

Hellal, J., Guédron, S., Huguet, L., Schäfer, J., Laperche, V., Joulian, C., Lanceleur, L., Burnol, A., Ghestem, J.-P., Garrido, F. & Battaglia-Brunet, F. (2015). 'Mercury mobilization and speciation linked to bacterial iron oxide and sulfate reduction: A column study to mimic reactive transfer in an anoxic aquifer', *Journal of Contaminant Hydrology,* 180, pp. 56-68.

Hill, S. J. & Fisher, A. S. (2017). 'Atomic Fluorescence, Methods and Instrumentation', in Lindon, J. C., Tranter, G. E. & Koppenaal, D. W. (eds.) *Encyclopedia of Spectroscopy and Spectrometry (Third Edition)*. Oxford: Academic Presspp. 65-69.

Hitachi (2021). *Principle of XRF Analysis* (Accessed: 30th July).

Hofacker, A. F., Voegelin, A., Kaegi, R. & Kretzschmar, R. (2013). 'Mercury Mobilization in a Flooded Soil by Incorporation into Metallic Copper and Metal Sulfide Nanoparticles', *Environmental Science & Technology,* 47(14), pp. 7739-7746.

Hong, Y.-S., Kim, Y.-M. & Lee, K.-E. (2012). 'Methylmercury exposure and health effects', *Journal of preventive medicine and public health = Yebang Uihakhoe chi,* 45(6), pp. 353-363.

Hu, H., Lin, H., Zheng, W., Tomanicek, S. J., Johs, A., Feng, X., Elias, D. A., Liang, L. & Gu, B. (2013). 'Oxidation and methylation of dissolved elemental mercury by anaerobic bacteria', *Nature Geoscience,* 6(9), pp. 751-754.

Huang, Y.-T., Hseu, Z.-Y. & Hsi, H.-C. (2011). 'Influences of thermal decontamination on mercury removal, soil properties, and repartitioning of coexisting heavy metals', *Chemosphere,* 84(9), pp. 1244-1249.

Hudson, R., Li, C.-J. & Moores, A. (2012). 'Magnetic copper–iron nanoparticles as simple heterogeneous catalysts for the azide–alkyne click reaction in water', *Green Chemistry,* 14(3), pp. 622-624.

Hung, Y. T. E., Wang, L. E., Wang, M. H. E., Shammas, N. E., Chen, J. E. & Wang, L. (2017). *Waste Treatment in the Service and Utility Industries*. Boca Raton: CRC Press.

Huttenloch, P., Roehl, K. E. & Czurda, K. (2003). 'Use of Copper Shavings To Remove Mercury from Contaminated Groundwater or Wastewater by Amalgamation', *Environmental Science & Technology,* 37(18), pp. 4269-4273.

Inglezakis, V. J., Kurbanova, A., Molkenova, A., Zorpas, A. A. & Atabaev, T. S. (2020). 'Magnetic Fe3O4-Ag0 Nanocomposites for Effective Mercury Removal from Water', *Sustainability,* 12(13).

INOVYN (2016a). *INOVYN confirms closure of last remaining mercury cellroom at Runcorn Site*: INOVYN. Available at: https://www.inovyn.com/news/inovyn-confirms-closure-of-last-remaining-mercury-cellroom-at-runcorn-site/ (Accessed: 5th December).

INOVYN (2016b). *INOVYN confirms closure of last remaining mercury cellroom at Runcorn Site (2)*: INOVYN. Available at: https://www.inovyn.com/news/inovyn-confirms-closure-of-last-remaining-mercury-cellroom-at-runcorn-site2/ (Accessed: 5th December).

Issaro, N., Abi-Ghanem, C. & Bermond, A. (2009). 'Fractionation studies of mercury in soils and sediments: A review of the chemical reagents used for mercury extraction', *Analytica Chimica Acta,* 631(1), pp. 1-12.

Iwahori, K., Takeuchi, F., Kamimura, K. & Sugio, T. (2000). 'Ferrous Iron-Dependent Volatilization of Mercury by the Plasma Membrane of Thiobacillus ferrooxidans', *Applied and Environmental Microbiology,* 66(9), pp. 3823-3827.

Jensen, S. & JernelÖV, A. (1969). 'Biological Methylation of Mercury in Aquatic Organisms', *Nature,* 223(5207), pp. 753-754.

Jew, A. D., Kim, C. S., Rytuba, J. J., Gustin, M. S. & Brown, G. E., Jr. (2011). 'New technique for quantification of elemental Hg in mine wastes and its implications for mercury evasion into the atmosphere', *Environmental science & technology,* 45(2), pp. 412-417.

Jiang, C.-y., Sheng, X.-f., Qian, M. & Wang, Q.-y. (2008). 'Isolation and characterization of a heavy metal-resistant Burkholderia sp. from heavy metal-contaminated paddy field soil and its potential in promoting plant growth and heavy metal accumulation in metal-polluted soil', *Chemosphere,* 72(2), pp. 157-164.

Jiang, S., Ho, C. T., Lee, J.-H., Duong, H. V., Han, S. & Hur, H.-G. (2012). 'Mercury capture into biogenic amorphous selenium nanospheres produced by mercury resistant Shewanella putrefaciens 200', *Chemosphere,* 87(6), pp. 621-624.

Jørgensen, B. B., Findlay, A. J. & Pellerin, A. (2019). 'The Biogeochemical Sulfur Cycle of Marine Sediments', *Frontiers in Microbiology,* 10(849).

Author (2011). *sickle - A windowed adaptive trimming tool for FASTQ files using quality*.Available at: https://github.com/najoshi/sickle.

Kaliva, M. & Vamvakaki, M. (2020). 'Chapter 17 - Nanomaterials characterization', in Narain, R. (ed.) *Polymer Science and Nanotechnology*: Elsevierpp. 401-433.

Karlin, R., Lyle, M. & Heath, G. R. (1987). 'Authigenic magnetite formation in suboxic marine sediments', *Nature,* 326(6112), pp. 490-493.

Kerin, E. J., Gilmour, C. C., Roden, E., Suzuki, M. T., Coates, J. D. & Mason, R. P. (2006). 'Mercury Methylation by Dissimilatory Iron-Reducing Bacteria', *Applied and Environmental Microbiology,* 72(12), pp. 7919-7921.

Kim, C. S., Brown, G. E. & Rytuba, J. J. (2000). 'Characterization and speciation of mercury-bearing mine wastes using X-ray absorption spectroscopy', *Science of The Total Environment,* 261(1), pp. 157-168.

Kim, C. S., Rytuba, J. J. & Brown, G. E. (2004). 'Geological and anthropogenic factors influencing mercury speciation in mine wastes: an EXAFS spectroscopy study', *Applied Geochemistry,* 19(3), pp. 379-393.

Kimber, R. L., Parmeggiani, F., Joshi, N., Rakowski, A. M., Haigh, S. J., Turner, N. J. & Lloyd, J. R. (2019). 'Synthesis of copper catalysts for click chemistry from distillery wastewater using magnetically recoverable bionanoparticles', *Green Chemistry,* 21(15), pp. 4020-4024.

Kocman, D., Horvat, M., Pirrone, N. & Cinnirella, S. (2013). 'Contribution of contaminated sites to the global mercury budget', *Environmental Research,* 125, pp. 160-170.

Kozich, J. J., Westcott, S. L., Baxter, N. T., Highlander, S. K. & Schloss, P. D. (2013). 'Development of a Dual-Index Sequencing Strategy and Curation Pipeline for Analyzing Amplicon Sequence Data on the MiSeq Illumina Sequencing Platform', *Applied and Environmental Microbiology,* 79(17), p. 5112.

Kusnadhi, F. (2015). *Agilent 7500 Series ICP-MS: An Introduction* (Accessed: 30th July).

Lamas, D. G., de Oliveira Neto, M., Kellermann, G. & Craievich, A. F. (2017). '5 - X-Ray Diffraction and Scattering by Nanomaterials', in Da Róz, A. L., Ferreira, M., de Lima Leite, F. & Oliveira, O. N. (eds.) *Nanocharacterization Techniques*: William Andrew Publishingpp. 111-182.

Lancaster, S. T., Brombach, C.-C., Corns, W. T., Feldmann, J. & Krupp, E. M. (2019). 'Determination of methylmercury using liquid chromatography – photochemical vapour generation – atomic fluorescence spectroscopy (LC-PVG-AFS): a simple, green analytical method', *Journal of Analytical Atomic Spectrometry,* 34(6), pp. 1166-1172.

Lemming, G., Hauschild, M. Z. & Bjerg, P. L. (2009). 'Life cycle assessment of soil and groundwater remediation technologies: literature review', *The International Journal of Life Cycle Assessment,* 15(1), p. 115.

Lewis, A. S., Huntington, T. G., Marvin-DiPasquale, M. C. & Amirbahman, A. (2016). 'Mercury remediation in wetland sediment using zero-valent iron and granular activated carbon', *Environmental Pollution,* 212, pp. 366-373.

Li, X.-q., Elliott, D. W. & Zhang, W.-x. (2006). 'Zero-Valent Iron Nanoparticles for Abatement of Environmental Pollutants: Materials and Engineering Aspects', *Critical Reviews in Solid State and Materials Sciences,* 31(4), pp. 111-122.

Li, Z., Greden, K., Alvarez, P. J. J., Gregory, K. B. & Lowry, G. V. (2010). 'Adsorbed Polymer and NOM Limits Adhesion and Toxicity of Nano Scale Zerovalent Iron to E. coli', *Environmental Science & Technology,* 44(9), pp. 3462-3467.

Lin, H., Ascher, D. B., Myung, Y., Lamborg, C. H., Hallam, S. J., Gionfriddo, C. M., Holt, K. E. & Moreau, J. W. (2021). 'Mercury methylation by metabolically versatile and cosmopolitan marine bacteria', *The ISME Journal,* 15(6), pp. 1810-1825.

Liu, J., Valsaraj, K. T. & Delaune, R. D. (2009). 'Inhibition of Mercury Methylation by Iron Sulfides in an Anoxic Sediment', *Environmental Engineering Science,* 26(4), pp. 833–840.

Liu, S. & Wiatrowski, H. A. (2018). 'Reduction of Hg(II) to Hg(0) by Biogenic Magnetite from two Magnetotactic Bacteria', *Geomicrobiology Journal,* 35(3), pp. 198-208.

Liu, T., Wang, Z.-L., Yan, X. & Zhang, B. (2014). 'Removal of mercury (II) and chromium (VI) from wastewater using a new and effective composite: Pumice-supported nanoscale zero-valent iron', *Chemical Engineering Journal,* 245(Supplement C), pp. 34-40.

Liu, Y. & Wang, J. (2019). 'Reduction of nitrate by zero valent iron (ZVI)-based materials: A review', *Science of The Total Environment,* 671, pp. 388-403.

Lovley, D. R., Phillips, E. J. P. & Lonergan, D. J. (1989). 'Hydrogen and Formate Oxidation Coupled to Dissimilatory Reduction of Iron or Manganese by Alteromonas putrefaciens', *Applied and Environmental Microbiology,* 55(3), p. 700.

Lu, X., Liu, Y., Johs, A., Zhao, L., Wang, T., Yang, Z., Lin, H., Elias, D. A., Pierce, E. M., Liang, L., Barkay, T. & Gu, B. (2016). 'Anaerobic Mercury Methylation and Demethylation by Geobacter bemidjiensis Bem', *Environmental Science & Technology,* 50(8), pp. 4366-4373.

Mackenzie, K., Bleyl, S., Georgi, A. & Kopinke, F.-D. (2012). 'Carbo-Iron – An Fe/AC composite – As alternative to nano-iron for groundwater treatment', *Water Research,* 46(12), pp. 3817-3826.

Mackenzie, K., Bleyl, S., Kopinke, F.-D., Doose, H. & Bruns, J. (2016). 'Carbo-Iron as improvement of the nanoiron technology: From laboratory design to the field test', *Science of The Total Environment,* 563-564, pp. 641-648.

MAGU (2021). *Manchester Analytical Geochemistry Unit: Inductively Coupled Plasma - Mass Spectrometry (ICP-MS).* Available at: https://www.ees.manchester.ac.uk/wrc/research/facilities/magu/ (Accessed: 31st July).

Mahbub, K. R., Bahar, M. M., Labbate, M., Krishnan, K., Andrews, S., Naidu, R. & Megharaj, M. (2017). 'Bioremediation of mercury: not properly exploited in contaminated soils!', *Applied Microbiology and Biotechnology*, pp. 1-14.

Mahbub, K. R., Krishnan, K., Megharaj, M. & Naidu, R. (2016). 'Bioremediation potential of a highly mercury resistant bacterial strain Sphingobium SA2 isolated from contaminated soil', *Chemosphere,* 144, pp. 330-337.

Manceau, A., Lemouchi, C., Enescu, M., Gaillot, A.-C., Lanson, M., Magnin, V., Glatzel, P., Poulin, B. A., Ryan, J. N., Aiken, G. R., Gautier-Luneau, I. & Nagy, K. L. (2015). 'Formation of Mercury Sulfide from Hg(II)–Thiolate Complexes in Natural Organic Matter', *Environmental Science & Technology,* 49(16), pp. 9787-9796.

Margalef-Marti, R., Carrey, R., Benito, J. A., Marti, V., Soler, A. & Otero, N. (2020). 'Nitrate and nitrite reduction by ferrous iron minerals in polluted groundwater: Isotopic characterization of batch experiments', *Chemical Geology,* 548, p. 119691.

Markovo, E. A. (1982). 'The new mineral kolymite, Cu7Hg6', *International Geology Review,* 24(2), pp. 233-237.

Martin, M. (2011). 'Cutadapt removes adapter sequences from high-throughput sequencing reads', *EMBnet.journal; Vol 17, No 1: Next Generation Sequencing Data AnalysisDO - 10.14806/ej.17.1.200*.

Masella, A. P., Bartram, A. K., Truszkowski, J. M., Brown, D. G. & Neufeld, J. D. (2012). 'PANDAseq: paired-end assembler for illumina sequences', *BMC Bioinformatics,* 13, p. 31.

Mason, R. P., Kim, E.-H., Cornwell, J. & Heyes, D. (2006). 'An examination of the factors influencing the flux of mercury, methylmercury and other constituents from estuarine sediment', *Marine Chemistry,* 102(1), pp. 96-110.

McCarthy, D., Edwards, G. C., Gustin, M. S., Care, A., Miller, M. B. & Sunna, A. (2017). 'An innovative approach to bioremediation of mercury contaminated soils from industrial mining operations', *Chemosphere,* 184, pp. 694-699.

Morgan, H., De Burca, R., Martin, I. & Jeffries, J. (2009). *Soil Guideline Values for mercury in soil* Environment Agency.

Muhamadali, H., Xu, Y., Ellis, D. I., Allwood, J. W., Rattray, N. J. W., Correa, E., Alrabiah, H., Lloyd, J. R. & Goodacre, R. (2015). 'Metabolic Profiling of Geobacter sulfurreducens during Industrial Bioprocess Scale-Up', *Applied and environmental microbiology,* 81(10), pp. 3288-3298.

Mukherjee, R., Kumar, R., Sinha, A., Lama, Y. & Saha, A. K. (2016). 'A review on synthesis, characterization, and applications of nano zero valent iron (nZVI) for environmental remediation', *Critical Reviews in Environmental Science and Technology,* 46(5), pp. 443-466.

Nakamura, K., Hagimine, M., Sakai, M. & Furukawa, K. (1999). 'Removal of mercury from mercury-contaminated sediments using a combined method of chemical leaching and volatilization of mercury by bacteria', *Biodegradation,* 10(6), pp. 443-447.

Nascimento, A. M. A. & Chatone-Sonza, E. (2003). 'Operon mer: Bacterial resistance to mercury and potential for bioremediation of contaminated environments', *Genet. Mol. Res.,* 2(1), pp. 92-101.

Neculita, C.-M., Zagury, G. J. & Deschênes, L. (2005). 'Mercury Speciation in Highly Contaminated Soils from Chlor-Alkali Plants Using Chemical Extractions', *Journal of Environmental Quality,* 34(1), pp. 255-262.

Nedwell, D. B. & Banat, I. M. (1981). 'Hydrogen as an electron donor for sulfate-reducing bacteria in slurries of salt marsh sediment', *Microbial Ecology,* 7(4), pp. 305-313.

Newsome, L., Morris, K., Cleary, A., Masters-Waage, N. K., Boothman, C., Joshi, N., Atherton, N. & Lloyd, J. R. (2019). 'The impact of iron nanoparticles on technetium-contaminated groundwater and sediment microbial communities', *Journal of Hazardous Materials,* 364, pp. 134-142.

Nurk, S., Bankevich, A., Antipov, D., Gurevich, A., Korobeynikov, A., Lapidus, A., Prjibelsky, A., Pyshkin, A., Sirotkin, A., Sirotkin, Y., Stepanauskas, R., McLean, J., Lasken, R., Clingenpeel, S. R., Woyke, T., Tesler, G., Alekseyev, M. A. & Pevzner, P. A. (2013). Assembling Genomes and Mini-metagenomes from Highly Chimeric Reads. *In:* Deng, M., Jiang, R., Sun, F. & Zhang, X., eds. Research in Computational Molecular Biology, 2013// 2013 Berlin, Heidelberg. Springer Berlin Heidelberg. pp. 158-170.

O'Connor, D., Hou, D., Ok, Y. S., Mulder, J., Duan, L., Wu, Q., Wang, S., Tack, F. M. G. & Rinklebe, J. (2019). 'Mercury speciation, transformation, and transportation in soils, atmospheric flux, and implications for risk management: A critical review', *Environment International,* 126, pp. 747-761.

O'Brien, T. F., Bommaraju, T. V. & Hine, F. (2005). in O'Brien, T. F., Bommaraju, T. V. & Hine, F. (eds.) *Handbook of Chlor-Alkali Technology: Volume I: Fundamentals, Volume II: Brine Treatment and Cell Operation, Volume III: Facility Design and Product Handling, Volume IV: Plant Commissioning and Support Systems, Volume V: Corrosion, Environmental Issues, and Future Development*. Boston, MA: Springer US.

O'Loughlin, E. J., Kelly, S. D., Kemner, K. M., Csencsits, R. & Cook, R. E. (2003). 'Reduction of AgI, AuIII, CuII, and HgII by FeII/FeIII hydroxysulfate green rust', *Chemosphere,* 53(5), pp. 437-446.

Olli, K. (2021). *Benthic mineralization processes of aquatic sediments*. Available at: https://kodu.ut.ee/~olli/eutr/html/htmlBook_93.html (Accessed: 31st July).

Olson, B. H. & Cooper, R. C. (1976). 'Comparison of aerobic and anaerobic methylation of mercuric chloride by San Francisco Bay sediments', *Water Research,* 10(2), pp. 113-116.

Olson, M. & Dewild, J. (1999). 'Techniques for the collection and species-specific analysis of low levels of mercury in water, sediment, and biota', *US Geological Survey Toxic Substances Hydrology Program - Proceedings of the Technical Meeting*.

Otto, M. & Bajpai, S. (2007). 'Treatment technologies for mercury in soil, waste, and water', *Remediation Journal,* 18(1), pp. 21-28.

Passariello, B., Barbaro, M., Quaresima, S., Casciello, A. & Marabini, A. (1996). 'Determination of Mercury by Inductively Coupled Plasma—Mass Spectrometry', *Microchemical Journal,* 54(4), pp. 348-354.

Paulo, L. M., Stams, A. J. M. & Sousa, D. Z. (2015). 'Methanogens, sulphate and heavy metals: a complex system', *Reviews in Environmental Science and Bio/Technology,* 14(4), pp. 537-553.

Phenrat, T. & Kumloet, I. (2016). 'Electromagnetic induction of nanoscale zerovalent iron particles accelerates the degradation of chlorinated dense non-aqueous phase liquid: Proof of concept', *Water Research,* 107, pp. 19-28.

Phenrat, T., Saleh, N., Sirk, K., Tilton, R. D. & Lowry, G. V. (2007). 'Aggregation and Sedimentation of Aqueous Nanoscale Zerovalent Iron Dispersions', *Environmental Science & Technology,* 41(1), pp. 284-290.

Phipps, O., Barrett, J., Hesketh, P., Brown, R. & NICOLE, o. b. o. (2013). 'Risked Based Management of Mercury Impacted Sites', *NICOLE*.

Pirrone, N., Cinnirella, S., Feng, X., Finkelman, R. B., Friedli, H. R., Leaner, J., Mason, R., Mukherjee, A. B., Stracher, G. B., Streets, D. G. & Telmer, K. (2010). 'Global mercury emissions to the atmosphere from anthropogenic and natural sources', *Atmos. Chem. Phys.,* 10(13), pp. 5951-5964.

Potts, P. J. (1987). 'X-ray fluorescence analysis: principles and practice of wavelength dispersive spectrometry', in Potts, P. J. (ed.) *A Handbook of Silicate Rock Analysis*. Dordrecht: Springer Netherlandspp. 226-285.

Poulin, B. A., Gerbig, C. A., Kim, C. S., Stegemeier, J. P., Ryan, J. N. & Aiken, G. R. (2017). 'Effects of Sulfide Concentration and Dissolved Organic Matter Characteristics on the Structure of Nanocolloidal Metacinnabar', *Environmental Science & Technology,* 51(22), pp. 13133-13142.

Poulton, S. W. (2003). 'Sulfide oxidation and iron dissolution kinetics during the reaction of dissolved sulfide with ferrihydrite', *Chemical Geology,* 202(1), pp. 79-94.

PSAnalytical (2021). *PSA Millennium Merlin 10.025* Available at: https://www.psanalytical.com/products/millenniummerlin.html (Accessed: 30th July).

Quast, C., Pruesse, E., Yilmaz, P., Gerken, J., Schweer, T., Yarza, P., Peplies, J. & Glöckner, F. O. (2013). 'The SILVA ribosomal RNA gene database project: improved data processing and web-based tools', *Nucleic acids research,* 41(Database issue), pp. D590-D596.

Randall, P. M. & Chattopadhyay, S. (2013). 'Mercury contaminated sediment sites—An evaluation of remedial options', *Environmental Research,* 125, pp. 131-149.

Raposo, R. R., Meléndez-Hevia, E. & Spiro, M. (2000). 'Autocatalytic formation of colloidal mercury in the redox reaction between Hg2+ and Fe2+ and between Hg22+ and Fe2+', *Journal of Molecular Catalysis A: Chemical,* 164(1), pp. 49-59.

Ravel, B. & Newville, M. (2005). 'ATHENA, ARTEMIS, HEPHAESTUS: data analysis for X-ray absorption spectroscopy using IFEFFIT', *Journal of Synchrotron Radiation,* 12(4), pp. 537-541.

Ravichandran, M. (2004). 'Interactions between mercury and dissolved organic matter—a review', *Chemosphere,* 55(3), pp. 319-331.

Ravichandran, M., Aiken, G. R., Ryan, J. N. & Reddy, M. M. (1999). 'Inhibition of Precipitation and Aggregation of Metacinnabar (Mercuric Sulfide) by Dissolved Organic Matter Isolated from the Florida Everglades', *Environmental Science & Technology,* 33(9), pp. 1418-1423.

Ren, W.-X., Li, P.-J., Geng, Y. & Li, X.-J. (2009). 'Biological leaching of heavy metals from a contaminated soil by Aspergillus niger', *Journal of Hazardous Materials,* 167(1), pp. 164-169.

Richter, R. B. & Flachberger, H. (2010). 'Soil Washing and Thermal Desorption: Reliable Techniques for Remediating Materials Contaminated with Mercury', *BHM Berg- und Hüttenmännische Monatshefte,* 155(12), pp. 571-577.

Roberts, A. P. (2015). 'Magnetic mineral diagenesis', *Earth-Science Reviews,* 151, pp. 1-47.

Ruiz, O. N., Hussein, H. S., Terry, N. & Daniell, H. (2003). 'Phytoremediation of Organomercurial Compounds via Chloroplast Genetic Engineering', *Plant Physiology,* 132(3), pp. 1344-1352.

Salame, P. H., Pawade, V. B. & Bhanvase, B. A. (2018). 'Chapter 3 - Characterization Tools and Techniques for Nanomaterials', in Bhanvase, B. A., Pawade, V. B., Dhoble, S. J., Sonawane, S. H. & Ashokkumar, M. (eds.) *Nanomaterials for Green Energy*: Elsevierpp. 83-111.

Sánchez, D. M., Quejido, A. J., Fernández, M., Hernández, C., Schmid, T., Millán, R., González, M., Aldea, M., Martín, R. & Morante, R. (2005). 'Mercury and trace element fractionation in

Almaden soils by application of different sequential extraction procedures', *Analytical and Bioanalytical Chemistry,* 381(8), pp. 1507-1513.

Santoro, A., Terzano, R., Blo, G., Fiore, S., Mangold, S. & Ruggiero, P. (2010). 'Mercury speciation in the colloidal fraction of a soil polluted by a chlor-alkali plant: A case study in the South of Italy', *Journal of synchrotron radiation,* 17, pp. 187-92.

Saouter, E., Gillman, M. & Barkay, T. (1995). 'An evaluation ofmer-specified reduction of ionic mercury as a remedial tool of a mercury-contaminated freshwater pond', *Journal of Industrial Microbiology,* 14(3), pp. 343-348.

Schwertmann, U. & Cornell, R. M. (2000). *Iron Oxides in the Laboratory: Preparation and Characterization*: Wiley-VCH.

Serrano, S., Vlassopoulos, D., Bessinger, B. & O'Day, P. A. (2012). 'Immobilization of Hg(II) by Coprecipitation in Sulfate-Cement Systems', *Environmental Science & Technology,* 46(12), pp. 6767-6775.

Serrano, S., Vlassopoulos, D. & O'Day, P. A. (2016). 'Mechanism of Hg(II) Immobilization in Sediments by Sulfate-Cement Amendment', *Applied geochemistry : journal of the International Association of Geochemistry and Cosmochemistry,* 67, pp. 68-80.

Siddiquee, S. (2017). 'The Basic Concept of Microbiology', *Practical Handbook of the Biology and Molecular Diversity of Trichoderma Species from Tropical Regions*, pp. 1-15.

Skyllberg, U. (2010). 'Chapter 13 - Mercury Biogeochemistry in Soils and Sediments', in Singh, B. & Gräfe, M. (eds.) *Developments in Soil Science*: Elsevierpp. 379-410.

Spectro (2021a). *ICP-OES Explained: Revealing the Sample's Secrets*. Available at: https://www.spectro.com/icp-oes-principle (Accessed: 30th July).

Spectro (2021b). *XRF Explained: The Fundamentals of XRF*. Available at: https://www.spectro.com/xrf-principle (Accessed: 30th July).

Subirés-Muñoz, J. D., García-Rubio, A., Vereda-Alonso, C., Gómez-Lahoz, C., Rodríguez-Maroto, J. M., García-Herruzo, F. & Paz-García, J. M. (2011). 'Feasibility study of the use of different extractant agents in the remediation of a mercury contaminated soil from Almaden', *Separation and Purification Technology,* 79(2), pp. 151-156.

Svensson, M., Allard, B. & Düker, A. (2006). 'Formation of HgS—mixing HgO or elemental Hg with S, FeS or FeS2', *Science of The Total Environment,* 368, pp. 418-423.

Swapp, S. (2021). *Scanning Electron Microscopy (SEM)*. Available at: https://serc.carleton.edu/research_education/geochemsheets/techniques/SEM.html (Accessed: 30th July).

Tada, Y., Marumoto, K. & Takeuchi, A. (2020). 'Nitrospina-Like Bacteria Are Potential Mercury Methylators in the Mesopelagic Zone in the East China Sea', *Frontiers in Microbiology,* 11(1369).

Trypuć, M. & Białowicz, K. (2011). 'CaCO3 production using liquid waste from Solvay method', *Journal of Cleaner Production,* 19(6), pp. 751-756.

Tungittiplakorn, W., Lion, L. W., Cohen, C. & Kim, J.-Y. (2004). 'Engineered Polymeric Nanoparticles for Soil Remediation', *Environmental Science & Technology,* 38(5), pp. 1605-1610.

Turner, R. R. & Southworth, G. R. (1999). 'Mercury-Contaminated Industrial and Mining Sites in North America: an Overview with Selected Case Studies', in Ebinghaus, R., Turner, R. R., de Lacerda, L. D., Vasiliev, O. & Salomons, W. (eds.) *Mercury Contaminated Sites: Characterization, Risk Assessment and Remediation*. Berlin, Heidelberg: Springer Berlin Heidelbergpp. 89-112.

UNEP (2019). *Global Mercury Assessment 2018*: UN Environment Programme, Chemicals and Health Branch Geneva, Switzerland.

USEPA (1997). *Mercury Study Report to Congress*: Office of Air Quality Planning & Standards and Office of Research and Development, U.S. Environmental Protection AgencyEPA/452/R-96/001A-H).

Vélez, E., Campillo, G. E., Morales, G., Hincapié, C., Osorio, J., Arnache, O., Uribe, J. I. & Jaramillo, F. (2016). 'Mercury removal in wastewater by iron oxide nanoparticles', *Journal of Physics: Conference Series,* 687, p. 012050.

Vernon, J. D. & Bonzongo, J.-C. J. (2014). 'Volatilization and sorption of dissolved mercury by metallic iron of different particle sizes: Implications for treatment of mercury contaminated water effluents', *Journal of Hazardous Materials,* 276, pp. 408-414.

Villar, E., Cabrol, L. & Heimbürger-Boavida, L.-E. (2020). 'Widespread microbial mercury methylation genes in the global ocean', *Environmental Microbiology Reports,* 12(3), pp. 277-287.

von Canstein, H., Li, Y., Timmis, K. N., Deckwer, W. D. & Wagner-Döbler, I. (1999). 'Removal of Mercury from Chloralkali Electrolysis Wastewater by a Mercury-Resistant Pseudomonas putida Strain', *Applied and Environmental Microbiology,* 65(12), pp. 5279-5284.

Wagner-Döbler, I., von Canstein, H., Li, Y., Leonhäuser, J. & Deckwer, W. D. (2003). 'Process-Integrated Microbial Mercury Removal from Wastewater of Chlor-Alkali Electrolysis Plants', *Engineering in Life Sciences,* 3(4), pp. 177-181.

Wang, J., Feng, X., Anderson, C. W. N., Xing, Y. & Shang, L. (2012). 'Remediation of mercury contaminated sites – A review', *Journal of Hazardous Materials,* 221–222, pp. 1-18.

Wang, L., Hou, D., Cao, Y., Ok, Y. S., Tack, F. M. G., Rinklebe, J. & O'Connor, D. (2020). 'Remediation of mercury contaminated soil, water, and air: A review of emerging materials and innovative technologies', *Environment International,* 134, p. 105281.

Wang, L., Wang, L.-a., Zhan, X., Huang, Y., Wang, J. & Wang, X. (2020). 'Response mechanism of microbial community to the environmental stress caused by the different mercury concentration in soils', *Ecotoxicology and Environmental Safety,* 188, p. 109906.

Wang, Q., Garrity, G. M., Tiedje, J. M. & Cole, J. R. (2007). 'Naïve Bayesian Classifier for Rapid Assignment of rRNA Sequences into the New Bacterial Taxonomy', *Applied and Environmental Microbiology,* 73(16), p. 5261.

Wang, Y., Freedman, Z., Lu-Irving, P., Kaletsky, R. & Barkay, T. (2009). 'An initial characterization of the mercury resistance (mer) system of the thermophilic bacterium Thermus thermophilus HB27', *FEMS Microbiology Ecology,* 67(1), pp. 118-129.

Wang, Y., Li, B., Zhang, L., Li, P., Wang, L. & Zhang, J. (2012). 'Multifunctional Magnetic Mesoporous Silica Nanocomposites with Improved Sensing Performance and Effective Removal Ability toward Hg(II)', *Langmuir,* 28(2), pp. 1657-1662.

Wasay, S. A., Arnfalk, P. & Tokunaga, S. (1995). 'Remediation of a soil polluted by mercury with acidic potassium iodide', *Journal of Hazardous Materials,* 44(1), pp. 93-102.

Watts, M. P., Coker, V. S., Parry, S. A., Pattrick, R. A. D., Thomas, R. A. P., Kalin, R. & Lloyd, J. R. (2015). 'Biogenic nano-magnetite and nano-zero valent iron treatment of alkaline Cr(VI) leachate and chromite ore processing residue', *Applied Geochemistry,* 54(Supplement C), pp. 27-42.

Watts, M. P. & Lloyd, J. R. (2012). 'Bioremediation via Microbial Metal Reduction', in Gescher, J. & Kappler, A. (eds.) *Microbial Metal Respiration: From Geochemistry to Potential Applications*. Berlin, Heidelberg: Springer Berlin Heidelbergpp. 161-201.

Weil, M., Mackenzie, K., Foit, K., Kühnel, D., Busch, W., Bundschuh, M., Schulz, R. & Duis, K. (2019). 'Environmental risk or benefit? Comprehensive risk assessment of groundwater treated with nano Fe0-based Carbo-Iron®', *Science of The Total Environment,* 677, pp. 156-166.

WHO (2017). *World Health Organisation: Mercury and Health*: World Health Organisation. Available at: https://www.who.int/news-room/fact-sheets/detail/mercury-and-health (Accessed: 27th July).

Wiatrowski, H. A., Das, S., Kukkadapu, R., Ilton, E. S., Barkay, T. & Yee, N. (2009). 'Reduction of Hg(II) to Hg(0) by Magnetite', *Environmental Science & Technology,* 43(14), pp. 5307-5313.

Wiatrowski, H. A., Ward, P. M. & Barkay, T. (2006). 'Novel Reduction of Mercury(II) by Mercury-Sensitive Dissimilatory Metal Reducing Bacteria', *Environmental Science & Technology,* 40(21), pp. 6690-6696.

Willey, J. M., Sherwood, L., Woolverton, C. J. & Prescott, L. M. (2009). *Prescott's principles of microbiology*. Boston: McGraw-Hill Higher Education.

Xiong, Z., He, F., Zhao, D. & Barnett, M. O. (2009). 'Immobilization of mercury in sediment using stabilized iron sulfide nanoparticles', *Water Research,* 43(20), pp. 5171-5179.

XPSSimplified (2021). *What is X-Ray Photoelectron Spectroscopy (XPS)?* Available at: https://xpssimplified.com/whatisxps.php (Accessed: 30th July).

Xu, J., Bland, G. D., Gu, Y., Ziaei, H., Xiao, X., Deonarine, A., Reible, D., Bireta, P., Hoelen, T. P. & Lowry, G. V. (2021). 'Impacts of Sediment Particle Grain Size and Mercury Speciation on Mercury Bioavailability Potential', *Environmental Science & Technology,* 55(18), pp. 12393-12402.

Yan, W., Herzing, A. A., Kiely, C. J. & Zhang, W.-x. (2010). 'Nanoscale zero-valent iron (nZVI): Aspects of the core-shell structure and reactions with inorganic species in water', *Journal of Contaminant Hydrology,* 118(3), pp. 96-104.

Yap, W., Zhang, W., Guo, Z. & Yang, Z. (2010). *Cold Vapor Atomic Fluorescence Spectrometry and ICP-MS for Sensitive Monitoring of Mercury in Water*.

Yin, Y., Allen, H. E., Li, Y., Huang, C. P. & Sanders, P. F. (1996). 'Adsorption of Mercury(II) by Soil: Effects of pH, Chloride, and Organic Matter', *Journal of Environmental Quality,* 25(4), pp. 837-844.

Zargoosh, K., Abedini, H., Abdolmaleki, A. & Molavian, M. R. (2013). 'Effective Removal of Heavy Metal Ions from Industrial Wastes Using Thiosalicylhydrazide-Modified Magnetic Nanoparticles', *Industrial & Engineering Chemistry Research,* 52(42), pp. 14944-14954.

Zhang, T., Kim, B., Levard, C., Reinsch, B. C., Lowry, G. V., Deshusses, M. A. & Hsu-Kim, H. (2012). 'Methylation of Mercury by Bacteria Exposed to Dissolved, Nanoparticulate, and Microparticulate Mercuric Sulfides', *Environmental Science & Technology,* 46(13), pp. 6950-6958.

Zhang, W.-x. (2003). 'Nanoscale Iron Particles for Environmental Remediation: An Overview', *Journal of Nanoparticle Research,* 5(3), pp. 323-332.

Zheng, W., Foucher, D. & Hintelmann, H. (2007). 'Mercury isotope fractionation during volatilization of Hg(0) from solution into the gas phase', *Journal of Analytical Atomic Spectrometry,* 22(9), pp. 1097-1104.

Zhizhaev, A. M., Merkulova, E. N. & Bragin, I. V. (2007). 'Copper precipitation from sulfate solutions with calcium carbonates', *Russian Journal of Applied Chemistry,* 80(10), pp. 1632-1635.